UNIVERSITY OF SOUTHAMPTON

Electrochemical, Photographic, Luminescent and Acoustic Characterisation of Cavitation

By
John Francis Power

A thesis submitted for the degree of

DOCTOR OF PHILOSOPHY

The Electrochemistry Group,
Department of Chemistry;
And
Fluid Dynamics and Acoustics Group,
Institute of Sound and Vibration Research,

Faculty of Engineering and Applied Science.

January 2003

UNIVERSITY OF SOUTHAMPTON

ABSTRACT

Faculty of Engineering and Applied Science
Department of Chemistry
Institute of Sound and Vibration Research

Doctor of Philosophy

Electrochemical, Photographic, Luminescent and Acoustic Characterisation of Cavitation

by John Francis Power

This project reports a study of inertial cavitation and its associated effects. By employing a global approach involving both chemistry and acoustics a reproducible ultrasonic reactor has been produced and characterised.

Initially, the sound field generated in the cylindrical ultrasonic reactor is characterised both theoretically and experimentally. The sound field is considered with a variable operating frequency. An acoustic model is developed to predict the spatial distribution of acoustic pressure, which is compared with experimental measurements of the spatial characteristics of luminescent emission from the cell. A sound speed (averaged in space and time) within the cavitation environment in the range of 868 - 1063 m s^{-1} was calculated for the first time. The implications for chemical activity within ultrasonic cells of this nature are discussed.

Chemical activity within the acoustically characterised model ultrasonic reactor is then investigated. A novel electrochemical technique is presented for the detection of radicals ($OH^{\bullet}$ and $H^{\bullet}$) produced as the result of cavitation induced by ultrasound. A study of four example reactions is reported; evidence for $OH^{\bullet}$ formation is found through the Weissler reaction, the Fricke reaction and the detection of H_2O_2; evidence for the production of $H^{\bullet}$ is obtained by a Cu^{+2}/Cu^{+} system. In all cases, redox active materials trap the oxidative or reductive radicals. Electrochemical detection within a flow cell is then used to sense redox active products of the reactions between a chosen trapping agent and radicals produced within an ultrasonically irradiated solution. The detectors are seen to be sensitive and to work reproducibly within an acoustically characterised cavitation environment.

The electrochemical sensors were then used to investigate the frequency dependence of the production of radicals in the model ultrasonic reactor. Radical production is shown to be highly frequency dependant in the range of 20 kHz to 160 kHz ultrasound. However, the dominant frequency dependence is not of the chemistry per se, but is a function of the ability of the acoustic reactor to provide sufficient inertial cavitation. MBS(C)L appears to predict at which frequency chemical activity should be expected to be most efficient within a particular cell. The variation of the rate of these reactions is correlated to MBS(C)L as a function of the frequency with a resolution of 1 kHz. The results obtained are discussed with reference to the acoustics, in particular to the modal nature of the cell employed.

The electrochemical radical sensors were then tested in a "standard" Branson ultrasonic bath (40 kHz) with a "standard liquid", designed by NPL (National Physics Laboratory). This was part of an attempt to develop a reference sensor for cavitation. Three sensors were successfully tested including the Weissler reaction, multi bubble sonoluminescence (MBSL) and multi bubble sonochemiluminescence (MBSCL). The results achieved from the study including those obtained by the various partners are critically analysed.

Finally an electrochemical, photographic and spectrophotometric study of single bubble sonoluminescence (SBSL) is preformed to probe the differences between MBSL and SBSL. The first electrochemical evidence for the production of radicals as a result of SBSL is reported using the electrochemical Weissler reaction.

CONTENTS

		Page
ONE	**INTRODUCTION**	1
1.1	The Nature of the Liquid	4
1.2	Factors Affecting the Ability of a Bubble to Undergo Inertial Cavitation	5
1.3	Approximations of the Lower and Upper Threshold for Inertial Cavitation	7
1.4	Physical Effects of Cavitation	10
1.4 .1	Microstreaming	10
1.4.2	Microjetting	13
1.4.3	Shockwave Formation	16
1.4.4	Acoustic Streaming	16
1.5	The Effects of Ultrasound on Electrochemical Processes	17
1.6	Detection of Radicals	20
1.7	Chemical Dosimetry	23
1.71	The Fricke Dosimeter	23
1.72	Terephthalate Dosimeter	25
1.73	The Weissler Reaction	26
1.74	Electrochemical Dosimeters	26
1.8	Chemiluminescence	27
1.9	Sonoluminescence	29
1.10	Single Bubble Sonoluminescence: The Experimental Facts	31
1.11	Theories for Light Emission	33
1.11.1	Thermal Mechanism	34
1.11.2	Electrical Mechanisms	34
1.11.3	Mechanochemical Mechanisms	35
1.11.4	Thermal Volume Emission (the Opacity Model)	35
1.11.5	Quantum Vacuum Radiation	36
1.12	Summary of Work Presented	36
TWO	**EXPERIMENTAL**	38
2.1	Sonochemical Equipment and Procedures for Multi Bubble Sonoluminescence	38

2.2	Sonoelectrochemical Equipment and Procedures (MBSL)	40
2.3	Radical Trap Experiments	43
2.4	Light Measurements	51
2.5	Sonochemiluminescent Pictures	54
2.6	Frequency Dependence of Equipment and Drive Voltage Measurements	54
2.7	Absorbance Spectroscopy	57
2.8	Audio Output in the Air	57
2.9	Pressure Measurements in the Liquid	57
2.10	Chemicals	58
2.11	Characterisation of Measures of Reference Acoustic Cavitation (COMORAC)	59
2.12	Protocol for COMORAC Test	62
2.13	Single Bubble Sonoluminescence (SBSL) - Equipment and Procedures	63
2.14	Electrochemical Analysis of Single Bubble Sonoluminescence – Experimental Equipment and Procedures Employed	64
2.15	Experimental Rig Employed for Investigation of Single Bubble Sonoluminescence	66
2.16	Experimental Rig Employed for Spectrophotometric Investigation of SBSL	67

THREE	**EXPERIMENATAL AND THEORETICAL CHARACTERISATION OF SONOCHEMICAL CELLS**	70
3.1	Sound Fields Generated From Cylindrical Cell (Theoretical Model)	70
3.2	How Modes are Assigned in a Sequential Sense	78
3.3	Experimental Results	80
3.4	Bubble Populations	90
3.5	Soft Wall Model	95
3.6	Consequences for Chemistry	98
3.7	Conclusions	99

FOUR	**ELECTROCHEMICAL DETECTION OF RADICALS AND RADICAL PRODUCTS**	101
4.1	The Weissler Reaction	103
4.2	Limits of Electrochemical Detection	111
4.3	The Fricke Dosimeter	113
4.4	Equivalent Dose Measurements	116
4.5	Electrochemical Detection of H_2O_2	120
4.6	Electrochemical Detection of ($H^{\bullet}$) Using Cu^{2+}	125
4.7	Effect of Heating During Irradiation Experiments	135
4.8	Conclusions	135
FIVE	**IMPACT OF ULTRASONIC FREQUENCY ON SONOCHEMISTRY AND SONOLUMINESCENCE**	137
5.1	Sonoluminescent and Sonochemiluminescent Light Emission	139
5.2	The Weissler Reaction	141
5.3	Experimental Protocol	143
5.4	The Fricke Reaction	143
5.5	Frequency Dependence of Ultrasonically Generated H_2O_2	144
5.6	Frequency Dependence of Ultrasonically Generated $H^{\bullet}$	145
5.7	Pressure Measurements	146
5.8	Audible Output of the Cell	149
5.9	Comparison of Detectors	150
5.10	Frequency Dependence of Chemical Rates	150
5.11	Conclusions	153
SIX	**COMORAC: CHARACTERISATION OF MEASURES OF REFERENCE ACOUSTIC CAVITATION**	154
6.1	Multi Bubble Sonochemiluminescence (MBSCL)	155
6.2	Multi Bubble Sonoluminescence (MBSL)	159
6.3	The Weissler Reaction	160

6.4	The 'Fricke' Reaction	164
6.5	Terephthalate Dosimetry	166
6.6	Discussion of the Sonochemical Results Achieved at COMORAC	168
6.7	Calorimetry	169
6.8	Acoustic Sensors	171
6.8.1	Focused-Bowl Hydrophone (Passive Acoustic Emission)	171
6.8.2	Cavitation Activity Indicator	173
6.9	Conclusions	174

SEVEN	**AN ELECTROCHEMICAL, PHOTOGRAPHIC AND SPECTROSCOPIC STUDY OF SINGLE BUBBLE SONOLUMINESCENCE**	176
7.1	Electrochemical Investigation of Single Bubble Sonoluminescence – Experimental Method	177
7.2	Single Bubble Sonoluminescence – The Weissler Reaction	179
7.3	The Weissler Reaction in the Presence of Carbonate Dianion	186
7.4	Electrochemical Investigation of SBSL – The Weissler Reaction Performed in the Presence of the Carbonate Dianion	188
7.5	Spectrophotometric Study of SBSL	191
7.6	Conclusions	192

EIGHT	**CONCLUSIONS AND FUTURE WORK**	193
8.1	Concluding Remarks	193
8.2	Future Work	196

REFERENCES	198
PUBLICATIONS	205

ACKNOWLEDGEMENTS

Firstly, I would like to acknowledge the support given by the EPSRC (ref. GR/M24615) for funding. In addition I would like to extend my gratitude to:

To Dr. Peter Birkin, my supervisor, for the constant interest and enthusiasm he has shown in this work. I would also like to thank him for his insight and encouragement when writing this thesis. I would like to express my gratitude to him not only for his patient supervision throughout the course of this research but also, for the friendship developed during the course of my PhD studies.

To Prof. Timothy Leighton, my supervisor, for the interest and enthusiasm he has shown in this work. I would also like to thank him for his insight in preparing this thesis. Finally, I would like to express my gratitude for his useful conversations on acoustics and his willingness to learn chemistry throughout the duration of this research.

To the partners involved in the COMORAC experiment; Dr. Gareth Price, Dr. Andy Coleman, Dr. Nikolai Dezhkunov and Prof. Tim Mason who kindly gave permission to publish their results in chapter 6 of this thesis. To Dr. Bajram Zeqiri and Mr. Mark Hodnett for the help they gave throughout the course of the COMORAC experiment.

To my colleagues on the 7th floor, especially the members of the victorious football team (Yannick, Matt, Doug, Tim, Richard and Mark). You will no doubt be lost without me (unless you pay for my return) next year!! To Doug, you will have to endure those Friday blessings without me from now on. To Yannick, I wish you good luck in your search for the 'perfect' woman. To Matt, I would like to express my gratitude for those VB programming lessons. Finally, to the Friday night staff club crew, I would like to thank you for making these three years more enjoyable.

To my family who has been a never-ending source of encouragement and support throughout the years.

To my girlfriend Yvonne who began this research with me and who is also finishing her thesis. We leave here as best friends and who knows what the future holds.

GLOSSARY OF SYMBOLS

A	area of electrode
'A'	A – weighting assigns to each frequency a "weight" that is related to the sensitivity of the ear at that frequency ($20 < f < 20$ kHz). The reference pressure is 20 μPa
A_λ	absorbance at optical wavelength λ
$A_{m,n,z}$	represents the pressure amplitude of the $(m,n,q)^{th}$ mode
a	radius of electrode
a_r	cylinder radius
b	distance of the bubble centre from a solid boundary
b_a	amplitude attenuation constant
b_1	acoustic model constant
b_2	acoustic model constant
b_3	acoustic model constant
b_4	acoustic model constant
c	concentration (moles)
c_b	concentration in the bulk
c_c	reduced speed of sound
c_o	speed of acoustic waves in the liquid
c_p	The heat capacity
CR	the slope of H_2O_2 calibration plot (current against concentration A mol^{-1} dm^{+3})
c_s	local concentration
D	diffusion coefficient
D_{rads}'	the equivalent dose of rads exposed to the test solution per second
d_j	internal nozzle diameter
E	potential
F	Faraday's constant
f	acoustic frequency
f_{0nq}	the natural resonance frequency of the $(0,n,q)^{th}$ cavity mode
$G(X)$	the chemical yield expressed as the number of molecules or ions liberated per 100 eV of equivalent radiation
H	the distance from the nozzle to the electrode surface in a flow cell
h_p	the height of the photon counter active element above the surface of the liquid
i	current (A)
i_L	the limiting current recorded at the mass transport limited potential

Δi	the difference between the initial background current ant the limiting current
j	diameter of liquid jet
$j_{m,n}$	the nth stationary value of the Bessel function of the first kind of order m
$j_m(k_r r)$	Bessel functions of the first kind
k	acoustic wavenumber
k_m	mass transfer coefficient
k'	ratio of diffusion coefficient of sonochemical product to the diffusion coefficient of the calibration species calibration
k_z	axial wavenumber
k_{zq}	the infinite set of axial wavenumbers
k_r	radial wavenumber
k_{rn}	the n'th radial wavenumber
k_{rxn}	rate constant
L	height of liquid in the cell
l	path length
n_e	number of electrons
n	an integer denoting the radial mode
n_b	The number of bands in a chemiluminescent plot
m	an integers denoting the azithmuthal mode
M	Mass
p	acoustic pressure
P_B	the minimum acoustic pressure at which a gas bubble of radius R_B will grow
P_A	negative acoustic pressure
P_o	hydrostatic pressure
P_m	the momentum of an acoustic wave
P_o	initial momentum of a progressive standing wave
p_σ	Laplace pressure
ΔP_{wall}	the time averaged pressure difference across the bubble wall
q	an integer denoting the axial mode
r	the distance measured in a radial direction
$R(r)$	a separable function of p (acoustic pressure) depending only on the radial direction
R_r	the radius of a bubble that would be in pulsation resonance with the incident sound field
R_1	the distance from the centre of ring pattern to the first ring when analysing the MBSCL pictures to assign acoustic modes
R_2	the distance from the centre of ring pattern to the second ring when analysing the MBSCL pictures to assign acoustic modes

R_3	the distance from the centre of ring pattern to the third ring when analysing the MBSCL pictures to assign acoustic modes
R_o	equilibrium radius of a spherical bubble
$R(\omega, \theta)$	the complex reflection coefficient at the cylinder wall
R_{crit}	the critical dimensions for the stability of a bubble with respect to changes in the hydrostatic pressure
R_m	the distance of the microelectrode from the bubble surface
R_{max}	the maximum radius reached by a bubble during expansion, prior to the collapse phase
R_{min}	the minimum radius reached by a bubble on the collapse phase
r_p	the radius of the active element of the photon counter
SCR	the gradient of the current time transient for H_2O_2 ($A\ s^{-1}$)
t	time
T	temperature
t_{grow}	net time for bubble growth in prompt response to negative sinusoidal pressure pulse
t_1	time taken, after start of negative-halfcycle of a sinusoidal pulse, for the magnitude of the negative acoustic pressure to exceed P_B
t_2	time until the liquid ceases to be in tension after start of negative-halfcycle of a sinusoidal pulse
Δt	time for the solution to be pumped from the ultrasonic reactor to the flow cell
Δt_I	delay in bubble growth caused by inertial effects
Δt_η	delay in bubble growth caused by viscosity
Δt_σ	delay in bubble growth caused by surface tension
Δt_x	delay time for the solution to be pumped from the ultrasonic reactor to the flow cell in the case of the continuous flow pump
Δt_y	delay time for the solution to be pumped from the ultrasonic reactor to the flow cell in the case of the peristaltic pump
V	voltage
v	kinematic viscosity
v_b	the volume of the bulk solution
V_f	volume flow rate
V_d	the volume change close to the bubble surface compared to the bulk solution
VF	void fraction
V_s	the local spherical volume
W	ultrasonic power
W_T	rate of conversion of ultrasonic power to heat
$Y_m(k_r r)$	Bessel functions of the second kind
z	the distance from the surface of the transducer ($z = L$) to the top of the liquid ($z = 0$)
$Z(z)$	a separable function of p (acoustic pressure) depending only on z
$Z(\omega, \theta)$	the locally reacting impedance at the wall

Greek Letter Symbols

η	liquid viscosity
θ	the angle of incidence
θ_f	the flare angle of the photon counter
$\Theta(\theta)$	a separable function of p (acoustic pressure) depending only on θ
κ	polytropic index
λ	wavelength
ε_λ	adsorption coefficient at wavelength λ
ρ	fluid density
ρ_o	equilibrium fluid density
σ	surface tension
σ_o	equilibrium surface tension
ϕ	the phase angle of an acoustic wave on reflection from a boundary
ϕ_v	velocity potential
ω	the angular frequency

GLOSSARY OF ABBREVIATIONS

Ag	Silver
COMORAC	characterisation of measures of reference acoustic cavitation
CV	cyclic voltammogram
DMPO	5,5-Dimethyl-1-pyrroline-N-oxide
EDTA	ethylenediaminetetraacetic acid
ESR	electron spin resonance
grnd	ground state
HPLC	high pressure liquid chromatography
NPL	National Physics Laboratory
MBSL	multi bubble sonoluminescence
MBSCL	multi bubble sonochemiluminescence
MTL	mass transfer limiting
MTLP	mass transfer limiting potential
PMMA	polymethylmethacrylate
PTFE	polytetrafluoroethylene
POBN	alpha-(4-pyridyl-1)-N-tert-butyl nitrone
PYBN	2-methyl-N-(4-pyridylmethylene)- N-oxyl
Pt	platinum
SBSL	single bubble sonoluminescence
SCE	saturated calomel reference electrode
UV-VIS-NIR	ultraviolet – visible – near Infrared

CHAPTER 1

INTRODUCTION

Ultrasound, defined as sound of a frequency above the human hearing (16 kHz)[1], has become a widely used tool in both research and industry. In the medical field it is used for therapy,[2] a diagnostic tool[2] and as a cleaning or sterilization agent. In cell biology it is used for the stimulation of enzyme activity and the destruction of cells.[3] In the food industry ultrasound is used to determine the degree of emulsification and the homogeneity of food samples.[4] In the pharmaceutical industry its applications include the extraction of bioactives from plant materials.[5] In sonochemistry it is used for the destruction of organic pollutants[6-10] and the catalysis of a variety of homogenous[11-15] and heterogeneous[16, 17] processes. The frequency ranges employed for these processes can be divided into two categories. For diagnostic applications the sound is in the megahertz range (1 - 80 MHz), while for the destruction of cells or pollutants, low frequency high-energy power ultrasound in the kHz range is normally used (20 kHz -1 MHz). A number of reasons determine the exact choice of pressure and frequency employed in a particular technique. For a given size of bubble nucleus, the threshold pressure required to generate inertial cavitation increases with frequency. Hence, if transient or inertial cavitation is required (normally stated as important for sonochemistry) lower frequencies are usually employed.

Many of the above applications of power ultrasound are reliant on a phenomenon known as acoustic cavitation.[18] Acoustic cavitation may be defined as the activation by acoustic pressure cycles of pre-existing nuclei within a liquid. The lifetime and termination of each individual bubble has been used to define two categories of acoustic cavitation. These two types of acoustic cavitation are called non-inertial (or 'stable' cavitation), and inertial (or 'transient' cavitation). Figure 1.1 illustrates a schematic graph (bubble radius against time) for inertial cavitation. The first stage is the initial preface of cavitation nuclei such as microbubbles or cavities. These nuclei experience a negative pressure during the rarefaction cycle of the imposed pressure wave, which causes the bubbles to grow. The tension in the liquid must exceed the Blake pressure to obtain explosive growth[2]. The Blake pressure[2] is given by equation (1.1).

$$P_B = p_o + \frac{8\sigma}{9}\sqrt{\frac{3\sigma}{2R_B^3\left(p_o + \left(2\sigma / R_B\right)\right)}} \qquad (1.1)$$

In this equation the threshold value of R_o (equilibrium bubble radius) is termed R_B, the Blake radius. Bubbles, which are smaller than R_B will not grow explosively. P_B is the minimum acoustic pressure at which a gas bubble of radius R_o will grow; p_o is the hydrostatic liquid pressure outside the bubble and σ is the surface tension of the liquid. The existence of surface tension σ means that, whatever the hydrostatic pressure p_o in the liquid outside a spherical bubble, the gas pressure at equilibrium inside the bubble must exceed p_o by the Laplace pressure (or surface tension pressure) p_σ given by equation (2.1):

$$p_\sigma = \frac{2\sigma}{R_o} \qquad (1.2)$$

This grouping is clearly visible in equation (1.1). Because this is inversely proportional to bubble radius a threshold exists for the explosive growth of small bubbles.

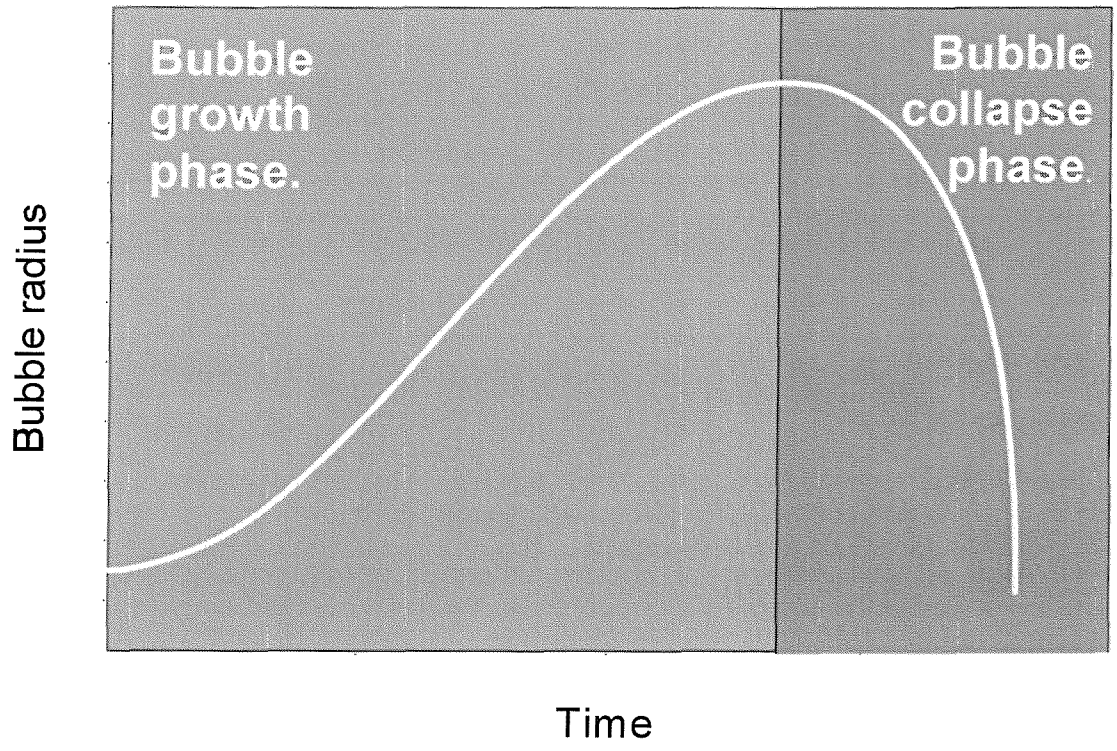

Figure 1.1 Schematic graph (radius against time) of bubble growth and collapse [19]

For inertial cavitation the bubbles collapse violently releasing large amounts of energy during compression cycles. The expansion of the bubble prevents the tension in the fluid being maintained. The growth stops and work is done on the bubble supplied by the kinetic energy of the spherical convergence of the surrounding liquid.[2] After reaching minimum size, the bubble rebounds emitting a pressure pulse into the liquid.[2] For stable cavitation the implosive collapse is halted and the bubble begins a second growth phase. There are thresholds in bubble radius and acoustic pressure associated with bubble growth and

collapse[2] (see section 1.3). For example if the bubble is too large, it does not have time to collapse in the compression phase of the sound cycle, and it is subjected to another rarefaction cycle before the collapse is complete. This halts the implosive bubble collapse in the first cycle. However, the bubble may collapse on the next cycle. While there is rich acoustics literature, and similarly a great deal written on sonochemistry, it is clear that the interface between the two types of cavitation, although vital has not been adequately addressed. A consequence of this mismatch is that sonochemical experiments are difficult to reproduce. However, the reasons for this are associated with the poor control of the acoustic field rather than differences in chemistry. Specific examples of this will be highlighted later in this thesis.

The main purpose of the research presented in this thesis is to measure and characterise 'cavitation' by performing carefully controlled experiments. Apfel[20] stated that an ultrasonic system consists of three components: The sound field (which includes the vessel in which the liquid is contained); a liquid (and all it contains); and a detection system to monitor the effects of cavitation.[20-22] A detailed understanding of these three components, and in particular how they impinge upon each other, is required to achieve a controlled reproducible system. Many separate studies exist where the authors attempted to characterise the effects of inertial cavitation (chemistry[23], erosion[24], sonoluminescence[23]). However, few have given due consideration to the design of the ultrasonic reactor and specifically the nature of the sound field (i.e. the acoustic modes excited and the effect of bubble population) within the reactor, either in interpreting results or performing experiments. The objective of this research is to show that by combining an understanding of chemistry with rigorous acoustics, a reproducible comprehensible system can be achieved.

A chapter-by-chapter summary of this thesis is given at the end of chapter 1 (see section 1.12). To give an overview, this thesis reports on a combined electrochemical, acoustic, photographic and luminescent study of acoustic cavitation. Care has been taken in the experimental design, and in particular the nature of the sound field within the systems employed, with the ultimate goal of achieving a combined understanding of both the acoustics and chemistry occurring in these notoriously complex systems. Initially the components of the systems employed are considered, notably the nature of the cavitating liquid (as the nature of the sound field will be discussed in detail in chapter 3). This is followed by a brief explanation of the factors, which influence the ability of a bubble to undergo inertial cavitation. The physical effects of cavitation are then discussed in detail, as

many of the detectors for cavitation 'activity' essentially measure these effects. The chemical effects of cavitation are then discussed, with particular emphasis on the radical chemistry and chemical dosimetry, as the majority of the chemical sensors used in this thesis are dependent on the formation of radicals and radical by-products. The current similarities and differences between single and multi bubble sonoluminescence are then discussed as both phenomena are investigated in this thesis. Finally a summary is given of each chapter presented in the thesis.

1.1 The Nature of the Liquid

In ultrasonic cavitation the nature of the liquid employed is the most difficult factor to control. This is because, in defining the properties of the liquid, the population of bubble nuclei is a key feature. The population is critically dependent on a number of factors including the following: the gas content; the solid bodies (container walls and suspended particles); presence of chemicals or impurities and the cavitation process itself.

For the onset of cavitation the tensile strength of the liquid is important. The tensile strength of a liquid is reduced by the presence of impurites (inhomogeneities and contaminants in the liquid in addition to the other factors). Therefore, the threshold for acoustic cavitation is usually not a measure of a property of a pure liquid, but more a reflection of the impurities present.[20] Bertholet [25, 2] carried out studies on the effect of tensile strength as early as 1850. He heated a closed glass tube, which was almost filled with liquid, the remainder of the volume being gas. On heating, the liquid expanded more than the glass, forcing the gas into the liquid, so that the latter filled the vessel. On cooling, the liquid adhered to the glass: since the liquid was thus restrained from contraction, tension was generated within it. The tension increased as the liquid cooled, until cavitation occurred. Thus, Bertholet measured the tensile strength of his water sample to be around 50 bar, though since cavitation initiated at the walls of the tube, rather than in the body of the liquid, it was the forces of adhesion between glass and liquid that were overcome, not the cohesion between the liquid molecules. This was perhaps the first demonstration where it was understood that it was not the properties of the liquid per se that determined the maximum tension the liquid could sustain, but that of the other bodies present within the liquid sample.

The gas, solid and impurity content of the liquid employed can affect the stability, the predictability and repeatability properties of the ultrasonic reactor. There are two possible ways to control the population of nuclei in a solution:[26]

(1) Try to remove the effect of random nucleation sites by filtering and degassing the solution. This method was used during the COMORAC experiment (characterisation of measures of reference acoustic cavitation, see chapter 6). This can be very difficult to control as the onset of cavitation is a function of the impurities that are not removed.
(2) Flood the solution with nucleation sites either by not degassing and or pretreating the solution to be irradiated with 'standard' nucleation sites. There are several options for standard nucleation sites including echocontrast agents, radiation, solid particles and again cavitation itself. This seeding approach may cause high levels of cavitation.

Unless specified as being otherwise, the work presented in this thesis was performed in aerobic deionised solutions (method 2). After establishing and controlling the content of the liquid it is necessary to consider the factors, which will govern the ability of a bubble to cavitate within that medium.

1.2 Factors Affecting the Ability of a Bubble to Undergo Inertial Cavitation

Normally inertial cavitation is associated with sonochemistry. Inertial cavitation approximately results from the isothermal expansion of a bubble during the rarefaction cycle of the pressure wave, which culminates in adiabatic collapse due to dominant effect of inertial forces.

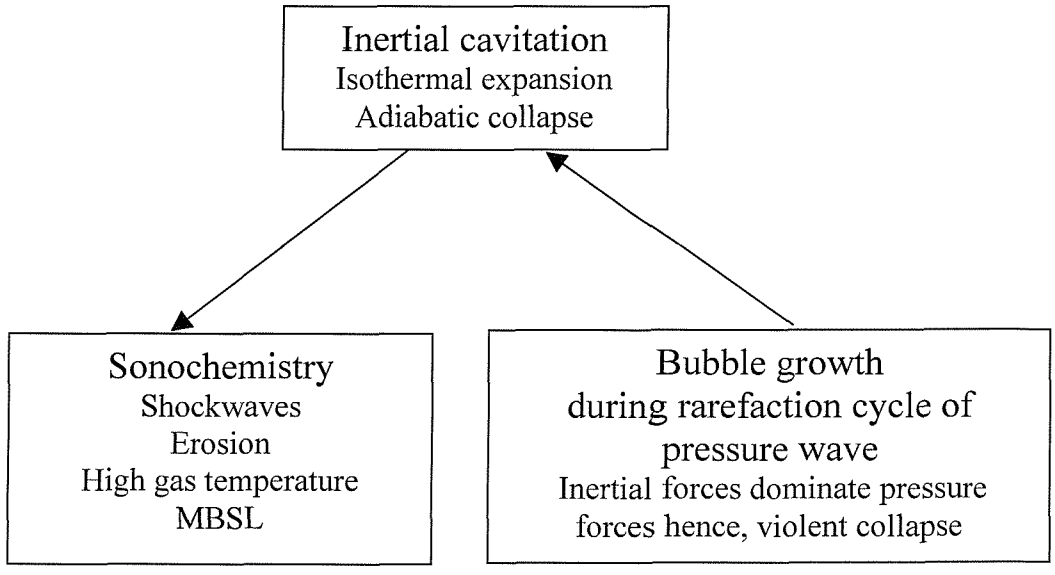

Figure 1.2 Figure showing a schematic diagram illustrating how inertial cavitation occurs and its associated effects including sonochemistry.

Figure 1.2 shows a schematic diagram illustrating how inertial cavitation occurs and its associated effects (including sonochemistry). The factors affecting the ability of a bubble to undergo inertial (transient) cavitation in a liquid are notoriously complex. They have been

investigated by a number of authors[2, 21, 27-29] and they include the following: the tensile strength of the liquid (including any added chemicals, impurities and dissolved gas, see section 1.1), the acoustic frequency, the acoustic pressure amplitude at the bubble and the equilibrium bubble size.

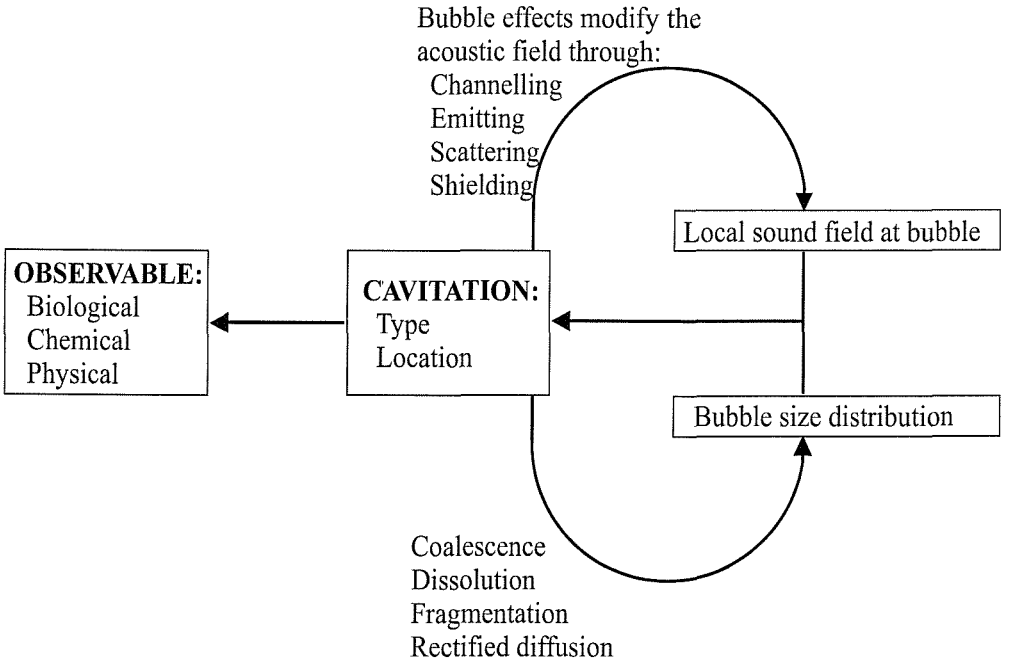

Figure 1.3 Schematic illustrations of how the various factors interact determine the types of cavitation, which occur, and hence the effect observed. The latter may be chemical, physical or biological. It depends both on the type of cavitation (e.g. transient, stable, jetting, fragmentary etc) and its location. Both these factors depend strongly on the local sound field at the bubble, and on the sizes of bubble present in the population. These two together, for example, characterise the transient cavitation threshold, and also where bubbles will migrate and accumulate under radiation forces. Such accumulation will in turn affect the local sound field, through the processes of channelling, scattering, and shielding; and will affect the bubble size distribution through its influence on the processes of coalescence, fragmentation, and rectified diffusion. In summary therefore, the observed effect depends on the characteristics of the cavitation present. After Leighton.[22]

Many of these key factors such as bubble size can be altered during insonification by many processes: Rectified diffusion, (bubble growth due to active pumping of gas, initially dissolved in the liquid into the bubble using the energy of the sound field) and coalescence (random collisions, bubbles may coalesce to form larger bubbles) provide ways to produce larger bubbles. Dissolution and fragmentation provide mechanisms by which bubble size reduction occurs.[2] These effects can be complex as a number of processes can occur in competition. What happens depends on the physical conditions at the location of the bubble. Bubbles may grow by rectified diffusion but rectified diffusion is not efficient above resonance bubble size and bubbles usually dissolve or fragment. Fragmentation and the

production of microbubbles can also lead to larger bubbles entering the resonant bubble population. In a standing wave sound field bubbles less than resonance size aggregate at pressure antinodes and bubbles greater than resonance size aggregate at nodes. These bubble aggregates can also have effects such as shielding or scattering. Leighton summarised how the various factors interacting determine the types of cavitation that occurs.[22] This is illustrated in figure 1.3.

Several theories exist for calculating the threshold in bubble radius/pressure, which determine whether a bubble undergoes inertial or stable cavitation. These theories will be discussed in section 1.3

1.3 Approximations of the Lower and Upper Threshold for Inertial Cavitation

There is a fundamental difference between the concepts of stable (non inertial) and transient (inertial) cavitation.[2] If there is a transition from one type of cavitation to the other it occurs at the 'transient' threshold. Several authors have investigated the theoretical threshold in bubble radius and acoustic pressure required for a bubble to undergo inertial cavitation.[2, 30-31] Calculations of this nature were performed in chapter 4 (see section 4.1, figure 4.3) using the method outlined below. Leighton[2] has performed an extensive review of these calculations.

If the negative acoustic pressure and the frequency conditions are appropriate to cause inertial cavitation in some bubbles, there is a lower limit to the initial bubble size that will undergo inertial cavitation. The lower threshold in bubble radius for inertial cavitations may be calculated using Blakes threshold pressure lower limit (see equation (1.1)).[2] The approximate criterion for inertial cavitation for this lower limit is that the bubble radius R_o must exceed R_{crit}, (the critical dimensions for the stability of a bubble with respect to changes in hydrostatic pressure) and the negative acoustic pressure P_A must exceed P_B. The more P_A exceeds P_B the wider the initial size range of bubbles that will undergo inertial cavitation.[2] It is important to note that under the conditions employed P_B is approximately ca. 100 kPa for initial bubble radii > 5 μm.

Holland and Apfel[31] proposed an analytical formulation incorporating both upper and lower radius thresholds. The model transient collapse is shown in figure 1.4 for the transient response of a bubble to a single acoustic cycle. Leighton[2] discusses this model in detail.

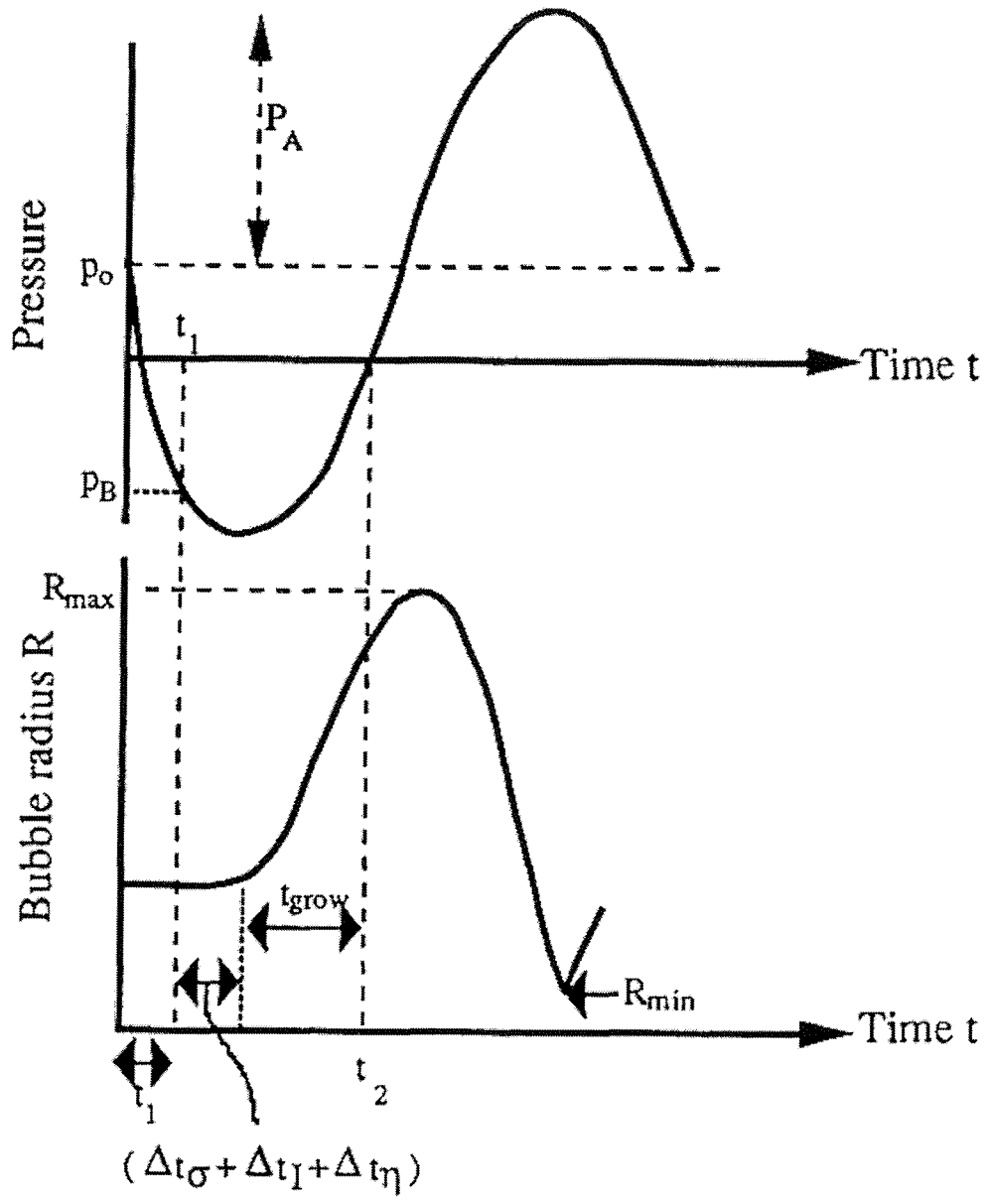

Figure 1.4 The model transient response of a bubble to a single acoustic cycle, where the negative phase of the sound pressure precedes the positive. The reader is referred to the text for explanation of this figure. This figure is from Leighton's[2] redrawing of Holland and Apfel.[31]

The negative phase of the sound field exceeds the positive so that the liquid initially goes into tension. At time $t = t_1$ the magnitude of the negative acoustic pressure in the liquid exceeds P_B (see equation (1.3) where ω is the angular frequency). There is a lag time before the bubble responds with rapid growth.

$$t_1 = \frac{1}{\omega}\left[\frac{\pi}{2} - \left[2\left(1 - \frac{P_B}{P_A}\right)\right]^{\frac{1}{2}}\right] \tag{1.3}$$

The time at which the liquid ceases to be in tension (t_2) is given by equation (1.4) and the duration of 'force', which causes the bubble to grow, is given by t_2- t_1 ((1.4) – (1.3)).

$$t_2 = \frac{1}{\omega}\left[\frac{\pi}{2} + \left[2\left(1 - \frac{P_B}{P_A}\right)\right]^{\frac{1}{2}}\right] \tag{1.4}$$

The force that drives the bubble growth can in estimation be quantified through the time averaged pressure difference across the bubble wall, ΔP_{wall}.[2, 31]

$$\Delta P_{wall} = \frac{1}{t_2 - t_1}\int_{t_1}^{t_2}(P_A \sin \omega t - \rho_o)dt \tag{1.5}$$

In addition there are delay times resulting from surface tension, inertia and viscosity equations (1.6 - 1.8) respectively.[2, 31]

$$\Delta t_\sigma = \frac{2\sigma}{P_A - P_B}\left[\frac{3P}{2(P_A - P_B)}\right]^{\frac{1}{2}} \tag{1.6}$$

$$\Delta t_I = \frac{2R_o}{3}\left[\frac{P}{\Delta P_{wall}}\right]^{\frac{1}{2}} \tag{1.7}$$

$$\Delta t_\eta = \frac{4\eta}{\Delta P_{wall}} \tag{1.8}$$

Therefore, the time for the bubble to grow t_{grow} is given by equation (1.9):

$$t_{grow} = (t_2 - t_1) - (\Delta t_\sigma + \Delta t_I + \Delta t_\eta) \tag{1.9}$$

Holland and Apfel[31] estimate the maximum radius attained by the bubble to be

$$R_{\max} = \left(R_o + \left[\frac{2\Delta P_{wall}}{3P}\right]^{\frac{1}{2}} t_{grow}\right)\left(\frac{\Delta P_{wall}}{P_o} + 1\right)^{\frac{1}{3}} \tag{1.10}$$

P_A was increased until $\frac{R_{\max}}{R_o} > 2.3$. These equations were incorporated into a visual basic program where R_o was varied and P_B was calculated for each time t, in which the negative acoustic pressure, $P_A > P_B$,. This yielded the (upper and lower) threshold limits presented in the results section (see chapter 4 section 4.1, figure 4.3). If an adiabatic collapse is assumed it is possible to relate the maximum temperature attained during the collapse to the insonation conditions.[2]

While this model appears in Apfel and Holland[31] and Leighton[2] it is the first time to the present knowledge of the author that the calculation has been performed for the sub MHz region (see chapter 4, section 4.1, figure 4.3). These calculations while being thorough encompass many approximations including the following:

- Holland and Apfel's model assumes that the internal temperature of the bubble should reach 5000 K. Leighton[2] discusses this point in detail and notes that several other authors have chosen different temperatures ranging from 960-5000 K.
- The model assumes that nuclei will cavitate after one acoustic cycle (called 'prompt cavitation).

Considering the above approximations, calculations of this nature yield only an indication of the approximate limits in pressure and radius thresholds for inertial cavitation.

When a bubble undergoes inertial cavitation the physical effects of the process can be used as a measure of 'cavitation activity'. Indeed many sensors measure the physical effects of cavitation (e.g. erosion sensors[32, 33]). Therefore an in-depth knowledge of these processes is required. The physical effects are discussed in detail in section 1.4.

1.4 Physical Effects of Cavitation

Cavitation can be detrimental as well as beneficial. Many authors have investigated the physical effects of cavitation.[1, 2] Indeed much of the theoretical work on cavitation began when erosion was observed in rotary hydraulic apparatus (ships propellers and water turbines[34]). However, there are other physical effects. These physical effects of cavitation include bubble motion, shockwave formation, acoustic streaming, microstreaming and microjet formation. These processes are important when interpreting chemical data and designing experimental procedures to characterise cavitation. Leighton[2] has described these processes in detail.

1.4.1 Microstreaming

Microstreaming arises from the frictional forces between a boundary and a medium carrying vibrations of circular motion.[2] This type of streaming is confined to a restricted volume near the sound source. Microstreaming has been found to be important when bubbles are located near solid boundaries, and when ultrasonic frequency drives bubbles at their resonant frequency. Elder[35] investigated the factors, which effect microstreaming by

examining the steady state circulation patterns of a suspension of aluminium particles in water. The bubble adhered to the bottom of a tank containing a liquid of known viscosity (water/water glycol mixture). The tank, which had transparent walls, was mounted on a vibrating steel piston that was driven at 10 kHz by a magetostrictive driver. Several circulation patterns were observed and the authors[35, 2] summarised four different characteristic regimes for microstreaming. These are illustrated in figure 1.5. The effect depends on the acoustic pressure amplitude in addition to the viscosity of the sonicated fluid. It is also affected by the presence or absence of surface-active material in the fluid. Figure 1.5 (a) illustrates the pattern observed if a surface contaminated bubble is driven at low amplitude in a low viscosity liquid. Figure 1.5 (b) shows the pattern observed over a wide range of driving amplitudes and liquid viscosities. Figure 1.5 (c) usually occurs in low viscosity liquids. Figure 1.5 (d) was observed at high driving amplitudes and low viscosities. In the figure the bubble wall is drawn to represent the orderly extremes of oscillation of surface waves. Elder attributes the onset of microstreaming to coincide with the acoustic excitation of the first surface mode. This is a threshold phenomenon, which requires the lowest driving pressure to excite close to bubble resonance. The more the driving pressure exceeds the threshold the more surface waves are excited.[36]

It has been demonstrated that microstreaming caused by the breathing mode of the bubble and surface wave excitation can produce significant enhancements of mass transfer to a microelectrode positioned next to the gas/liquid boundary.[37, 38]

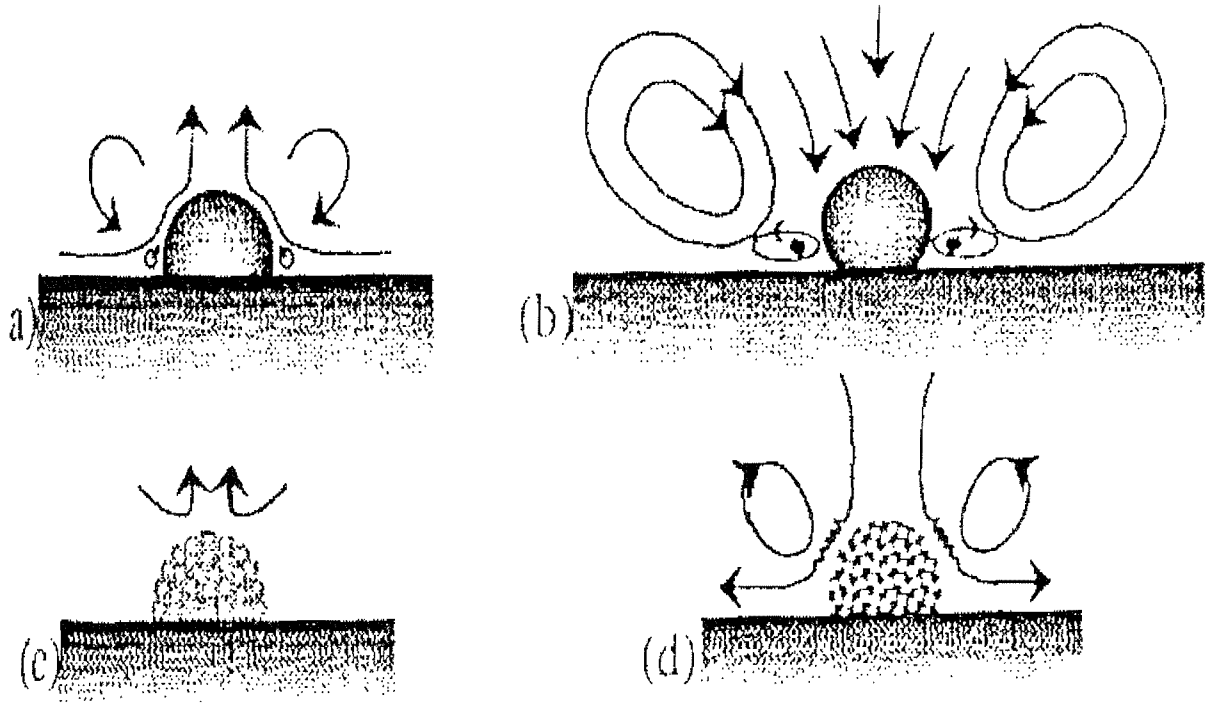

Figure 1.5 Schematic illustration of microstreaming (figure from Leighton's[2] redrawing of Elder[35]).

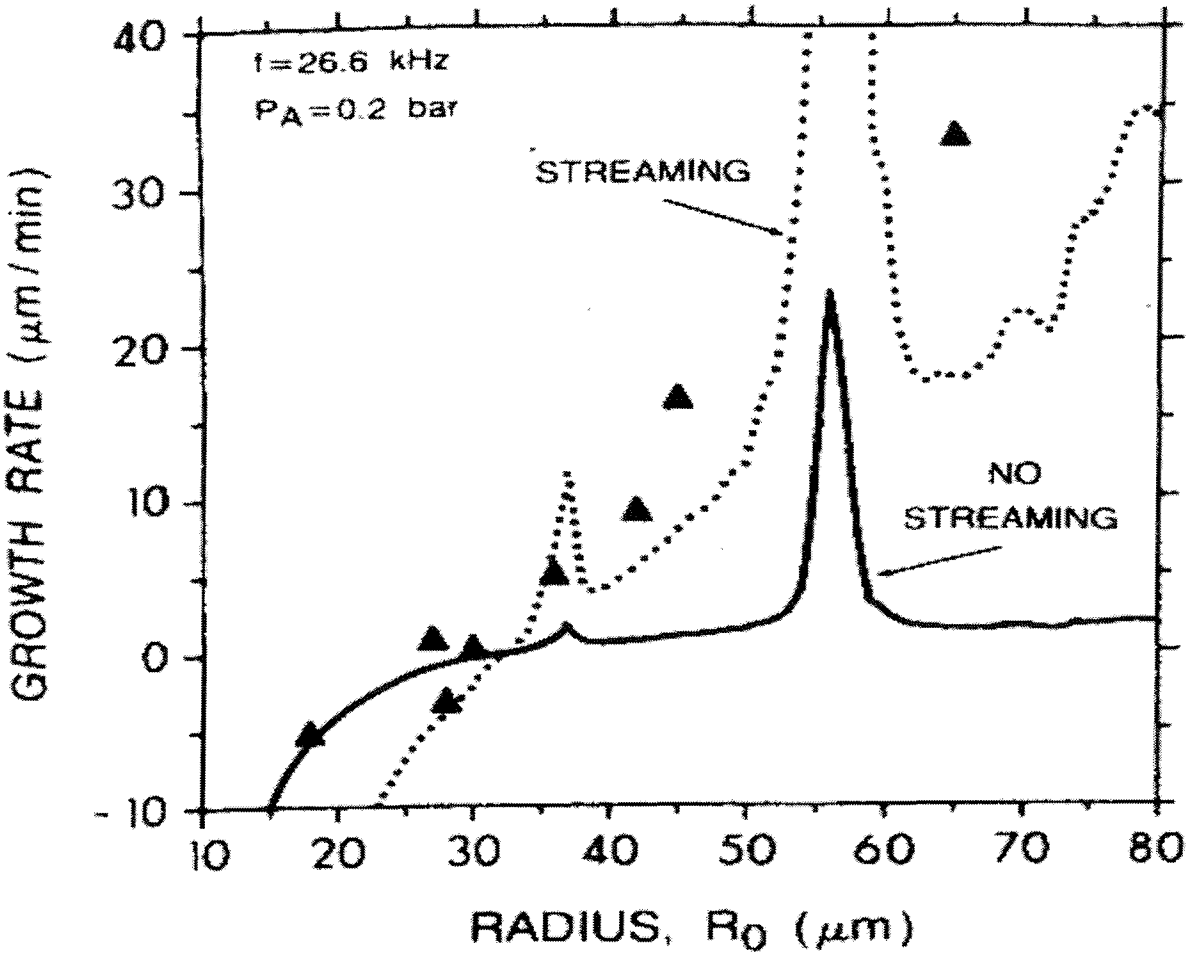

Figure 1.6 Bubble growth rates at 26.6 kHz, acoustic pressure 2 x 10^4 Pa, with and without microstreaming as predicted by Church.[39] These are compared to Eller's data[40] (after Church [39]).

The effect of microstreaming on the rate of bubble growth due to rectified diffusion has been studied by a number of authors.[39, 40] The enhancement in the rate of bubble growth (for bubbles larger than a critical dimension see figure 1.6) through rectified diffusion can be explained by considering the flux of material between the liquid and gas phase. An asymmetric gas transfer dictates the rate of bubble growth. This is attributed to differing fluxes across the gas/liquid interface during the expansion and contraction phases of bubble oscillation. This process causes a depletion of dissolved gas in the liquid phase directly adjacent to the bubble wall. If there is no flow induced by bubble oscillation, then the rate at which the deficit is met depends on the rate of mass transfer of gas from regions farther out from the bubble. However, if microstreaming does occur, this rate of gas transfer is enhanced through forced convection of the liquid surrounding the bubble. Church[39] calculated the predicted growth rates in a 26.6 kHz field (acoustic pressure = 2 x 10^4 Pa)

with and without microstreaming as a function of the equilibrium bubble radius. Church then compared his predictions to Eller's[40] experimental data. The results are shown in figure 1.6, which shows that microstreaming assisted growth will occur for equilibrium bubble radius > 35 μm. This limit is dictated by bubble dissolution (which can be assisted by microstreaming) processes that are prevalent at small bubble radii (< 35 μm from Church's predictions) and are associated with Laplace pressure.

These processes will effect the bubble population, through bubbles either growing or dissolving within the acoustic field. This can affect the cavitation process itself by allowing some bubbles to grow sufficiently and cross the boundary from stable to inertial (transient) cavitation.

1.4.2 Microjetting

Microjets are formed through the asymmetric collapse of a cavity near a solid surface. This is one of the mechanisms for cavitation-induced erosion.[2] Asymmetric bubble collapses are caused by the inhibition of fluid motion due to the solid interface. Erosion and damage can occur when the high speed liquid jet impacts on a surface leaving characteristic 'pits' that are approximately one-tenth the radius of the original cavity.[41] Neppiras[42] studied the nature of cavities in the neighbourhood of a solid boundary employing high-speed photography. He studied the collapse of an initially spherical bubble in water generated by laser action filmed at 3 x 10^5 frames per second. Under these conditions jetting first occurs towards the solid boundary and on the rebound a counter jet is formed. After that the bubble disintegrates.

Lauterborn *et al.*[43, 44] also investigated liquid jets using high-speed photography. Jets with velocities of 120 m s^{-1} were observed. Lauterborn's experimental work enabled numerical calculations of bubble collapse near a solid boundary to be confirmed experimentally.

Figure 1.7 shows the excellent agreement between the theory developed by Plasset and Chapman[45] and the experimental work by Lauterborn and Bolle.[43] The jet may traverse the bubble interior, to penetrate the remote bubble surface. A beautiful picture of this effect, taken by Crum (published in reference 46) is shown in figure 1.8.[46]

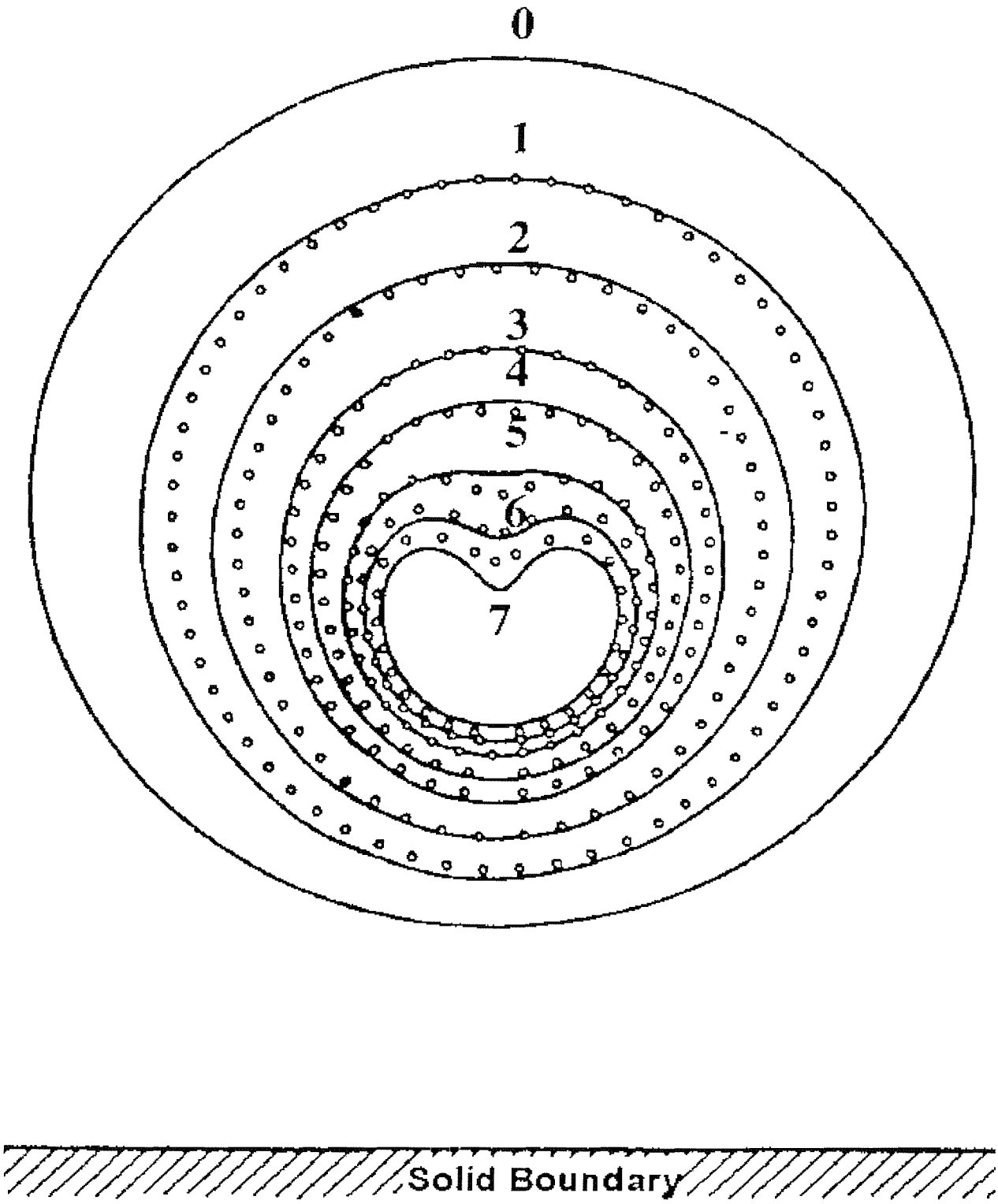

Figure 1.7 Plot showing the comparison of experimentally determined bubble shapes on collapse (o) (After Lautherborn and Bolle)[43] of a spherical bubble near a plane solid wall with theoretical curves taken from Plasset and Chapman[45] (—). Lautherborn and Bolle experimental analysis employed a framing rate of 3×10^5 frames s^{-1}. The initial bubble radius was 2.6 mm and the distance of the bubble centre from the wall was 3.9 mm.

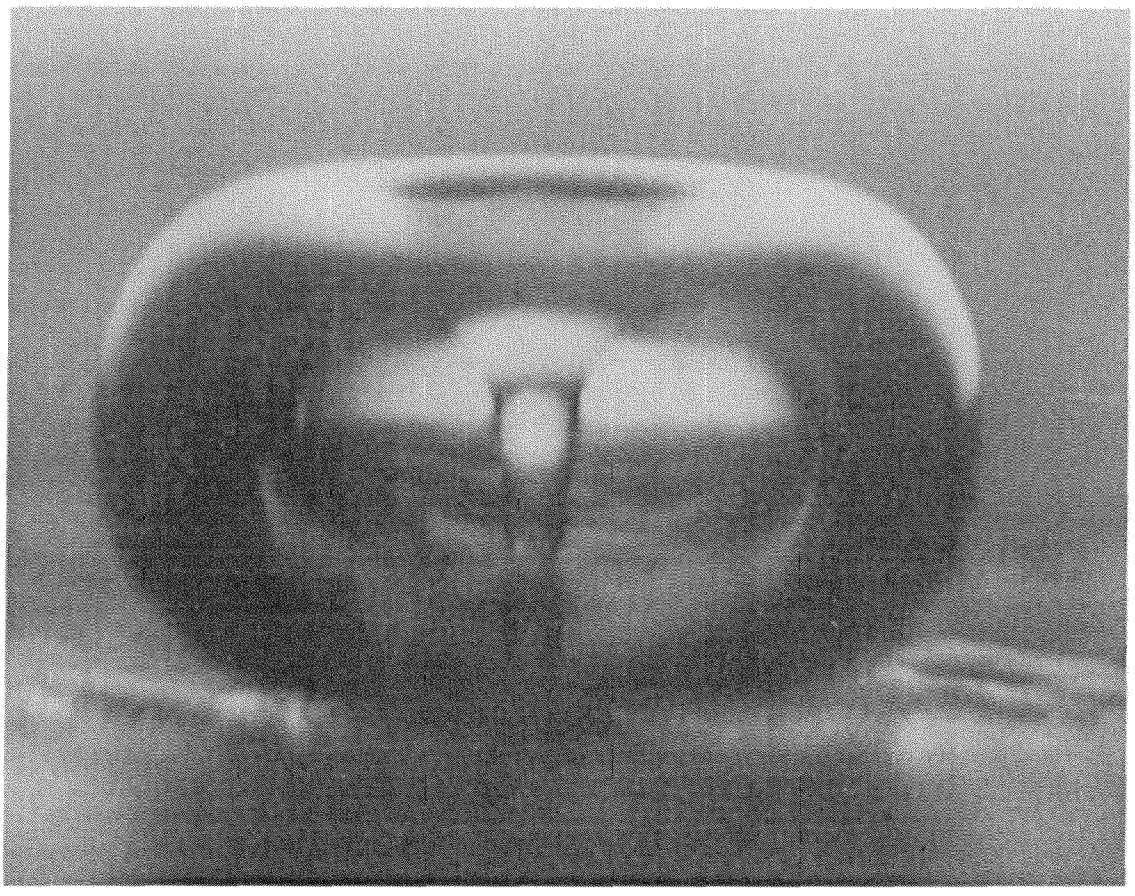

Figure 1.8 Jet formation during the collapse of an oscillating gas-vapour bubble at low pressure (400-5000 Pa) in a 60 Hz sound field. The bubble size is approximately 0.2 cm (published in reference[46]).

Blake *et al.*[47-49] modelled jetting bubble collapses assuming an incompressible liquid. Path lines and pressure contours were calculated for rigid[47] and free[48, 49] boundaries. The production of a liquid jet can also result from the transient pressure pulse engendered by a shock wave. Ball *et al.*[50] have performed CFD simulations of jetting bubble collapses, which include compressibility effects. A Free-Lagrange CFD code was used to simulate the collapse of a cylindrical air cavity in water by a 1.9 GPa incident shock.

The transient effects of microjetting may also be monitored chemically. Birkin *et al.*[51] have shown how electrochemistry may be used to monitor the erosion and corrosion processes associated with surface damage as the result of cavitation bubble collapse near a surface caused by jetting or shockwave impact. Passivated microelectrode surfaces of aluminium and lead were employed to investigate individual erosion and corrosion events produced by a 22.5 kHz ultrasonic horn. By monitoring the repassivation currents, individual erosion events were recorded with a resolution within the sub millisecond time scale. Another process responsible for cavitation erosion is shock wave formation. This is discussed in section 1.4.3.

1.4.3 Shockwave Formation

The other possible source of erosion involves the pressure pulse emitted into the surrounding liquid when a cavity collapses.[2] Plesset and Properetti[52, 53] have reviewed much of the early work on spherical collapsing bubbles. The emitted shockwave may have an amplitude of up to 1 GPa. In the case of isolated bubble collapses, the shock is so rapidly attenuated that only surfaces within about the initial bubble radius of the centre of the collapse may be damaged.[52, 53] However, under certain circumstances the collapse of one may initiate the collapse of a neighbour and the shock from these so called 'cavitation clouds' can cause damage at much greater distances.[54] Attenuation effects make electrochemistry (specifically the use of microelectrodes) ideal tools for investigating these events. These electrodes detect disturbances in the fluid up to ca. 10 (electrode) radii away from the surface. The specific advantages of microelectrodes for this type of analysis are discussed in section 1.5.

1.4.4 Acoustic Streaming

Acoustic streaming results from attenuation of the sound field within the liquid resulting in a pressure gradient and subsequent liquid motion in the direction of propagation of the sound the wave. A progressive standing[2] wave travelling in the x direction might therefore be described as:

$$P_m = P_o e^{i(\omega t - kx)} e^{-b_a x} \tag{1.11}$$

where P_m is the momentum of an acoustic wave, b_a is the amplitude attenuation constant and k is a wavenumber. This attenuation is highly frequency dependent varying approximately with the square of the frequency[2] up to ca. 1 MHz (see equation 1.12):

$$b_a \ \alpha \ f^2 \tag{1.12}$$

where f is the acoustic frequency. Attenuation in the MHz range is discussed in the literature.[55] Streaming speeds of up to 10 cm s^{-1} can be demonstrated from clinical ultrasonic equipment.[2] Acoustic streaming can be measured electrochemically as it affects the rate of mass transport of ions to the electrode surface.[19]

Mass transport sensors placed within a cavitating media are sensitive to a broad range of phenomena (acoustic streaming, bubble motion and bubble oscillations). However, erosion sensors are only sensitive to microjetting and shockwave formation. If a microelectrode is held at a potential required to detect mass transport it will be sensitive to

the entire range of phenomena that will cause fluid flow. In turn, the current time case recorded would reflect this as a large number of events occur per second. These events are of ms order duration. However, if the potential of the microelectrode were changed so that it is no longer sensitive to mass transport but rather detects surface repassivation, which immediately follows erosion, the current time trace would show fewer events of much shorter duration (reflecting the fewer mechanisms responsible for these processes). The order of these events would be (100-10000 μs).[19]

Acoustic streaming, microstreaming, microjetting and shock wave formation can have a dramatic effect on many electrochemical processes, as outlined in sections (1.4.1-1.4.4). As electrochemistry is the chief analytical tool employed in the research it is important to summarise the work performed by other authors using similar techniques. It is also important to investigate how ultrasound affects electrochemical processes. These topics are discussed in the next section.

1.5 The Effects of Ultrasound on Electrochemical Processes

The study of the effects of ultrasound on electrochemical processes has been wide spread and dates back to the early 1930's.[56] Bard investigated the employment of ultrasound as a mass transport enhancement tool in 1963.[57] Ultrasound has many valuable effects on electrochemical processes including enhanced mass transport,[32, 33, 58, 59] increased yields and current efficiencies,[60] electrode surface activation,[61] electrochemiluminescence,[62] production of radicals and alteration of reaction mechanisms.[63] The latter processes have led to a dearth of information on ultrasonically enhanced electrochemistry in the literature.[56, 64] The use of ultrasonic irradiation has led to advances in electroplating,[64] electrosynthesis [64, 65] and the electrodeposition of polymers films.[64] However, few papers exist on the characterisation of cavitation activity using electrochemistry.

Compton *et al.*[66-68] have undertaken a number of studies investigating the effects of dual activation, coupling ultrasound to electrochemistry. These experiments were performed using an ultrasonic horn operating at fixed frequency (20 kHz) and varying the electrode tip distance (i.e. the distance from the tip of the ultrasonic horn to the electrode surface). The authors demonstrated the huge effect of ultrasound on mass transport measured at the electrode surface using various voltammetric techniques. In particular they demonstrated how sonovoltammetry enables fast rate constants to be measured under steady state conditions at macroelectrodes.[66] To achieve this the authors investigated the dehalogenation

of aromatic compounds, 3– and 4–bromobenzophenone in N,N-dimethylformamide. In addition the authors compare the electrochemical results at the electrode solution interface to the chemistry in the bulk by monitoring the sonochemical destruction of aqueous dilute cyanide solution in 0.1 mol dm^{-3} NaOH.[66] The authors concluded that the factors that govern the violence of interfacial cavitation are proportional to the factors that make cavitation in the bulk chemically efficient. It is important to note that these systems need to be calibrated under the conditions employed to achieve quantative reproducible results.

In addition, Maisonhaute *et al.*[24] detected violent cavitation events close to a vibrating ultrasonic horn (20 kHz). The author's used 4 and 6 mm diameter platinum electrodes positioned close to an ultrasonic vibrating horn and studied the oxidation of ferrocene in dimethylformamide and the reduction of $Ru(NH_3)_6^{3+}$ in 0.1 mol dm^{-3} KCl. They detected violent cavitation events in the form of current peaks superimposed on the average limiting current. The author's attribute these enhancements of mass transport to diffusion inside a thin layer present between the electrode and the bubble and developed a quantitative model[67] for explaining bubble behaviour leading to estimation of the diffusion layer thickness (25 nm for high acoustic pressure estimated by the authors to be 250 bar).

Goldfarb *et al.*[68] also studied the effect of pressure on cavitation and acoustic streaming in electrochemical processes. The reversible one electron reduction of $Ru(NH_3)_6^{3+}$ in 0.1 mol dm^{-3} KCl was again employed at a 25 μm platinum electrode with varying concentrations of dissolved argon and carbon dioxide. The resulting cathodic response was interpreted as being composed of a steady state macroscopic streaming induced component and a transient spike-like component detected after the onset of cavitation. The authors reported that the cavitation process was strongly dependent on pressure and increased monotonically in the presence of argon. However, the threshold appeared at lower ultrasonic power when pressurising with CO_2 and even decreased at higher pressures. The results were interpreted in terms of the mechanical pressure, the surface tension and the formation of a liquid CO_2 phase.

Reisse[69] and co-workers introduced the idea of employing the titanium horn itself as a working electrode, which was reported as capable of acting as either a cathode or an anode. Compton *et al.*[70] introduced a modified version of this by altering the titanium tip of the horn to enable the insertion of a platinum disk (so called Pt sonotrode). They studied the reduction of p-benzoquinone in KCl and the oxidation of ferrocene in acetonitrile. The magnitude of the limiting currents (and thus the diffusion layer thickness adjacent to the

electrode) were substantially larger compared to experiments where the titanium horn is positioned above the working electrode.

Birkin *et al.*[32, 33] have shown that single cavitation events could be monitored using microelectrodes on a μs timescale. They recorded the electrochemical oxidation of ferrocence on gold microelectrodes irradiated with ultrasound under mass transport limited conditions (MTL). Microelectrodes were employed for the electrochemical investigation of single bubble sonoluminescence (see chapter 7).

The employment of microelectrodes into a fluid, which is undergoing cavitation, has several key advantages:

- Microelectrodes can be fabricated down to the nm length scale and hence are small in comparison to cavitation events. Individual bubble collapses may shield the microelectrode from other events that may occur within the same cavitation bubble cloud at the same instant. Information may therefore be discerned on an individual rather than a spatially averaged basis.
- Microelectrodes have fast diffusion field relaxation enabling the measurement of individual mass transport events to high temporal resolution.
- These small electrodes are able to penetrate well-controlled acoustic fields with minimum disruption to the associated sound field. This is particularly important for the employment into a standing wave sound field similar to those required for the generation of single bubble sonoluminescence (SBSL).

The above advantages illustrate that the employment of microelectrodes within a cavitation cloud can probe local environments for specific events. This information is not available using spectro/photographic techniques as a result of the inherent light scattering phenomena associated with dense cavitation bubble clouds.

However, although the employment of electrodes within a cavitation environment has several significant advantages as outlined above, quantitative electrochemical experiments require an accurate knowledge of the mass transfer coefficient. Birkin *et al.*[71] has shown that the nature of cavitation within cylindrical cells results in the generation of active regions within the cell. In the absence of these active cavitation regions, little or no enhancement of mass transport to a microelectrode (which is already efficient) can be detected.[71] The authors demonstrated that the mass transport coefficient varies dramatically in a cylindrical ultrasonic reactor, depending on a number of factors including the ultrasonic frequency, the acoustic pressure and the position of the electrode. The authors concluded that the contribution of acoustic streaming to mass transfer is negligible compared to

cavitation in cells of this nature. In addition it was shown that the mass transport coefficient could change dramatically with time when keeping all conditions constant (i.e. position of electrode, ultrasonic frequency etc). This effect was attributed to a moving streamer.[71] The latter difficulties make quantitative electrochemical analysis difficult by placing electrodes directly into the ultrasonic reactor. In order to avoid these problems a flow cell was employed for the radical trap experiments performed in chapter 4.

In addition to the physical effects of cavitation (see section 1.4), it is also possible to measure the chemical effects of cavitation using electrochemical techniques (see chapter 4, section 4.1). The chemical effects of inertial cavitation are predominantly due to the extreme temperatures and pressures generated in the collapsing bubble. Flint and Suslick [63] have inferred that temperatures of 5000 K and pressures of up to ca. 500 atmospheres are generated during bubble collapse. These high temperatures and pressures are believed to lead to the breakdown of the solvent matrix resulting in the formation of radicals.[72, 73] The production of radicals as a result of inertial cavitation has been investigated by many authors and is discussed in section 1.6.

1.6 Detection of Radicals

Weissler[73] initially established the production of radicals by detecting the presence of ultrasonically generated H_2O_2, the geminate recombination product of hydroxyl radicals. The ultrasonic yield of H_2O_2 in water in the presence of various scavengers (acrylamide, formic acid and allythiorea) was also investigated. The results showed that a radical scavenger could be efficient even though relatively unvolatile, and therefore present in low concentrations inside the cavitation bubble. The presence of both hydroxyl and hydrogen atoms was confirmed by Makino *et al.*[74, 75] Diamagnetic nitroso or nitrone spin traps 5,5-Dimethyl-1-pyrroline-N-oxide (DMPO), 2-methyl-N-(4-pyridylmethylene)- N-oxyl (PYBN) and alpha-(4-pyridyl-1)-N-tert-butyl nitrone (POBN) were used to convert short lived radicals into relatively longer lived nitroxyl radicals that are ESR (electron spin resonance) observable. The spin traps and the spin adducts are illustrated in reactions [1.1] to [1.3] inclusively where *R* represents $OH^{\bullet}$ or $H^{\bullet}$.

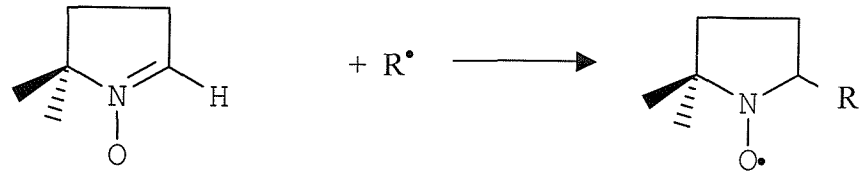

DMPO [1.1]

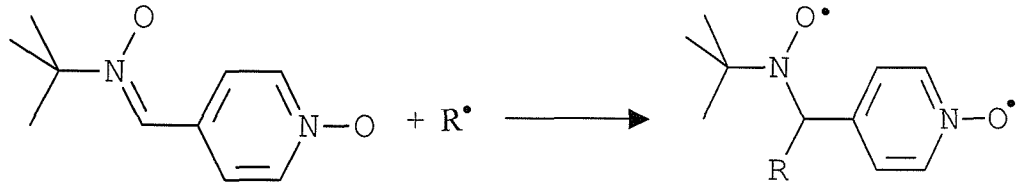

POBN [1.2]

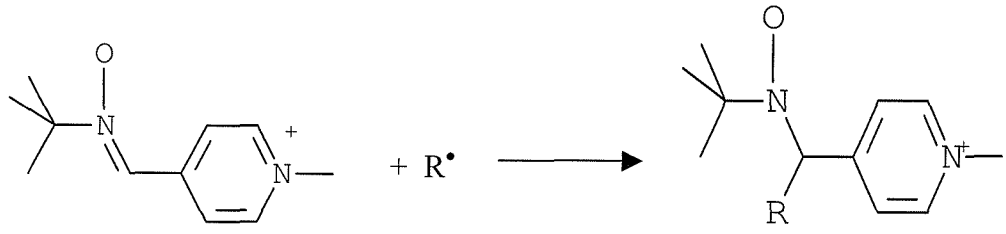

PYBN [1.3]

The spin adducts always have one β hydrogen, except for the H adducts which have two hydrogen atoms in the β position. Therefore, a secondary doublet is observed in the ESR spectrum in the case of $OH^{\bullet}$ and a secondary triplet in the case of $H^{\bullet}$. It is estimated that only 10 % of the radicals generated from water vapour in the cavitation bubbles reach the liquid phase.[76] In addition it has been proposed that the local concentration of radicals generated around a single cavitation event[76] can reach the order of 4 mmol dm^{-3}. However, the radicals are not homogeneously distributed in the liquid phase, and a high concentration of solute is necessary to scavenge them efficiently.[77]

The detection of radical species using electrochemical detection methods has had limited attention. Compton and coworkers[78] reported that direct electrochemical detection of radical species within a cavitation cloud produced by high intensity ultrasound was possible. In this technique a stable radical species, generated through the reduction of fluorescein, was produced in the cavitation plume in front of an operating ultrasonic horn. The authors investigated the reduction of fluorescein at the mass transport limiting potential (MTLP). They observed a higher mass transfer limiting current than expected (from mass transfer effects alone). This was assigned as evidence for the presence of radicals (see

reaction [1.4]). In this respect a *sono-EC'* mechanism was proposed in which the radical product of the electrochemical reduction was reconverted to fluorescein through reaction with hydroxyl radicals (generated by ultrasonic cavitation). *EC'* indicates a coupled chemical reaction following an electrochemical redox reaction. In this case it is referred to as *sono- EC'* because the effect is caused by acoustic cavitation. The mechanism for this process is illustrated in reaction [1.4]. The overall process regenerates the original species so increasing the current recorded. It is important to note that this process requires mass transfer calibration. However, few other examples of direct electrochemical detection of radicals produced by cavitation can be found within the literature.

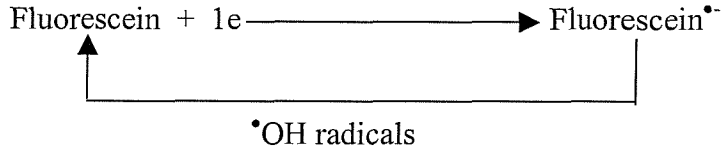

[1.4]

Sonochemists working on the detection or quantification of radicals have focused predominantly on hydroxyl radicals. There is little evidence in the literature for the detection of $H^{\bullet}$, despite the fact that it is generated in equivalent quantities when compared to $OH^{\bullet}$ in the primary solvent degradation step (see reaction [1.5]). The chemical nature of these two radical species is quite different (see reactions [1.5-1.8]).[79-84]

$$H_2O \longrightarrow OH^{\bullet} + H^{\bullet} \quad [1.5]$$

$$H^{\bullet} + O_2 \longrightarrow HO_2^{\bullet} \quad [1.6]$$

$$H^{\bullet} + H_2O \longrightarrow H_2 + OH^{\bullet} \quad [1.7]$$

$$OH^{\bullet} + H_2 \longrightarrow H^{\bullet} + H_2O \quad [1.8]$$

The $OH^{\bullet}$ radical species is known to initiate a number of different reactions within solution[83] and many chemical dosimeters have been established for this system. In contrast the $H^{\bullet}$ atom can be rapidly consumed directly by molecular oxygen[84] (reaction [1.6]). The $H^{\bullet}$ radical can also be converted to $OH^{\bullet}$ through reaction [1.7]. Reaction [1.7] is endothermic. However, the temperature within a collapsing bubble is high and the number of water molecules within the cavitating bubble exceeds the number of radicals. Hence, a considerable amount of the originally formed $H^{\bullet}$ may be converted to $OH^{\bullet}$ radicals. It is important to note that reaction [1.7] is reversible (see reaction [1.8]) and it is this reaction, which prevents H_2 accumulation in irradiated solutions.[85] Less attention has been placed on

$H^{\bullet}$ perhaps as a result of these quenching reactions. Hart and Henglein showed that it was possible to detect $HO_2^{\bullet}$ using a Cu^{2+} system.[86] These authors used the Fricke dosimeter in the absence and the presence of Cu^{2+} to estimate $HO_2^{\bullet}$ concentration. This is due in part to the presence of $H^{\bullet}$. Mark *et al.*[87] used the same system to estimate $H^{\bullet}$ concentration.

To determine the efficiency of radical production in a given ultrasonic reactor, and to compare different radical trapping systems, sonochemists have adapted the system used in radiation studies (chemical dosimetry) to quantify ultrasonic radical production. This system is discussed in section 1.7.

1.7 Chemical Dosimetry

In chemical dosimetry, the radiation dose is determined from the chemical change produced in an appropriate medium. Any well-characterised and quantitative chemical reaction may serve as the basis for a dosimeter. However, to be usable such a system must meet a number of requirements. No single reaction is likely to be found that is universally applicable. Fricke and Hart[83] have outlined the properties of the ideal dosimeter. These include the following:

- It must have satisfactory sensitivity. Aqueous chemical dosimeters e.g. the Fricke dosimeter can measure doses between $10 - 10^{10}$ rads with an absolute accuracy of 1-2 %. Absorbance spectroscopy based dosimeters are unable to quantify dose levels below 10 rads. This as a result of their dependence on the value of the absorption coefficient.
- It must possess satisfactory stability before and after irradiation.
- The dosimeter should show an independence of product yield on the dose rate, quality of radiation and temperature.
- A linear relationship between the amount reaction product and dose is desirable.

Sonochemists have used numerous dosimeters for the determination of $OH^{\bullet}$ radical formation in the sonolysis of aqueous solutions. The most common dosimeters in current use are the Fricke, the terephthalate and the iodide systems.[85, 87, 88] Each of these systems will be discussed in brief.

I.7.1 The Fricke Dosimeter

The Fricke reaction has been used extensively in the assessment of ionising radiation.[83] In this system an acidified solution of Fe^{2+} is irradiated with ionising radiation, which is

thought to produce hydroxyl radicals. These hydroxyl radicals and hydrogen atoms oxidise Fe^{2+} to Fe^{3+}. The mechanism for this process is summarised in reaction [1.9-1.13]. It is important to emphasise that no ionising radiation is used in the work presented in this thesis. Radicals are generated by cavitation (see chapter 4 section 4.3). Several authors have used the Fricke reaction to measure the production of radical species as the result of acoustic cavitation.[87, 88] In these reports UV absorption spectroscopy was used to measure the production of Fe^{3+}.

$$Fe^{+2} + OH^{\bullet} \longrightarrow Fe^{+3} + OH^{-} \quad [1.9]$$

$$H^{\bullet} + O_2 \longrightarrow HO_2^{\bullet} \quad [1.10]$$

$$Fe^{+2} + HO_2^{\bullet} \longrightarrow Fe^{+3} + HO_2^{-} \quad [1.11]$$

$$Fe^{+2} + H_2O_2 \longrightarrow Fe^{+3} + OH^{\bullet} + OH^{-} \quad [1.12]$$

$$Fe^{2+} + H^{\bullet} + H^{+} \longrightarrow Fe^{+3} + H_2 \quad [1.13]$$

The concentration of the generated Fe^{3+} can be determined analytically and the equivalent dose exposed to the test solution calculated. In order to calculate the equivalent dose it is necessary to employ equation (1.13), which has been adapted from radiochemical dose equivalent calculation: [83]

$$D_{rads}' = \frac{\left(dc/dt\right) \times 9.64 \times 10^{8}}{G(X)\rho} \quad (1.13)$$

where D_{rads}' represents the equivalent dose of rads exposed to the test solution per second, *G(X)* represents the chemical yield expressed as a number of molecules or ions liberated per 100 eV of equivalent radiation and ρ the density of the test solution. Dosimetry applied to cavitation has been suggested by a number of authors. As an example Mark *et al.*[87] quoted a number of *G(X)* values depending on the gas content within their reactor. The authors assumed that by employing calorific measurements, it is possible to relate the energy input to the cavitation dynamics. However, cavitation is a non-linear threshold phenomenon, and as such equating the power in to the yield of products is not realistic. Hence, although the authors are thorough in their approach, it is unlikely that the *G(X)* values quoted are generally accurate but rather give an indication of the results achieved using varying gas content. However, a more physically realistic approach may be made by comparison to radiation studies (as is performed in chapter 4 section 4.3), which does not suffer from these problems.

1.7.2 Terephthalate Dosimeter

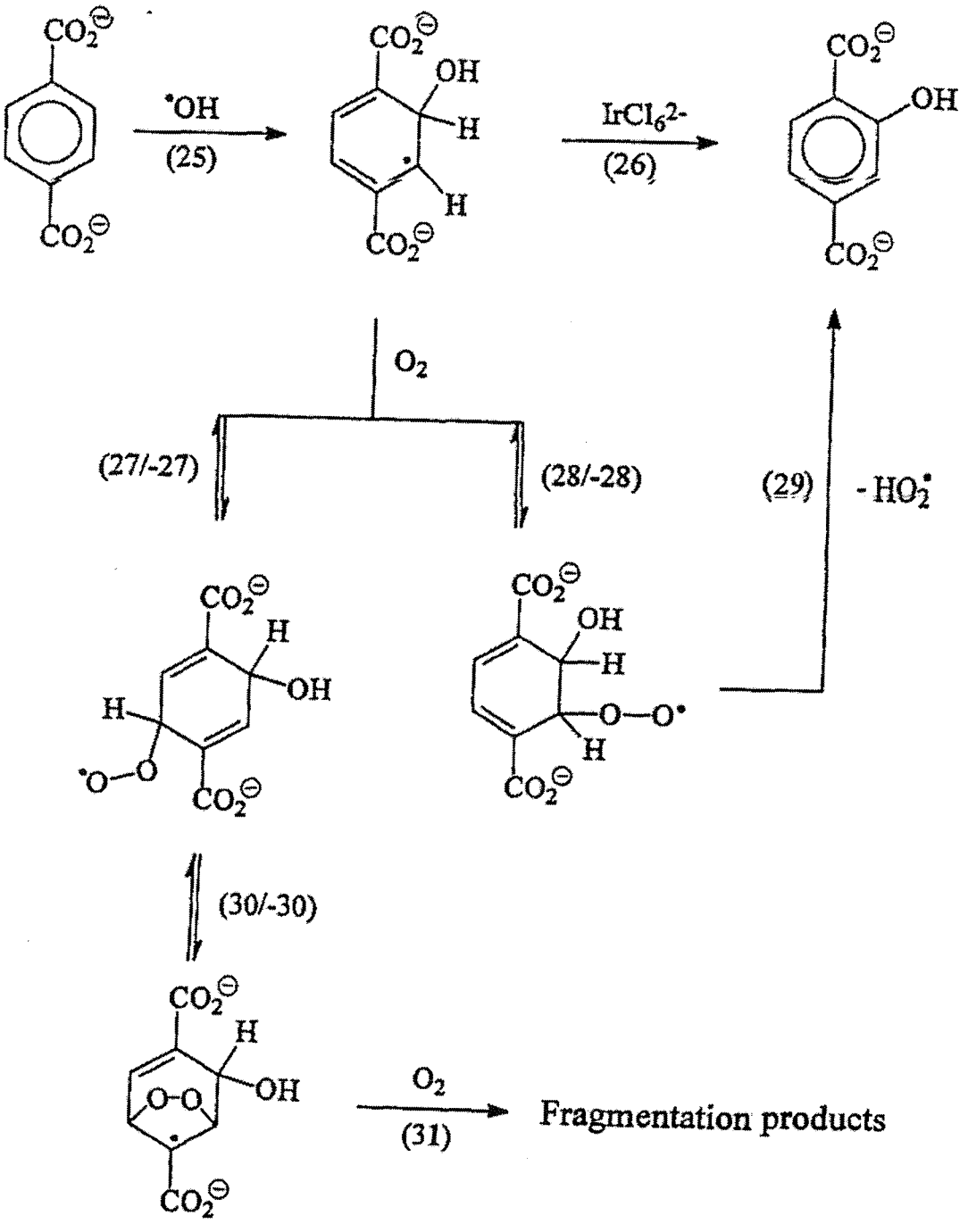

Figure 1.9 Mechanism for OH• radical determination using terephthalate (after von Sonntag *et al.*[85])

The terephthalate dosimeter makes use of the OH• radical induced hydroxylation of the terephthalate ion. Like the Fricke reaction it was originally developed for the dosimetry of ionising radiation. The OH• reacts at a diffusion control rate preferentially (85%) to the 2-position (see reaction 25 in the figure 1.9). The indicator product is 2-hydroxyterephthalate,

which is determined on the basis of its fluorescence (see figure 1.9). The mechanism for this reaction has been elucidated in depth[85, 89] and is illustrated in figure 1.9. In the presence of oxygen, competitive pathways (reactions 27, 28 and 30 in figure 1.9) may occur. The advantage of this dosimeter is its specificity for the hydroxyl radical formation. However, There is a significance dependence of response on the radiation energy. The fluorescence instruments used for measurements require calibration prior to each experiment and the dosimeter must be calibrated to a source of known dose rate.[90]

1.7.3 The Weissler Reaction

Weissler[14] first reported the oxidation of potassium iodide by ultrasound in 1950. Since then several authors have investigated the reaction for sonochemically formed hydroxyl radical determination.[76, 85, 91] In this dosimeter I^- is converted to I_3^- through a cascade of reactions involving $OH^\bullet$ or radical products thereof (see reaction scheme [1.14-1.17]).[85]

$$I^- + {}^\bullet OH \longrightarrow {}^-OH + I^\bullet \qquad [1.14]$$

$$I^\bullet + I^- \longrightarrow I_2^{\bullet-} \qquad [1.15]$$

$$2I_2^{\bullet-} \longrightarrow 2I^- + I_2 \qquad [1.16]$$

$$I_2 + I^- \longleftrightarrow I_3^- \qquad [1.17]$$

1.7.4 Electrochemical Dosimeters

The only evidence for electrochemical dosimetry in the literature is based on a ceric sulphate system. This system is sensitive to both hydrogen atoms and hydroxyl radicals (see mechanism [1.18-1.21][83]). Mathews[92] used differential potentiometry to determine the radical population in an irradiated sample. Matthews measured the difference between the electrochemical potential of the irradiated and unirradiated solution. This Ceric dosimeter is not regularly used because it has some significant disadvantages, including photoreduction by exposure of solutions to sunlight.

$$Ce^{4+} + H^\bullet \longrightarrow Ce^{3+} + H^+ \qquad [1.18]$$

$$Ce^{4+} + HO_2^\bullet \longrightarrow Ce^{3+} + H^+ + O_2 \qquad [1.19]$$

$$Ce^{3+} + OH^{\bullet} \longrightarrow Ce^{4+} + OH^{-} \quad [1.20]$$

$$Ce^{4+} + H_2O_2 \longrightarrow Ce^{3+} + H^{+} + HO_2^{\bullet} \quad [1.21]$$

In addition, Compton and coworkers[78] performed electrochemical detection of hydroxyl radicals using the Fluorescein system. The mechanism for this reaction was discussed in section 1.6.

Detecting light emission from chemiluminescent reactions may also be used to monitor radical production. This technique is used in this project and it is described in the next section.

1.8 Chemiluminescence

Chemiluminescence can be defined as the emission of light as a result of the generation of electronically excited states formed as a result of a chemical reaction. It is well known that alkaline solutions of luminol emit light when submitted to ultrasound of sufficient intensity to produce inertial cavitation. This is an oxidative chemiluminescent process involving sonochemically generated $OH^{\bullet}$. It is in essence a trapping system for hydroxyl radicals. The mechanism for the process has been elucidated in depth by many authors.[93, 94] The proposed mechanism[94] is illustrated in figure 1.10. Previous studies have show that the process is most efficient at high pH, and that the emission of light is strongly influenced by H_2O_2 concentration.[94 - 96] The study of sonochemiluminescence of luminol in the presence of H_2O_2 is potentially complicated by a background non sonochemical process of chemiluminescence catalysed by divalent metal cations. A chelating agent (EDTA) binds the metal cations that may be introduced into the solution by leaching from equipment or from impurities in reagents and thus prevents this non sonochemical background reaction. The addition of H_2O_2 to the solution generates the $O_2^{\bullet -}$ radical species[94] required for reaction (ii) in figure 1.10. The hyperoxyl anion (HO_2^-) is formed form the dissociation of H_2O_2 (pka $10^{-11.65}$).[94] The $OH^{\bullet}$ radical has a redox potential[94] of 2.8 V and is readily capable of oxidising both H_2O_2 and HO_2^-. Thus when significant concentrations of H_2O_2 exist in solution reactions, [1.22] and [1.23] become important. In this way two $OH^{\bullet}$ radicals are required to complete the light emission process (see mechanism in figure 1.10).

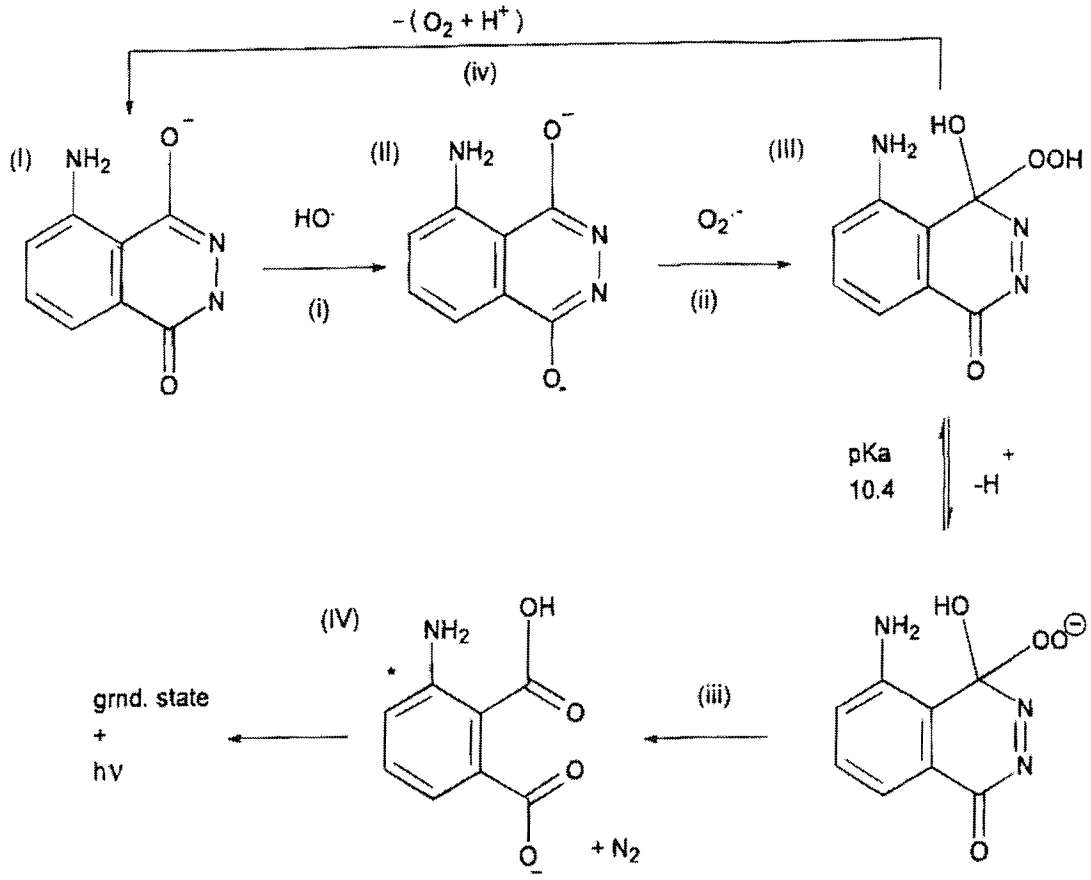

Figure 1.10 Proposed mechanism for the chemiluminescence of luminol (After McMurray *et al.*[94]). The reader is referred to the text for discussion of individual steps.

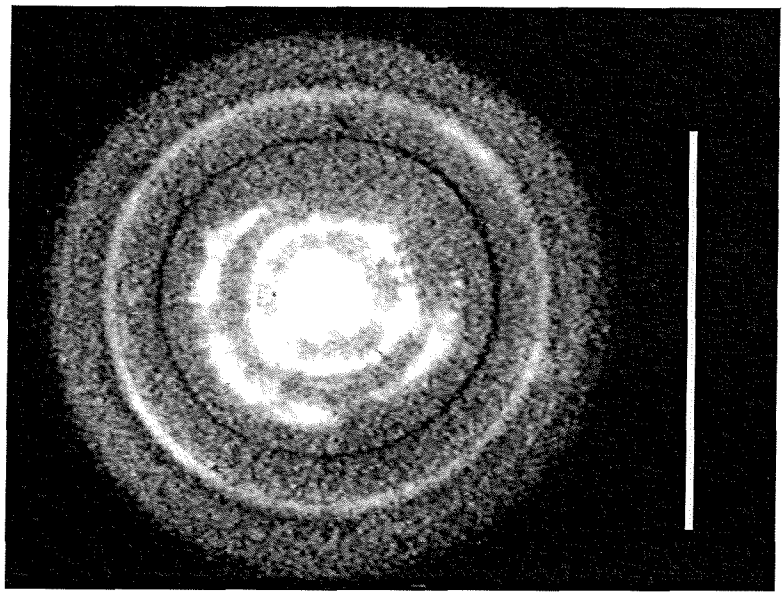

Figure 1.11 Frame showing the light emission from a cylindrical single walled cell (9.4 cm internal diameter) recorded from above. The driving frequency was maintained at 132.44 kHz. The cell contained an aqueous solution of 50 μmol dm^{-3} luminol, 0.1 mmol dm^{-3} EDTA, 0.1 mmol dm^{-3} H_2O_2 and 100 mmol dm^{-3} Na_2CO_3. The picture was recorded under ambient conditions (*ca.* 20-23 °C) in aerobic media. The solution height was maintained at 14 cm. The acoustic pressure amplitude was 76 kPa. Picture from chapter 3. The scale bar represents 9.4 cm.

$$OH^{\bullet} + H_2O_2 \longrightarrow O_2^{\bullet-} + H_3O^{+} \quad [1.22]$$

$$OH^{\bullet} + HO_2^{-} \longrightarrow O_2^{\bullet-} + H_2O \quad [1.23]$$

The formation of the crucial intermediate 3-amino phthalic acid (compound (iv) see figure 1.10) leads to emission of light, maximum wavelength (λ_{max}) ca. 425 nm depending on the pH employed.[97] The maximum fluorescence for compound (iv) occurs at pH 11. This is the decisive factor in luminol type chemiluminescence. This is because the fluorescence quantum yield affects the quantum yield of chemiluminescence and hence, the reason for employing highly basic conditions (100 mmol dm^{-3} Na_2CO_3).

This reaction has been used to visualise the spatial distribution of cavitation in solution photographically.[71] This application is illustrated in figure 1.11. The sonochemiluminescence of luminol has been used to investigate the onset of the chemical effects of cavitation by a number of authors. Henglein *et al.*[76] used a pulsed ultrasonic field and recorded the initial onset of sonochemiluminescence using a luminol solution (see figure 1.10 for mechanism of light formation). The critical numbers of pulses required to achieve the full luminescence signal were recorded. A number of parameters such as gas content, presence or absence of nucleation sites and pre-irradiation were investigated. For the generation of high temperatures within the collapsing bubble monatomic and diatomic gases are thought to be the most effective. This is because of the large specific heat ratios of these gases are favourable for obtaining high temperatures in the oscillating or collapsing bubble produced in an ultrasonic field.[98] In addition, it is important to note that the light output from chemiluminescence is orders of magnitude more intense than the natural sonoluminescence of aerated water.[93-96, 99]

Whilst sonochemiluminescence produces light from cavitation, the origin of the light is chemical in nature. However, the light emission from cavitation itself has been known since 1934. This will now be discussed.

1.9 Sonoluminescence

Sonoluminescence, the conversion of sound energy to light energy is a process which has captivated researchers for decades. The phenomenon was discovered in 1934 when Frenzel and Schultes[100] exposed a photographic plate to acoustic waves generated in a water bath. They observed a darkening of the plate and attributed this effect to luminescence from

the sound field. The luminescence did not result from the sound field directly but from the process of cavitation. However, the exact mechanism for the generation of the light is still a matter of debate today. Sonoluminescence has been separated into two types: single bubble sonoluminescence (SBSL) and multi-bubble sonoluminescence (MBSL). The phenomenon of MBSL occurs when the acoustic pressure amplitude in the bulk of a liquid exceeds the threshold for cavitation. If the solution cavitates, sonoluminescence occurs. Many separate cavitation events take place, each emitting discrete bursts of light.

Gaitan *et al.*[101] are credited with the discovery of SBSL. However it is likely Saksena and Nyborg[102] initially discovered SBSL in 1970. SBSL was achieved using a standing wave sound field with one pressure antinode in the container. A single pulsating bubble may be levitated stably for hours.[101] This discovery allowed cavitation research to focus on individual cavitation events and to study the resulting electromagnetic radiation. Single bubble sonoluminescence was successfully generated in Southampton and is illustrated in figure 1.12. To the unaided eye the bubble looks very stable and a seemingly steady glow may be seen. However, rapid bubble oscillations actually take place and subnanosecond light bursts occur with clockwork precision.[101, 103] The experimentally observed properties of this remarkable process have been summarised in a number of excellent reviews.[103-106] A brief overview of these experimentally observable facts will be given in the next section.

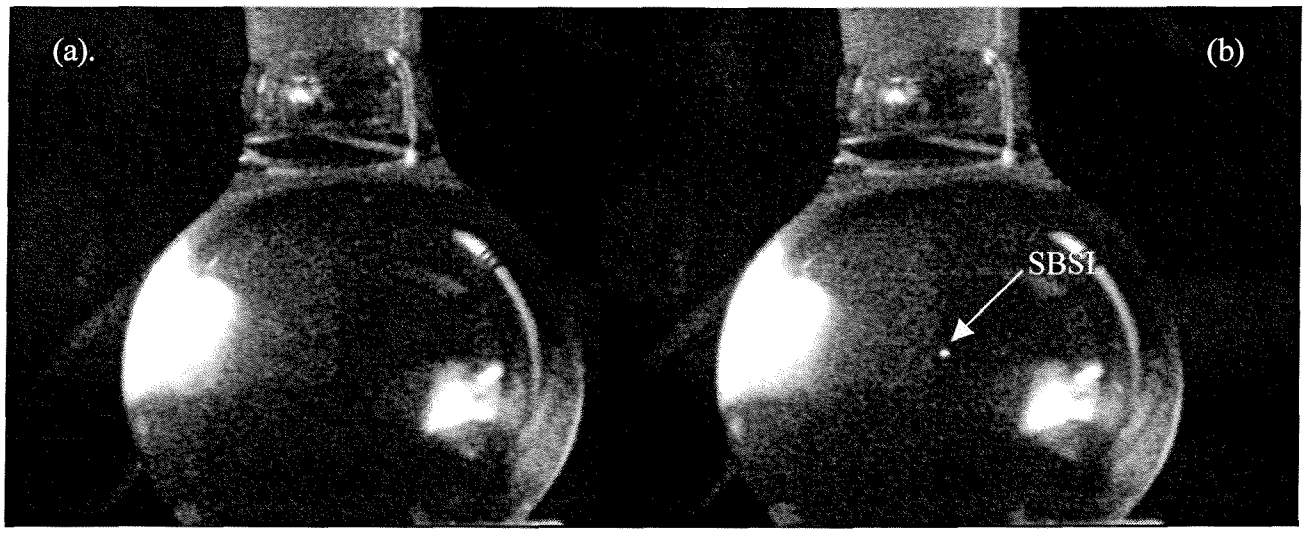

Figure 1.12 Frames showing the generation of single bubble sonoluminescence in a degassed water solution. The ultrasonic frequency was 27.744 kHz and the acoustic pressure amplitude was 140 kPa. Frame (a) shows the cell before generation of SBSL and frame (b) shows the luminescing bubble in the centre of the cell. The pictures were recorded using an image intensified CCD camera. The other light present on frames (a) and (b) is due to reflections from a lamp.

1.10 Single Bubble Sonoluminescence: The Experimental Facts

The parameter space in which SBSL occurs has been summarised by Gaitan *et al.*[101] and Matula[107] as a function of acoustic driving pressure. The threshold for stable SBSL is approximately 1.2 atm, depending on the liquid, its temperature and other parameters of the experiment. However, stable sonoluminescent regions[101, 107] exist up to approximately 1.6 atm. Single bubble sonoluminescence demonstrates a number of remarkable features. Whereas the driving field has a typical period of tens of microseconds, the duration of the sonoluminescent pulse has been measured to be 50-250 ps depending on the conditions.[108] It is important to note that this is one hundred times shorter than the shortest (visible) lifetime of an excited hydrogen atom.[109] Single bubble sonoluminescence pulses are isotropic and unpolarised. The light emission occurs on bubble collapse and the phase of the emissions stays rigorously fixed over a number of acoustic cycles.[110] This is illustrated in figure 1.13.

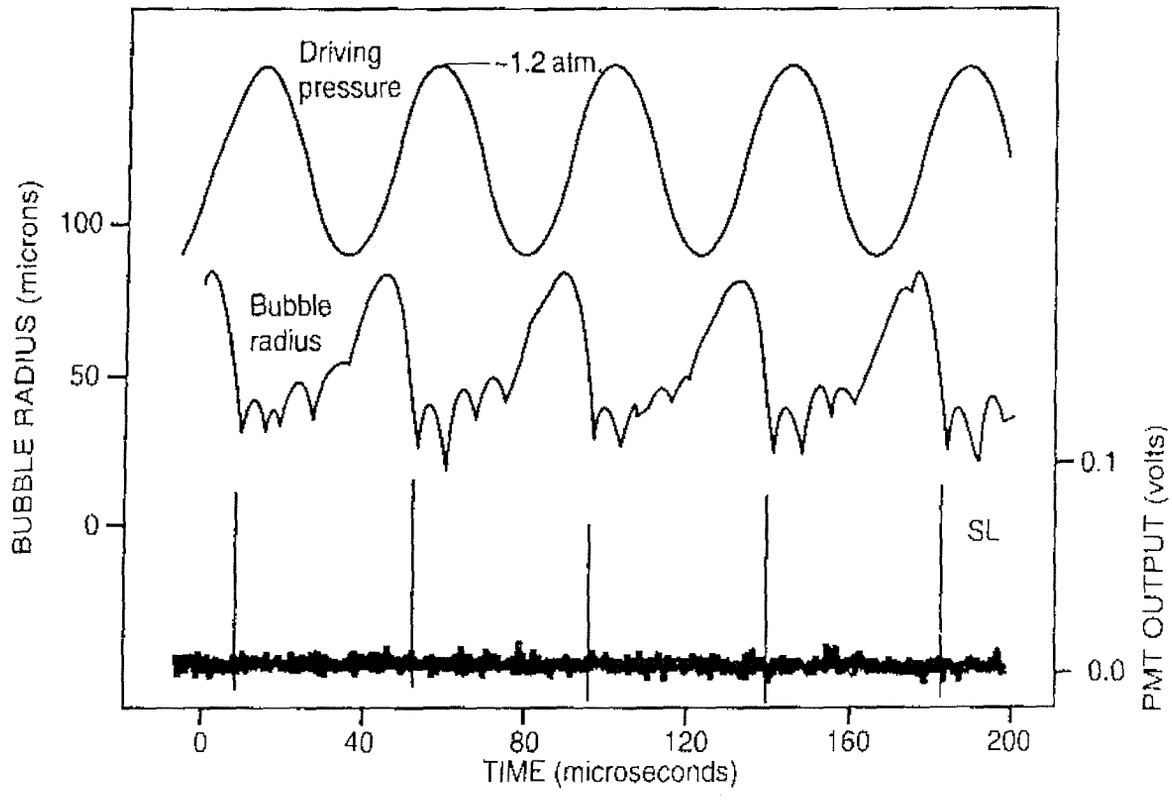

Figure 1.13 Synchronous relationships between the acoustic field (top), the measured radius versus time curve (middle) and the SBSL emissions measured with a photomultiplier tube (bottom) from Crum.[110]

The spectrum of light emitted as the result of MBSL has been shown to be different when compared to that recorded for SBSL. Figure 1.14 shows a comparison of the spectra

taken from the recent literature.[111] It has been known for years that MBSL in water containing NaCl exhibits sodium lines.[2] The MBSL spectrum (see figure 1.14) exhibits two distinct emission peaks attributed to Na^* and OH^* in addition to a continuum. In contrast the SBSL spectrum (see figure 1.14) exhibits only a continuum. Both experiments were performed under identical aqueous conditions ($NaCl_{(aq)}$). As $NaCl_{(aq)}$ is the source of the Na^* emission peak it is difficult to understand how it gets into the interior of the collapsing bubble (as the vapour pressure of NaCl is low). The evidence suggests the existence of at least two mechanisms or bubble environments that could be responsible for the emission of light observed (one associated with MBSL and one with SBSL). It should also be noted that the duration of emission of MBSL[109] is ca. 1.1 ns. This is again in contrast to SBSL (see section 1.10). However, multiple bubbles do not collapse at a uniform time. Rather a population of bubbles will have different lifetimes.

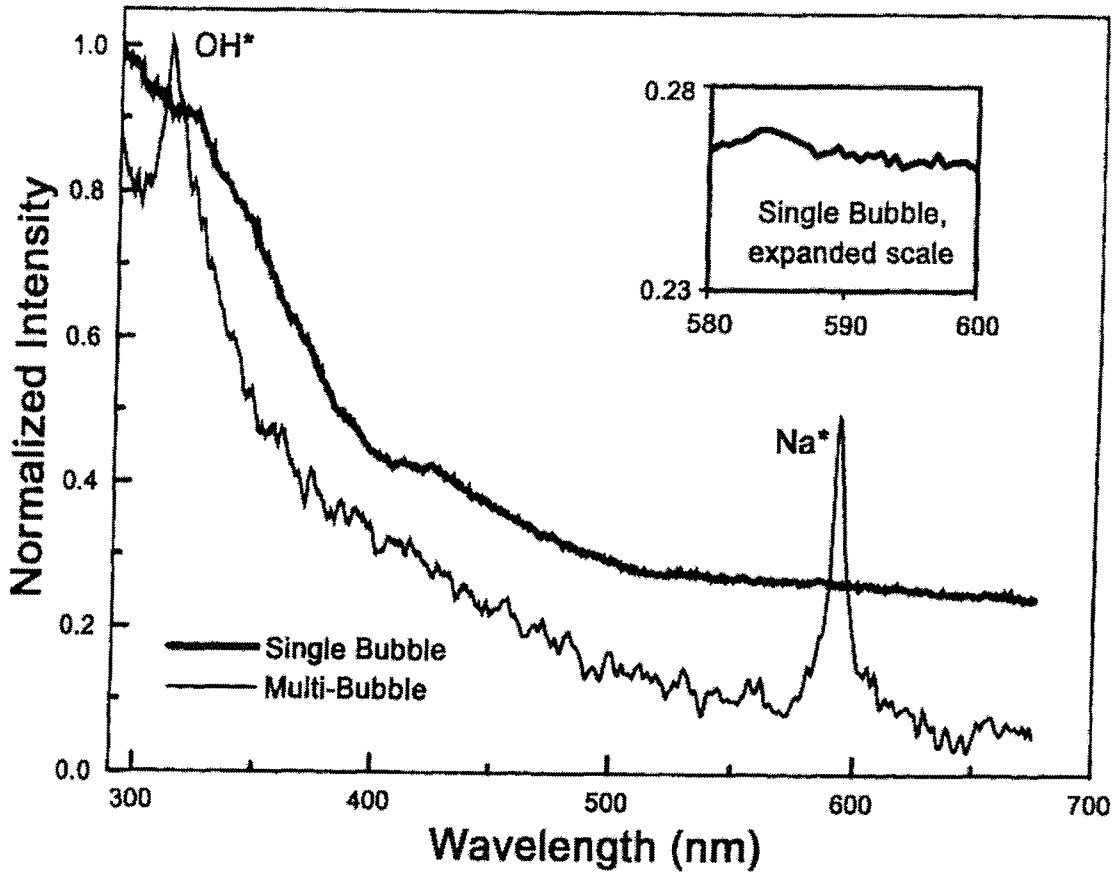

Figure 1.14 Spectrum showing the key differences between single and multiple bubble sonoluminescence spectra (after Matula *et al.*[111]).

In addition to these differences, no stable SBSL has been observed in air saturated water. It is necessary to degas the water. However, a small rare gas content of the bubble is necessary. It is believed that the process of rectification (removal of other molecular gases

from the bubble over time) leads to rare gas accumulation in the bubble and that the small argon content of air is responsible for the glow of sonoluminescent air bubbles.[112] O_2 and N_2 dissociate at bubble temperatures of several 1000 K. The resulting radicals are believed to react to form compounds such as NO, OH and NH, which dissolve in water vapour to form e.g. H_2O_2, HNO_2 and HNO_3.[112] If this theory of rectification, is correct the original bubble must shrink dramatically. This effect is illustrated schematically in figure 1.15. This may make electrochemical generation difficult.

Several theories exist to explain the spectroscopic emission of light observed from MBSL and SBSL. However, no universally accepted satisfactory mechanism has been achieved. These light emissions theories will be discussed in the next section.

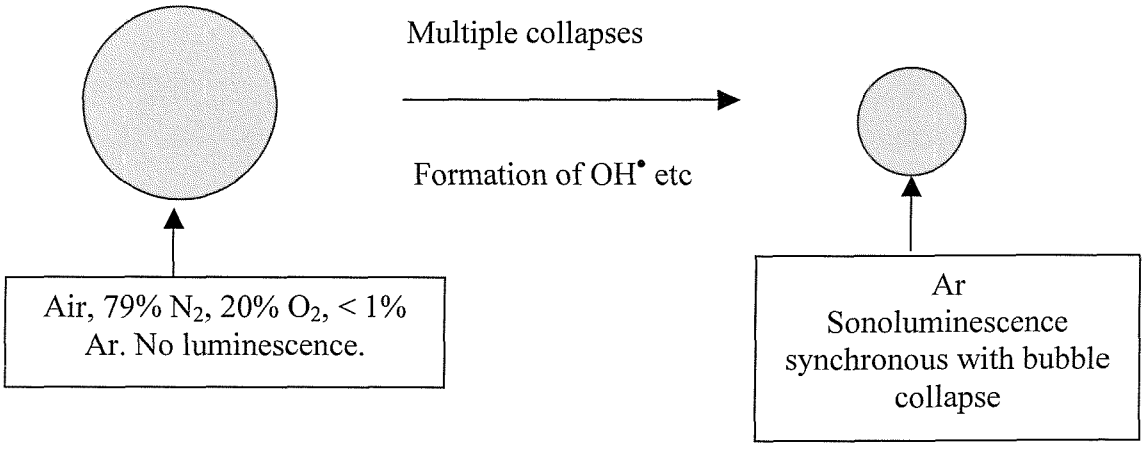

Figure 1.15 Schematic illustrating rectified diffusion coupled to sonoluminescence.

1.11 Theories for Light Emission

There is much debate over the mechanism for light emission in sonoluminescence.[103-106, 112] A number of theories have been proposed including thermal, mechanochemical, electric, opacity and a quantum theory. Most of the theories were initially proposed for MBSL and have been adapted to explain the short pulse time for SBSL. However, the mechanism is still a controversial issue as no theory has satisfied the collective scientific community working in this field. The various theories are summarised in the following subsections:

1.11.1 Thermal Mechanism

Griffing[113] proposed that heat is generated by the compression of gas and vapour during bubble collapse. This theory employs the Raleigh-Plesset equation, which describes the local heating of the intracavity gaseous phase through adiabatic compression. The heat cannot be dissipated because thermal transport is slower than the bubble collapse. In the high temperatures and pressures generated in these hot spots, radicals and molecular excited states are produced. The recombination of these radicals and the relaxation of the excited species, generate the light emission. This theory is supported by the fact that sonoluminescent spectra of hydrocarbons show vibrationally resolved bands that can be attributed to emission from the excited state of diatomic molecules.[114] However, although this model can predict intracavity temperatures of several thousand Kelvin it fails to explain the extremely short duration of the flashes of light and the emission versus wavelength band width.[106]

1.11.2 Electrical Mechanisms

In 1940 Frenkel[115] proposes that the light emission results from an electronic discharge from charge separation inside a plasma. This proposal follows from a plasma diagnostic analysis which reveals that a single argon bubble is characterised by a spark like plasma. Lepoint *et al.*[116] assume that the bubbles expansion and a major part of its collapse is governed by Rayleigh-Plesset dynamics. It is speculated that several ns before the collapse the bubble interface becomes unstable and needle like jets invade the bubble symmetrically. Each jet (radius ca. 65 nm) reaches a distance equal to half the radius of the bubble and releases a droplet (radius 150 nm), so that the intracavity spray is released 3 ns before the time of collapse. It is proposed that the acoustic pressure at which inward jets form constitutes the sonoluminescent threshold. Because of the serious distortion of the electrical double layer surrounding the bubble, both jets and droplets are electrically (but oppositely) charged. The shockwave electric field is so high that electron emission occurs to such an extent that within 16 fs an enormous amount of energy is released in the jet volume (lifetime < 10 ps). The jets are ablated and a microplasma highly charged with energy expands resulting in the formation of a diverging jet. An overpressure accompanies the microplasmic formation and this is believed to induce strong deceleration of the bubble

wall. However, this theory fails to explain why light emission is observed in liquid mercury.[2]

1.11.3 Mechanochemical Mechanisms

In 1960 Jarman[117] proposed that sonoluminescence is caused by the spherical micro-shock waves propagating within the bubble. Similar mechanisms have been supported by Barber and Putterman[118] and Lofstedt *et al.*[119] Their hypothesis consists of an imploding shockwave launched from the cavity walls which are assumed to reach supersonic speeds by the end of the bubble compression. This proposal stimulated numerical coupling of the Rayleigh-Plesset and Euler equations by Wu and Roberts[120] and Moss *et al.*[121] These computations predict that the gaseous nucleus at the centre of the bubble could be energised by a shockwave so that thermodynamic temperatures between 10^5 and 10^6 K could be reached. Light emission would then result from Bremsstrahlung radiation. A complement to this approach based on more modest heating was introduced by Frommhold and Atchley.[122] They showed that collision induced emission of atom-atom or atom-molecule pairs excited by a shockwave is an alternative to emission by Bremsstrahlung.

1.11.4 Thermal Volume Emission (the Opacity Model)

This model assumes that radiation from the whole body of a transparent body reaches the detector rather than only the surface emission of a black body. The fact that opacity could play a role in sonoluminescence was first recognised by Kamath *et al.*[123] who speculated that radicals in the outer layer of the bubble could resonantly absorb and scatter the radiation coming from the centre, and thus shut off the observed light. Moss *et al.*[121, 124]discussed the possibility that SBSL might be transparent to its own photons. Using tabulated absorption coefficients of different gas species they concluded that there was only a small region of opaque gas in the very centre of the bubble (induced in their model by a converging shockwave) but the rest of the bubble volume was optically thin. Moss *et al.*[121, 124] did not explicitly calculate pulses of emitted light at different wavelengths and other features of their model lead to pulses that are much shorter than observed. However, this is the only model of SBSL light emission that leads to wavelength independent emission spectra. Brenner *et al.*[106] discuss a simple model for opacity illustrating mathematically how the opacity model leads to a wavelength independent emission.

1.11.5 Quantum Vacuum Radiation

Eberlein explains sonoluminescence in terms of quantum vacuum by moving interfaces between media of different polarization.[125, 126] This theory is supported by the fact that no photons in the UV are emitted. In addition the duration of the pulse lengths support this theory.

This section described in brief the main theories for light emission caused by sonoluminescence. Many other possible theories exist in the literature including a number of review papers.[103-106, 112] Each individual theory has its own merits. However, no theory has succeeded in thoroughly satisfying the observed experimental phenomena (see section 1.10).

1.12 Summary of Work Presented

Apfel[20] wrote the three golden rules for any cavitation experiment: "know thy liquid, know thy sound field, know when something happens." These rules were rigidly followed in the work presented in this thesis.

Chapter 2 describes the experimental procedures employed in obtaining the results presented in chapters 3-7. It contains schematic illustrations of the experimental rigs used, in addition to detailed explanations concerning the performing of experiments, the conditions employed and the interpretation of results.

Chapter 3 ("know thy sound field")[20] discusses the sound field generated from a cylindrical sonochemical cell in depth. This sound field is considered with a variable operating frequency. An acoustic model is employed to predict the spatial distribution of acoustic pressure. This is compared with experimental measurements of the spatial characteristics of luminescent emission from a cylindrical cell. A sound speed within the cavitation environment in the range of 868 - 1062 m s^{-1} was calculated from measurements. This corresponded to a bubble void fraction range of 2.9 - 4.2 x 10^{-3} % assuming that the bubbles present have equilibrium sizes smaller than that would be resonant with the sound field.[2] The implications for electrochemical and chemical activity within cylindrical cells are discussed.

Chapter 4 ("know when something happens")[20] presents the development of four novel electrochemical sensors for radical detection generated by cavitation. The detectors are shown to be working reproducibly within a cavitation environment. The results achieved are

the first strong electrochemical evidence for the presence of free radicals. The electrochemical detectors are shown to be extremely sensitive with very low detection limits. Equivalent dose measurements are recorded for the ultrasonic reactor by comparison to ionising radiation studies.

Chapter 5 investigates the frequency dependencies of sonochemical reactions within the acoustically characterised model ultrasonic reactor. Recently, a large number of papers have examined the frequency dependence of sonochemical reactions at a few fixed frequencies.[23] This chapter undermines the attempts of such studies to explain optimal frequencies in terms of cavitation bubble dynamics alone. In addition the correlation between the radical trap sensors and MBSL is investigated. The frequency dependence of MBSL correlates remarkably with the radical trap detectors. MBSL is proposed as a possible detector for chemical activity in ultrasonic reactors. Its performance is critically analysed with respect to other possible reference sensors.

Chapter 6 describes an international experiment first proposed and coordinated by Prof. Leighton. This involved an attempt to develop a reference sensor for cavitation in collaboration with the National Physics Laboratory (NPL) and other partners using an ultrasonic cleaning bath ("know thy sound field")[20] and a 'standard liquid' ("know thy liquid")[20] designed by NPL. Results are presented from three sensors successfully tested in the bath including MBSL, MBSCL and the electrochemical Weissler reaction. A comparison is made between the results achieved using our sensor and the chemical and acoustic results achieved from other partners.

Chapter 7 presents an electrochemical and spectroscopic study of single bubble sonoluminescence. It describes how a novel experimental rig was designed to perform the first electrochemical study of this phenomenon. The chapter outlines the first electrochemical evidence for radical formation from SBSL. In addition the spectrum of SBSL was recorded and discussed.

Finally, chapter 8 discusses the conclusions of the results presented in addition to future work. It summarises the amassed insight acquired from the results achieved and gives recommendations for future work.

CHAPTER 2

EXPERIMENTAL

2.1 Sonochemical Equipment and Procedures for Multi Bubble Sonoluminescence

Two cylindrical ultrasonic cells were employed in the investigation of multi-bubble sonoluminescence. Cell (A), illustrated in figure 2.1 and 2.2 was the principal ultrasonic reactor employed in this project. This consisted of a water-jacketed glass cell with an inner diameter of 5.8 cm and a height of 12 cm. The transducer (Morgan Electro Ceramics Ltd, resonance frequency 27 kHz, with transducer properties[§] (air) Q factor 900 ± 200, resonant impedance 15 ± 5 ohms, effective coupling coefficient 0.37 ± 0.02 and shunt capacitance 3.7 nF) was attached to the cell using slow drying epoxy resin (Struers). The volume of liquid in the cell was kept constant at 100 cm^3 in all cases unless otherwise stated in the appropriate figure legend. The solutions were temperature controlled at 25 °C by employing a water jacket.

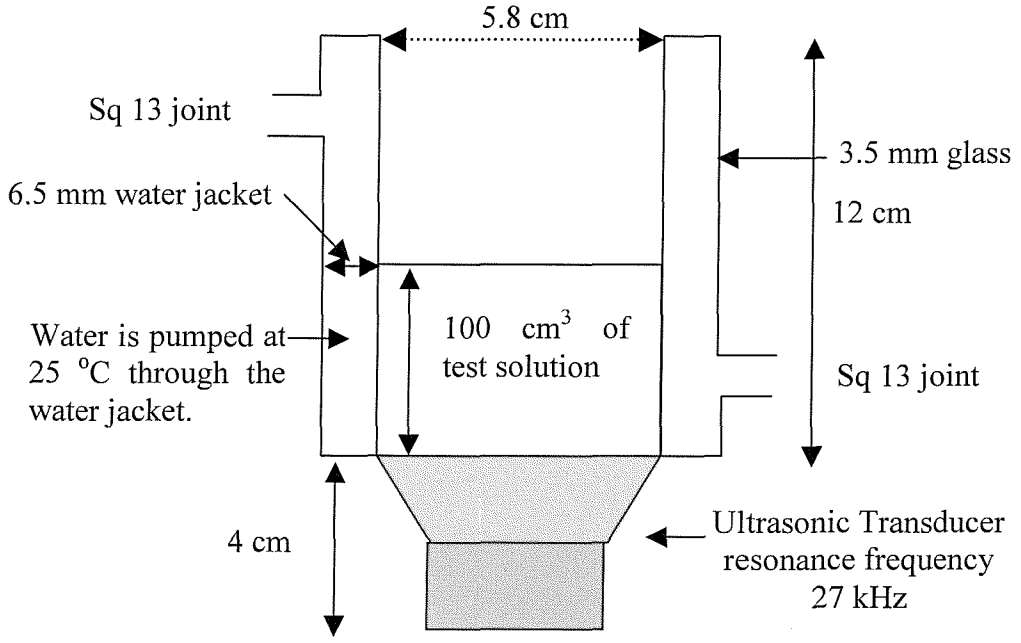

Ultrasonic Reactor Cell A

Figure 2.1 Schematic illustration of cylindrical ultrasonic reactor cell (A), employed for the investigation of multi-bubble sonoluminescence (from a side on view).

[§] Information supplied by Morgan Electro Ceramics.

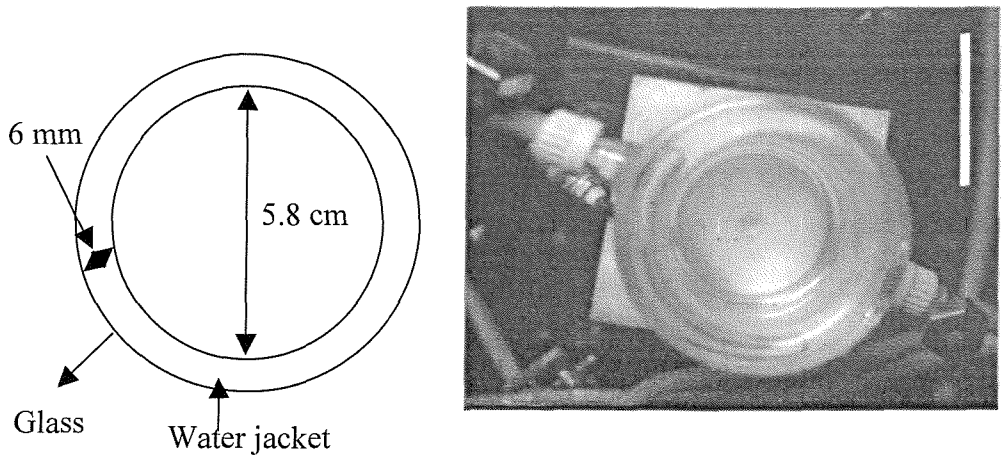

Figure 2.2 Schematic illustration of cylindrical ultrasonic reactor cell (A), employed for the investigation of multi-bubble sonoluminescence viewed from above. In addition the figure contains a picture of the cell recorded using an image-intensified camera. (Picture from chapter 3). The scale bar represents 5.8 cm.

Cell (B), illustrated in figure 2.3 and 2.4 was employed for recording some luminescent images using multi-bubble sonochemiluminescence (see chapter 3 section 3.3). This single walled cell was fabricated from polymethylmethacrylate (PMMA). It had an internal diameter of 9.4 cm and a height of 16 cm. The transducer (Morgan Electro Ceramics Ltd) had a resonance frequency of *ca.* 33 kHz (resonant impedance 5 - 15 ohms, effective coupling coefficient 0.36 - 0.38 and shunt capacitance 6.7 - 7.3 nF) [+] was attached to a steel base plate using slow drying epoxy resin (Struers Epofix resin).

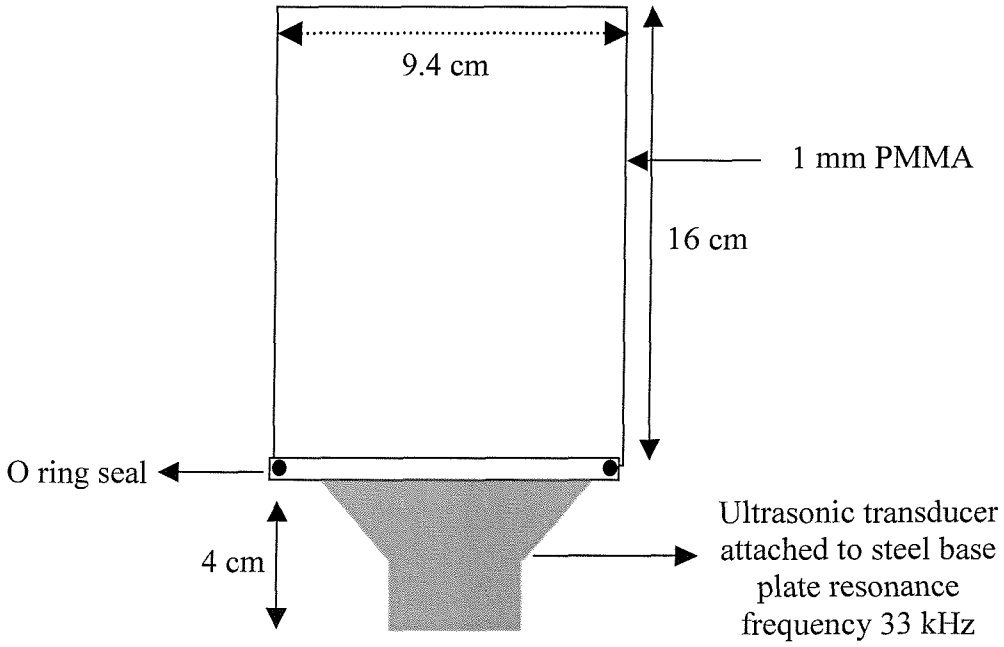

Figure 2.3 Schematic illustration of cylindrical ultrasonic reactor cell (B), employed for the investigation of multi-bubble sonoluminescence (from a side on view).

[+] Information supplied by Morgan Electro Ceramics.

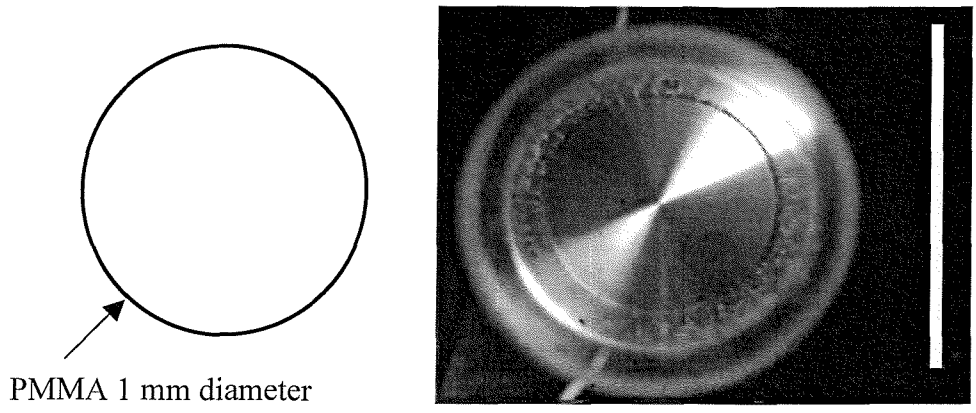

Figure 2.4 Schematic illustration of cylindrical ultrasonic reactor cell (B), employed for the investigation of multi-bubble sonoluminescence viewed from above. In addition, the figure contains a picture of the cell recorded using an image-intensified camera. (Picture from chapter 3). The scale bar represents 9.4 cm.

Cavitation was generated within the reactors (see figures 2.1-2.4) using piezoelectric transducers. The electrical signal that drove the piezoelectric transducer was generated by a Thurlby Thandar TG1010 function generator and amplified by a Bruel & Kjear 2713 power amplifier. The voltage amplitude to the piezoelectric transducer was recorded on a Tektronix TDS 224 digital oscilloscope.

2.2 Sonoelectrochemical Equipment and Procedures (MBSL)

Electrochemical measurements were made using a 3-electrode arrangement comprising of a working electrode, (a disk either 0.5 mm diameter platinum or 3 mm diameter glassy carbon sealed in glass) a steel counter electrode and a home made saturated calomel reference electrode (SCE). The working electrode employed in each case is reported in the appropriate figure legend. Electrochemical measurements were made using an electrochemical workstation and recorded on a PC using an ADC card (Computer Boards CIO DAS08 PGL) programmed using in-house written software. The majority of electrochemical measurements of sonochemical reactions reported in this thesis were performed in a flow cell. The flow cell was fabricated from PMMA. In addition to being cheap PMMA has the merit of allowing visual inspection of the interior of the cell (used for confirming the absence of macroscopic air bubbles). A schematic illustration of this cell is illustrated in figure 2.5. This is a wall-tube electrode flow cell.[127]

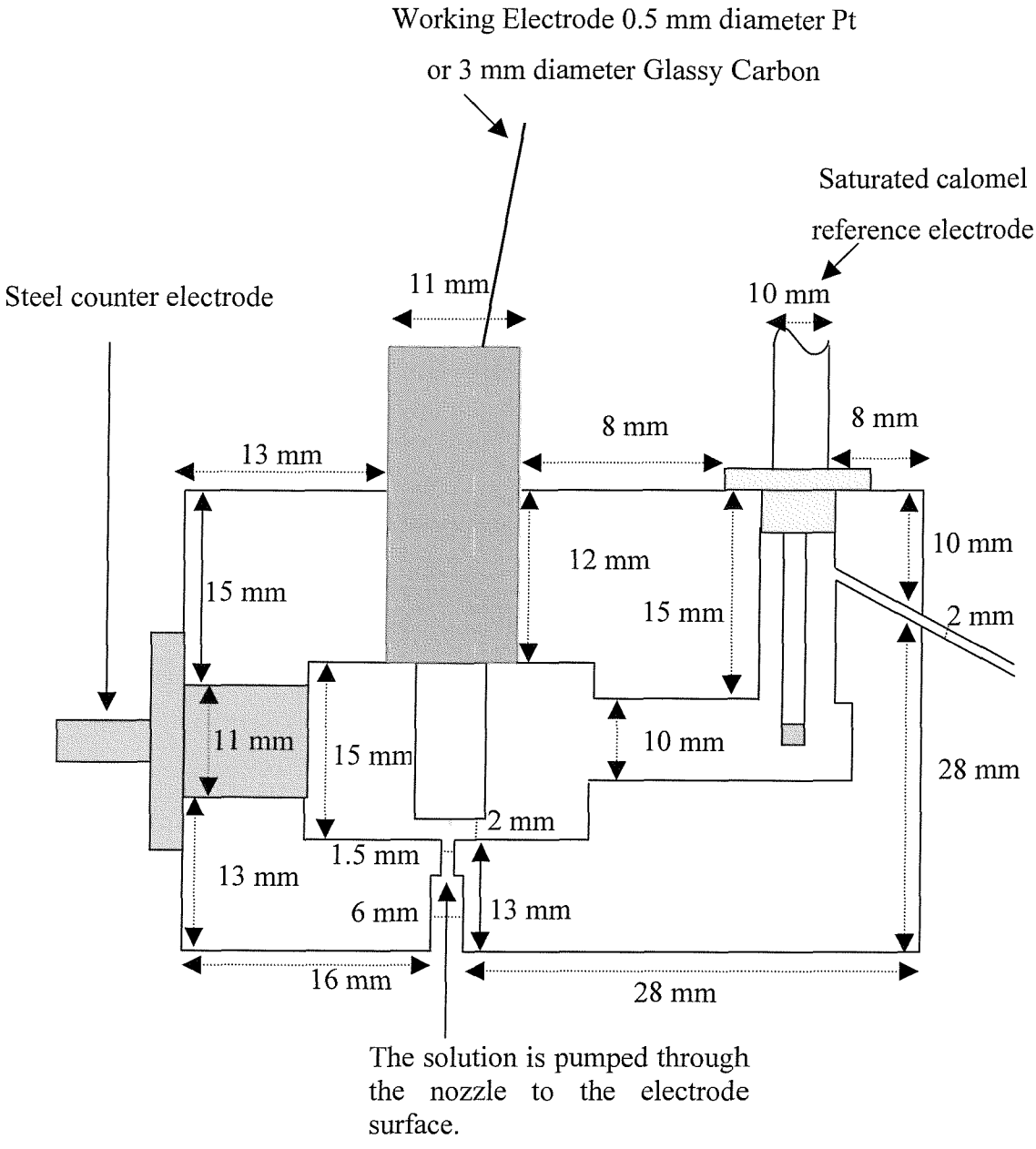

Figure 2.5 Schematic illustration of the electrochemical flow cell employed for the radical trap experiments.

The wall-jet electrode is a well-defined hydrodynamic electrode. It is commonly used in electrochemical machining erosion, and other industrial processes.[127] It is composed of a submerged circular jet of electrolyte incident on a flat plate normal to the direction of flow. The electrode is a circular disk embedded on the flat plate of the stagnant point as shown in figure 2.6. This geometry is attractive because of a high mass transport rate. The flow characteristics of the impinging jet have been extensively investigated.[127] When the jet collides perpendicularly with the electrode four distinct flow regimes exist. These have been discussed in detail by Chin *et al.*[127] and are illustrated in figure 2.6 (zones 1-4).

(1) Mixing zone: As the flow discharges from the nozzle the electrolyte in the jet starts to mix with the surrounding fluid. The mixing zone grows in width along the downstream direction of the jet.

(2) Flow region: In this region the centre line velocity of the jet starts to decrease. Its magnitude is inversely proportional to the distance from the nozzle exit.

(3) Stagnant region: This is the layer of fluid on the flat plate in which the jet is deflected form axial direction to a radial direction.

(4) Wall jet region: This is the region adjacent to the flat plate some distance from the stagnant point where the radial velocity starts to decay and the thickness of the boundary layer increases with radial positions.

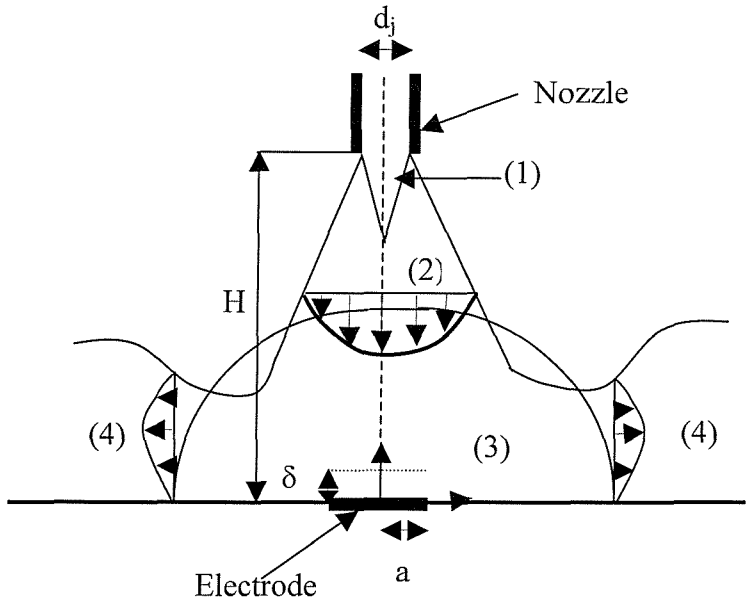

Figure 2.6 The flow regimes of the wall jet electrode redrawn from Chin *et al.*[127] Regions (1), (2), (3) and (4) represent the mixing zone, the flow region, the stagnant region, and the wall jet region respectively. The reader is referred to the text for detailed explanation of this figure.

If one limits the value of the electrode radius[127] to less than 1 nozzle diameter the system possesses a 'uniform accessibility' to the diffusing species in the electrolyte and a constant surface concentration could be maintained throughout the electrode.* A theoretical and experimental study of mass transport to a wall jet electrode was modelled by Chin *et al.*[127] A plot of i_L versus the square root of the flow velocity should be linear. Figure 2.7 shows a plot of i_L (see figure 2.9) versus the square root of the flow velocity for the flow cell system illustrated in figure 2.5 (in addition, see figure 2.8). The flow rate was

* Note in the experimental arrangement employed d_j (the nozzle diameter) is 1.5 mm. Hence for both the carbon and platinum electrodes employed 'uniform accessibility' is possible.

determined by measuring the volume output of the flow system as a function of the pump setting over a fixed known period of time. The value of a/d_j (radius of electrode/nozzle diameter) is important for these systems. 'Uniform accessibility' is achieved for values of a/d_j from 0.1 to 1.0 for turbulent flow and from 0.1 to 0.5 for laminar nozzle flow. Two electrodes were employed in the experiments performed in the results section with this flow system; 0.5 mm diameter platinum $a/d_j = 0.17$ and 3 mm diameter glassy carbon $a/d_j = 1.0$. The wall jet region[127] is found to begin at a/d_j approximately equal to 4.

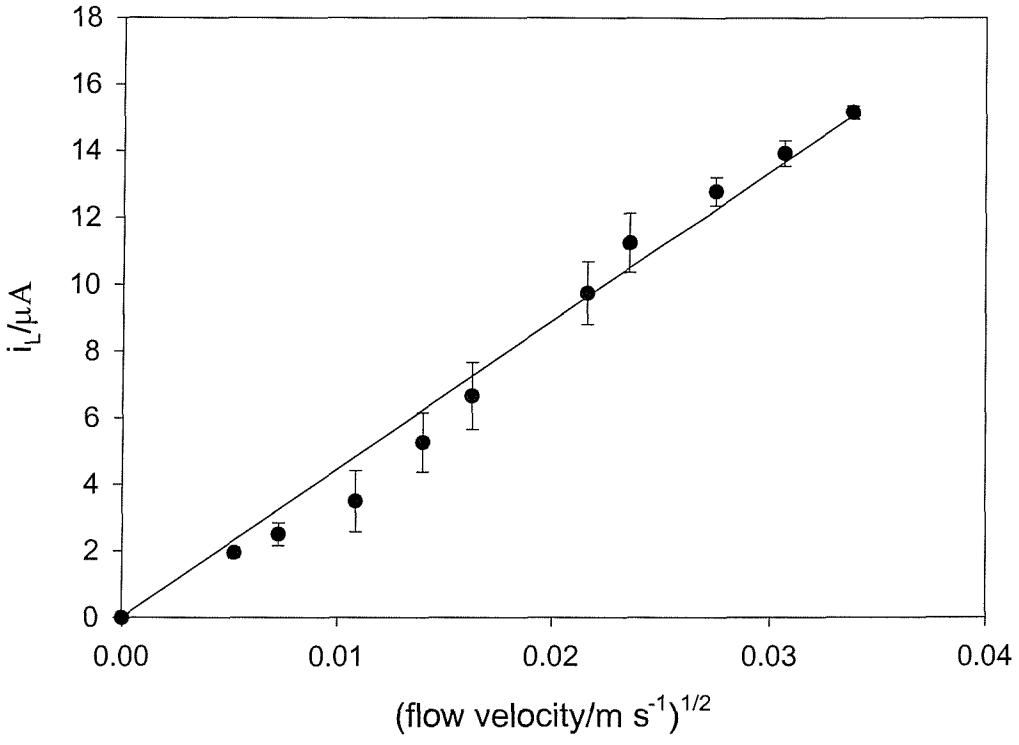

Figure 2.7 A plot of i_L versus the square root of the flow velocity for the reduction of a degassed 5 mmol dm^{-3} solution of $Ru(NH_3)_6Cl_3$ in 0.1 mol dm^{-3} KCl recorded using a 0.5 mm diameter Pt working electrode in the wall tube electrode flow cell. The solution was thermostated at 25 °C. The mass transport limiting current was recorded at –0.4 V versus SCE. The error bars were calculated using the average current recorded at each flow rate (see figure 2.9). They represent plus or minus one standard deviation of the mass transport limited current. The maximum flow rate employed for all experiments using the peristaltic pump was 6 x 10^{-2} cm^3 s^{-1}.

2.3 Radical Trap Experiments

Figure 2.8 shows a schematic representation of the experimental rig employed for radical trap experiments. The flow cell was kept in a Faraday cage to minimise electrical noise. The solution was pumped from the ultrasonic reactor through the flow cell and back to the reactor using a peristaltic pump (Pharmacia Fine Chemicals, P-1) or a gear pump (PQ -12 from

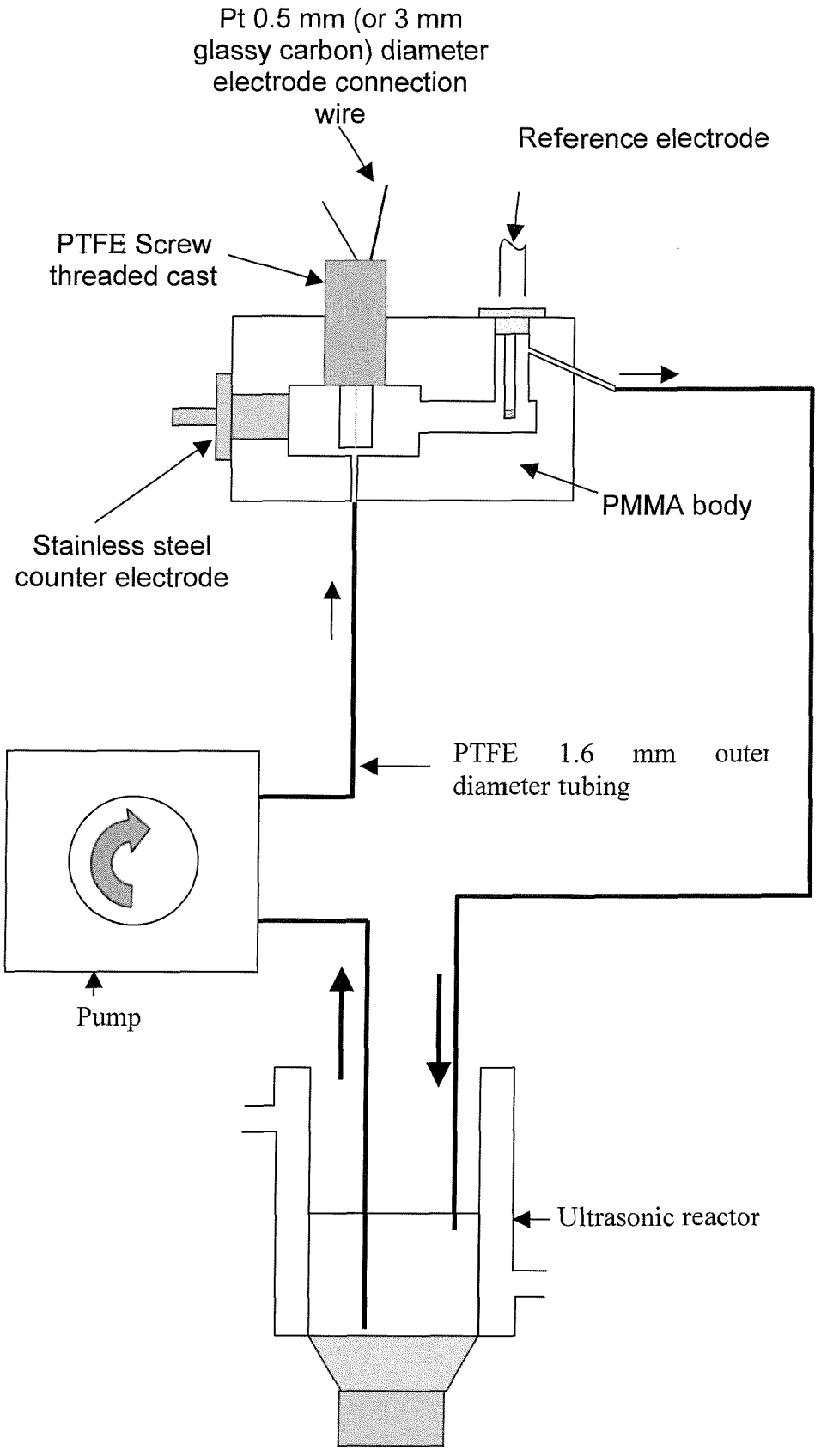

Figure 2.8 Schematic showing the flow cell and sonochemical system used for electrochemical measurements of radical production. The solution is pumped to and from the ultrasonic reactor via a pump into the flow cell during the ultrasonic irradiation of the test liquid. The direction of liquid flow is indicated by the arrows.

Greylor, USA). The piping for the flow cell (PTFE, ca. 50 cm, 1.6 mm outside diameter, 0.8 mm internal diameter) was positioned so that the inlet remained at the base of the sonochemical reactor for all experiments. The flow cell and piping had a volume of ca. 6 cm^3. The flow cell system was primed with the appropriate solution used in each experiment. This ensured that the volume within the reactor remained constant (normally 100 cm^3) throughout the experiment as a closed loop system was employed. The peristaltic pump was operated at maximum flow rate during all experiments unless otherwise stated in the appropriate figure legend (6 x 10^{-2} cm^3 s^{-1}). A gear pump was also employed in some experiments (see figure 2.10).

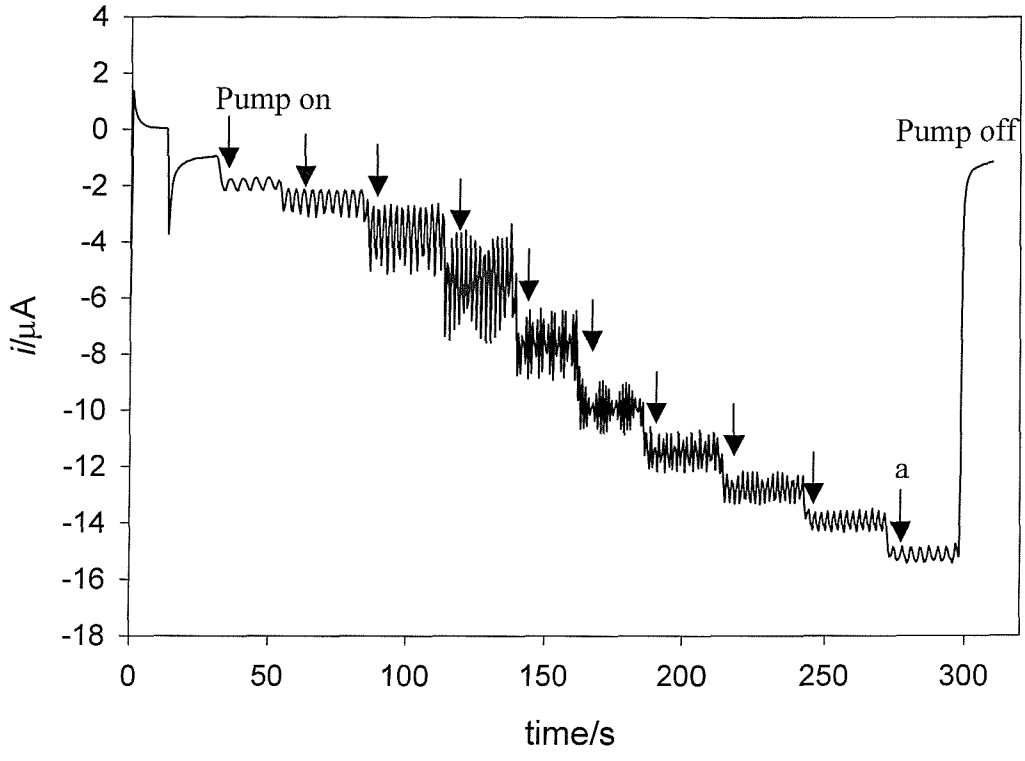

Figure 2.9 Calibration plot for the flow cell. The figure shows how the mass transport to the electrode surface varies with flow rate. The flow rate was sequentially increased illustrated by the arrows. The calibration was performed using a degassed 5 mmol dm^{-3} $Ru(NH_3)_6Cl_3$ in 0.1 mol dm^{-3} KCl solution at 25 °C using a 0.5 mm diameter Pt electrode. The potential was held at –0.4 V vs. SCE. The oscillation features are discussed in the text. The maximum flow rate employed for all experiments using the peristaltic pump was 6 x 10^{-2} cm^3 s^{-1} (see position 'a').

The flow cell was calibrated by recording the steady state current for a 5 mmol dm^{-3} solution of $[Ru(NH_3)_6]Cl_3$ in 0.1 mol dm^{-3} KCl as a function of flow rate. This is illustrated in figure 2.9. In this experiment the platinum electrode was held at –0.4 V vs. SCE which corresponds to a mass transfer limiting potential for this redox system. Figure 2.9 shows that as the pump rate of the liquid through the flow cell was raised the steady state current increased. The oscillation component superimposed on the signal is caused by the pressure

fluctuations of the peristaltic pump. The mass transfer coefficient of the electrode cell arrangement was calculated using equation (2.1):

$$k_m = \frac{i_L}{n_e FAc} \qquad (2.1)$$

where k_m is the mass transfer coefficient, i_L is the mass transfer limiting current, n_e is the number of electrons ($n_e = 1$ for $Ru(NH_3)_6Cl_3$), F is Faradays constant, A is the electrode area and c is the concentration (of $Ru(NH_3)_6Cl_3$). The mass transfer coefficient obtained depended on the electrode/jet arrangement employed within the flow cell. In the case shown in figure 2.9, a 0.5 mm diameter platinum electrode was employed. Mass transfer coefficients of the order of 0.018 ± 0.001 cm s^{-1} were obtained at 6 x 10^{-2} cm^3 s^{-1}. The calibration experiment was repeated if any of the components of the flow system were changed. The value of the mass transfer coefficient obtained is accurate. This value was verified in chapter 4 (see section 4.3) on several occasions by injection analysis.

In all subsequent results the actual mass transfer coefficient of the flow cell at that time was used to calculate the rate of the reactions reported. The Weissler, Fricke, Cu^{2+} and H_2O_2 reactions were studied employing cell A (see figure 2.1). When performing experiments, the working electrode was held at the mass transport limiting potential (MTLP) for the product of interest, and the current was monitored as a function of the time. A linear plot was obtained (see figure 4.1) and the slope of this plot (di/dt) was used to calculate the rate of generation of the product of the redox-trapping agent with the target analyte using equation (2.2):

$$\frac{dc}{dt} = -\frac{\left(\frac{di}{dt}\right)}{n_e FAk' k_m} \qquad (2.2)$$

where i represents the current, t represents time, and k' the ratio of the diffusion coefficient of the sonochemical product to the diffusion coefficient of the calibration species (normally 9 x 10^{-6} cm^2 s^{-1} for $[Ru(NH_3)_6]Cl_3$). Note the negative sign in this formula is for cathodic reactions only. The values of the required diffusion coefficients were determined experimentally, or the cell was calibrated with a known concentration of the target analytical species.

In addition to the peristaltic pump, a continuous flow pump (PQ – 12 DC from Greylor, USA) was also employed for the electrochemical detection of sonochemical radical

production. This has a number of advantages compared to the peristaltic pump including the following:

- The continuous flow pump removes the oscillation component of the signal caused by the pressure fluctuations of the peristaltic pump.
- With the consequent reduction in this oscillatory 'noise' it was possible to reduce the detection limit of the system. The continuous flow pump is illustrated in figure 2.10.

The pump is controlled by a DC power supply (Thandar TS30215). The flow rate of the liquid through the pump can be adjusted by adjusting the current manually. The piping for the flow cell consisted of (PTFE, ca. 20 cm, 1.6 mm outside diameter, 0.8 mm internal diameter). The volume of the flow cell including the tubing was 6.1 cm^3. The flow rate at a current of 1 A was 0.45 $\pm$0.01 cm^3 s^{-1}. This flow rate was employed for all experiments with this pump unless otherwise stated. Using these values for the flow rate and cell volume, the time required to completely fill the pump and tubing with new solution during an experiment was ca. 14 s.

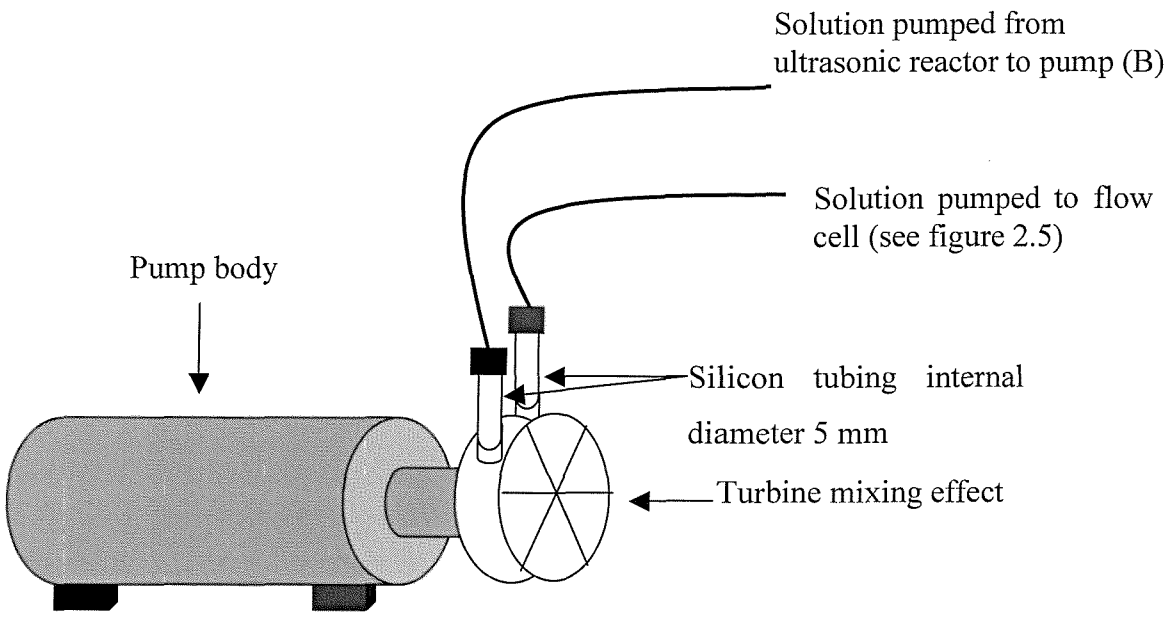

Figure 2.10 Schematic of continuous flow pump (pump (B)). This pump replaced the peristaltic pump in the flow system illustrated in figure 2.8 for some measurements presented in chapter 4. In all cases this is reported in the appropriate figure legend.

The calibration of the pump with the flow cell (see figure 2.5 and 2.8) was performed with a degassed 20 μmol dm^{-3} $Ru(NH_3)_6Cl_3$ solution in 0.1 mol dm^{-3} KCl using a 0.5 mm platinum working electrode. The potential was maintained at –0.4 V versus SCE (MTLP). The solution and the pump were sparged with argon for 30 minutes prior to the experiment

to remove molecular oxygen from the system, which is active on platinum at the potential employed. A similar experimental set-up was employed as shown in figure 2.8; however, the peristaltic pump (A) is replaced with the continuous flow pump (B). The calibration plot obtained is illustrate in figure 2.11. It can be seen that with a continuous flow pump there is no longer any oscillations in the current signal (compared with figure 2.9) due to pressure fluctuations. The value of the k_m was determined to be ca. 0.018 ± 0.001 cm s^{-1} at 0.45 cm^3 s^{-1}. Given the increase in flow rate, this value appears low compared to the k_m obtained from the peristaltic pump. This value has been checked and verified on a number of occasions. The lower value must be due to slightly different conditions employed for these experiments (i.e. different position of the electrode in the flow system, different tubing employed etc). This emphasises the need to calibrate the system regularly under the conditions employed to achieve reproducible results. It is worth noting that the calibration illustrated in figure 2.11 was performed within the concentration range of the results reported in the results section.

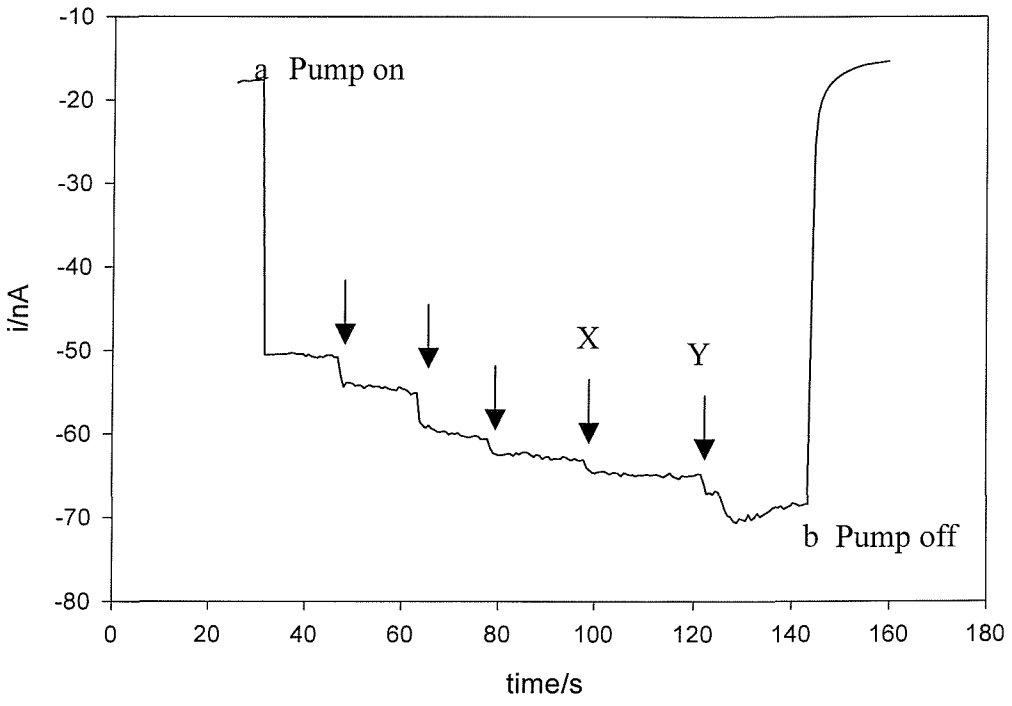

Figure 2.11 Calibration plot for the flow cell using pump (B). The figure shows how the mass transport to the electrode surface varies with flow rate. The calibration was performed using an argon degassed solution of 20 μmol dm^{-3} $Ru(NH_3)_6Cl_3$ in 0.1 mol dm^{-3} KCl at 25 °C using a 0.5 mm diameter Pt electrode. The potential was held at –0.4 V vs. SCE. The flow rate was sequentially increased illustrated by the arrows. The pump is turned on and off at the points 'a' and 'b' respectively. The region between X and Y arrows corresponded to a flow rate of 0.45 cm^3 s^{-1}. The MTL current at this flow rate was used to calculate k_m as this was the flow rate used for further experiments. The reason for this is that the flow characteristics of the system operated best at this flow rate.

While operating the continuous flow pump, it was noticed that mixing occurs in the turbine (see figure 2.10). This has obvious implications for the detection of target analytes

such as Fe^{3+} generated within the ultrasonic reactor. A mixing delay factor is introduced by the pump cavity as the solution is pumped from the ultrasonic reactor to the flow cell where detection takes place. The mixing delay factor is explained in detail in figures 2.12 and 2.13 and the associated text.

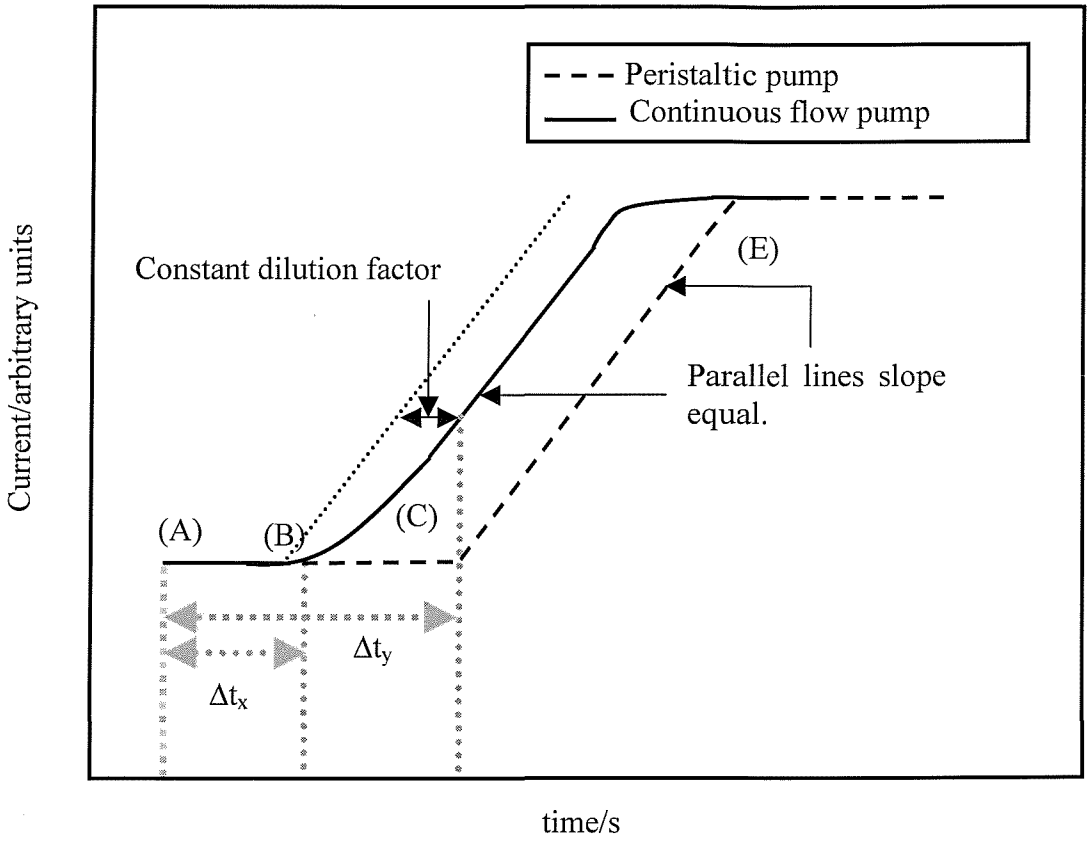

Figure 2.12. Theoretical models for radical trap experiments using the continuous flow pump and the peristaltic pump. The model assumes that both the mass transfer coefficients and the pumps flow rates are the same. The reader is referred to the text for a thorough explanation of this figure (see also figure 2.13 and subsequent discussion).

Figure 2.12 illustrates a schematic plot explaining the mixing delay factor associated with the turbine pump. This figure compares the responses observed from both the peristaltic pump and the gear pump. With the peristaltic pump, there is no dilution of the solution as it is pumped from the reactor to the flow cell. This is represented in the figure by the dashed line (----) and the continuous flow pump is represented by the solid line (—). The flow cell is primed with the starting solution. Both pumps and the ultrasound are turned on at point (A) in figure 2.12. With the peristaltic pump (----) it takes time Δt_y (ca. 20 s) for the solution to be pumped from the ultrasonic reactor to the flow cell at which time the current proceeds linearly. With the gear pump the current time response is curved (see points (B)-(C) in figure 2.12) owing to mixing within the turbine. In this case the current increases after time Δt_x (ca. 5 s). However, it takes ca. 14-20 s (depending on the flow rate employed) for

the solution in the pump turbine to equilibrate as a result of turbulent mixing, at which point the current signal precedes parallel to the peristaltic pump signal. The reason why the pump signals are parallel is that it is assumed that there is a constant dilution factor within the turbine section of the pump. This assumption has been validated experimentally (see figure 2.13). If a peristaltic pump were operating at the same flow rate as the gear pump the signal represented by dotted line (.....) would be achieved. At the point (E) the ultrasound is switched off. The current continues to proceed anodically until the time required for fresh solution to reach the flow cell has elapsed, at which point a plateau is reached. In the case of the continuous flow pump the plateau region is curved for reasons explained previously. To calculate the rate of reaction, the slope of the linear section of the line is required. As the lines are parallel, this will be the same in both cases. Hence both pumps may be employed to determine the rates of sonochemical reactions. It is important to note that the continuous flow pump could not be positioned after the flow cell (see figure 2.8) as this resulted in the generation of bubbles within the flow cell.

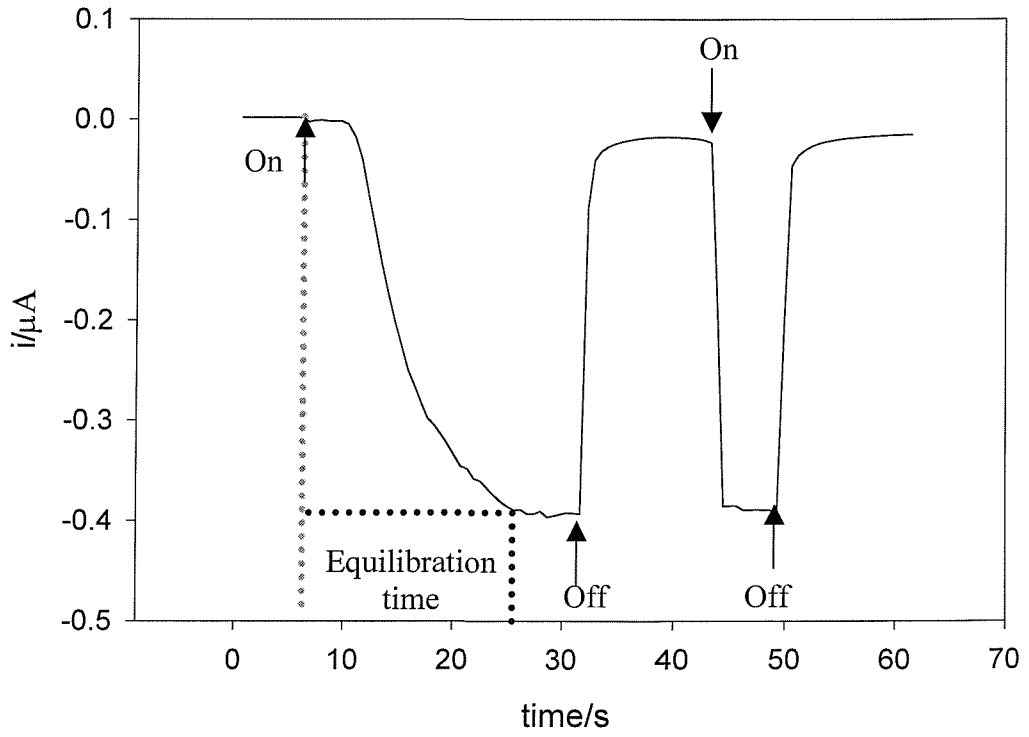

Figure 2.13 In this experiment the flow cell and piping was primed with a solution containing 10 mmol dm^{-3} KI in 90 mmol dm^{-3} KCl. A cell temperature controlled at 25 °C was filled with a solution containing 60 μmol dm^{-3} I_3^-, 90 mol dm^{-3} KCl and 10 mmol dm^{-3} KI. Electrochemical measurements were performed using a 0.5 mm platinum working electrode at +0.2 V versus SCE. The current was monitored from time t = 0 s. The continuous flow pump was turned on and off as illustrated in the figure. Note that the flow rate in this experiment was 0.31 ± 0.01 cm^3 s^{-1}. Hence the equilibration time is ca. 20 s.

Figure 2.13 shows how the pump cavity mixing effect described previously and illustrated in figure 2.12 is supported by the experimental results achieved. In this experiment the flow cell and piping was primed with a solution containing 10 mmol dm^{-3} KI in 90 mmol dm^{-3} KCl. A cell temperature controlled at 25 °C was filled with a solution containing 60 μmol dm^{-3} I_3^- 90 mol dm^{-3} KCl and 10 mmol dm^{-3} KI. The current was monitored at + 0.2 V verses SCE from time t = 0 s (MTLP for I_3^-). The continuous flow pump was switched on at t = 5 s in the figure 2.13, which is marked by a slight change in background current due to mass transfer enhancement of impurities. The current proceeds cathodically at time t =11 s (corresponding to the reduction of I_3^-) and the plateau is reached after ca. t = 25 s. The sloped response of the cathodic current signal is due to mixing occurring in the pump turbine (as explained for figure 2.12). The time difference between these two points corresponds to the time required to fill the pump at the flow rate employed (0.31 ± 0.01 cm^3 s^{-1}, hence the predicted equilibration time in this case is ca. 20 s). At t = 30 s the pump is switched off. The pump is turned on again at time t = 45 s and the current drops immediately to the initial cathodic plateau and remains steady until the pump is again switched off again at time t = 49 s. Confirmation that the time required to reach a defined plateau is the result of mixing is provided when the pump is turned off and then switched back on at time t = 45 s. The current immediately drops to form a cathodic plateau, as the pump is now full with the target analyte solution and mixing becomes irrelevant. The k_m of the cell can be calculated as 0.017 ± 0.001 cm s^{-1} from equation (2.1). This is in agreement with the value obtained through the calibration performed in figure 2.11.

2.4 Light Measurements

The emission of light from multi bubble sonoluminescence (MBSL) and multi bubble sonochemiluminescence (MBSCL) was measured using an EG&G Photon Counting module (SPCM-200-PQ). The photon counter was positioned vertically above the cell at a fixed distance of 40 ± 2 mm from the solution. It is important to note that the photon counter exhibits a finite footprint. If this footprint is sufficiently large the photon count will in general follow the amplitude of the driving field (above the cavitation threshold) as it measures over the complete volume of the cylinder. The footprint of the photon counter was determined using a pinhole in a β Lamp source. The data obtained from this experiment is illustrated in figure 2.14. The photon counter was placed 10 cm directly above a pinhole β lamp source at distance = 0 (see figure 2.14). The β lamp source was then moved in

increments of 1 cm relative to the photon counter and the photon count was recorded as a function of distance until the signal was no longer detectable. Using this data the flare angle θ_f was calculated as 21.8°.

The active element of the photon counter is 0.23 mm in diameter.* When the photon counter is positioned at a height h_p (h_p = 4 cm under the conditions employed in the results section unless otherwise stated) above the ultrasonic reactor, the fraction of photons detected by the photon counter is given by equation (2.3)

$$\frac{\pi r_p^2}{4\pi h_p^2} \qquad (2.3)$$

where r_p is the radius of the active element of the photon counter. If h_p approaches zero equation (2.3) approaches 1. Employing appropriate values in equation (2.3) (from experimental conditions) it can be calculated that under the conditions employed the photon counter detects ca. 1 in every 500000 photons.

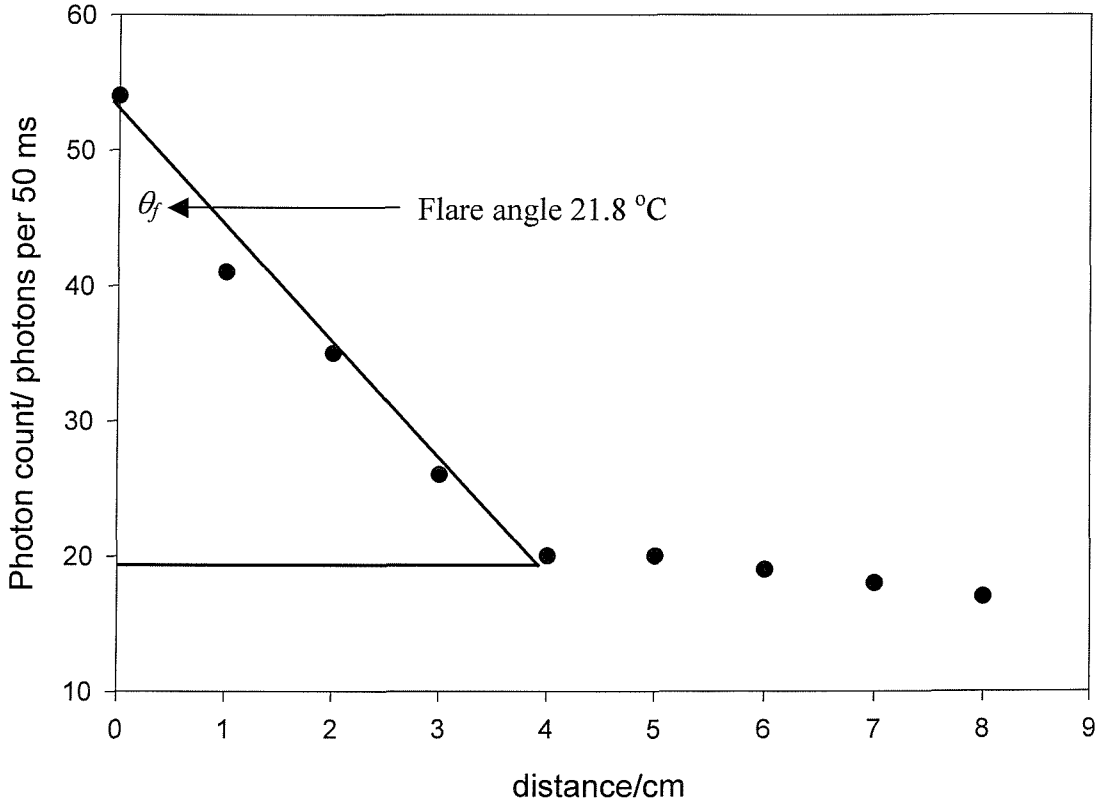

Figure 2.14 Plot showing the light sensitive angle dependence of the photon counter. The photon counter was placed 10 cm directly above a pinhole β lamp source at distance = 0. The β lamp source was then moved in increments of 1 cm relative to the photon counter and the photon count was recorded as a function of distance. The flare angle θ_f was calculated as 21.8 ° as indicated in the figure.

* Information supplied by PerkinElmer.

Figure 2.15 shows a schematic illustration of the photon counter positioned above the surface of the liquid in cell (A). The solution height and the cell radius were 4 cm and 2.9 cm respectively (see figure 2.1). Employing basic trigonometry the footprint of the photon counter (the volume of the cell over which the photon counter is detecting light) can be determine using the calculated flare angle (see figure 2.14). It can be calculated that, in order to detect the entire volume of the cell (5.8 cm diameter) the photon counter must be ca. 7 cm above the detection area (the liquid surface). Under the conditions employed in the results section the photon counter was positioned at a height of 4 cm above the liquid surface. Therefore (as indicated in figure 2.15) the photon counter only detects light from the full cell volume at a depth of 3 cm below the liquid surface. Figure 2.15 illustrates that the photon counter will not detect light in a small region at the edges of the cell. It is important to note that a balance had to be achieved between equation (2.3) (the fraction of photons detected by the photon counter), which depends on h_p and the footprint of the photon counter, which is also dependent on h_p. This balance is illustrated in figure 2.15.

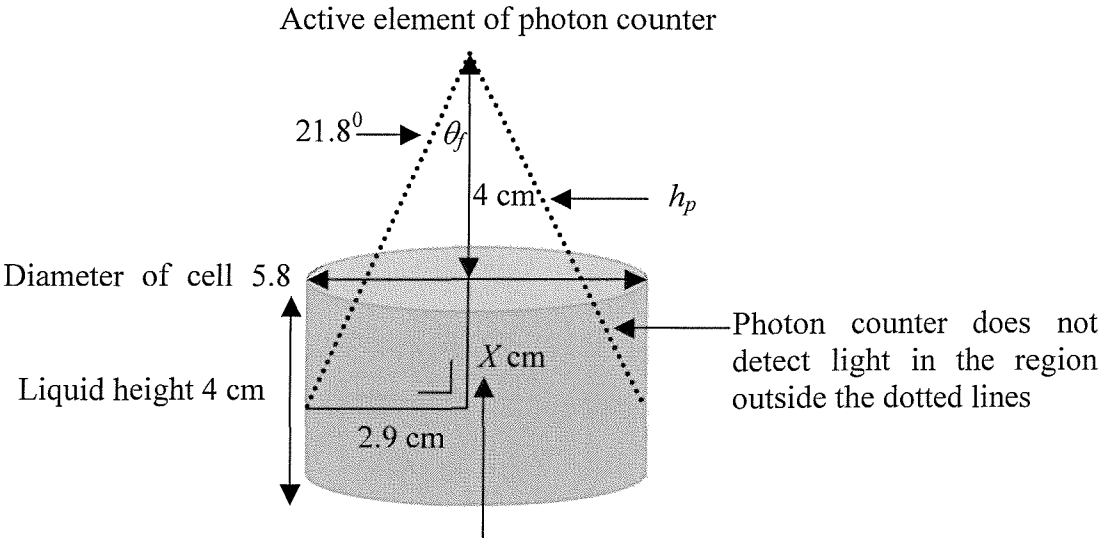

Figure 2.15 Schematic illustrating how the footprint of the photon counter was calculated. The reader is referred to the text for thorough explanation of this figure.

When comparing light measurements to chemical rates, the volume of the solution in the cell was maintained constant throughout both techniques. Sonoluminescent and sonochemiluminescent experiments were performed in a dark room. The drive voltage applied to the transducer was recorded and reported in the appropriate figure legend. In each set of experiments, the applied voltage to the transducer was maintained at a constant level

across the frequency range employed. The drive voltage was a convenient experimental measure. However, it is not sufficient on its own, contrary to the protocol adapted in many papers.[78, 91] This is because inertial cavitation depends on the sound field at the bubble and within the vessel the sound field is often inhomogeneous. Hence key to bubble dynamics and cavitation is the acoustic pressure amplitude. This was measured in the experimental arrangement employed (see section 2.9). The photon counter module records light emission every 20 ms (and hence the figure label MBS(C)L_{20} is used to indicate this fact). Light emission was recorded for twenty seconds at each frequency and the average photon count was determined. The ultrasound was switched off for a further period of 20 s prior to the next measurement to reduce the effect of seeding the solution from cavitation bubbles produced in the previous measurement.[62] Error bars in the appropriate figure legend represent plus or minus one standard deviation in uncertainty.

2.5 Sonochemiluminescent Pictures

Photographic data was recorded within a dark room. A Darkstar intensifier CCD camera from Photonic Science and a Nicam video recorder were employed to record and capture the data respectively. Two cylindrical cells were employed. They consisted of a water-jacketed cell and a larger non-jacketed cylindrical cell (cells A and B respectively see figure 2.1 and 2.3). The exact dimensions and construction of these cells are described in detail (see figures 2.1 and 2.3). Pictures were recorded in two positions, above the cell and with a side on view (see figure 2.16). The orientation of the camera relative to the cell is shown in figure 2.16.

2.6 Frequency Dependence of Equipment and Drive Voltage Measurements

Figure 2.17 shows a schematic of the frequency dependencies of the equipment employed for generating and measuring sonochemical activity. Any drive voltage measurements reported in the results section were always recorded in the manner indicated in figure 2.17.

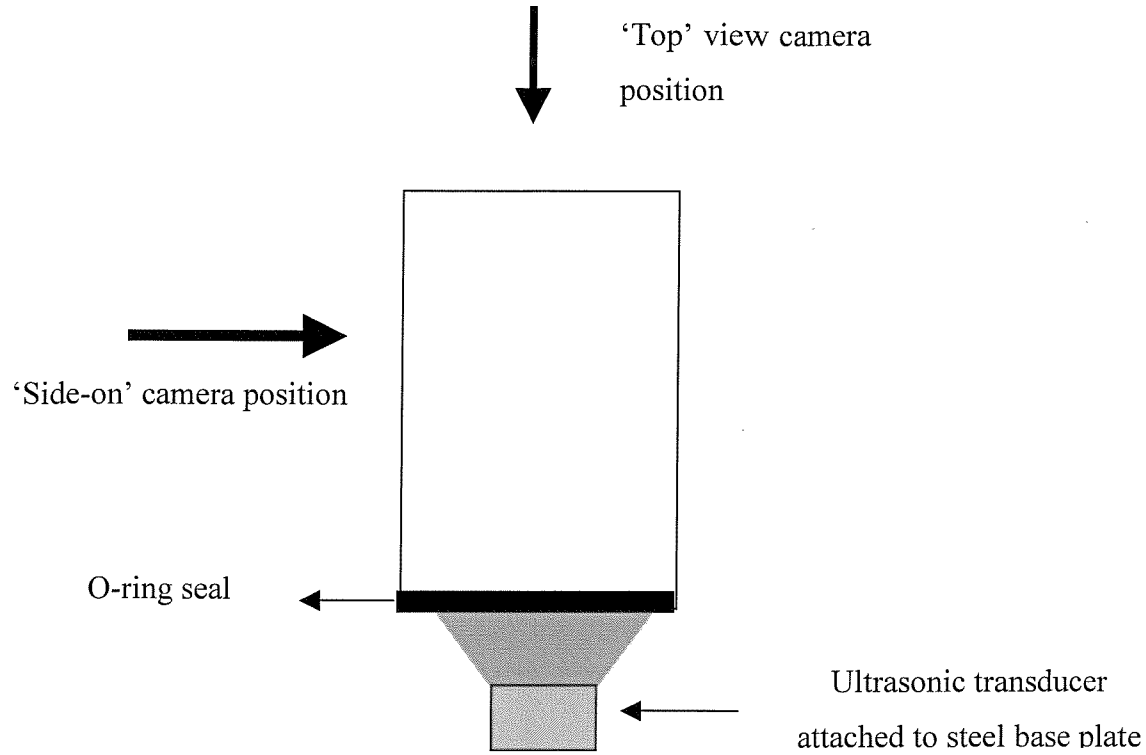

Figure 2.16 Schematic demonstrating the orientation of the camera with respect to the ultrasonic cells. The illustration employs ultrasonic cell (B) however measurements were performed with both cells in the results section (see figure 2.1 and 2.3).

Figure 2.17 illustrates that while the frequency dependencies of the signal generator, power amplifier and ultrasonic transducer are usually well controlled,[23] it appears normal practice to ignore the frequency dependencies of the reaction vessel and the detector.* It should be noted that if the acoustic pressure field within the vessel is mapped, none of these dependencies need be known, bar that of the detector. Mapping the field is not a difficult task when there is no cavitation, but it is time consuming, and often a measurement of the spatial peak pressure is adequate (e.g. for threshold measurements). This thesis will demonstrate that the frequency dependence of these factors cannot be ignored, and rather that a global approach is required.

* Most commercial systems rely on electrical matching of the transducer to the amplifier. Although this leads to a high-energy transfer to the transducer it does not necessarily correspond to a high resonance of the cell.

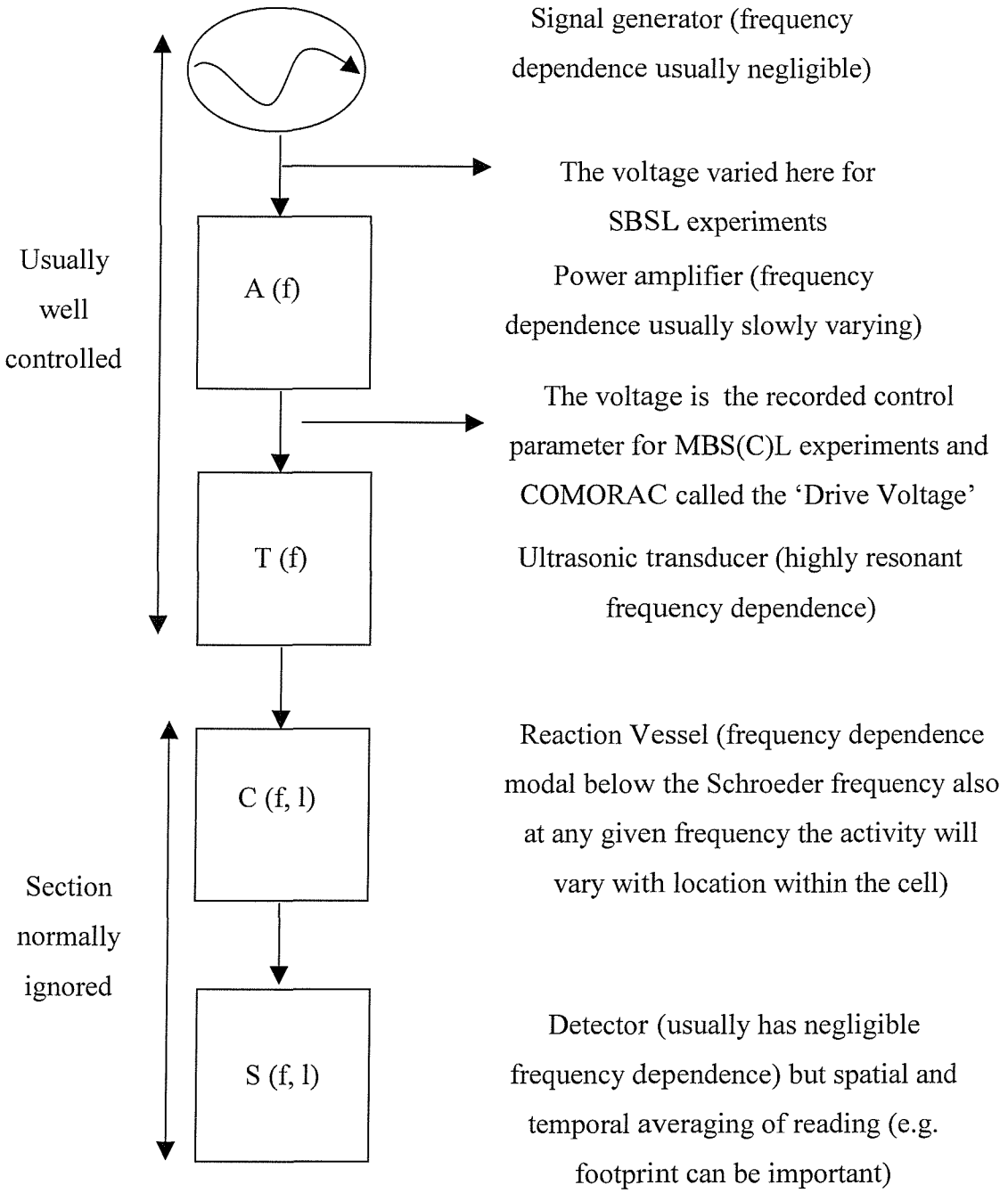

Figure 2.17 Diagram showing the components and their various frequency dependencies commonly employed in sonochemical experiments. All the components have frequency dependence to a greater or lesser extent. Some are controlled better than others. The frequency dependencies of the signal generator, the power amplifier and the transducer are usually well characterised. However the frequency dependencies of the detector and the cell are often ignored.

2.7 Absorbance Spectroscopy

An Avantes UV100-2 spectrometer with an Avantes mini D2 UV-VIS-NIR light source was used to record UV-Vis spectra (Anglia Instruments). Quartz or Perspex cuvettes (depending on the wavelength of interest) with a path length of 1 cm were used for experimental measurements and the concentration of target analytes was calculated using equation (2.4)

$$A_\lambda = \varepsilon_\lambda c l \qquad (2.4)$$

where A_λ is the absorbance at wavelength λ, ε_λ is the extinction coefficient in mol^{-1} dm^{+3} cm^{-1} l = path length in cm, and c is the concentration in mol dm^{-3}.

2.8 Audio Output in the Air

Broadband audio frequency cavitation noise measurements were performed with a 4133-condenser microphone and a Bruel and Kjaer measuring amplifier type 2609. The frequency response was 'A' rated ($20 < f < 20$ kHz).[128] The microphone was clamped 7.5 cm above the surface of the liquid, and the apparatus was enclosed in a Faraday cage.

2.9 Pressure Measurements in the Liquid

It is necessary to measure accurately the acoustic pressure amplitude within the cell. Acoustic pressure measurements in the cavitating liquid were made with a Bruel & Kjaer 8103 hydrophone and a Bruel & Kjaer 2635 charge amplifier. The dimensions of the active element* (hollow cylinder) are 6 mm by 6 mm.* Note that due to the finite size of the hydrophone active element the spatial maximum zero-to-peak pressure amplitudes cited in the results section are likely to be under estimates because of spatial averaging.[2] In order to measure the spatial variation of the sound field in the cavity in the absence of cavitation, a GRAS 10 CF hydrophone was employed. The hydrophones were positioned in the cell and moved with a micrometer and stage (Newport MUR5.25 25 mm travel with 20 μm

* Information supplied by Bruel & Kjaer

resolution in the z direction and 16 mm travel and 20 μm resolution in the x and y directions).

The output in both cases was recorded on a Tektronix TDS 224 oscilloscope. A hydrophone, placed within a liquid, monitors the time-varying component of the pressure field, which comprises two components: the applied sound field generated by the transducer (the 'driving' field); and (to a lesser extent at most times) the acoustic and hydrodynamic pressure fluctuations, which result from cavitation. At any given location within the cylindrical vessel, the amplitude of the driving field will depend on the frequency responses of both the driving transducer and the vessel for a given drive voltage as shown in figure 2.17. It has been shown that for vessels of the size used and within the frequency range studied, that the driving field is strongly modal (see chapter 1, section 1.11). As a result, the driving acoustic pressure amplitude exhibits spatial maxima and minima. The acoustic pressures recorded in the results section represent the maximum pressure recorded under the conditions employed. The hydrophone was clamped in the centre of the cell ca. 1.5 cm below the surface of the irradiated solution. It was attached to an x, y and z stage. The hydrophone was moved using the x, y, z stage until the acoustic pressure reached a maximum value.

2.10 Chemicals

Sodium chloride (BDH, 99.9 %), sulphuric acid (BDH 98%), potassium iodide (Hogg, 99 %), iron(II) sulfate heptahydrate (Aldrich 99%), copper (II) sulfate 5- hydrate (BDH, 99%) potassium sulfate (BDH, 99.5%), sodium sulfate (BDH, 99%), hexaamine ruthenium (III) chloride, (Strem Chemicals, 99 %), ammonium ferrous sulphate (BDH, 99 %), luminol (tri-aminophtalhydrazine, Aldrich 97%), sodium carbonate (BDH, 99.5%), potassium dihydrogen orthophosphate (BDH, 98%), hydrogen peroxide (29-31 % by mass, BDH), citric acid (BDH, 99.7%) and ethylenediaminetetraacetic acid (EDTA Lancaster Synthesis) were used as received. Aqueous solutions were prepared with water purified from either an USF Elga Elect 5® or Vivendi Purelab Option 10 water purification system.

2.11 Characterisation of Measures of Reference Acoustic Cavitation (COMORAC)

COMORAC describes an attempt to develop a reference sensor for cavitation in collaboration with the National Physics Laboratory (NPL). NPL developed a 'standard ultrasonic system' comprising of a 'standard water bath' 'a standard liquid' and a 'standard reference sensor' (see figure 2.18). Prof. Leighton proposed an international collaboration to test these with a range of alternative sensors. The experimental rig is shown in figure 2.18.

The National Physics Laboratory (NPL) (see chapter 6) constructed the entire apparatus. The cleaning bath used in this system was a Branson bath, operating at 40 kHz, with 12 transducers. It had 1 kW nominal power, internal dimensions 500 x 300 x 400 mm. The internal surface of the wall was earthed metal. The power output was adjustable at a coarse level locally, or with finer resolution via a power supply. The associated scanning rig (Time and Precision) was made of square section tubular construction frame, with a single carriage that forms the main support for the devices used to scan the cleaning bath field. Motor-controlled movement is provided in the longitudinal, transverse and vertical directions, with a positional resolution of 0.005 mm. A Windows PC, via an ISA interface, controls the whole system. The rig also provided a platform for a baseboard, from which various other sensors could be deployed. The baseboard contained a hole through which the CCD camera monitored the positions of the various sensors. The surrounding enclosure was 1.4 m^2, and 1.5 m high, with clear doors at the front, and an opening lid. The panels were double glazed, and at the back, ports were provided for water inlet and outlet to the tank, with brush holes for cables. The purpose of the enclosure was to minimise manual intervention and to restrict the amount of 'atmospheric contamination'. In addition suitable blackout could be added to the enclosure and antivibrational feet were used on the mount, which supported the cleaning bath, to minimise vibration transfer.

The drive voltage to the BRANSON vessel and the resultant acoustic power levels, are adjusted using the LD3205 regulated dual DC power supply. The I/O card is wired through the box used to switch the ultrasound ON and OFF. This generates a DC output signal related to the electrical power being delivered to the twelve transducers in the cleaning bath. This DC output voltage is measured using an ISOTECH digital voltmeter (see figure 2.17). Guideline figures for the relationship between the power supply settings, the resultant DC output voltage and the electrical power (expressed as a % of the maximum output power) are shown in table 2.1. Settings tabulated in table 2.1 were reference conditions for the various

tests that made up COMORAC. It is important to note that the use of drive voltage measurements for this study was imposed upon the partners by NPL.

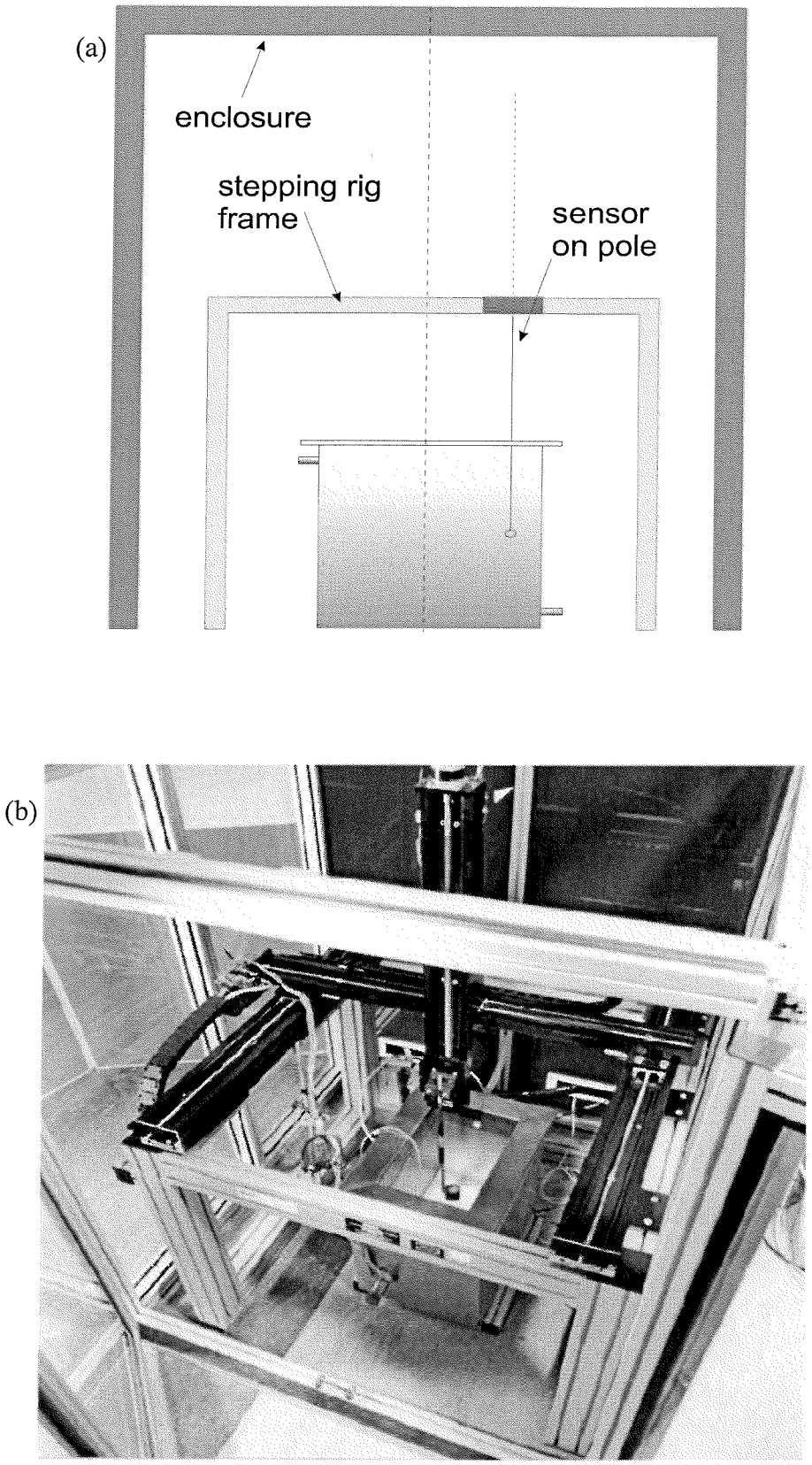

Figure 2.18 Schematic (a) and photographic (b) representation of bath, scanning rig and enclosure employed for the COMORAC experiment (not to scale).

Power supply voltage (V)	DC output voltage (V)	Nominal power level (% of maximum)
9.6	1.0	5%
9.3	1.5	10%
9.0	1.9	15%
8.4	2.8	20%
7.0	4.8	40%
5.0	7.1	65%
3.1	9.3	85%
2.5	10.0	95%

Table 2.1 Tabular summary of the relationship between the power supply, voltage set and the resultant power delivered to the BRANSON cleaning vessel, expressed as a percentage of the maximum power.

All sonochemical sensors used sample chambers made from the finger of a latex glove. This is illustrated in figure 2.19.

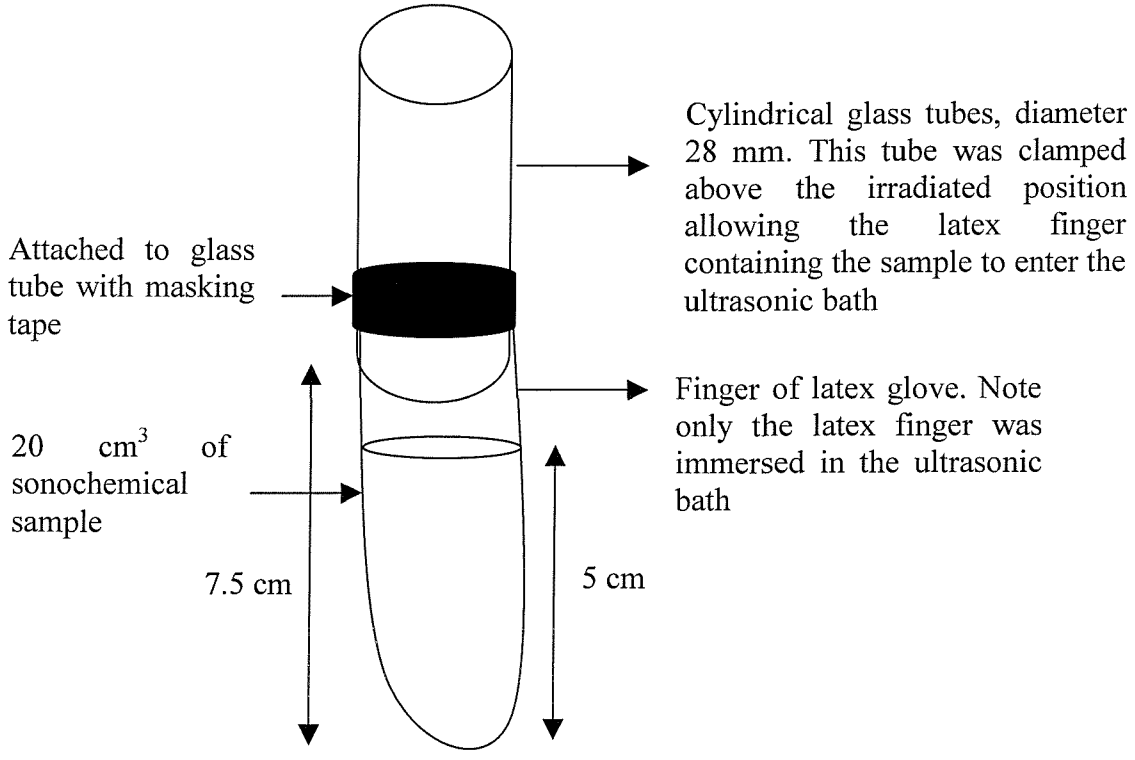

Figure 2.19 Sonochemical sample holder used in COMORAC experiments for chemical tests. The sample holder was positioned in the hot or cold spot respectively and 20 cm^3 of the sonochemical sample was added.

The latex finger was attached to a cylindrical glass tube diameter 28 mm. The finger containing the chemical sample (20 cm^3) was positioned in the bath. Care was taken to ensure that the glass support did not enter the liquid, and the sample being insonificated was completely submerged in the bath. This procedure was followed for the Weissler reaction, the Fricke dosimeter and the terephthalate dosimeter. In addition the baseboard contained a hole through which the CCD camera monitored the positions of the various sensors. When monitoring the photon count, the photon counter was clamped above (ca. 20 cm; see appropriate figure legends) either a hot spot or a cold spot, located using MBSCL pictures obtained using an image-intensified camera.

2.12 Protocol For COMORAC Test

The BRANSON cleaning vessel was filled with filtered de-ionised water (20 litres) degassed to 1.5-2 ppm, in the temperature range 21-22.5°C. The dissolved oxygen content of the water and its temperature were measured using the HANNA HI 9145 meter. This was completed both at the beginning and end of the measurement runs. A typical COMORAC test involved the following steps:

- The hot spot was located using the image intensified CCD camera and MBSCL pictures. The photon counter was then position above it (ca. 20 cm) and its height above the surface of the liquid recorded.
- The water temp and O_2 content were then recorded.
- Chemical samples (20 cm^3) were placed within the acoustically transparent sample holder and this was placed at the hot spot.
- The chemical tests and MBS(C)L were performed simultaneously at the each power setting.
- The temperature and O_2 content were recorded where possible after each chemical test.
- The chemical sample was placed in the cold spot located using the CCD camera and MBSCL. The latter three steps were then repeated.

2.13 Single Bubble Sonoluminescence (SBSL) - Equipment and Procedures

A cell was successfully designed for the generation of single bubble sonoluminescence. This cell is illustrated in figure 2.20. It consisted of a glass round bottom flask with a ground glass joint. A transducer, resonance frequency 27 kHz (Morgan Matroc Electro Ceramics) with transducer properties[ξ] (air) Q factor 900 ± 200, resonant impedance 15 ± 5 ohms, effective coupling coefficient 0.37 ± 0.02 and shunt capacitance 3.7 nF) was attached to the end of the cell using slow drying epoxy resin. The electrical signal that drove the piezoelectric transducer was generated by a Thurlby Thandar TG1010 function generator and amplified by a Bruel & Kjear 2713 power amplifier. The voltage amplitude to the piezoelectric transducer was recorded on a Tektronix TDS 224 digital oscilloscope.

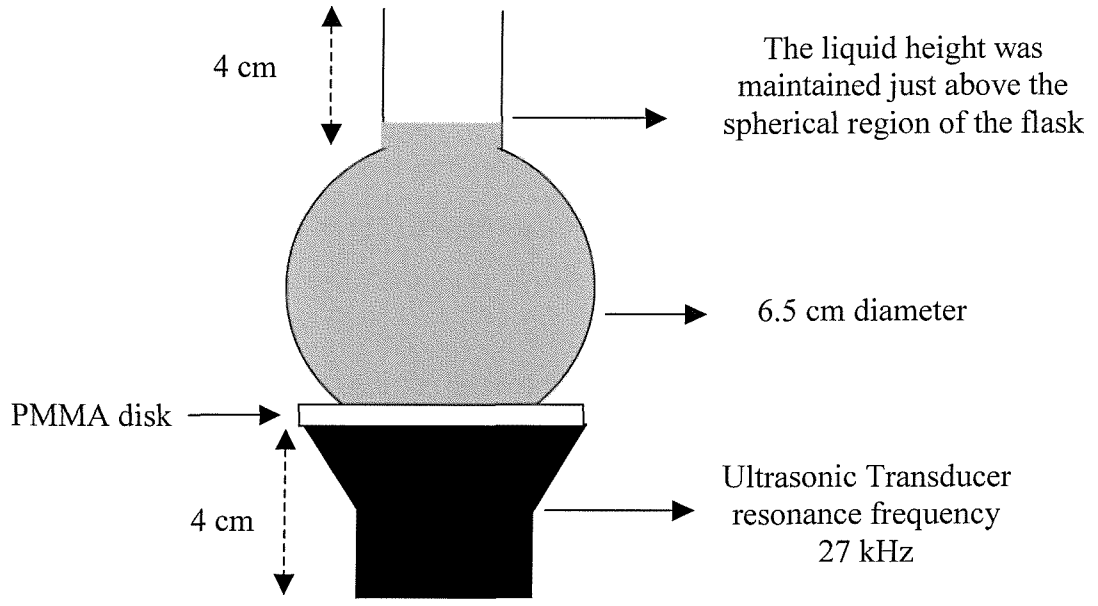

Figure 2.20 Schematic of cell used for the generation of single bubble sonoluminescence.

In order to generate SBSL the solution was first filtered using a vacuum filtration apparatus and sterile Millipore filters (pore size 0.22 μm). It is also necessary to degas the solution in the cell. This was achieved by placing a stopper on the cell and attaching a vacuum line (water pump) for a period of 30 minutes prior to experiments. After degassing the solution, the stopper was removed and the solution irradiated at the appropriate frequency 27.744 kHz and (ca. 1.2-1.6 atm) in our case. These values can only be

[ξ] Information supplied by Morgan Electro Ceramics.

determined by experiment. SBSL may then be achieved by entrainment of bubbles using a pipette. Sometimes it is necessary to vary the voltage (and therefore increasing acoustic pressure) to see the bubble luminescing. Although the emission of light is visible to the human eye, experiments were performed in a darkroom so the bubble could be located using an image intensified CCD camera.

2.14 Electrochemical Analysis of Single Bubble Sonoluminescence – Experimental Equipment and Procedures Employed

A set of microelectrodes was constructed using a 76 mm hypodermic syringe 0.45 mm internal diameter (Orme Scientific Equipment, (a) in figure 2.21) and 50 μm platinum wire insulated with polyester (Goodfellow). A schematic diagram illustrating the fabrication process described below is illustrated in figure 2.21.

(a) Needle hypodermic syringe

(b) A 10 cm piece of polyester insulated platinum wire was threaded up through the hypodermic syringe.

(c) Epoxy resin (Struers) was pumped down the hypodermic syringe from the top using a 2.5 cm^3 syringe until the epoxy resin could be viewed escaping from the bottom of the hypodermic syringe.

(d) The polyester insulation is removed by soaking the platinum wire in concentrated H_2SO_4 for one hour.

(e) The insulation was removed from a piece of multicore wire and it was threaded through a 3.5 cm piece of soda glass. An electrical contact was made to the exposed platinum wire using solder. The piece of soda glass was initially cut so that it just fitted over the top of the hypodermic syringe. This enabled the soda glass to be sealed to the hypodermic syringe using epoxy resin. The tip of the hypodermic syringe (*ca.* 1 mm) was then cut using a wire cutter, and the electrode was placed between two pieces of PMMA designed to support the needle. The electrode was then polished flat using 0.3-micron alpha alumina (Buehler) on microcloth (Buehler).

(f) The finished needle electrode with a magnified illustration of the polished needle tip.

These electrodes were tested by recording a cyclic voltammogram (CV) using a 10 mmol dm^{-3} of $[Ru(NH_3)_6]Cl_3$ prepared in 0.1 mmol dm^{-3} KCl. The CV is illustrated in figure 2.22. The steady state current of 118 nA is higher than the predicted value of 87 nA which was calculated from equation (2.5). This increase in i_L may be due to interactions with the

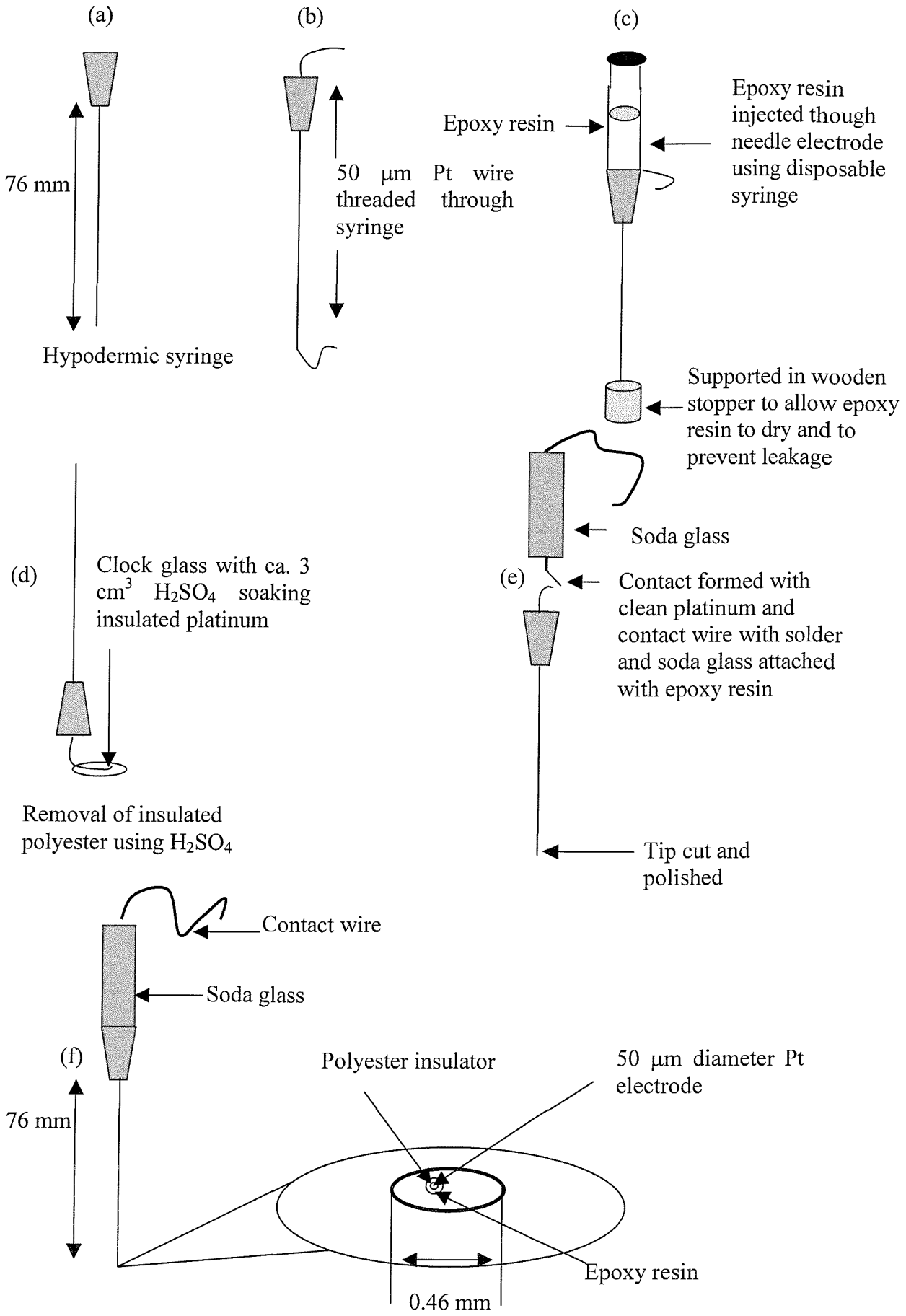

Figure 2.21 Schematic illustrating the fabrication process for the needle microelectrode employed for SBSL experiments. The reader is referred to the text for explanation of each stage in the fabrication process.

steel. It may also be due to a geometric phenomenon associated with the electrode design. If the surround is less that the diffusion layer then i_L will be higher.

$$i_L = 4n_eFaDc \qquad (2.5)$$

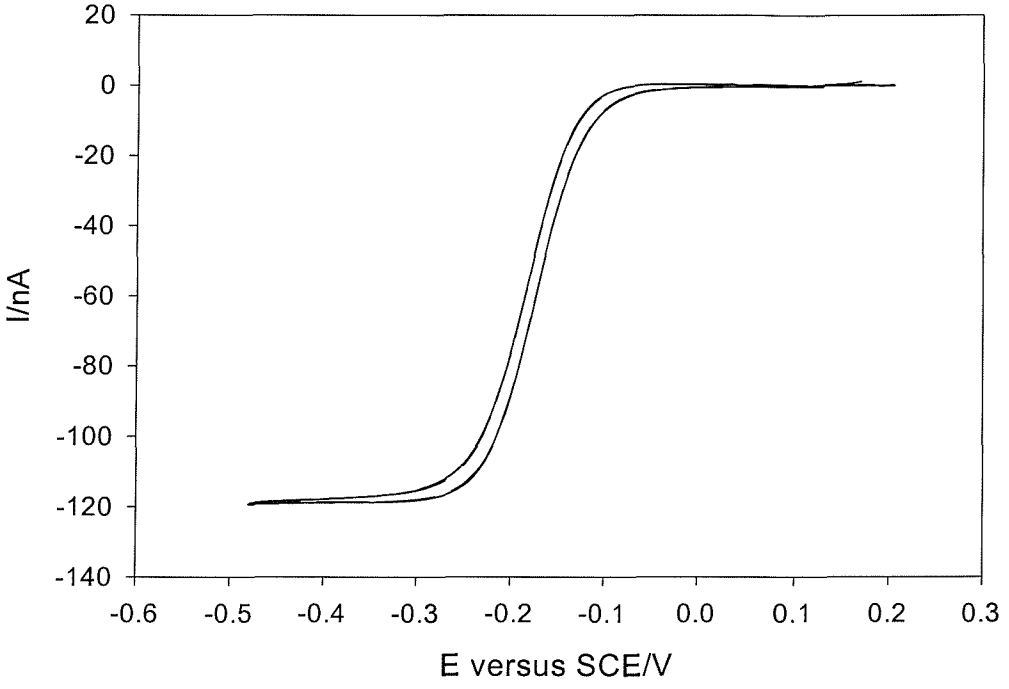

Fig 2.22 Cyclic Voltammogram of a 50 μm platinum needle electrode in a solution containing 10 mmol dm^{-3} $Ru(NH_3)_6Cl_3$ in 0.1 mol dm^{-3} KCl. The solution was degassed with argon. The potential was swept at 5 mVs^{-1} versus SCE and the solution was temperature controlled at 25 °C.

2.15 Experimental Rig employed for investigation of Single Bubble Sonoluminescence

The experimental rig employed for electrochemical analysis of SBSL is illustrated in figure 2.23. The electrode can be moved in the *z* direction using a motorised unislide (Time and precision, A1506VP 144 mm travel) attached to a stepper motor (L25i Paragon stepper drive system form Parker Automation, 0.125 μm resolution) interfaced to a PC via RS232 port and programmed using in-house written software. The cell can be moved relative to the electrode using an *x*, *y*, *z* stage, (Newport M- 462 series 25 mm travel with resolution of 10 μm in all directions). The MTL current recorded at the electrode can be used to determine the location of the bubble in the cell. As the electrode approaches the luminescing bubble surface, an increase in the MTL current is observed. This enables accurate control over the position of the electrode relative to the bubble surface. A two-electrode arrangement was employed in all experiments with a low noise battery operated current follower (T. Young)

enabling both high gain (up to 1 X 10^{10} V A^{-1}) and low noise acquisition of the experimental data.

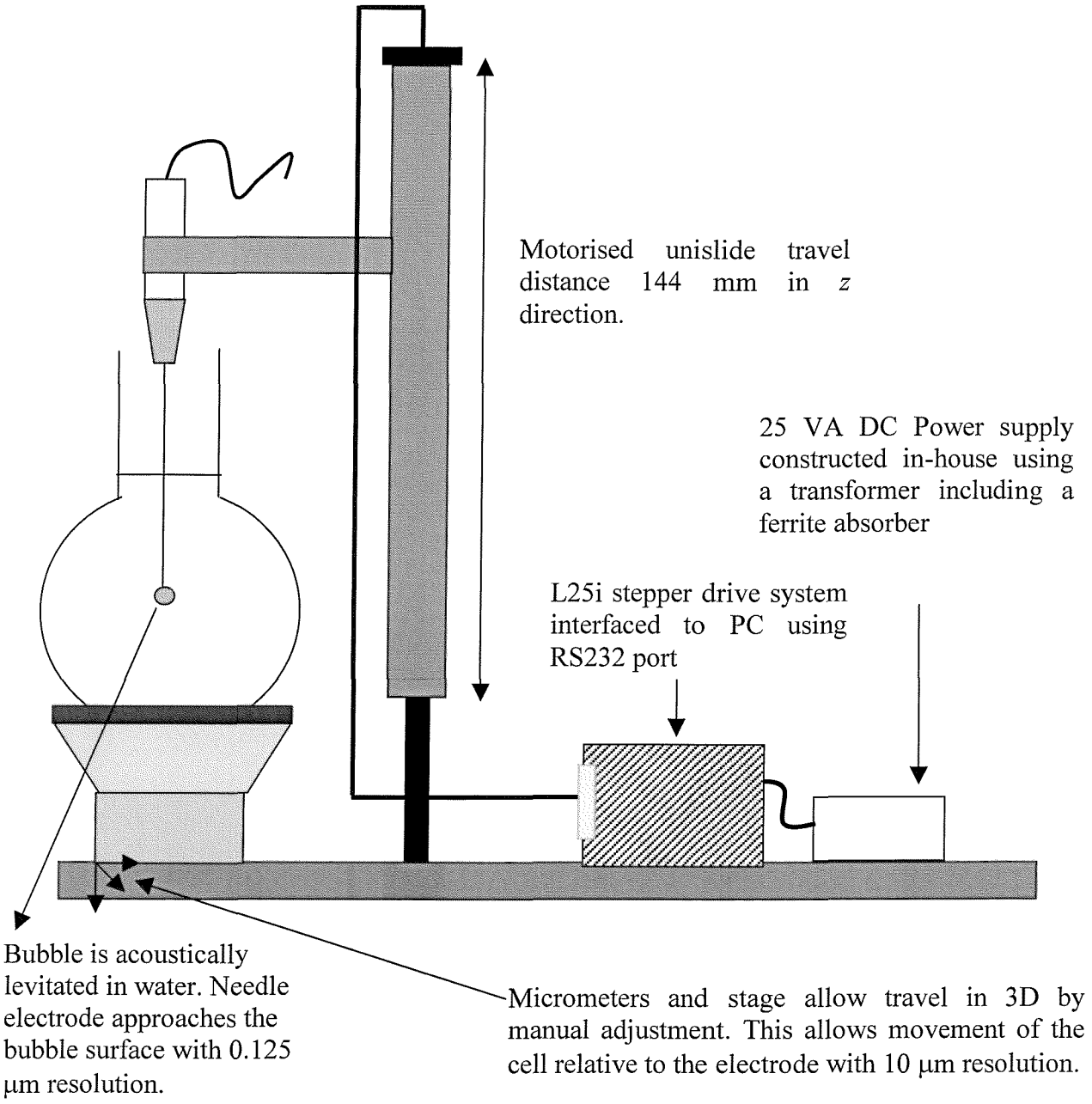

Figure 2.23 Schematic of the experimental rig employed for the electrochemical investigation of SBSL.

2.16 Experimental Rig Employed for Spectrophotometric Investigation of SBSL

To record light emission spectrum of SBSL the experimental rig illustrated in figure 2.24 was employed.

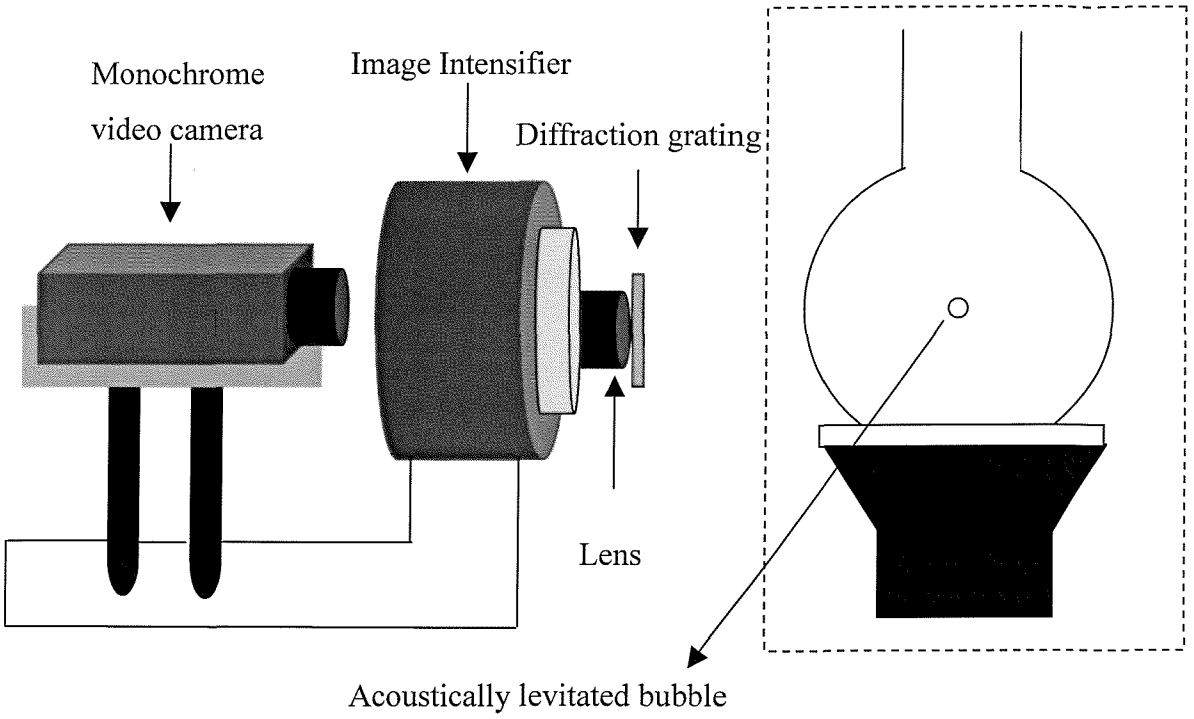

Figure 2.24 Schematic of the experimental rig employed for the spectrophotometric investigation of SBSL. The reader is referred to the text for a detailed discussion of the components of this system.

It consists of a low-level light emission image intensified camera. The high gain camera set-up consisted of an MCP 325 image intensifier (Photek LtD). This contained the following components:

- An input window capable of transmitting light over the range UV-visible-near IR, with a photocathode deposited on its inner surface.
- A microchannel plate (MCP 325) to provide electron gain. The radiant gain at W/W (500 nm) was 2 x 10^7 and the resolution was 251 pixels/mm.*
- The gain of the intensifier was controlled by MCP control unit 2.3 (Photek LtD). The gain was varied using a single turn potentiometer within the tube which increased/decreased the MCP voltage.
- An output window on which is deposited a suitable luminescent screen.
- The wavelength dependence of the image intensifier is plotted in figure 2.25.

A monochrome video camera (Jai Corporation) was focused on the photocathode plate. This was interfaced to a PC via a frame grabber (PXC200A, Imagenation Vision). Images were transferred to the PC using (Imagenation Vision) software.

* Information supplied by Photek LtD

This low-level light emission image intensified camera may be converted to a spectrometer by placing a diffraction grating in front of the objective lens. Diffraction gratings with 500 and 1000 lines per mm (Edmund Optics) were employed for this study.

The spectrometer was calibrated to wavelength by illuminating a pin (positioned in the same position as the SBSL bubble) with a red laser (known wavelength) and recording the spectrum using the spectrometer.

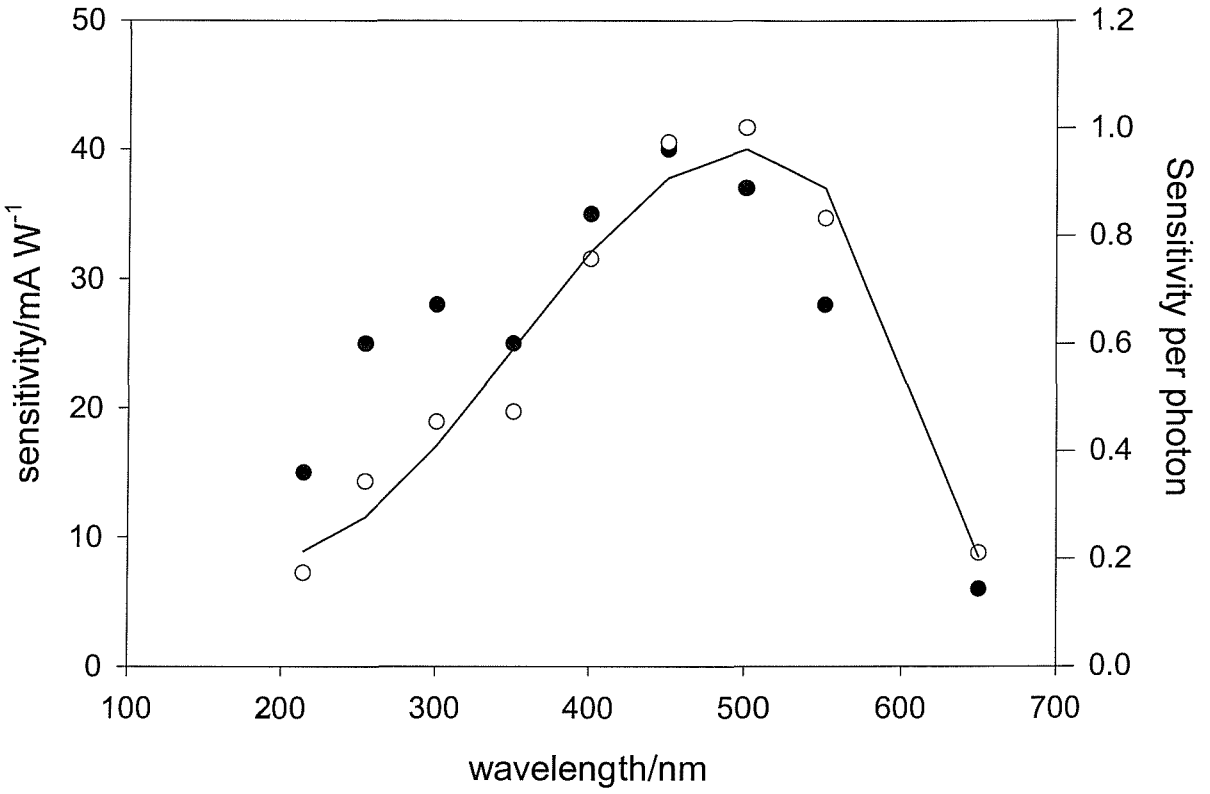

Figure 2.25 The sensitivity of the MCP 325 image intensifier plotted as a function of wavelength. The (•) represents the sensitivity calculated as a function of energy. The (o) represents the sensitivity per photon.

This section outlined the experimental apparatus and the techniques employed to obtain the results presented in the results section (chapters 3 –7).

Chapter 3 presents the acoustic characterisation of the ultrasonic reactors employed for chemical measurements. This was performed prior to chemical experiments, as a detailed understanding of the acoustics of the reactors will aid in the interpretation of the chemical results achieved in chapters 4-7.

CHAPTER 3

EXPERIMENTAL AND THEORETICAL CHARACTERISATION OF SONOCHEMICAL CELLS

This chapter reports the development of an acoustic model and relevant experimental verification of that model aimed at understanding the acoustics of ultrasonic reactors. In particular the spatial characteristics of the resultant sound field will be addressed with relevance to the sonochemical activity within such a reactor.

The sound field in a cylindrical sonochemical cell is discussed in terms of acoustic modes. For the first time a sonochemically active sound field is modelled with appropriate consideration of the boundary conditions at the vessel walls. An acoustic model is developed to predict the spatial distribution of acoustic pressure, which is compared with experimental measurements of the spatial characteristics of luminescent emission from a cylindrical cell. The specific reaction is the oxidation of an activated luminol (3-aminophthalhydrazide) solution by oxidants produced by cavitation.[94-96] Comparing the experimental data with the theoretical model allowed estimates of the effective sound speed within a cavitation environment. These compare well with the only previous estimation of sound speeds during inertial cavitation.[129] From this, the void fraction of bubbles within a cavitating liquid was estimated for the first time. Two cells were used for these experiments details of which can be obtained in the experimental section (see chapter 2 figure 2.1and 2.3). The theoretical model is summarised in the next section.

3.1 Sound Fields Generated from Cylindrical Cell (Theoretical Model)

In order to discuss the sound field generated within a cell arrangement, it is important to consider the geometry of the sound source under consideration. In this particular example, a cylindrical cell was chosen as our model system (see chapter 2 figure 2.1). However, other geometries could be considered using a similar approach to the one presented below.

A sound field in an enclosed cylindrical cavity can be decomposed into its natural modes. Consider a cylinder standing on a flat base. There will be modes entirely in the axial (here the vertical direction) direction. There will also be entirely transverse modes, some of which will have rotational symmetry about the axis (i.e. no azimuth variation), and some of which

will not. Summed appropriately, they will combine to produce the spatial variation of the sound field within the cylinder. Initially, however, the nature of azimuthal and radial modes will be examined separately.

The characteristics of these acoustic modes, is discussed as this will assist in the interpretation of the sonochemiluminescence plots presented subsequently.

The homogeneous acoustic wave equation[130] is given by equation (3.1):

$$\nabla^2 p - \frac{1}{c_o^{\,2}} \frac{\partial^2 p}{\partial t^2} = 0 \tag{3.1}$$

where p represent the acoustic pressure, c_o is the speed of sound, t is time and r, θ and z, represent the cylindrical co-ordinate system. In a cylindrical co-ordinate system (r, θ, z), we seek separable, harmonic solutions to equation (3.1) of the form of Eq. (3.2):

$$p(r,\theta,z,t) = \Theta(\theta)R(r)Z(z)e^{i\omega t} \tag{3.2}$$

where Θ, R and Z are independent functions of θ, r and z, respectively. When the operator ∇^2 is expressed in cylindrical coordinates[130] general solutions to Eq. (3.1) are obtained of the form

$$\Theta(\theta) = e^{im\theta} \tag{3.3}$$

$$R(r) = b_1 J_m(k_r r) + b_2 Y_m(k_r r) \tag{3.4}$$

$$Z(z) = b_3 \sin(k_z z) + b_4 \cos(k_z z) \tag{3.5}$$

where b_1, b_2, b_3 and b_4 represent constants, $J_m(k_r r)$ and $Y_m(k_r r)$ are Bessel functions of the first and second kind, respectively, of order m, where m is confined to integer values to ensure periodicity of the solution in the θ - direction Substituting equations (3.3, 3.4, 3.5) into equation (3.1), shows that radial and axial wavenumbers k_r and k_z are coupled via

$$k_z^2 + k_r^2 = k^2 \tag{3.6}$$

The wavenumbers k_r and k_z are determined from the boundary conditions at the vessel walls. The water-air boundary at $z = 0$ is, to a good approximation, pressure-release, such that $Z(0) = 0$. The base of the cell at $z = L$ is regarded as a rigid boundary, such that the axial particle velocity is zero and hence $\partial Z(z)/\partial z\big|_{z=L} = 0$. These boundary conditions preclude the cosine term in equation (3.5) as a possible solution. The infinite set of axial wavenumber k_{zq} that satisfies these boundary conditions is given by equation (3.7):

$$k_{zq} = \frac{(2q+1)\pi}{2L} \tag{3.7}$$

where q takes the integer values (0, 1, 2...).

The boundary condition at the curved walls is potentially more complicated. Even with a single glass wall, the acoustic wave encounters a water/glass/air interface, and the existence of a water jacket makes this more complicated. A rigorous calculation of the reflection coefficients of a cell of this nature was performed for the first time and applied here.[131] An acoustic model was used to determine the reflection coefficient (see figure 3.1) and phase angle (see figure 3.2) upon reflection at the discretely layered boundary presented by the inner cell wall.[131] While this approach in calculating the boundary conditions at the walls of the vessel is not unique for layered media in sediment acoustics,[132] this is the first time, to the knowledge of the authors, it has been performed for the boundary conditions of a sonochemical cell. The modelling was achieved using MATLAB following a reported method that can be found elsewhere.[133]

Figure 3.1 is a plot showing the modulus of the reflection coefficient as a function of ultrasonic frequency and angle of incidence (θ). Figure 3.1 shows that, for the majority of the incidence angle/frequency space, the magnitude of the reflection coefficient is close to 1. This indicates that the inner interface at the cell wall can be considered as highly reflecting with the energy of the acoustic wave 'trapped' within the inner cylindrical cavity.

Figure 3.2 shows that the phase angle (ϕ) on reflection is non-zero. It is apparent from this figure that the phase angle is neither zero nor 2π over the incidence angle/frequency space considered. This implies that the inner wall cannot be truly considered as rigid. For this reason, in the experimental results the term 'soft wall' is used to describe the boundary under these conditions.

Assuming unity reflection coefficient, the complex reflection coefficient at the cylinder wall may be written as[131]

$$R(\omega,\theta) = \mathrm{e}^{i\phi(\omega,\theta)} \tag{3.8}$$

The equivalent, locally reacting impedance at the wall is then given as

$$\frac{Z(\omega,\theta)}{\rho c_o} = \frac{1+\mathrm{e}^{i\phi}}{1-\mathrm{e}^{i\phi}} \tag{3.9}$$

which simplifies to

$$\frac{Z(\omega,\theta)}{\rho c_o} = i\cot\tfrac{1}{2}\phi(\omega,\theta) \tag{3.10}$$

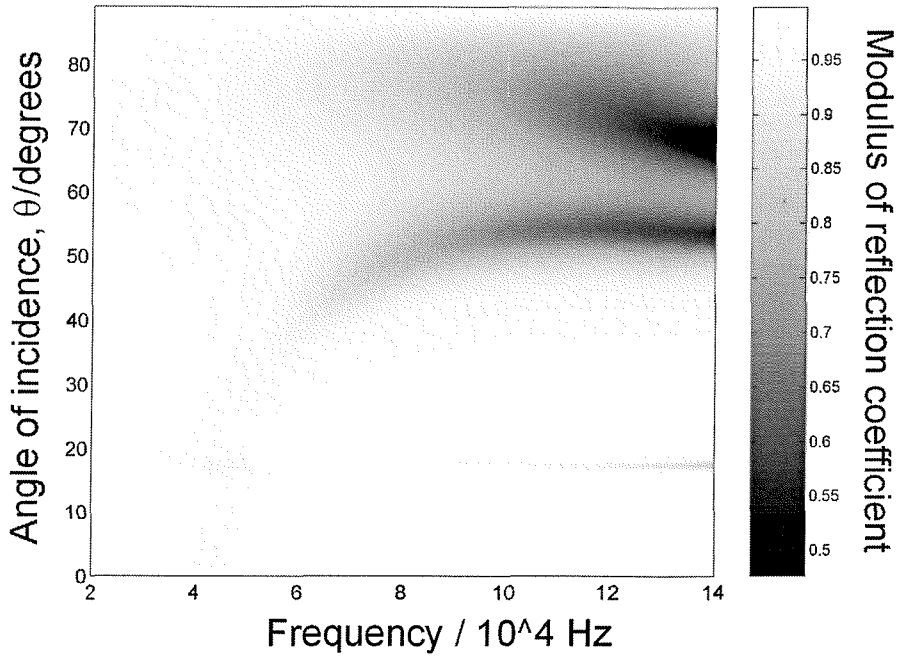

Figure 3.1 Plot showing the modulus of the reflection coefficient as a function of ultrasonic frequency and angle of incidence (θ). The acoustic model for the layered wall is solved as described in the text. The values of the parameters employed in the model were 1000 kg m^{-3} for the density of water, 1597 m s^{-1} for the speed of sound in the water phases, 2320 kg m^{-3} for the density of the glass used, 5640 m s^{-1} for the longitudinal wave speed of sound in the glass, 3280 m s^{-1} for the shear wave speed of sound in the glass, 3.5 mm for the thickness of both glass layers, 6.5 mm for the separation of the glass layers comprising the water jacket, 1.2 kg m^{-3} for the density of air and 345 m s^{-1} for the velocity of sound in the air phase. These calculations were performed by M. Simpson.[131]

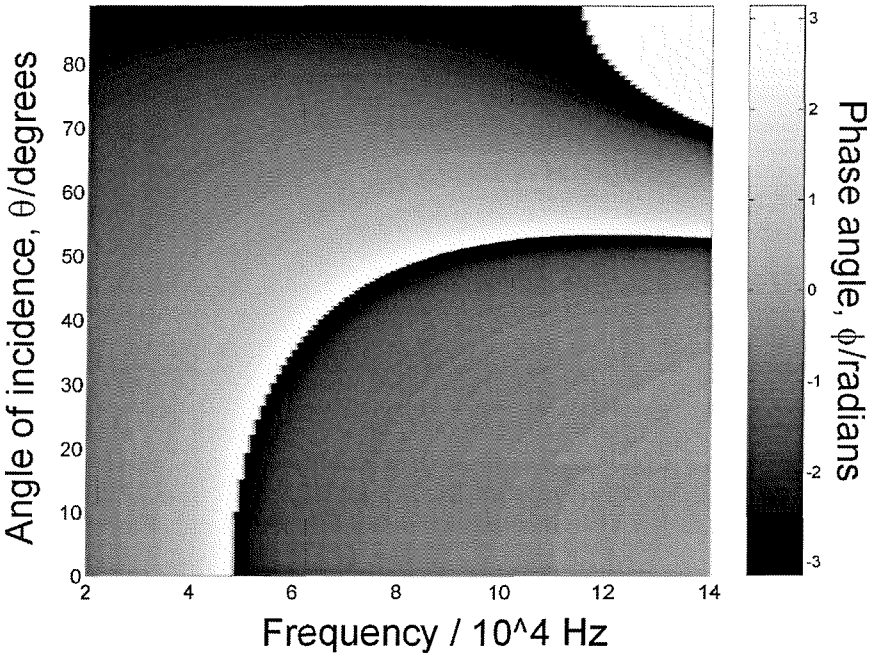

Figure 3.2 Plot showing the phase angle on reflection (ϕ) as a function of ultrasonic frequency and angle of incidence (θ). The acoustic model for the layered wall is solved as described in the text. The values of the parameters employed in the model were identical to those reported in figure 3.1. These calculations were performed by M. Simpson.[131]

In the absence of energy loss at the cylinder wall, we assume solutions in the radial direction of the form of $p = J_m(k_r r)$, whose impedance is given by equation (3.11).

$$\frac{Z}{\rho c_o} = i\frac{k}{k_r}\frac{J_m(k_r r)}{J'_m(k_r r)} \tag{3.11}$$

Equating (3.10) and (3.11) yields the following transcendental equation for the n'th radial wavenumbers k_{rn}

$$\frac{k}{k_{rn}}\frac{J_m(k_{rn} r)}{J'_m(k_{rn} r)} = \cot\tfrac{1}{2}\phi(k_{rn}) \tag{3.12}$$

Equation (3.12) can be solved graphically (the 'soft wall' model see section 3.5, figure 3.15 and table 3.11). The crossing points of the two functions give values of k_{rn} that are solutions of equation (3.12). This will be discussed in detail in section 3.5.

Equation (3.12) can only be employed to determine the value of k_{rn} when the speed of sound in the system is known. It is important to note that accurate knowledge of the speed of sound is not possible in a system undergoing inertial cavitation. In these circumstances it is necessary to assume, that the inner surface of the innermost glass wall approximates to a rigid boundary ('hard wall' model). Experimental evidence presented in section 3.5, illustrates that this assumption is validated under the conditions employed (see figure 3.17). Hence the appropriate boundary conditions in the radial direction at $r = a$ (for the 'hard wall' model) is

$$\partial R(r)/\partial r\big|_{r=a} = 0 \tag{3.13}$$

This boundary conditions preclude the possibility of Y_m in Eq. (3.4) as a possible solution. Equation (3.13) restricts possible k_r values to those for which $\partial J_m(k_{rmn} r)/\partial r\big|_{r=a} = 0$ so that k_{rmn} is given by equation (3.14):

$$k_{rmn} = \left[\frac{j_{mn}}{a_r}\right] \tag{3.14}$$

where j_{mn} is the nth stationary value of the Bessel function of the first kind of order m and a_r is the cylinder radius.

Combining equations (3.3-3.5) and omitting the time dependence, the spatial variation of acoustic pressure in the vessel at a single frequency may be expressed in the form:

$$p(r,\theta,z) = \sum_{m=-\infty}^{\infty} \sum_{n=0}^{\infty} \sum_{q=0}^{\infty} A_{mnq} e^{im\theta} J_m[k_{rmn} r] \sin(k_{zq} z) \qquad (3.15)$$

where A_{mnq} represents the amplitude of the $(m,n,q)^{th}$ mode, and m, n and q are the model integers denoting the azithmuthal, radial and axial mode integers, respectively.

If, for example, the driving system is axisymmetric, then the resultant sound field may be considered to be axially symmetric: There is no θ dependence and the θ term may be ignored. If this is the case, then we restrict ourselves to a zero order Bessel function for which $m = 0$. Hence, we are left to consider the r and z terms only and equation (3.15) reduces to:

$$p(r,z) = \sum_{n=0}^{\infty} \sum_{q=0}^{\infty} A_{0nq} J_0[k_{r0n} r] \sin(k_{zq} z) \qquad (3.16)$$

From Equations (3.6), (3.7) and (3.14), the natural resonance frequency f_{0nq} of the $(0,n,q)^{th}$ cavity mode is given by

$$f_{0nq} = \frac{c_o}{2\pi} \sqrt{\left(\frac{j_{0,n}}{a_r}\right)^2 + \left(\frac{(2q+1)\pi}{2L}\right)^2} \qquad (3.17)$$

The horizontal pattern corresponds to a central maximum (if $m = 0$, 'spot' as viewed from above, see table 3.4) and rings of local maxima in the radial direction. If the spatially averaged sound speed is known, then it is possible to use this model to predict natural frequencies of the modes (it should be noted that damping would impart to a given mode a finite bandwidth about its natural frequency and a small shift in frequency in the standard manner[128]). To do this one needs to know the dimensions of the vessel and the spatially averaged sound speed in the liquid. The latter requirement demonstrates one of the most important findings of this study, because when acoustic fields are calculated for sonochemical studies (which is rare) the sound speed of bubble free water is assumed (e.g. *ca.* 1500 m s^{-1}). The actual sound speed in bubbly water in a reaction vessel is calculated in this chapter.

Table 3.1 shows the frequencies of the first few axisymmetric modes for a reaction vessel, calculated using sound speeds of 1500 m s^{-1} (bubble free water) and 1000 m s^{-1} (a bubbly mixture).

If, however, departures from axisymmetry occur, (for example if the driving transducer is not totally symmetric in nature) then we must consider higher order Bessel functions. As a

result the θ variation of the resultant sound field becomes apparent. In this case it is appropriate to use equation (3.18) to predict the mode frequency:

$$f_{m,n,q} = \frac{c_o}{2\pi}\sqrt{\left(\frac{j_{m,n}}{a_r}\right)^2 + \left(\frac{(2q+1)\pi}{2L}\right)^2} \qquad (3.18)$$

The horizontal pattern of the sound field now can include a series of rings split by the θ dependence in the radial direction with bands in the axial direction.

		n					
		2	3	4	5	6	7
q	0	32.00 (21.34)	58.01 (38.67)	83.95 (55.97)	109.93 (73.29)	135.76 (90.51)	161.59 (107.73)
	1	34.99 (23.33)	59.70 (39.80)	85.14 (56.76)	110.84 (73.89)	136.49 (91.00)	162.21 (108.14)
	2	40.30 (26.87)	62.97 (41.98)	87.45 (58.30)	112.63 (75.08)	137.95 (91.97)	163.44 (108.96)
	3	47.16 (31.44)	67.56 (45.04)	90.82 (60.55)	115.26 (76.84)	140.11 (93.41)	165.26 (110.18)
	4	54.99 (36.66)	73.24 (48.83)	95.12 (63.41)	118.68 (79.12)	142.93 (95.29)	167.67 111.78
	5	63.44 (42.29)	79.78 (53.19)	100.24 (66.83)	122.82 (81.88)	146.39 (97.59)	170.62 (113.75)
	6	72.28 (48.19)	86.98 (57.98)	106.06 (70.70)	127.61 (85.07)	150.43 (100.29)	174.10 (116.07)
	7	81.39 (54.26)	94.68 (63.12)	112.46 (74.98)	132.98 (88.66)	155.02 (103.34)	178.08 (118.72)
	8	90.69 (60.46)	102.78 (68.52)	119.37 (79.58)	138.87 (92.58)	160.09 (106.73)	182.52 (121.68)

Table 3.1. Table showing the lowest few natural frequencies in kHz of the modes of a cylindrical cell calculated using equation 3.17. The cell had a radius to the inner wall of *ca.* 2.9 cm and a liquid height of 7.5 cm. The integers n corresponds to the axial order of the mode. Note in this case $n \neq 1$ is a consequence of the boundary condition at the cell wall ($\partial j_{m,n}/\partial r = 0$). This implies that the first available mode will have to have a pressure maximum at the wall ('ring') and a pressure maximum in the centre of the cell ('spot'). For each mode two frequencies are shown. The upper corresponds to a spatially averaged sound speed of 1500 m s^{-1} (bubble free water). The lower, in brackets, corresponds to 1000 m s^{-1} (i.e. possible for bubbly water).

In this chapter the aim was to characterise the acoustic modes excited within the ultrasonic reactor employed (see chapter 2, figure 2.1 and 2.3). Initially a bubble free sound speed was assumed. Sonochemiluminescent pictures were recorded at a given frequency from above and from the side of the reactor (see chapter 2, section 2.5). The spacing between the rings and the number of bands were used to experimentally determine the acoustic mode. The frequency at which the experimental mode occurred was compared to the calculated frequency using the model. These values do not agree as expected. A back

		n						
		1	2	3	4	5	6	7
m	0	-	3.84	7.02	10.18	13.34	16.48	19.62
	1	1.86	5.34	8.54	11.72	14.88	18.02	21.18
	2	3.06	6.72	9.98	13.18	16.36	19.52	22.68
	3	4.22	8.02	11.36	14.6	17.8	20.98	24.16
	4	5.32	9.3	12.7	15.98	19.2	22.42	25.6
	5	6.42	10.52	14	17.32	20.58	23.82	27.02
	6	7.52	11.74	15.28	18.64	21.94	25.2	28.42
	7	8.58	12.94	16.54	19.96	23.28	26.56	29.8
	8	9.66	14.12	17.78	21.24	24.6	27.9	31.16
	9	10.72	15.3	19.02	22.52	25.9	29.22	32.52
	10	11.78	16.46	20.24	23.78	27.18	30.54	33.86

Table 3. 2 Table showing the values of $j_{m,n}$ at $\partial j_{m,n}/\partial r = 0$ for zero and higher order modes.

		n						
		1	2	3	4	5	6	7
m	0	-	159.24 (106.16)	162.03 (108.02)	166.31 (110.88)	172.01 (114.67)	178.92 (119.28)	186.95 (124.63)
	1	158.32 (105.55)	160.36 (106.90)	163.91 (109.27)	168.92 (112.61)	175.25 (116.83)	182.73 (121.82)	191.31 (127.54)
	2	158.80 (105.87)	161.70 (107.80)	166.00 (110.67)	171.67 (114.46)	178.63 (119.09)	186.68 (124.45)	195.71 (130.47)
	3	159.49 (106.33)	163.22 (108.82)	168.28 (112.19)	174.64 (116.43)	182.17 (121.45)	190.74 (127.16)	200.25 (133.50)
	4	160.34 (106.89)	164.97 (109.98)	170.75 (113.83)	177.74 (118.49)	185.81 (123.88)	194.93 (129.96)	204.83 (136.55)
	5	161.38 (107.59)	166.86 (111.24)	173.36 (115.57)	180.96 (120.64)	189.60 (126.40)	199.19 (132.79)	209.50 (139.67)
	6	162.61 (108.40)	168.96 (112.64)	176.14 (117.43)	184.33 (122.89)	193.51 (129.01)	203.54 (135.70)	214.25 (142.83)
	7	163.96 (109.31)	171.21 (114.14)	179.06 (119.38)	187.88 (125.25)	197.53 (131.69)	207.97 (138.65)	219.05 (146.04)
	8	165.51 (110.34)	173.61 (115.74)	182.12 (121.41)	191.48 (127.65)	201.63 (134.42)	212.47 (141.65)	223.90 (149.27)
	9	167.19 (111.46)	176.18 (117.46)	185.33 (123.56)	195.23 (130.16)	205.81 (137.20)	217.02 (144.68)	228.86 (152.57)
	10	169.03 (112.69)	178.87 (119.25)	188.65 (125.77)	199.07 (132.71)	210.04 (140.03)	221.68 (147.79)	233.84 (155.89)

Table 3.3 Table showing the frequencies in kHz corresponding to the $(2q + 1) = 59$ system. These frequencies where calculated by employing equation (3.17), $a' = 4.7$ cm, L = 14 cm. For each mode two frequencies are shown. The upper corresponds to a spatially averaged sound speed of 1500 m s^{-1} (bubble free water). The lower, in brackets, corresponds to 1000 m s^{-1} (i.e. possible for bubbly water).

calculation was performed to determine the real sound speed in the reactor. This was then used to estimate the void fraction (see section 3.4). Table 3.2 shows the stationary values of $j_{m,n}$. This model predicts that the integer values of m, n and q will be involved in the calculations of the natural frequencies and as such a 2 dimensional table is inappropriate. However, if we calculated q from the rings and bands (see table 3.4), it is possible to predict values of the natural frequencies of a circular cell.

Table 3.3 shows the values of the natural frequencies assuming $q = 29$ (a value chosen from the results shown in figure 3.5). The number of rings, spots and bands can be counted and used in conjunction with the formulae shown in table 3.4 to assign the appropriate mode.

Model Parameter	Experimental consequence for observation of luminescence.
$q = 0, 1, 2...$	$(q + 1)$ bands in z direction (including a band at the base).
$m = 0$	Axially symmetric mode. Zero order Bessel function implies a central spot followed by rings when the cell is viewed from above (see figure 3.5)
$m = 1, 2, 3....$	Non-axially symmetric system. Higher order Bessel function implies no central spot but a series of rings when the cell is viewed from above (see figure 3.8). The θ dependence also implies the rings are sliced into $2m$ segments.
$n = 1, 2, 3.....$	Number of rings and spot ($m = 0$, $n \neq 1$) or rings ($m > 0$, $n = 1, 2, 3..$) when the cell is viewed from above.

Table 3.4 Table showing the variables discussed in the acoustic model described in the text and the experimental consequences of each variable on the patterns of luminescence (assuming bright luminescence is associated with spatial maxima in acoustic pressure).

3.2 How Modes are Assigned in a Sequential Sense

Prior to presenting the experimental results, it is appropriate first to describe how the acoustic modes excited in the cell are assigned in a set of sequential steps. To assign a mode MBSCL pictures were recorded from above and from the side of the cell (see experimental section 2.5 and figure 3.3). Both these pictures are then analysed to assign the mode as follows:

Transverse

(1) Figure 3.3 (A) shows an image of the sonochemical cell prior to recording sonochemiluminescent pictures from above. Schematic (B) illustrates how the sonochemiluminescent pictures (see figure 3.3) were analysed to determine distances R_1, R_2 and R_3 (see table 3.5). When measured, the experimental distances R_1, R_2 and R_3 are compared to predicted acoustic modes until the values of R_1, R_2 and R_3 agree with the experimental data.

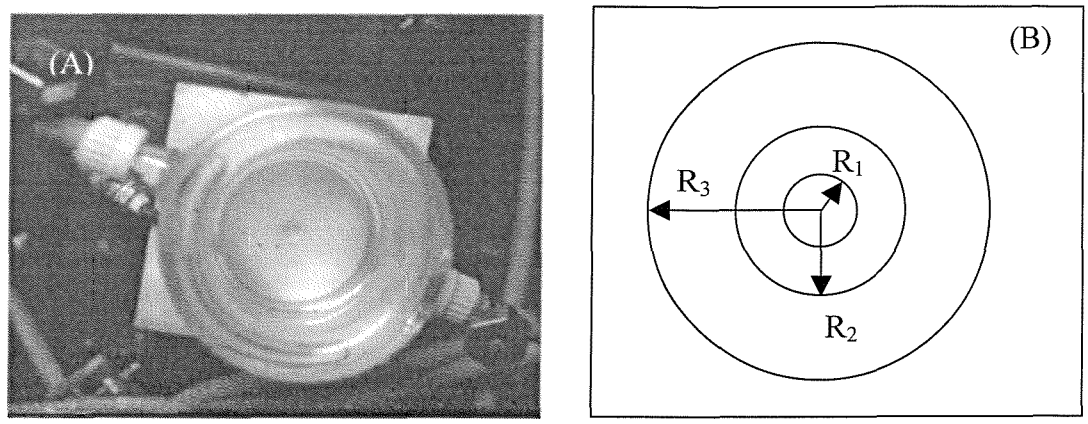

Figure 3.3 Picture (A) illustrates the ultrasonic reactor from above and schematic (B) is a plot showing how the distances between the rings are measured.

(2) Assign value of $j_{m,\,n,\,q}$ and fit to model to determine the theoretical frequency employing equation (3.18) and table 3.4.

Axial

Figure 3.4 (C) illustrates a side view of the ultrasonic cell. L is the height of the liquid q, is the number of bands and $q = n_b\text{-}1$ (where n_b is equal to the number of bands estimated from the MBSCL image). Schematic (D) illustrates the band structure. The number of bands may be calculated by counting and using the relationship: band spacing = liquid height/(q + 0.5). There is a pressure minimum at the air liquid interface and a pressure maximum at the transducer glass interface.

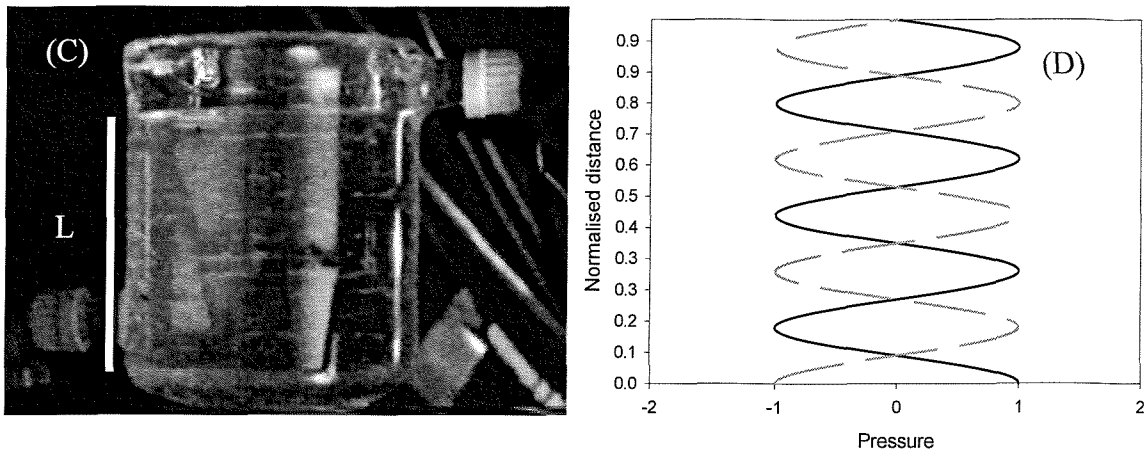

Figure 3.4 Picture (C) showing the ultrasonic cell (side on view) and a schematic (D) plotting pressure fluctuation as a function of the vertical distance through the cell. Note there is a pressure minimum at the air liquid interface (1.0) and a pressure maximum at the transducer glass interface (0). *L* (7.5 cm) represents the liquid height.

3.3 Experimental Results

Figure 3.5 illustrates a series of frames recorded from above (frames 'a', 'c', 'e' and 'g') and side on (frames 'b', 'd', 'f' and 'h') the cylindrical cell. The positioning of the image-intensified camera for these experiments has been discussed in the experimental section (see chapter 2 section 2.5). The figure illustrates a series of concentric circles from above the cell and a series of bands when viewed from the side. This is in agreement with the acoustic model. The figure shows the effect of varying the acoustic pressure amplitude at constant frequency (132.44 kHz). As the power was reduced the emission of light becomes concentrated in the centre of the cell. This effect is best illustrated by frame (g) where a single bright spot appears in the centre of the cell. It is important to note that this may be due to the camera detection limit.

Table 3.5 shows the measurements made from frame (c) of the position of the rings within the cell. The number of bands has been estimated at 30 from frame (b). This corresponds to a $q = 29$ (see table 3.4). It can be seen that the predicted natural frequency is much higher than the driving frequency. The reason for this discrepancy is attributed to the speed of sound in the cavitation environment (see section 3.4 table 3.10).

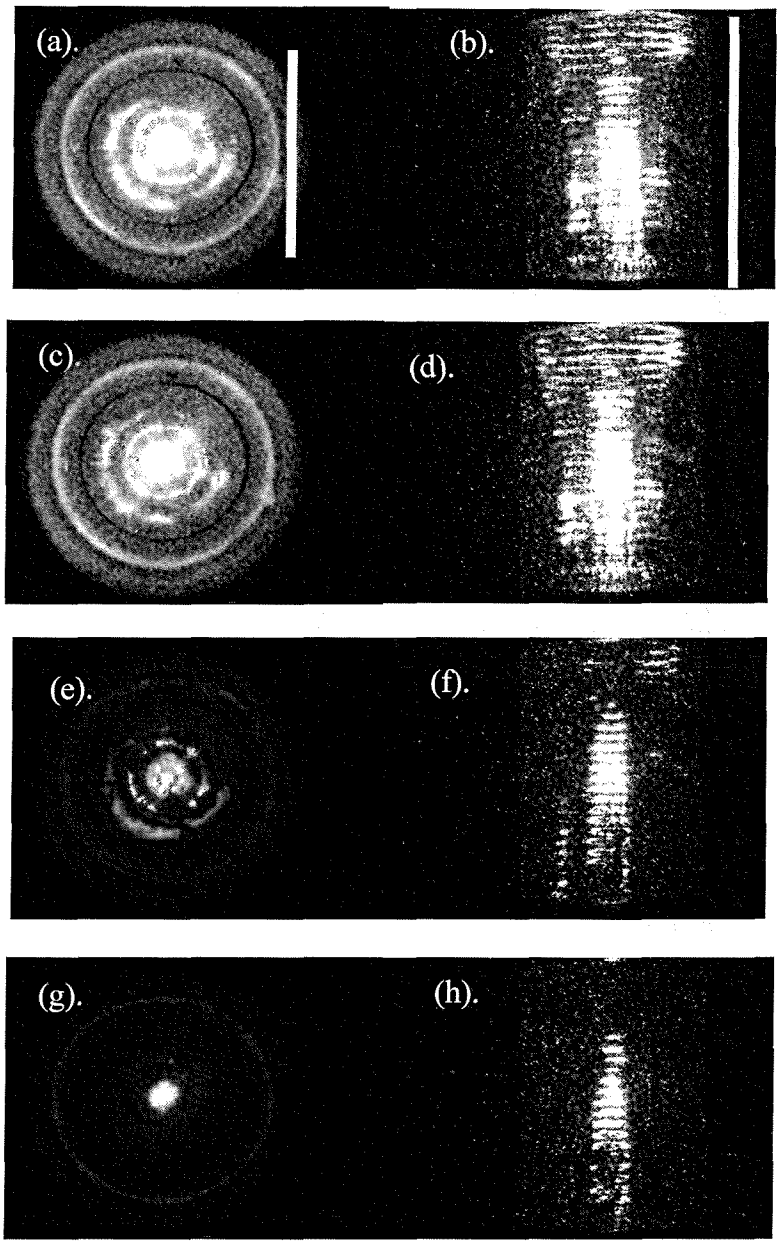

Figure 3.5 Frames showing the light emission from a cylindrical single walled cell (cell (B) 9.4 cm internal diameter) recorded from above (frames 'a', 'c',' e' and 'g') and to the side (frames 'b', 'd', 'f', 'h'). In all cases the driving frequency was maintained at 132.44 kHz. The cell contained an aqueous solution of 50 μmol dm^{-3} luminol, 0.1 mmol dm^{-3} EDTA, 0.1 mmol dm^{-3} H_2O_2 and 100 mmol dm^{-3} Na_2CO_3. The pictures were recorded under ambient conditions (*ca.* 20-23 °C) in aerobic media. The solution height was maintained at 14 cm. The acoustic pressure amplitude was 76 kPa for frames 'a', and 'b', 63 kPa for frames 'c' and 'd', 52 kPa for frames 'e' and 'f' and 44 kPa for frames 'g' and 'h'. The scale bar in frame 'a' represents 9.4 cm and applies to frames 'a', 'c', 'e', 'g' while the scale bar in frame 'b' represents 14 cm and applies to frames 'b', 'd', 'f' and 'h'.

	Measured distance/cm	Predicted distance/cm
Ring 1	0.72 ± 0.2	0.9
Ring 2	1.67 ± 0.2	1.66
Ring 3	2.70 ± 0.2	2.45
m,n	--	0,7
$j_{m,n}$	--	19.62
$f_{0,7,29}^{natural}$/kHz	--	186.8

Table 3.5 Table showing the measured and predicted ring spacing for the data shown in figure 3.5. These values were calculated using the parameters reported in table 3.4 and an assumed sound speed of 1500 m s^{-1}.

Figure 3.6 emphasizes how under certain circumstances changing the gain of the image-intensified camera may be beneficial. It shows how the data may be misinterpreted if care is not taken. For example frame (b) in figure 3.6, a spot and an extra ring can be seen when the gain is reduced. If the gain were not reduced it could lead to an incorrect mode assignment. In all the MBSCL pictures presented the gain of the camera was kept constant unless otherwise stated in the appropriate figure legend. However, in all experiments the gain was varied to check for spot formation in the centre of the cell (see figure 3.6). This enabled correct mode assignment to be achieved.

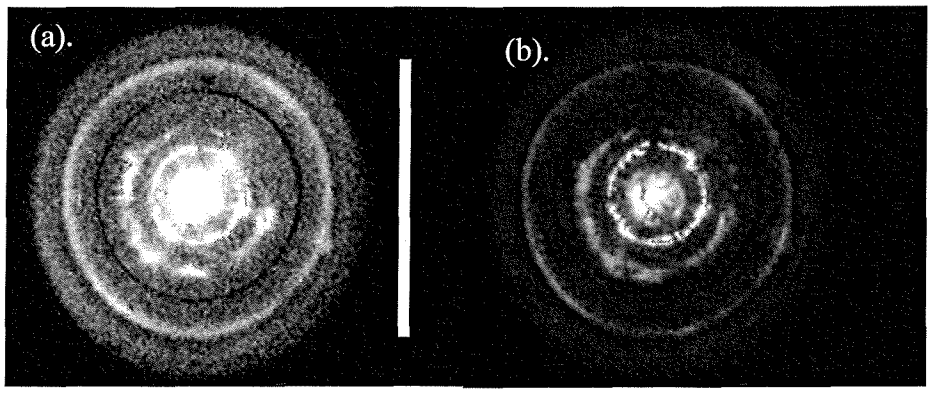

Figure 3.6. This figure shows the effect of varying the gain of the image-intensified camera. Frame (a) and (b) were recorded under the exact same conditions as figure 3.5, frequency 132.44 kHz, acoustic pressure amplitude 76 kPa. However the gain of the image-intensified camera was reduced in going from frame (a) to fame (b). The scale bar represents 9.4 cm.

Figure 3.7 shows a series of frames recorded in a glass jacketed cell (Cell (A)). In this case frames 'a', 'c', 'e' are from above the cell and frames 'b', 'd' and 'f' are from the side on view. The predicted pattern is again visible. A central spot was observed which implies a

zero order Bessel function for this particular mode. The mode was determined to be the $J_{0,6,13}$ (see table 3.6) with a predicted natural frequency of 191.39 kHz. This was higher than the drive frequency (120.15 kHz).

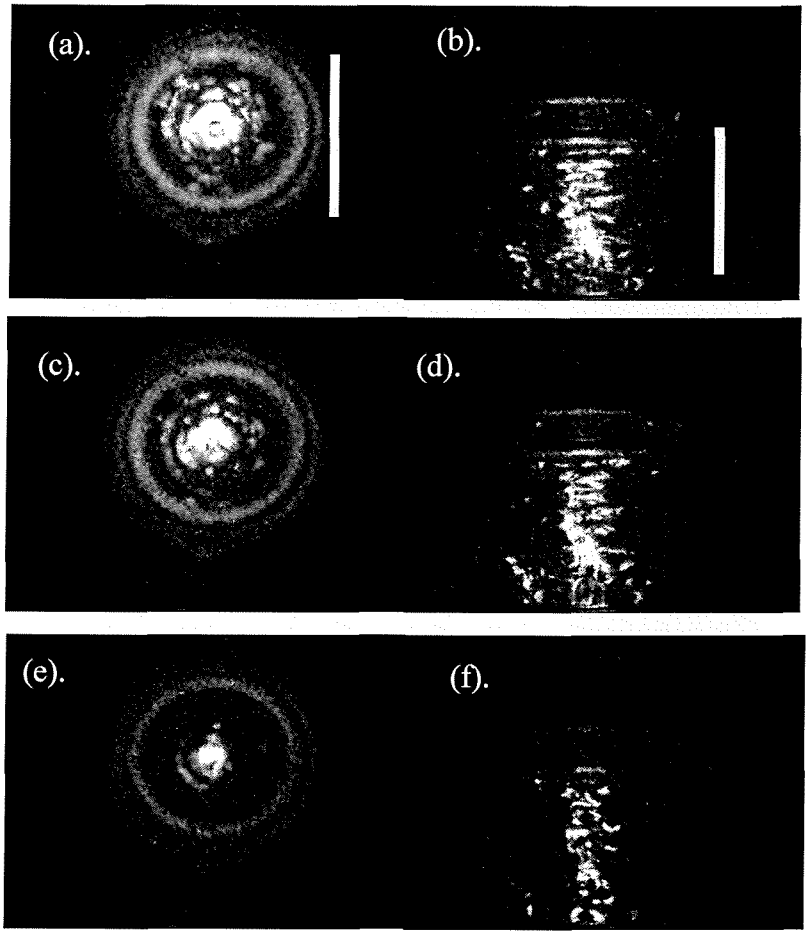

Figure 3.7 Frames showing the light emission from a cylindrical double walled cell (cell (A) 5.8 cm internal diameter) recorded from above (frames 'a', 'c' and 'e') and from the side (frames 'b', 'd' and 'f'). In all cases the driving frequency was maintained at 120.15 kHz. The cell contained an aqueous solution identical to that reported in the legend of figure 3.5. The solution height was 7.5 cm. The cell was jacketed at 25 ^{0}C under aerobic conditions. The acoustic pressure amplitude was 217 kPa for frames 'a' and 'b', 176 kPa for frames 'c' and 'd' and 124 kPa for frames 'e' and 'f'. The scale bar in frame 'a' represents 5.8 cm and applies to frames 'a', 'c' and 'e' while the scale bar in frame 'b' represents 7.5 cm and applies to frames 'b', 'd' and 'f'.

	Measured distance/cm	Predicted distance/cm
Ring 1	0.63 ± 0.2	0.65
Ring 2	1.31 ± 0.2	1.25
Ring 3	1.84 ± 0.2	1.80
Ring 4	2.37 ± 0.2	2.35
m,n	--	0,6
$j_{m,n}$	--	16.48
$f_{0,6,13}^{natural}$/kHz	--	191.39

Table 3.6 Table showing the measured and predicted ring spacing for the data shown in figure 3.7. These values were calculated using the parameters reported in table 3.4 and an assumed sound speed of 1500 m s^{-1}.

Figure 3.8 illustrates how the frequency employed alters the mode excited within the cell. The experimental conditions are identical to those reported in figure 3.7, except that the frequency was altered by less than 2 kHz to 121.85 kHz. The mode assignment and measurement of the ring spacing are shown in table 3.7.

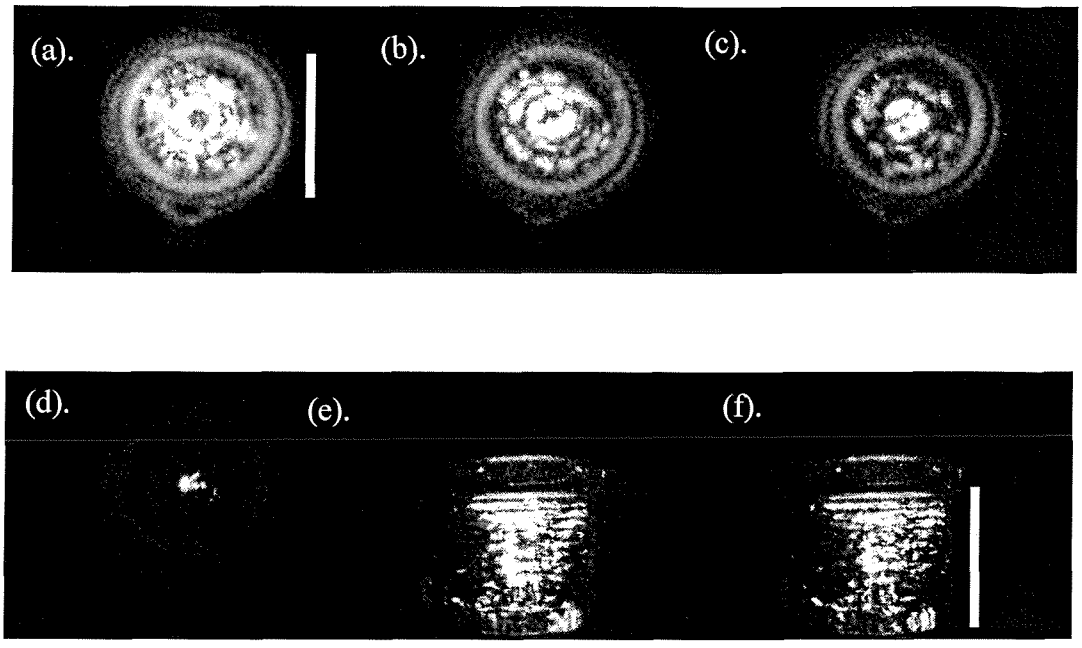

Figure 3.8 Frames showing the light emission from a cylindrical double walled cell (5.8 cm internal diameter ultrasonic reactor cell (A) see figure 2.1) recorded from above (frames 'a', 'b', 'c' and 'd') and from the side (frames 'e' and 'f'). In all cases the driving frequency was maintained at 121.83 kHz. The cell contained an aqueous solution identical to that reported in the legend of figure 3.5. The solution height was 7.5 cm and the cell was jacketed at 25 °C under aerobic conditions. The acoustic pressure amplitude was 214 kPa for frames 'a' and 'e', 160 kPa for frames 'b' and 'f', 123 kPa for frame 'c' and 62 kPa for frame 'd'. The scale bar in frame 'a' represents 5.8 cm and applies to frames 'a – d' while the scale bar in frame 'f' represents 7.5 cm and applies to frames 'e – f'.

Figure 3.8 shows no spot is observable in the centre of the cell. Hence, the mode excited in the cell has altered in comparison to figure 3.7. This has obvious implications when one is considering the frequency dependence of sonochemical reactions and the importance of frequency resolution. A small change in frequency can have a dramatic effect on the cavitation activity in the cell. In chapter 5 the frequency dependence of a number of reactions sensitive to radical production were reported. The rates of these reactions were observed to vary remarkably with frequency. Indeed, a 3 kHz change in ultrasonic drive frequency resulted in the rate altering by 3 orders of magnitude (see chapter 5, figure 5.5). The photographic results reported in this section agree with the results obtained using the chemical sensors. Altering the frequency by a less than 2 kHz results in a different acoustic

mode being excited in the cell. This effect is even more evident in figure 3.10 where images of the sound field in the cell were recorded with a 1 kHz frequency resolution.

	Measured distance/cm	Predicted distance/cm	Predicted distance/cm
Ring 1	0.74 ± 0.2	0.9	0.8
Ring 2	1.58 ± 0.2	1.50	1.4
Ring 3	2.11 ± 0.2	1.95	1.9
Ring 4	2.64 ± 0.2	2.45	2.4
m,n	--	5,5	4,5
$j_{m,n}$	--	20.58	19.20
$f_{m,n,12}^{natural}$/kHz	--	210.54	201.54

Table 3.7. Table showing the measured and predicted ring spacing for the data shown in figure 3.8. Note in this case that the acoustic model predicts two possible modes for the data shown in figure 3.8 (and hence the presence of two predicted distance columns). These values were calculated using the parameters reported in table 3.4 and a sound speed of 1500 m s^{-1}.

Figure 3.9 shows the same cell driven at 125.23 kHz. In this particular case the mode appears to be $J_{3,4,15}$. The assignment and measurement of the ring spacing is shown in table 3.8. Again the predicted frequency (196.14 kHz) is in excess of the applied frequency.

	Measured distance/cm	Predicted distance/cm
Ring 1	0.84 ± 0.2	0.85
Ring 2	1.68 ± 0.2	1.60
Ring 3	2.31 ± 0.2	2.25
m,n	--	3,4
$j_{m,n}$	--	14.60
$f_{3,4,15}^{natural}$/kHz	--	196.14

Table 3.8. Table showing the measured and predicted ring spacing for the data shown in figure 3.9. These values were calculated using the parameters reported in table 3.4 and a sound speed of 1500 m s^{-1}.

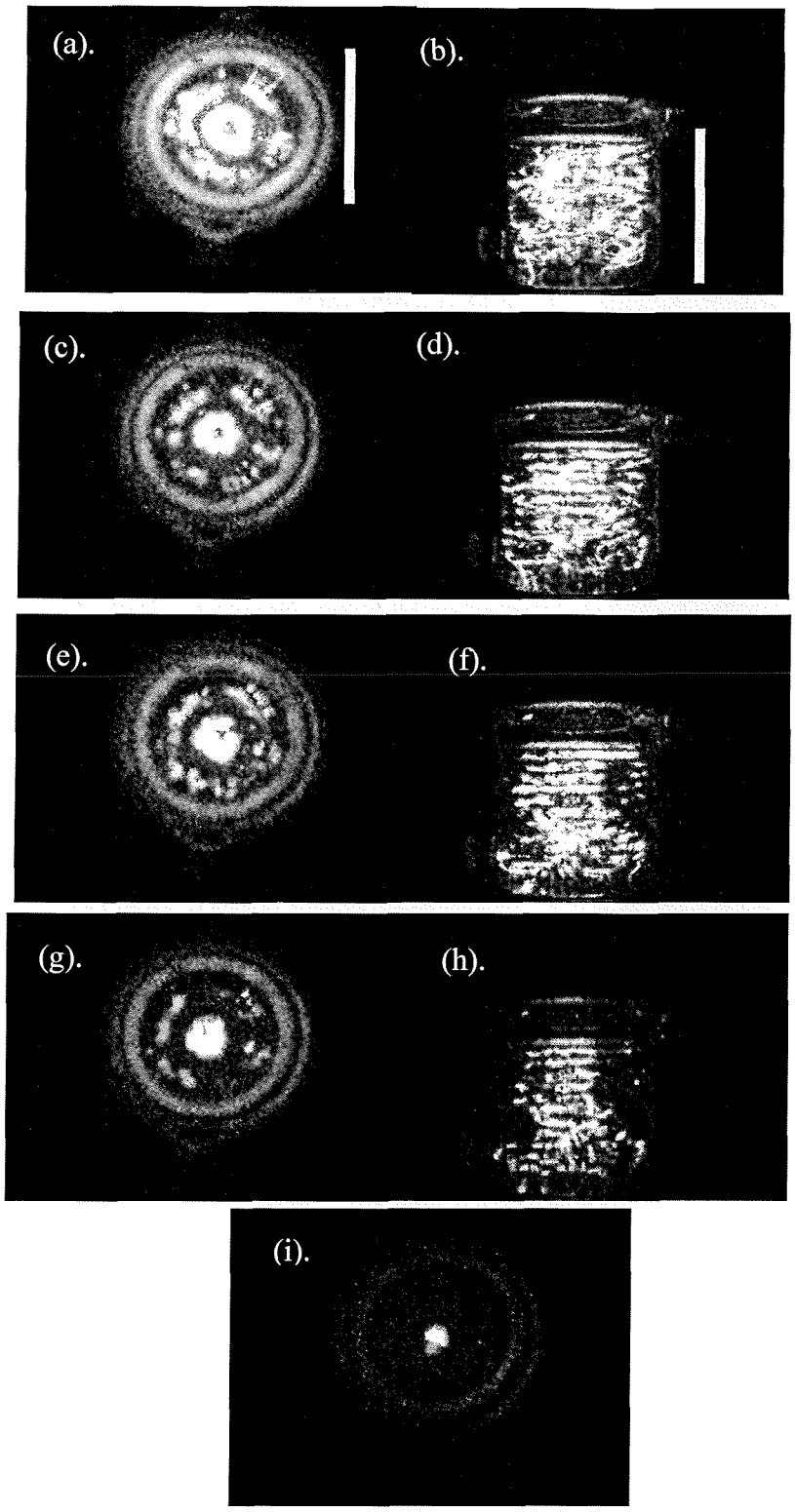

Figure 3.9 Frames showing the light emission from a cylindrical double walled cell (5.8 cm internal diameter ultrasonic reactor cell (A)) recorded from above (frames 'a', 'c', 'e', 'g', and 'i') and from the side (frames 'b', 'd', 'f' and 'h'). In all cases the driving frequency was maintained at 125.23 kHz. The cell contained an aqueous solution identical to that reported in the legend of figure 3.5. The solution height was 7.5 cm and the cell was jacketed at 25 °C under aerobic conditions. The acoustic pressure amplitude was 255 kPa for frames 'a' and 'b', 186 kPa for frames 'c' and 'd', 141 kPa for frame 'e' and 'f', 93 kPa for 'g' and 'h' and 77 kPa for frame 'i'. The scale bar in frame 'a' represents 5.8 cm and applies to frames 'a', 'c', 'e', 'g' and 'i' while the scale bar in frame 'f' represents 7.5 cm and applies to frames 'b', 'd', 'f' and 'h'.

The effect of varying the frequency is outlined in figure 3.10. The frequency was increased from 116 kHz to 131 kHz in 1 kHz increments. Figure 3.10 clearly shows that as the frequency was increased the modal structure within the cell altered dramatically. This is demonstrated in frames 'f', 'g' and 'h' where in the space of a 2 kHz change in drive frequency (representing a 1.6 % change) the modal pattern changes dramatically.

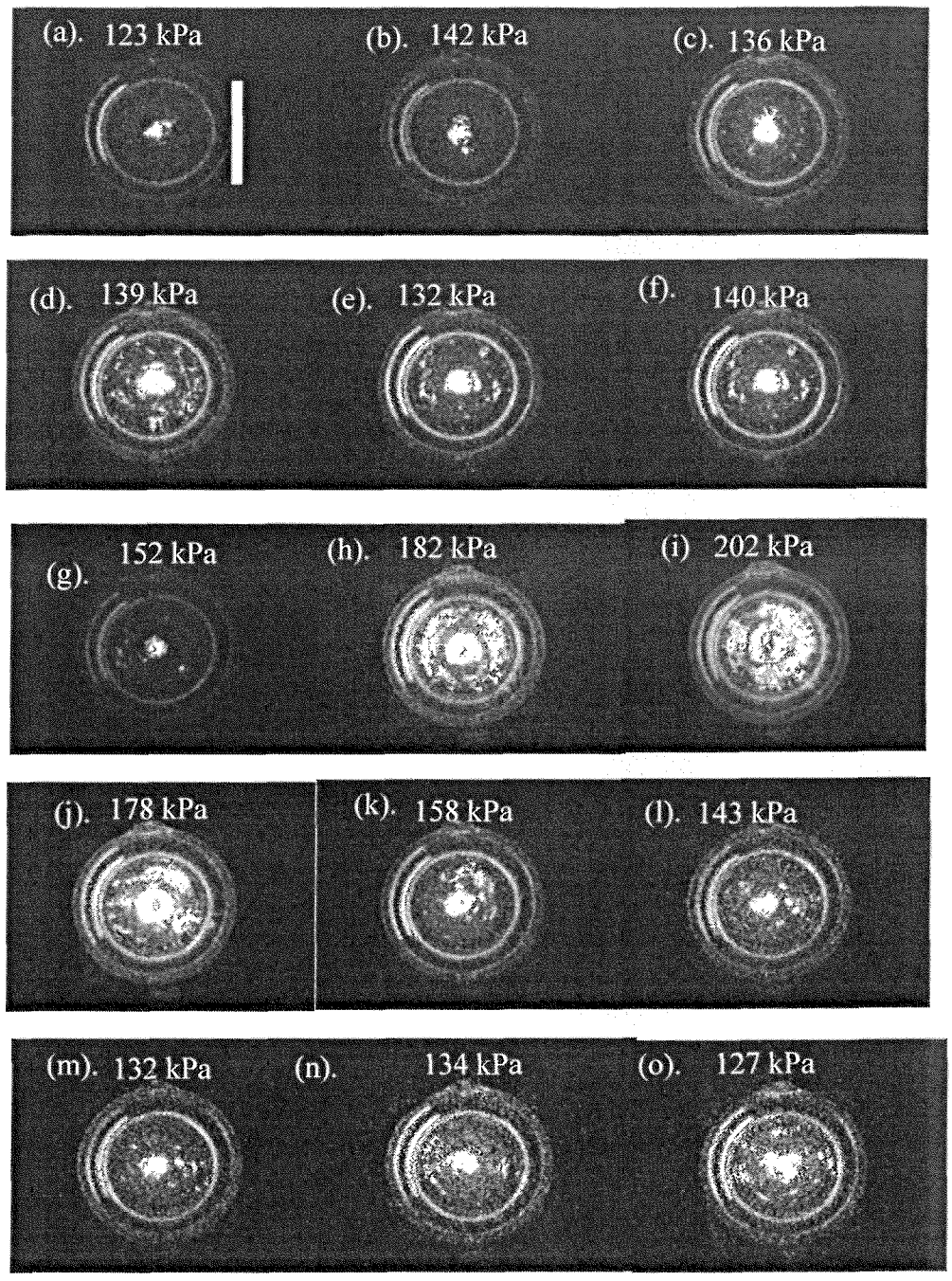

Figure 3.10 Frames showing the light emission from a cylindrical double walled cell (5.8 cm internal diameter ultrasonic reactor cell (A)) recorded from above. The cell contained an aqueous solution identical to that reported in the legend of figure 3.5. The cell was jacketed at 25 °C under aerobic conditions. The applied voltage was maintained at 95 V. The corresponding acoustic pressure amplitudes at each frequency are labelled on the pictures. The liquid height was 8 cm for all frames. The driving frequency was increased from 116 kHz to 130 kHz in 1 kHz steps through frames 'a' to 'o' inclusively. The scale bar represents 5.8 cm.

Figure 3.10 shows that a relatively small change in the drive frequency can have dramatic effects on the cavitation activity within the cell. These results have implications for sonochemists comparing chemical reaction rates at dramatically different frequencies, which will be discussed later. In addition two points should be noted; first at sufficiently high frequencies (> Schroeder frequency[134]) individual modes overlap and the modal nature of the sound field will disappear. Second, bubbles are not the only source of sound speed change. For every 1°C rise in water temperature around room temperature, the sound speed (and hence the modal frequency) changes by 0.3%. Therefore, a 3°C rise in temperature, which is not uncommon as a result of transducer heating in vessels that are not temperature controlled, would be sufficient to cause the mode detuning seen in figure 3.10 with similar major changes in reaction yield. Indeed this rise in temperature is relied upon when calorific quantification of the transducer is measured.

Figure 3.11 shows the effect of increasing the ultrasonic drive frequency on the band separation (see table 3.4). As the frequency rises the measured spaces between the bands reduces. This is in line with the model as q is expected to increase at higher frequencies (see figure 3.11 (f)).

The results presented in figure 3.11 and in figures 3.5, 3.7, etc; show that the definition of the bands within the cell changes as the acoustic pressure amplitude was varied. Indeed some bands were no longer detectable at low driving pressures. Several mechanisms contribute to this effect. First, the detection system (e.g. the image intensified camera) will have a critical light intensity below which a band will not be detected even though there is a pressure antinode in that position. Second, the critical pressure amplitude responsible for the light emission process imaged (e.g. the pressure amplitude for cavitation induced $OH^{\bullet}$ generation) is a complex matter relating cavitation bubble dynamics, bubble populations and other physical parameters. Hence, considering these two points implies that the experimental determination of a band presence or absence through luminescent imaging is complex, and may not be expected to be uniform throughout the cell. However, the model presented here does not attempt to predict the absolute pressure fluctuations (which can be measured using a hydrophone) but the position of the pressure antinodes and nodes, which can then be used to assign the mode. If all the bands are not visible, it is still possible to assign the mode by measuring the band spacing where visible and using the relationship, band spacing = liquid height/(q + 0.5).

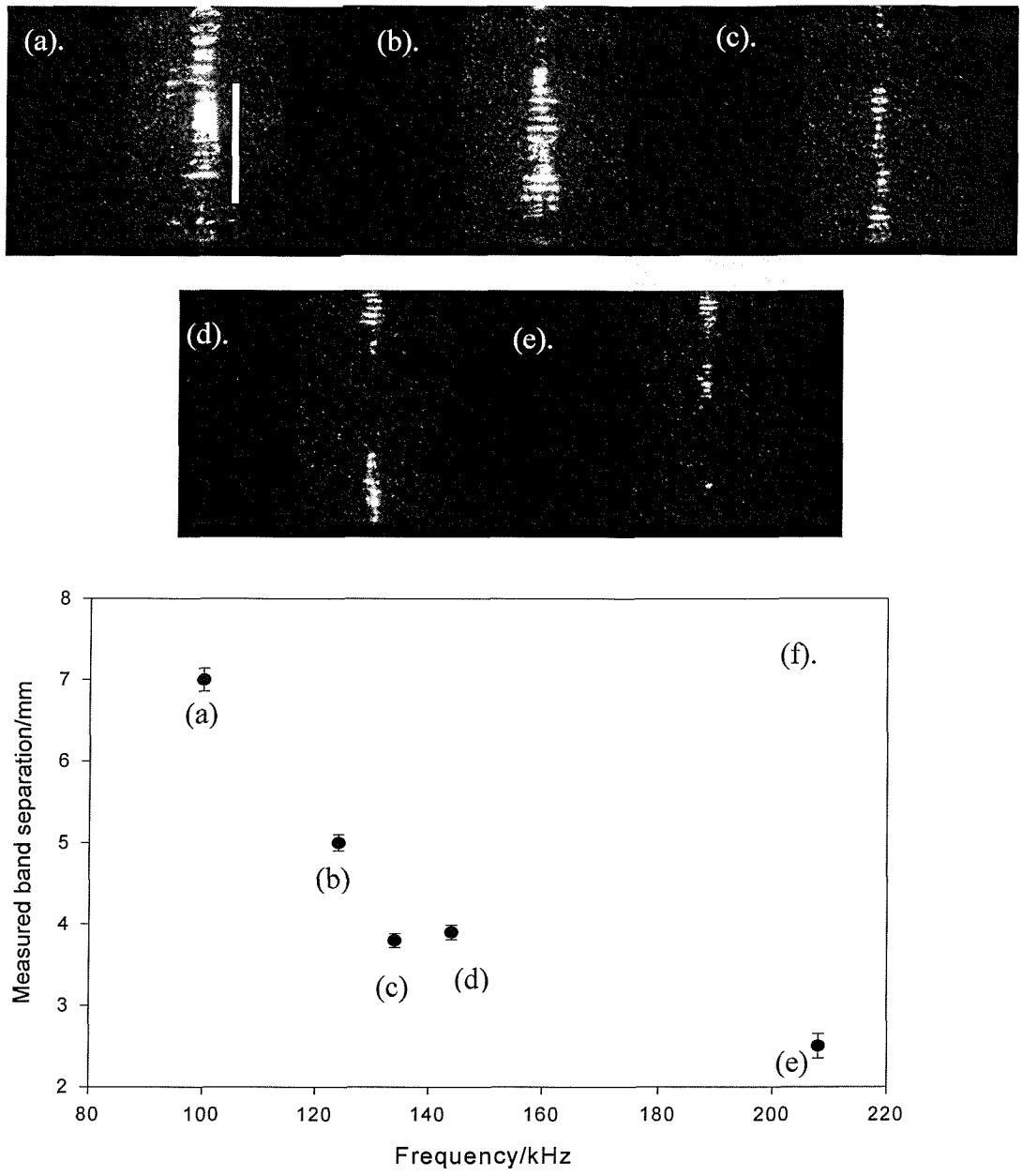

Figure 3.11 Frames showing the light emission from a cylindrical single walled cell (9.4 cm internal diameter ultrasonic reactor cell (B)) recorded from the side. In all cases the driving voltage was maintained at 90 V. The cell contained an aqueous solution identical to that reported in the legend of figure 3.5. The pictures were recorded under ambient conditions (*ca.* 20-23 °C) in aerobic media. The solution height was maintained at 14 cm. The applied frequency was 100.87 kHz for frame 'a', 125.97 kHz for frame 'b', 147.83 kHz for frame 'c', 164.04 kHz for frame 'd' and 202 kHz for frame 'e'. The scale bar in frame 'a' represents 7 cm and applies to frames 'a – e'. (f) is a plot of the band separation (data from frames 'a-e') against the frequency. Error bars represent ± one standard deviation in uncertainty in the measured band distances.

Figure 3.12 shows the effect of changing the solution height within the cell. As the solution height is progressively increased it is clear that the pattern of bands (and hence the mode structure) changes within the cell. This can be clearly seen particularly through frames b, c, and d. Frame c shows that under these conditions, even though the frequency and drive voltage remain the same, there is little or no cavitation activity. It should be noted however

that the acoustic pressure amplitude would change even though the drive voltage amplitude change remained fixed. If the solution height is reduced or increased (see frames b and d respectively) then a clear pattern re-appears. Figure 3.12 clearly shows that the dimensions of the cavity (in this case through the solution height) are important in determining the cavitation activity within the reactor. It illustrates the importance of exciting a mode in the cell at the frequency employed The frequency dependences of the equipment employed for generating and measuring sonochemical activity was discussed in depth in section 2.6. The most important factors to control are the frequency dependencies of the reaction vessel and the detector (see chapter 2, section 2.6).

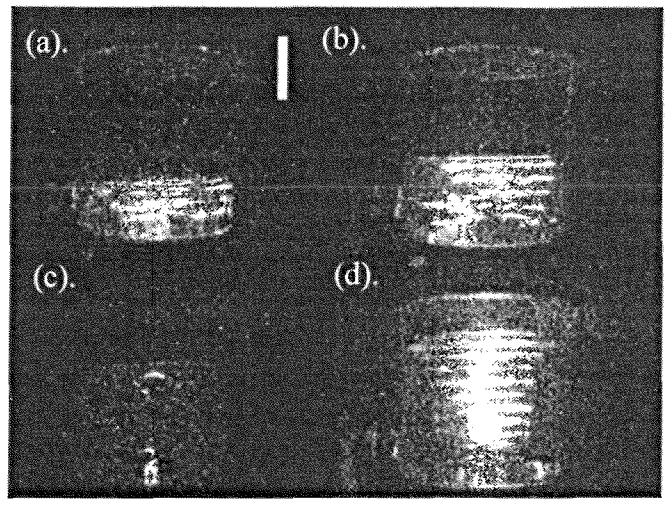

Figure 3.12 Frames showing the light emission from a cylindrical double walled cell (5.8 cm internal diameter) ultrasonic reactor (cell (A) recorded from the side. In all cases the driving voltage was maintained at 130 V. The cell contained an aqueous solution identical to that reported in the legend of figure 3.5. The cell was jacketed at 25 °C under aerobic conditions. The applied frequency was 104 kHz for all frames. In frame 'a' the solution height was 28 mm, frame 'b', 42 mm, frame 'c', 61 mm and frame 'd', 80 mm. The scale bar represents 28 mm.

3.4 Bubble Populations

The experimental results presented thus far have indicated an effective speed of sound in the cavity < 1500 ms^{-1} (a value assumed for a bubble free environment). Clearly this indicates that either the assumptions made in the model or the speed of sound is not that assumed in the calculations. In order to verify the model, it is necessary to perform experiments in the absence of cavitation. This is because the presence of bubbles within a liquid can perturb the speed of sound within the medium.[2] The effective speed of sound can

either be greater or less than the bulk value (assumed here to be 1500 m s^{-1}) depending on the size distribution and applied ultrasonic frequency. As an example Fox *et al.* [135] reported speeds of sound in the range 500-2500 m s^{-1} in bubbly liquids. Bubbles that have a resonant frequency below (e.g. having radii larger than resonance bubbles) the applied ultrasonic frequency raise the speed of sound while bubbles with a higher resonant frequency (e.g. having radii smaller than resonance bubbles) reduce the speed of sound.[2]

The model was verified by measuring a number of modes at low driving pressures. This further confirmed that there is a reduction in the effective speed of sound within the vessel in the presence of cavitation. The low driving pressure ensured that bubbles were not generated within the liquid hence enabling the bubble free sound speed to be determined. Figure 3.13 shows the response of a hydrophone measured as a function of radial position within the cell. The solid line on the figure represents the predicted pressure pattern for a $J_{1,5\,q}$ mode in this particular case (assuming a rigid wall model). It should be noted that in this experiment it is not the absolute pressure values that are important, but the position and spacing of the pressure maximums and minimums.

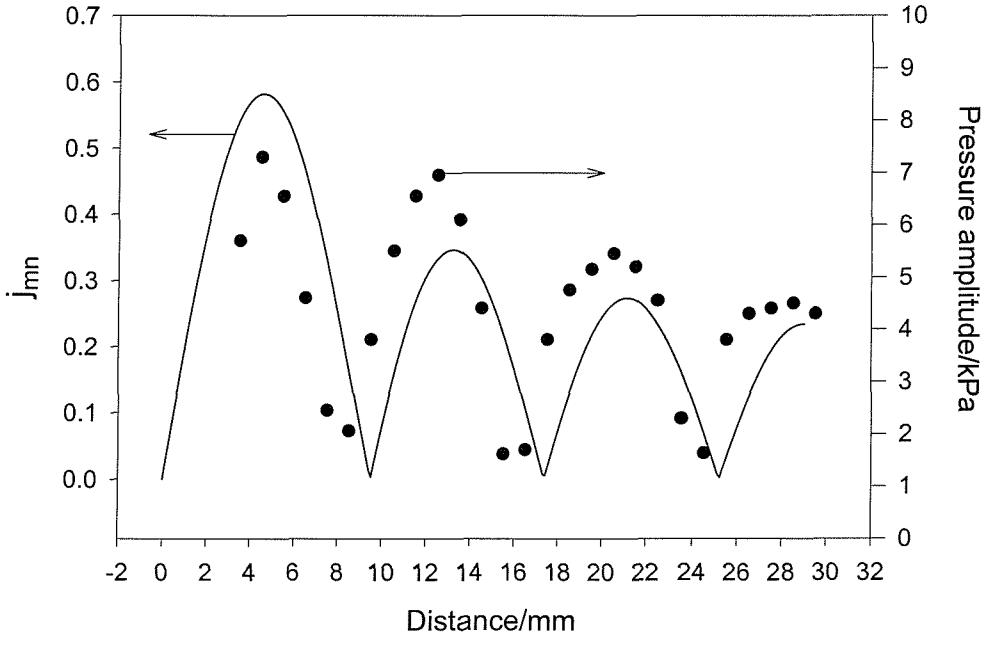

Figure 3.13 Plot showing the variation of the acoustic pressure amplitude (•) as a function of position as a hydrophone was scanned from the centre of the cell to the wall (assuming a rigid wall model). The solid line predicts the pressure profile for the $J_{1,5\,q}$ mode. A cylindrical double walled cell (cell (A) see chapter 2 figure 2.1) was employed containing 200 cm^3 50 mmol dm^{-3} Na_2SO_4. The experiment was performed under aerobic conditions at 25 °C. A sound frequency of 117.3 kHz was employed.

Experimental Frequency/kHz	104.3[b]	117.3	121.4
Mode $j_{m,n,q}$	1, 3, 4	1, 5, 5	1, 3, 8
R_1-R_2 Separation/mm Experimental	10.5 ± 1.5	7.0 ± 1.5	13.0 ± 1.5
R_1-R_2 Separation/mm Theory	11.8	7.9	11.8
Band Separation/mm Theory	11	13.5	8.7
Band Separation/mm Experimental	11.3 ± 1.5	14.0 ± 1.5	8.0 ± 1.5
Liquid height/mm	51	74	74
$f^{natural}$/kHz Theory[a]	102.8	118.6	118.3

Table 3.9 Table showing the measured mode assignment in the absence of cavitation (assuming a rigid wall model). The symbols R_1 and R_2 refer to the first and second rings in the radial direction. [a]Note a speed of sound of 1597 m s^{-1} was employed. Ultrasonic cell (A) containing a 50 mmol dm^{-3} Na_2SO_4 solution was employed at 25 °C. [b]Solution degassed and filtered through a 0.22 μm filter. The errors shown are estimated from the size of the hydrophone employed.

Table 3.9 shows a set of three frequencies with the measured spacing and predicted distances of both the ring-to-ring separation and band-to-band separation (assuming a rigid wall model). Table 3.9 shows that there is close agreement (± 1.5 mm) between the measured spacing and the model. The spacing of the bands in the *z* direction was also measured, and from these two sets of data for a particular frequency the mode assignment was determined. In order to predict the mode frequency, it is necessary to determine the speed of sound within the bubble free environment. This sound speed measurement was achieved by measuring the 'propagation delay', i.e. the time taken for an acoustic signal generated by the transducer to propagate a given distance to a hydrophone placed on-axis within the vessel. Since changes in the location of this axially-positioned hydrophone can be measured to much greater accuracy than can the absolute distance over which the acoustic signal travels (which might also incur a systematic error), the sound speed was inferred from the gradient of a plot of the arrival time of the start of the signal as the hydrophone was moved to a variety of on-axis locations.

Figure 3.14 shows the propagation delay time measured in this manner plotted as a function of distance. A pulsed signal was generated by applying a voltage step (-5 V to 5 V) to the transducer. In order to reduce complications due to the cell wall reflection, the distance between the hydrophone and cell base was always less than the distance between the cell wall and the hydrophone. The distance dependence of the propagation delay time of the hydrophone enabled the speed of sound within the media to be estimated independent of the transducer and hydrophone response times. Figure 3.14 clearly shows a linear

dependence, as expected, and also indicates that full degassing of the liquid and filtering have no significant effects on the speed of sound within the media. This technique produced a speed of sound in a bubble free environment of 1597 ± 25 m s^{-1} (95% confidence interval). This value, when used with the model presented here, enabled the mode frequency to be calculated. Table 3.9 indicates that the predicted mode frequencies and the actual mode frequencies are very similar. Clearly this demonstrates that the model presented here is accurate supporting the assumptions made about the boundary conditions within the cavity.

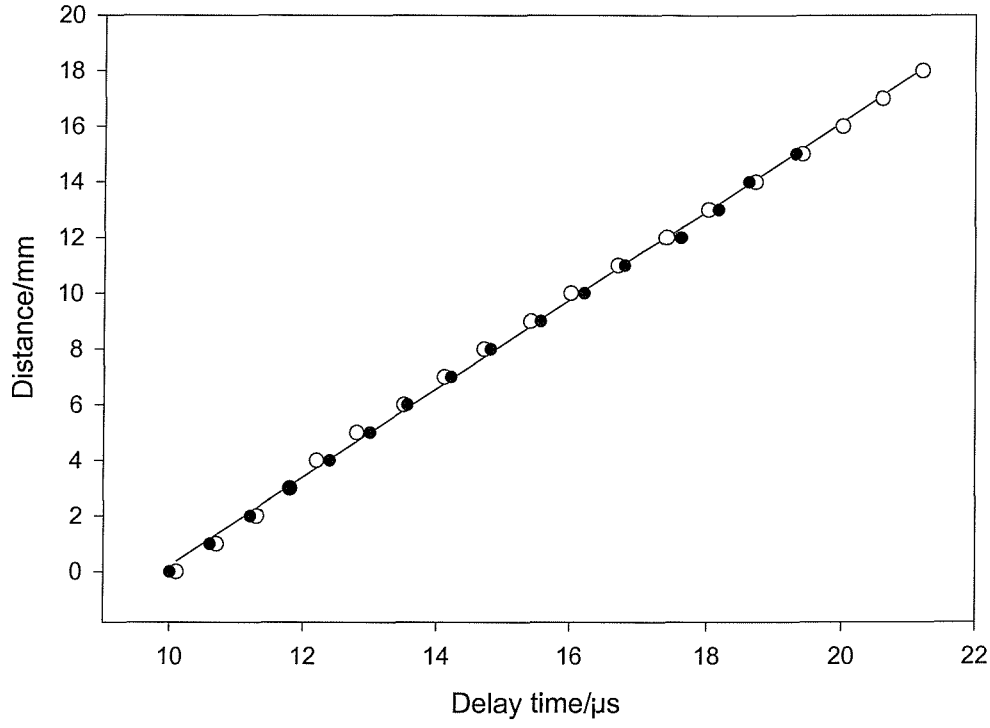

Figure 3.14 Plot showing the variation in the distance as a function of the delay time for a hydrophone placed centrally in a cylindrical cell (5.8 cm internal diameter, 8.5 cm external diameter and height 12 cm). The cell contained 100 cm^3 50 mmol dm^{-3} Na_2SO_4 at 25 °C under either aerobic (•) or degassed, 0.22 μm filtered (o) conditions. The speed of sound was 1597 ± 25 m s^{-1} (95 % confidence) for filtered and degassed data.

In the results reported (see table 3.10) it was noted that for a given frequency, the frequency predicted by the acoustic model (assuming c_o = 1500 ms^{-1}) was in excess of the applied frequency when that mode was observed. However, the speed of sound is altered by the presence of bubbles in the liquid. Therefore, as the model has been verified by mode assignment in the absence of cavitation, the discrepancy between the predicted frequency (using the acoustic model) and the applied frequency (experiment) can be accounted for by this effect. The modes determined by the photographic evidence can be combined with equations (3.17) or (3.18) (depending on the particular case) to determine the actual sound speed within the cell. As an example figure 3.5 shows a $J_{0,7,29}$ mode. Employing equation

(3.17) and a sound speed of 1500 m s^{-1} (bubble free liquid) would predict a mode frequency of 186.8 kHz. Hence, from this comparison it is possible to estimate that the speed of sound has been reduced to *ca.* 1062 m s^{-1} within the bubbly liquid within the cell. Further evidence for the effects of bubbles on the speed of sound is evident from acoustic modes analysed in the result section and illustrated in table 3.10.

Figure Number	$f_{experimental}$/ kHz	J_{mnq}	f_{theory}/ kHz	$c_{experimental}$/ m s^{-1}
3.5	132.44	0, 7, 29	186.8	1062
3.7	120.15	0, 6,13	191.39	958
3.8	121.83	4, 5,12	201.54	907
3.8	121.83	5, 5, 12	210.54	868
3.9	125.23	3, 4,15	196.14	957

Table 3.10. Table summarising the results achieved including the determined modes and the calculated speed of sound under the conditions employed (assuming a hard wall model).

In all the measurements made, it appears that the speed of sound within the cavity is significantly reduced (in the range 868-1062 m s^{-1}) when compared to bubble free media. It is possible to calculate the void fraction (*VF*), the proportion of volume present in the 'bubbly liquid' which is gas/vapour rather than liquid, within the cell from the reduction in the sound speed using a Woods-type equation (equation (3.19)):[2]

$$c_c = c_o\left\{1-\frac{1}{2}(VF)\frac{\rho c_o^{\,2}}{\kappa p_o}\right\} \qquad (3.19)$$

where c_c represents the reduced sound speed, κ the polytropic index and p_o the hydrostatic pressure. A key assumption for this to be valid would be that all the bubbles present have equilibrium sizes smaller than that which would be resonant with the sound field.[2] Whilst probably not true at all times, there is sufficient reasoning to suggest this (rather than, say, the opposite), assumption would be a reasonable starting position. This is, first, because the bubbles, which emit luminescence from the pressure antinodes, will have equilibrium sizes smaller than resonance, because of Bjerknes forces.[2] Second, whilst in a cavitating sound field bubble fragmentation and coalescence will occur, at the equilibrium size of a bubble, so

too does its tendency be removed from the population by buoyancy or fragmentation (considering only the effect of surface tension and not the amplitude of pulsation of the wall, and neglecting radiation forces). Hence, a reasonable starting position is the assumption that all the bubbles present in the vessel have equilibrium sizes that are smaller than resonance.

Employing appropriate values within equation (3.19) and sound speeds in the range of 868-1062 m s^{-1} it is possible to calculate the void fractions within the cell to be 2.91-4.24 x 10^{-5} (corresponding to 2.91-4.24 x 10^{-3} %). If we assume an average bubble radius of 10 μm then this corresponds to a bubble population of 2.02 x 10^{6} within the 200 cm^3 employed in the cell (see figure 3.9). This corresponds to an average spacing of *ca.* 460 μm between each bubble.

Given that the acoustics within the cell, and hence the particular mode, will be dependent on the bubble population through the apparent speed of sound, one can see that a mode once set up, could detune through the generation of strong cavitation changing the speed of sound and hence the mode frequency. It is interesting, however, to speculate on the possibility that a mode will self-tune. As an example if the bubble population is reduced in number because a mode detunes, then the speed of sound will change and in turn the mode frequency will change. Under the correct conditions this could re-excite the original mode, hence increasing the bubble population, and so on. In this way, a particular mode could be very stable with respect to time. This observation is noted experimentally (see figure 3.9, 3.10 etc.). Indeed the fact that a mode is stable over minutes, despite the obvious effect of cavitation on the speed of sound, suggests such a stabilising mechanism or ('bubble population feedback') must occur.

3.5 Soft Wall Model

Since the (bubble free) sound speed is now known accurately for the system, (see figure 3.14) it was possible to employ the 'soft wall' model (see section 3.1 equation (3.12)). Figure 3.15 shows the functions in equation (3.12) plotted as a function of k_r for 117 kHz (see table 3.9). The crossing points of the two functions give values of k_{rn} that are solutions of equation (3.12). Table 3.11 shows a collection of the k_{rn} values obtained using this method and their associated natural frequencies. In order to determine which value of k_{rn} is required to calculate the natural frequency of the cavity, it is illustrative to compare the pressure distance data shown in figure 3.13 with the predicted dependence from the theory. This comparison is shown in figure 3.16 for k_{r4} and k_{r5}.

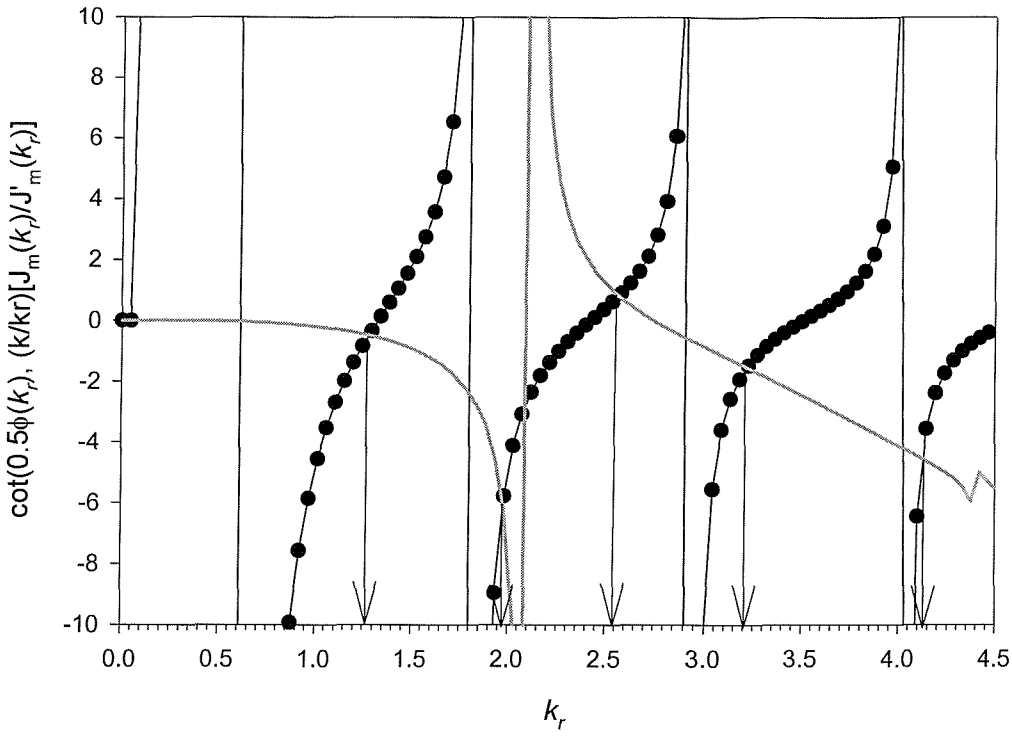

Figure 3.15 Plot showing the functions shown in equation (3.12) plotted as a function of k_r. (•) represents the term containing the Bessel functions while (—) represents the cot term. The arrows show the crossing points. This plot was constructed considering a frequency of 117 kHz and a sound speed of 1597 m s^{-1}.

Experimental Frequency/kHz	k_r value at crossing points	Natural frequency at k_r/kHz
104	k_{r1} = 1.20	76.8
	k_{r2} = 2.43	93.4
	k_{r3} = 3.24	**108.4**
117	k_{r1} = 1.25	67.3
	k_{r2} = 1.97	77.6
	k_{r3} = 2.505	97.0
	k_{r4} = 43.2	100.7
	k_{r5} = 4.25	**123.3**
121	k_{r1} = 1.30	97.5
	k_{r2} = 2.05	105.5
	k_{r3} = 2.6	113
	k_{r4} = 3.225	**123**
	k_{r5} = 4.15	139.8

Table 3.11. Table showing the correction caused by the non-zero phase angle determined from the graphical method described in figure 3.15. The numbers in bold represent the likely natural frequency of the cell.

Figure 3.16 clearly shows that the k_{r5} value is appropriate for this example. It is also interesting to compare the soft wall model described here in detail with the hard wall assumption shown in section 3.1.

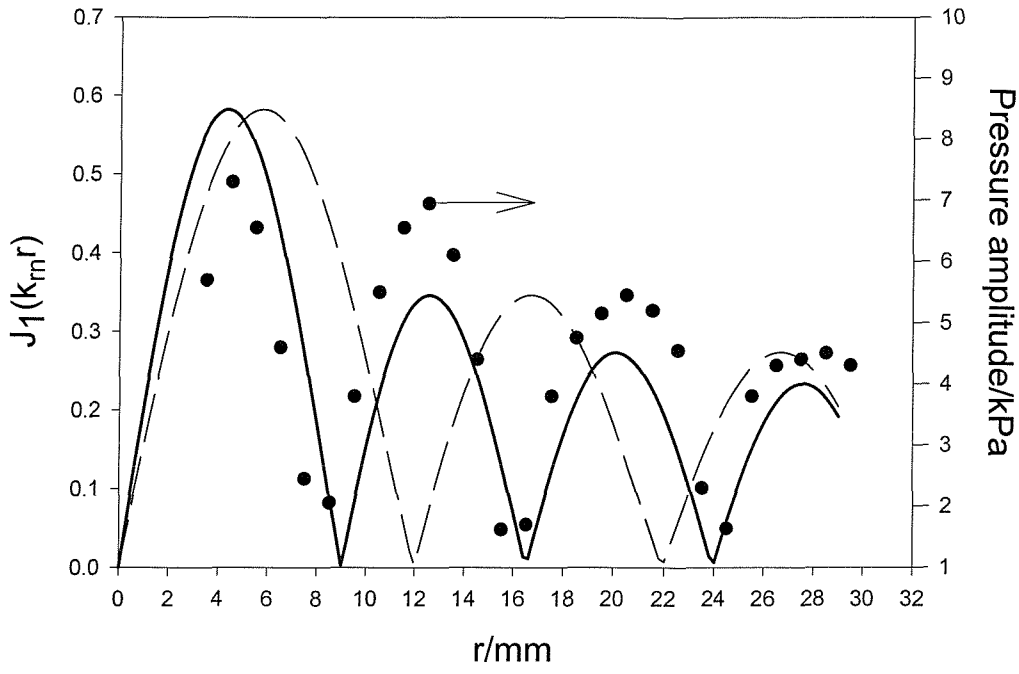

Figure 3.16. Plot showing the predicted variation of the pressure field plotted as a function of distance for k_{r4} (– – –) and k_{r5} (—). The actual measured pressure is also shown (•). The experimental conditions are reported in figure 3.13.

Figure 3.17 shows the k_{r5} function, compared with the pressure distance dependence determined from counting the rings in figure 3.13 and using the hard wall approximation. Figure 3.17 shows that the although the soft wall model (k_{r5}) is the most accurate at predicting the position of the pressure maxima and the slight down turn in the pressure amplitude at the wall (r = 2.9 cm), the hard wall model (dashed line) is still reasonably good. In turn if we consider the prediction of the natural frequencies of the modes reported in table 3.9 (hard wall) and table 3.11, it is clear that the discrepancy between the hard wall and soft-wall models in comparison with the experimental data is small. Indeed a maximum error of 5 % (difference in the experimental natural frequency and the predicted natural frequency) was found for these measurements in comparison to theory. The modification of the natural frequency of the cell is relatively small, and cannot explain the variation in the speed of sound in the cavity determined from the luminescent pictures shown in the results section. It is also important to note that the soft wall approach described here cannot be applied to the cavitation experiments (see figures 3.5, 3.7, 3.8,

and 3.9) as the model requires a prior knowledge of the speed of sound within the cell (e.g. to calculate the k value). In this instance the hard wall model has to be adopted. However, the error in this approach is small (*ca.* 5% difference in the experimental natural frequency and the predicted natural frequency) and cannot explain the difference in the sound speeds observed (up to *ca.* 46 %) in the presence of cavitation.

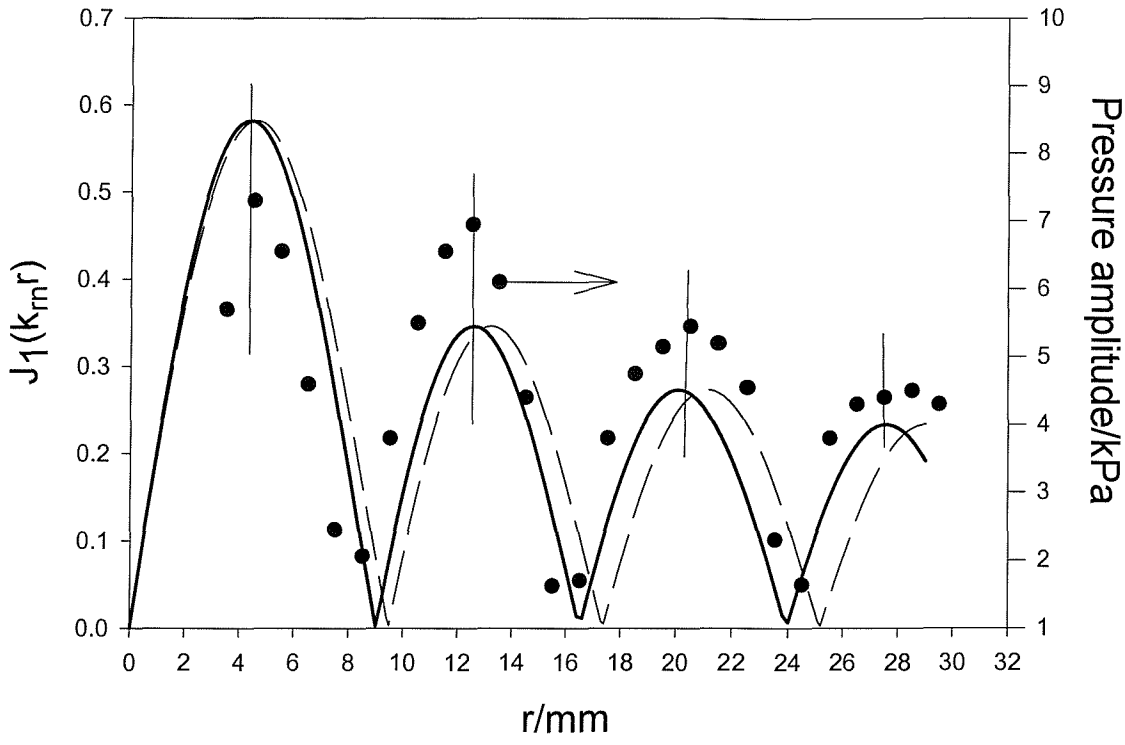

Figure 3.17 Plot showing the predicted variation of the pressure field plotted as a function of distance for the soft wall model $k_{r,5}$ (—) and the hard wall model (– – –). The actual measured pressure is also shown (•). The vertical lines are illustrative of the improved agreement between theory and experiment. The experimental conditions are reported in figure 3.13.

3.6 Consequences for Chemistry

Employing a cylindrical ultrasonic cell for sonochemical purposes requires that a number of factors be considered. These include the cell geometry, the frequency, the height of the solution, the construction of the cell walls (different boundary conditions) the bubble population and the efficiency of the transducer at the frequency employed. In general it can be seen that the light output from the cell under the conditions studied is greatest from 110-130 kHz. This can be accounted for as the modal structure is more complex at higher frequencies, and in addition it has been reported that radical production increases with frequency.[136]

The importance of exciting a mode in the cell at the frequency employed is clear when viewing the MBSCL images. This is emphasised by frame (c) in figure 3.12 where altering the height of the liquid changes the mode and has a dramatic effect on the extent of the solution, which is active (e.g. producing light, and hence with a high radical density) through the production of cavitation. If "optimum rates" under a given set of physical conditions from an ultrasonic reactor are required, the use of luminescent measurements to determine the frequency of highest light output would seem beneficial. The results shown here demonstrate that a 1 kHz frequency resolution (as illustrated in chapter 5, section 5.4) is desirable. There are a large number of frequencies where one may expect a modal wave pattern to exist. However, the efficiency of the transducer at these frequencies will also be a factor in addition to the bubble population.

Finally it is important to note the 'footprint' of the cavitation sensor employed. Even at a fixed frequency, with a given mode set up, the reading from a cavitation sensor (which may operate by detecting luminescence, erosion, sonochemistry, acoustic emission etc.) will vary with its 'footprint'. Clearly, if the sensor is sufficiently small in size, the reading will be large if it is placed in a pressure anti-node, and small in a pressure node. If its 'footprint' covers several anti-node bands, then increasing the drive frequency will mean more 'bands' of activity might be included in the sensors field of view, but each band will tend to be narrower than at lower frequency.[22]

3.7 Conclusions

In the cylindrical cell configuration, it was demonstrated that the activity of the solution was related to the modal sound field of the cavity in the frequency range studied. It is important to realise that, unless the cell is driven below the first mode or above the Schroeder frequency[134], the spatial variation in reaction (once a mode has been excited) and the frequency dependence of the yield (dictated by the frequency dependent efficiency of the ultrasonic source, the modal acoustics of the cell and possibly bubble dynamics)(see figure 3.10) will be the key factors in determining the yield in all sonochemical reactors. It is concluded that the 3 D geometry, frequency, reactor wall construction, transducer efficiency, temperature and bubble population are all-important factors in determining the effect of ultrasound on a particular system. It is anticipated that, up to the Schroeder frequency, the frequency dependence of a reactor will follow a modal structure, as shown here, which can be modelled. The comparison between the model and the experimental

results allows measurement of the reduction in sound speed within the cavity, which would be expected as the result of bubbles within the cavitating liquid. In addition if the mode is measured within a cylindrical cell (in the absence of cavitation), the model can be used to determine the bubble free speed of sound.

The modelling of the acoustics within the cylindrical chamber indicates that the inner wall can be considered as largely reflecting. However, the phase angle on reflection at the inner wall is non-zero. Nevertheless the correction to the experimental natural frequency of the cavity compared to the predicted value owing to this complication is small (*ca.* <5 %) and to a first approximation can be ignored.

In addition, small changes in the physical conditions, such as temperature, solution volume, wall materials and construction or frequency (of the order of 1-2 %) can have dramatic effects on the experimental observations and ultimately the conclusions drawn from the study.

In this chapter the ultrasonic reactor has been acoustically characterised. The acoustic analysis shows that to achieve reproducible results care has to be been taken in all cases to keep conditions constant within the reactor i.e. solution height, temperature, volume, etc if varied will cause the acoustic mode excited in the cell to change. In the next chapter, a number of novel chemical sensors for cavitation "activity", which are sensitive to radical production, are designed and tested within the "model" ultrasonic reactor, which was characterised in this chapter. Following Apfel's rules ("know when something happens") the objective of this study is to achieve reproducible chemical results in the acoustically characterised vessel.

CHAPTER 4

ELECTROCHEMICAL DETECTION OF SONOCHEMICAL RADICALS AND RADICAL PRODUCTS

As well as the physical effects of cavitation (erosion, acoustic emission, etc) it is well known that chemical reactions take place as a result of cavitation action. These chemical processes can be subdivided into a number of classes. These are as follows:

- Heterogeneous chemistry[12, 16, 17] - cavitation abrasion initiates or activates solid liquid reactions.
- Gas phase chemistry – reactions that occur in the interior of a collapsing bubble.[1, 69, 136]
- Liquid phase chemistry – reactions that occur in the liquid phase of the media under investigation.[6-14]

Of these three classes perhaps the most diverse is liquid phase chemistry. Much of this chemistry is involved with the generation of radical species produced through the pyrolysis of the solvent. However, although there is strong evidence for the production of radicals (ESR, organic destruction, trapping reactions)[81, 82] little electrochemical evidence has been reported detailing the effects of radicals on electrochemical processes.

In the context of this thesis, it would be interesting to probe radical production in the model reactor using a sensitive analytical technique. With this aim in mind, a series of novel electrochemical experiments has been designed, not only to measure radical production, but also to quantify the rate of production.

Four novel electrochemical systems for the detection of radicals and radical products produced by cavitation are presented. Three of the sensors detect evidence for hydroxyl radicals ($OH^{\bullet}$) or radical recombination products thereof, and the fourth detects evidence for hydrogen atoms ($H^{\bullet}$). Prior to this study, the majority of research on the determination of radicals or radical recombination products has been performed through the employment of methods reliant on spectrophotometry. This chapter presents the first quantitative electrochemical study of radical production (produced by ultrasonic cavitation) to the present knowledge of the author. This electrochemical technique was developed to investigate these processes for a number of reasons including the following:

- The sensitivity of spectrophotometric detection is reliant on the extinction coefficient of the target species (for example I_3^-). If the product of the particular reaction is weakly absorbing, then the sensitivity of the technique is compromised.
- The majority of absorbance measurements are recorded *ex-situ* and can take a considerable time after the acoustic experiment has been completed. Other reactions may occur in solution leading to inaccurate results. For example hydrogen peroxide can be destroyed by trace metal ions.[94]
- *In-situ* electrochemistry, although interesting, has the disadvantage that cavitation is extremely spatially and temporally variable. As a consequence careful calibration of the experiment is necessary.[66-68]

In order to circumvent these problems, an electrochemical technique involving a flow cell was employed. This allows measurements on a semi-real time scale, and avoided the problem of removing aliquots from the cell allowing absolute rates of reaction to be determined. Removing aliquots from the cell would also change the height of liquid in the cell and hence this may result in the acoustic mode shape changing (see chapter 3, figure 3.12). The technique was possible as most of the products of radical recombinations (H_2O_2) or radical traps produce electrochemically active products. Most of the detectors work by employing a redox active agent, which reacts with the radical species as they are formed in the cavitation process. The redox probe is either oxidised (in the case of $OH^\bullet$) or reduced (in the case of $H^\bullet$) by the highly oxidising or reducing radical species produced. These reactions produce new redox species, which act as a 'chemical memory' of the existence of the radical species. Lastly it is important to note that the sonochemical reaction is essentially 'frozen' once the liquid enters the flow system as the wavelength of the sound employed is large compared to the dimensions of the piping (see chapter 2 section 2.3).

Radical solution chemistry is extremely complex. In the trapping systems presented in this section, many possible processes occur in competition. The experimental results achieved were critically analysed. In addition control experiments were performed, where feasible, to compile information about the reactions taking place. Each system is now presented in turn.

4.1 The Weissler Reaction

The irradiation of a solution containing iodide ions is thought to provoke the oxidation of iodide through a cascade of reactions involving hydroxyl radicals (see chapter 1 section 1.7.3). The oxidation of iodide results in the generation of a compound (specifically I_3^-) with a redox state different to the initial radical trap (e.g. I^-). Hence, an electrode poised at an appropriate potential, will detect the production of I_3^-. This is akin to an "electrochemical fluorescence" experiment. Fluorescence is a particularly sensitive technique due to the emission process occurring at a longer λ compared to the excitation λ. Hence, low-level detection is possible as the signal is seen against a "black" background. The radical detection process is similar, as the "trapping reaction" produces the product (I_3^-) in a solution where no I_3^- was actually present. Hence, the electrochemical signal is against a "black" electrochemical signal.

To detect the I_3^- a flow cell housing a 0.5 mm Pt working electrode held at +0.2 V vs. SCE was employed. This potential corresponds to the mass transport limiting potential (MTLP) for the reduction of I_3^-. Hence, at the electrode surface the following reaction occurs:[137]

$$I_3^- + 2e \longrightarrow 3I^- \qquad [4.1]$$

This enables the determination of the time varying concentration of I_3^-. Figure 4.1 illustrates an example of the detection of I_3^- using this technique. The ultrasound was turned on at time $t = 0$ s and the current monitored as a function of time. There is an initial delay of about 30 s while the solution is pumped from the ultrasonic reactor into the flow cell. Then, there is a linear increase in negative current (cathodic current). This represents the reduction of I_3^- to I^- (see reaction [4.1]). The current time transient shown in figure 4.1 can be used to calculate the rate of I_3^- production. The slope of the linear section of the plot between the dotted lines may be used to calculate $\frac{di}{dt}$ and the rate $\frac{dc}{dt}$ may be calculated using equation (2.2) (see chapter 2 section 2.3).

In order to obtain quantifiable results it was necessary to calibrate the flow system under the conditions employed (tubing, electrode position within the flow cell etc). This calibration experiment was performed using a solution of $Ru(NH_3)_6Cl_3$ (see section 2.3, figure 2.9). The diffusion coefficient of $Ru(NH_3)_6Cl_3$ is 9×10^{-6} cm^2s^{-1}. As this diffusion coefficient is

different than the product being detected (I_3^-), it is necessary to know accurately the diffusion coefficient of I_3^-. The diffusion coefficient of I_3^- was calculated as 7.6 x 10^{-6} cm^2s^{-1} under the conditions employed in this experiment. Solutions containing various concentrations of I_2 and I^- were prepared in KCl maintaining the ionic strength of each solution constant at 0.1 mol dm^{-3}. I_2 and I^- react together to yield I_3^- (see chapter 1, section 1.7.3 reaction [1.17]). Hence, each solution contained a mixture of I_3^- and I^- in a KCl electrolyte. Cyclic voltammograms were recorded of the aerobic solutions on a 25 μm Pt working electrode. Using the steady state currents achieved the average value of D was calculated from equation (2.5) (see chapter 2 section 2.14). The value achieved agrees with the literature value which is 8 x 10^{-6} cm^2s^{-1}.[138] A value of k' of 0.85 was employed in equation (2.2) (see section 2.3) to calculate the rate (k' represents the ratio of the diffusion coefficients of the species being detected, in this case I_3^-, and the diffusion coefficient of the redox species used to calibrate the flow cell, in this case $Ru(NH_3)_6Cl_3$).

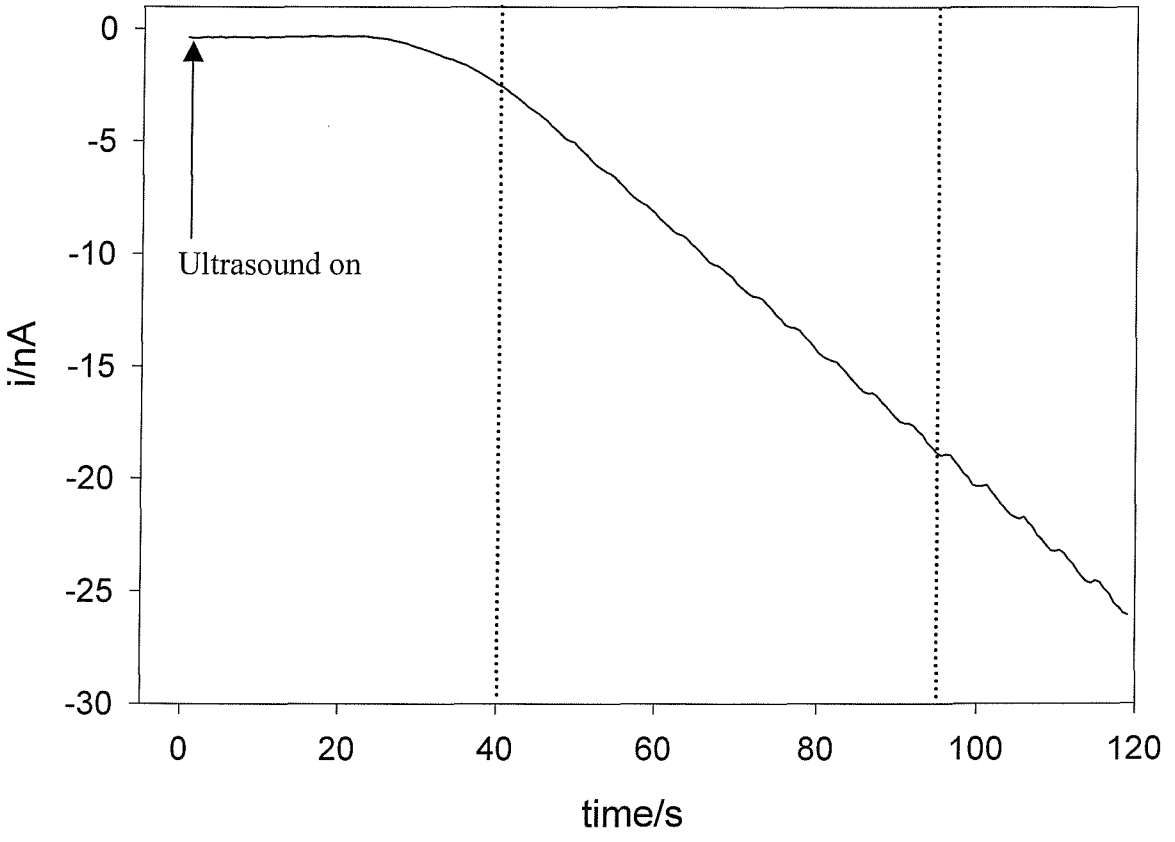

Figure 4.1 Plot showing the variation of current as a function of time for the Weissler reaction. The cell contained 100 cm^3 of aerobic 0.1 mol dm^{-3} $KI_{(aq)}$ thermostated at 25 °C. The electrode potential was held at +0.2 V vs. SCE. The irradiation of the liquid at 125 kHz was initiated at time t = 0. The segment of the graph between the two dotted lines was used to calculate the slope (di/dt), which was required to determine the rate of the reaction (see chapter 2 section 2.3 equation (2.2)).

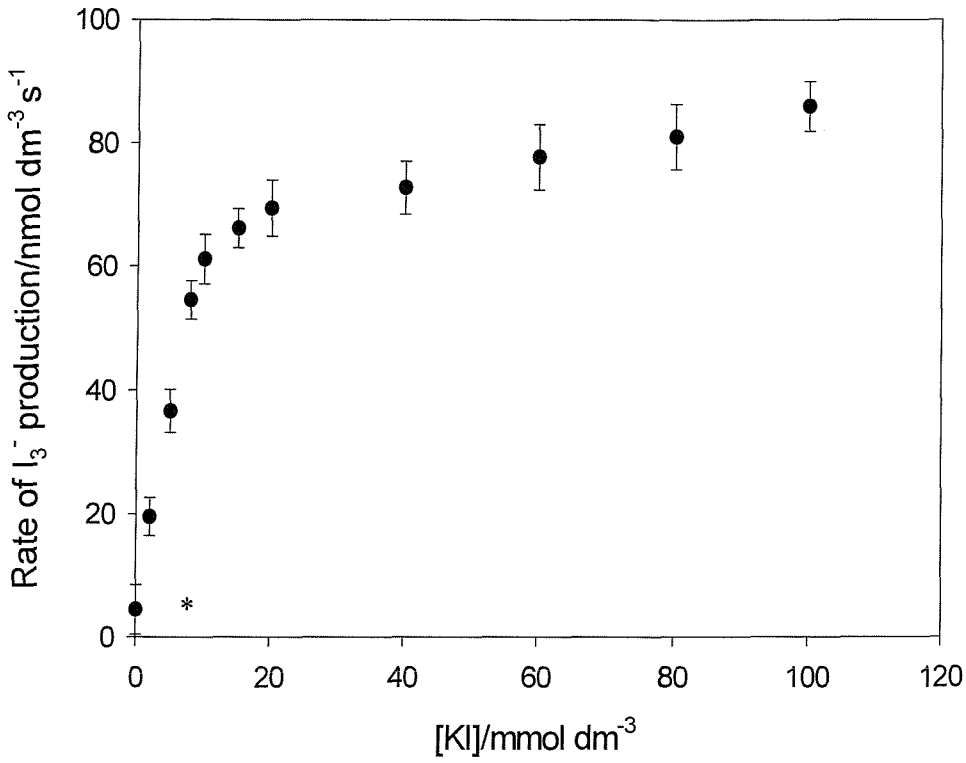

Figure 4.2 Plot showing the variation in the rate of the Weissler reaction as a function of KI concentration. The ionic strength of the aerobic solution was maintained at 100 mmol dm^{-3} by adding an appropriate amount of KCl. The ultrasonic frequency was 125 kHz and the spatial maximum acoustic pressure amplitude was 258 kPa, which corresponded to a drive voltage amplitude of 100 V. Error bars represent one standard deviation calculated using three measurements. Experiments were performed using cell (A) and the peristaltic pump operating at maximum flow rate.

Figure 4.2 shows the dependence of the rate of production of I_3^- on the KI concentration. In this experiment the ionic strength of the solution was maintained by adding potassium chloride to the solution. Maintaining the ionic strength constant was found to be necessary to achieve reproducible results. This is not surprising, owing to the tuning effect of the sound field (see chapter 3, figure 3.10). Initially the rate increases linearly with concentration up to 10 mmol dm^{-3} KI. This is interesting because it implies that the rate is a first order process with respect to [I^-]. In excess of this concentration, the rate appears to plateau with respect to [I^-]. However, it should be noted that the rate is still dependant on the KI concentration. Heinglein[76] has noted this dependence in rate on [I^-] and has proposed that this was due to competition between the I^- ion to capture $OH^\bullet$ and formation of H_2O_2 by recombination.

In addition the measurements performed in the absence of KI (100 mmol dm^{-3} KCl indicated by * in figure 4.2) demonstrated a small but significant response of the system under the conditions stated. This response of the electrode is believed to be due to the presence of Cl^- in the electrolyte solution. The production of $OH^\bullet$ radicals within a

cavitating media has been well documented.[73-76] Hydroxyl radicals are extremely powerful oxidising agents with a formal potential[94] of +2.8 V. This is in excess of the formal potential for Cl^- (+1.328 V) and it can be expected that free Cl_2 could be generated. In aqueous solution free chlorine reacts readily to form HOCl and Cl^- [139] (see reactions [4.2] -[4.5]). The HOCl species is known to be electrochemically active on platinum.[140, 141] Hence it is suspected that this signal, in the absence of I^-, represents reduction of the OCl^- produced within the electrolyte (see reaction [4.6]).

$$Cl^- + OH^\bullet \longrightarrow Cl^\bullet + OH^- \quad [4.2]$$

$$Cl^\bullet + Cl^\bullet \longrightarrow Cl_{2(aq)} \quad [4.3]$$

$$Cl_2 + H_2O \longleftrightarrow H^+ + Cl^- + HOCl \quad [4.4]$$

$$HOCl \longleftrightarrow H^+ + OCl^- \quad [4.5]$$

$$OCl^- + H^+ + 2e \longrightarrow Cl^- + OH^- \quad [4.6]$$

This assumption is further supported by two additional control experiments:

- A control experiment was performed in 100 mmol dm^{-3} potassium fluoride (KF). In this case no background signal was obtained. Hence, the effect was observed in chloride-based electrolytes only.
- Two aerobic solutions were irradiated with ultrasound of frequency 125 kHz for five minutes. Solution (a) contained 100 cm^3 of 1.5 mol dm^{-3} NaCl and solution (b) contained 100 cm^3 of 1.5 mol dm^{-3} of KF. The spatial peak acoustic pressure at the centre of the cell was 2.56 atm. A known volume was removed from each solution and treated with KI and acetic acid. This is a known test for free aqueous chlorine (reaction [4.7]).[142] The concentration of liberated iodine was determined by absorbance spectroscopy. However, H_2O_2 also liberates free iodine (reaction [4.8]).[142] This is the reason for the control (solution (b)).

$$Cl_2 + 2I^- \longrightarrow I_2 + 2Cl^- \quad [4.7]$$

$$H_2O_2 + 2H^+ + 2I^- \longrightarrow I_2 + 2H_2O \quad [4.8]$$

The concentration of H_2O_2 generated in solution (b) was 28 μmol dm^{-3}. 273 μmol dm^{-3} of I_2 was liberated from solution (a). If we assume that the concentration of H_2O_2 is the same

as that produced in solution (b), the concentration of liberated Cl_2 was 245 μmol dm^{-3}. This is good evidence for the production of free chlorine in chloride-based solutions irradiated with ultrasound.

However, the rate of reaction of I^- with $OH^\bullet$ (see chapter 1, section 1.7.3 reaction [1.14]) is known to be virtually diffusion controlled, with rate constant,[143] $k_r = 1.02 \times 10^{10}$ mol dm^3 s^{-1} at pH 7. The pH of the solutions used in this work was pH = 6.4. Previous studies have shown that the rate constant for reaction of I^- with $OH^\bullet$ is ten thousand times quicker than reaction [4.2] across a range of pH values.[144] Thus, in the presence of both I^- (a very efficient $OH^\bullet$ scavenger) and Cl^-, reaction ([1.14] see chapter 1 section 1.7.3) of $OH^\bullet$ with I^- will dominate (in the concentration range employed). The low rate constant for reaction [4.2] also explains the low value of the rate achieved for 100 mmol dm^{-3} KCl in figure 4.2.

Figure 4.3 shows the dependence of the rate of I_3^- production on the acoustic pressure amplitude recorded at the centre of the cell (see chapter 2, section 2.9 for experimental details) and the post amplification drive voltage (see section 2.6). The dotted line represents the Blake Pressure (see chapter 1 equation (1.1)). The tension in the liquid must exceed the Blake pressure to obtain explosive growth[2]. The dashed line shows the predicted acoustic pressure amplitude for the onset of inertial cavitation (ca. 150 kPa, see chapter 1 section 1.3 for details of how this calculation was performed). Figure 4.3 shows that the Weissler reaction gives a small but measurable signal down to 66 kPa, corresponding to voltage amplitude of 20 V. This may suggest that the breakdown of the solvent matrix is occurring below the threshold for inertial cavitation (i.e. stable cavitation) and that a small concentration of radicals is being produced in the hot gas. These low pressure rate measurements were performed with the continuous flow pump (pump (B)), which had the benefit of no oscillatory pressure fluctuation 'noise' (see chapter 2, section 2.3, figure 2.11). At low acoustic pressure amplitude there is little variation of the rate (<151 kPa). There is low cavitation and this results in low rates. However it is difficult to access if the acoustic pressure amplitude measurements are accurate. Due to the finite size of the hydrophone active element the spatial maximum zero-to-peak pressure amplitudes cited are likely to be under estimates because of spatial averaging (see chapter 2 section 2.9). Whether a bubble undergoes inertial cavitation depends on the acoustic pressure at the bubble (the spatial peak rather than the spatially averaged acoustic pressure). The sound field generated in the cylindrical ultrasonic reactor used for these experiments is highly modal in the frequency range employed (see chapter 3, section 3.3). Even though the acoustic pressure amplitudes

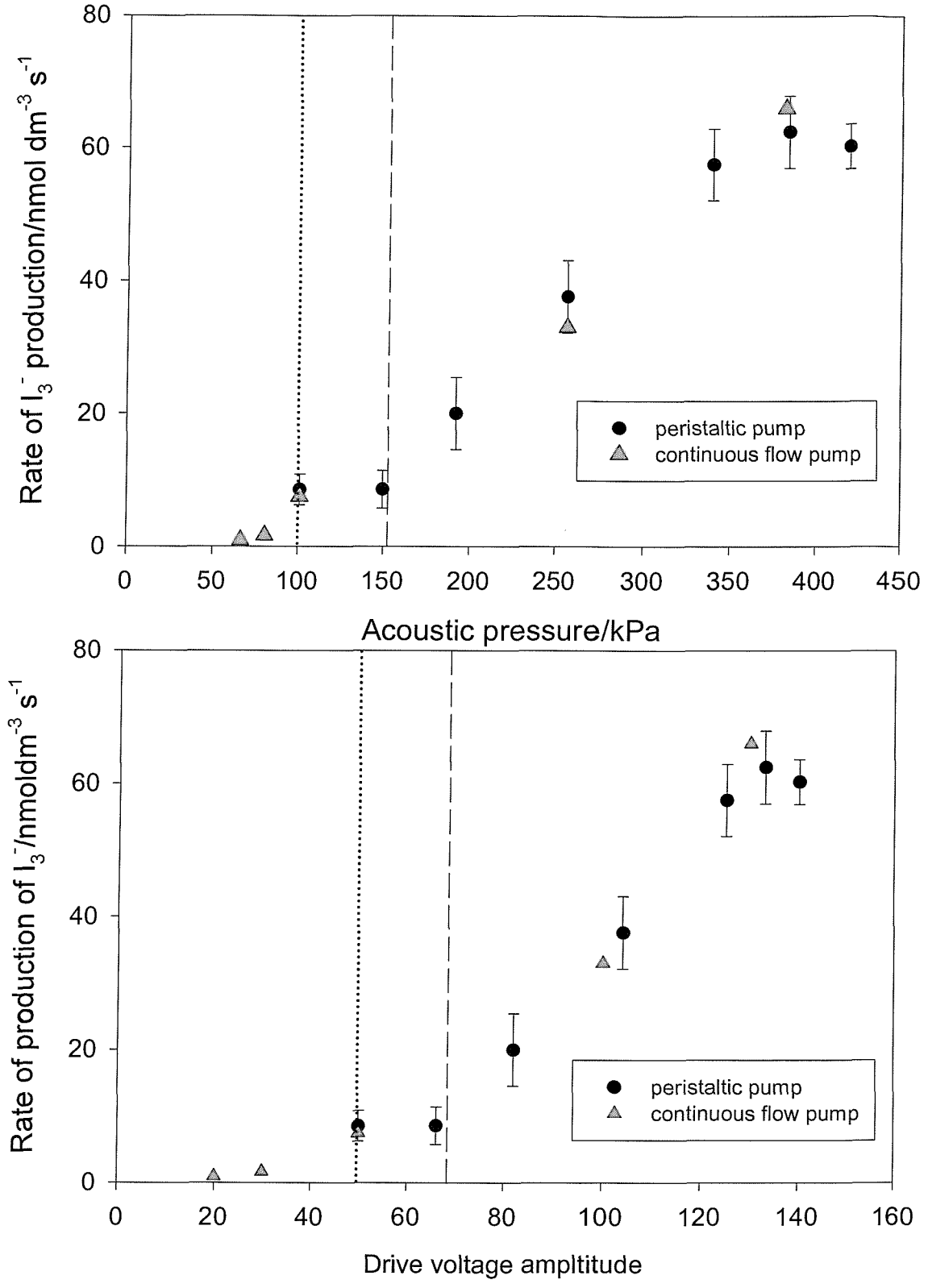

Figure 4.3 Plot showing the variation in the rate of the Weissler reaction as a function of acoustic pressure (see chapter 2 section 2.9) and drive voltage amplitude (see chapter 2 section 2.6). The aerobic irradiated solution contained 100 cm^3 of 10 mmol dm^{-3} KI and 90 mmol dm^{-3} KCl thermostated at 25 °C. The ultrasonic frequency was 125 kHz. Error bars represent one standard deviation calculated using three separate measurements. The majority of measurements were made with the peristaltic pump (•). However some measurements at lower acoustic pressure amplitude were recorded using the continuous flow pump. The dotted line represents the Blake pressure calculated using equation (1.1). The dashed line represents the predicted acoustic pressure for the onset of inertial cavitation (see chapter 1, section 1.3).

quoted represent the maximum pressure measured using the hydrophone, it is possible that the hydrophone is spatially averaging which would result in lower pressure readings. To solve this problem a needle hydrophone calibrated in the frequency range employed would be required. Unfortunately it was not possible to procure such a device during the course of this research. In addition these hydrophones are normally expensive and too fragile for a cavitation environment.

In excess of the threshold for stable cavitation, the rate of the Weissler reaction increases linearly with acoustic pressure amplitude up to 400 kPa, where it begins to plateau with respect to the error. This is understandable because as the acoustic pressure amplitude increases the level of cavitation 'activity' also increases in tandem. Several authors have observed a plateau in the rate of radical trap reactions as a function of drive voltage.[88] The reason for the presence of the plateau region at high acoustic pressures is unclear. One possible explanation could be that, at high pressures, the high bubble population shields large volumes of the solution from the true acoustic field.[22] This would cause a saturation mechanism to be triggered. This plateau effect is also indicated by measurements of sonoluminescence, as the light decreases at high acoustic pressure (see chapter 5 section 5.2). The rate as a function of drive voltage for the Weissler reaction is also illustrated in figure 4.3. Plotting the rate as a function of (acoustic pressure amplitude) rather than drive voltage means the experimental conditions can be replicated more easily. Therefore (with the exception of COMORAC see chapter 6) this is the only drive voltage plot presented in this thesis.

In order to verify that the rate of I_3^- determined electrochemically was accurate, a measurement of final iodide concentration was determined spectrophotometrically. The results are illustrated in figure 4.4. The Weissler reaction was conducted in the apparatus described previously (see experimental section 2.3, figure 2.8) and the current time transient recorded. An aliquot from the ultrasonic reactor was then removed and the concentration of I_3^- was determined spectrometrically at 350 nm (ε_{350} = 26500 mol^{-1} dm^{+3} cm^{-1})[91] using a UV-Vis spectrometer (see insert in figure 4.4). The concentration of I_3^- predicted by the spectrophotometric method was 8.73 x 10^{-9} mol cm^{-3}. The current expected for this quantity of I_3^- can be calculated as –4.412 x 10^{-8} A. The actual current change (Δi) was –4.389 x 10^{-8} A. This experiment shows an excellent agreement between the electrochemical detection of I_3^- and the spectrophotometric method (0.5 % difference).

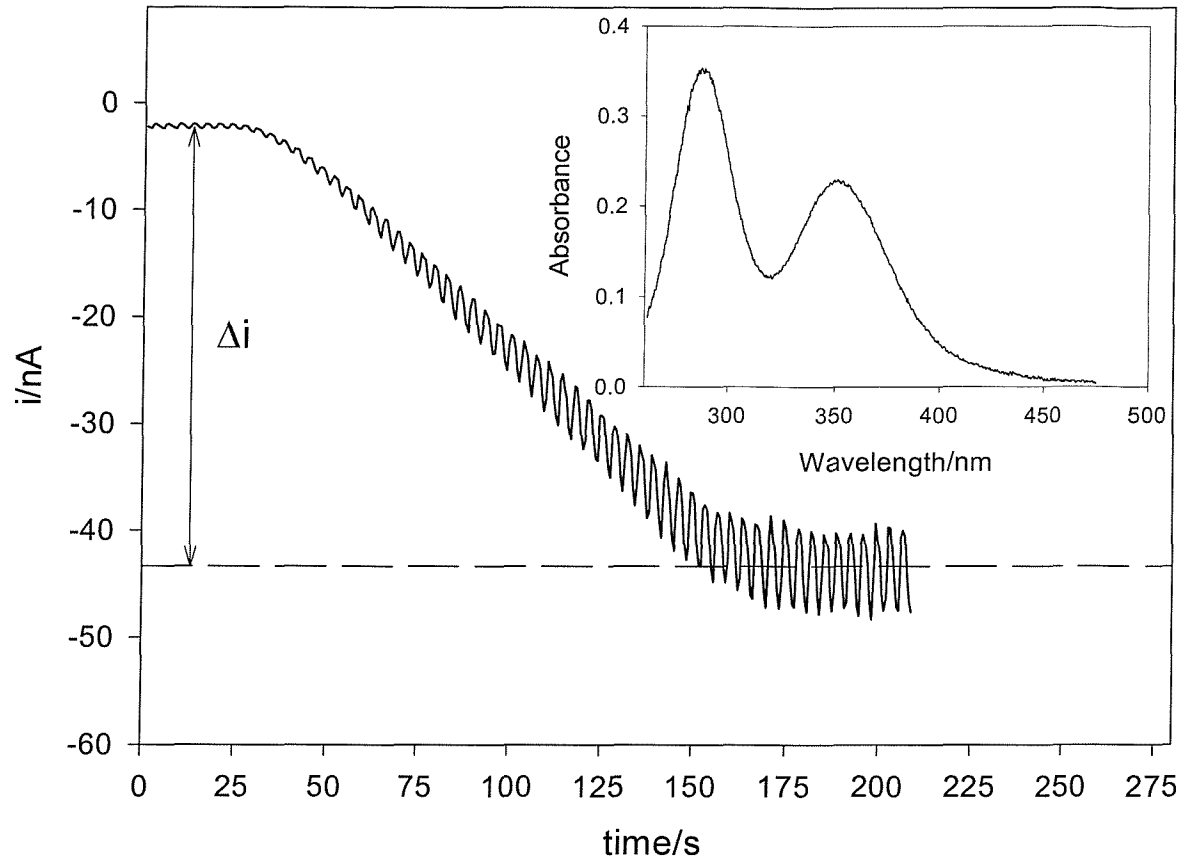

Figure 4.4 Plot showing a comparison between the electrochemical technique and spectrophotometry. The aerobic irradiated solution contained 10 mmol dm^{-3} KI and 90 mmol dm^{-3} KCl. The frequency was maintained at 125 kHz. The acoustic pressure amplitude recorded in the centre of the cell was 259 kPa. The ultrasound was turned on at time $t = 0$ s. The electrochemical experiment was performed using the peristaltic pump operating at maximum flow rate using ultrasonic reactor cell (A). The insert shows the absorbance of the solution after the irradiation of the liquid with ultrasound had been terminated. The background was the pre-irradiated solution.

It is also interesting to note, that because of subsequent reactions in the Weissler system, it is theoretically possible that the follow up reactions (see chapter 1 section 1.7.3 reactions [1.15]-[1.17]) may not be complete before the solution reaches the flow cell. Note that reaction [1.14] is known to be virtually diffusion controlled, (the rate constant = 1.1 x 10^{10} mol^{-1} dm^{-3} s^{-1}).[143] However, in the experiments performed, no evidence of this follow-up effect was observed. If one expects that this is indeed the case, then on termination of ultrasonic irradiation of the solution a slow relaxation transient to a steady state would be observed. However, the current time behaviour indicates a sharp 'off' response (see figure 4.4). This implies that the following reactions are complete before the solution reaches the flow cell. Hence, the quantity of I_3^- measured is expected to be the total yield of reaction [1.14] considering the equilibria in the scheme shown (see chapter 1 section 1.7.3 reactions

[1.14]-[1.17]). In addition the spectroscopy backs this assumption up, as this measurement is recorded minutes after the electrochemistry was completed.

4.2 Limits of Electrochemical Detection

The electrochemical radical trap detection system described in section 4.1 is not sensitive to the extinction coefficient (ε_λ), compared to radical trap sensors analysed using spectrophotometric techniques. With absorbance spectroscopy, the detection limit of this technique is governed by the extinction coefficient of the target analyte. Considering the latter it was considered important to determine the limits of detection of the electrochemical system. To achieve this objective, a set of control experiments were performed to illustrate that the electrochemical flow system employed in the radical trap measurements was able to detect the low levels of target analytes reported in figure 4.3. Two solutions of I_3^- in 10 mmol dm^{-3} KI and 90 mmol dm^{-3} KCl were prepared. Solution (A) contained 100 μmol dm^{-3} I_3^- and solution (B) contained 0.1 μmol dm^{-3} I_3^-. The flow cell was primed with a solution containing 10 mmol dm^{-3} KI and 90 mmol dm^{-3} KCl. Solution (A) was placed within a temperature controlled cell and the continuous flow pump (B) was turned on at time t = 10 s (see figure 4.5). The current proceeds cathodically corresponding to the reduction of I_3^-. After time t = 25 s a steady state current was observed. The experiment was repeated for solution (B). The current time response for this solution is plotted as an insert in figure 4.5. The reason for the sloped nature of the current time signal is discussed in the experimental section (see chapter 2 section 2.3).

Equation (4.1) is employed to calculate the predicted current for solutions A and B respectively (k_m = 0.018 cm^2 s^{-1}, k' = 0.85).

$$i = n_e F A k' k_m c \qquad (4.1)$$

For solution (A), Δi_{1cal} = 5.8 x 10^{-7} A and Δi_{1exp} = 5.85 x 10^{-7} A. For solution (B), Δi_{2cal} = 5.8 x 10^{-10} A and Δi_{2exp} = 5.83 x 10^{-10}A. In both cases there is excellent agreement between the predicted and experimental current. The predicted steady state current for the injected concentration of I_3^- agrees within 1% of the calculated values taking into account the background current in both cases. At this stage it is appropriate to refer back to figure 4.3. At low acoustic pressure amplitude (or drive voltage) the lowest measured chemical rate is ca. 1 nmol dm^{-3} s^{-1} Solutions are irradiated for 100 s so the final concentration of I_3^- is

equivalent to 0.1 μmol dm^{-3}. This demonstrates that the electrochemical flow system is indeed accurate at these low levels of target analytes. Owing to the low background currents achieved at +0.2 V versus SCE (MTLP for I_3^-) on platinum, the electrochemical Weissler reaction is particularly useful for detecting low levels of I_3^-, as the system is detecting against a "black" background. For this reason the Weissler reaction was chosen for the analysis of radical formation from SBSL (see chapter 7).

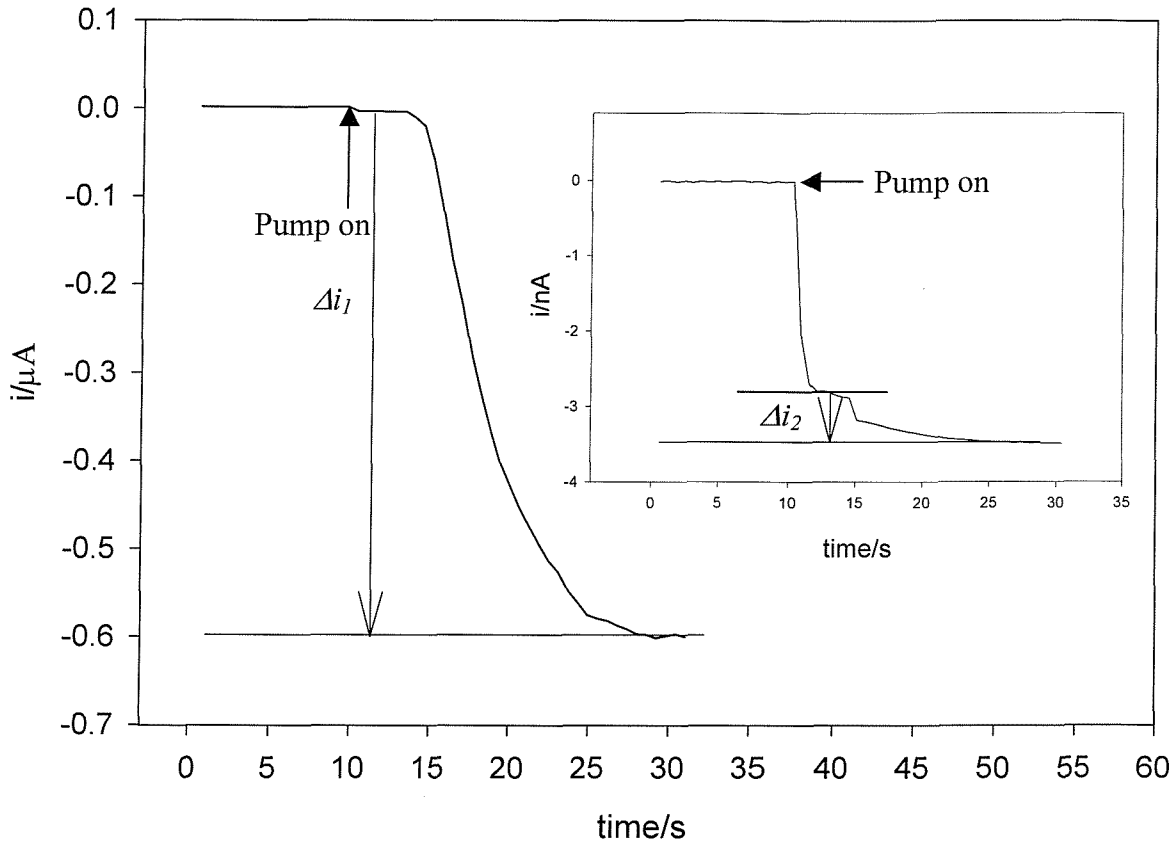

Figure 4.5 Calibration of the electrochemical flow cell using known concentrations of I_3^-. The flow cell was primed with a solution containing 10 mmol dm^{-3} KI and 90 mmol dm^{-3} KCl. The continuous flow pump was turned on at time t = 10 s. Solution (A) plotted in the main graph contained 100 μmol dm^{-3} I_3^- in 10 mmol dm^{-3} KI and 90 mmol dm^{-3} KCl. Solution (B) plotted as an insert contained 100 nmol dm^{-3} I_3^- in 10 mmol dm^{-3} KI and 90 mmol dm^{-3} KCl. Both solutions were temperature controlled at 25 °C.

4.3 The Fricke Dosimeter

Hydroxyl radicals produced by cavitation oxidise Fe^{2+} to Fe^{3+} through a number of reactions (see chapter 1, section 1.7.1). The concentration of the generated Fe^{3+} can be determined using UV absorption spectroscopy. While this provides a useful and accurate dosimeter for radiation, several problems are encountered when the same system is adapted for cavitation. Firstly, the extinction coefficient of Fe^{3+} the product of the reaction is relatively low ($\varepsilon_{224\ nm} = 4565\ mol^{-1}\ dm^{+3}\ cm^{-1}$, $\varepsilon_{304\ nm} = 2197\ mol^{-1}\ dm^{+3}\ cm^{-1}$ at 25 °C[83]) and so relatively large doses of radiation (ca. 100 rads[83]) are required to generate a detectable signal. Considering that the amount of Fe^{3+} generated (or equivalent dose) due to cavitation is relatively low (see figure 4.9), this poses a considerable disadvantage when considering low levels of cavitation particularly around the cavitation threshold. Secondly it is desirable to make *in- situ* measurements to enhance both accuracy and speed of measurement.

An electrochemical version of the Fricke reaction is presented here for the determination of radicals produced from ultrasonic cavitation. It is possible to determine the concentration of Fe^{3+}, as a function of time, using an electrochemical flow cell. It is important to point out that, for each hydroxyl radical generated under aerobic conditions, it is theoretically possible to form two molecules of Fe^{3+} (see chapter 1, section 1.7.1).[83]

$$Fe^{+3} + 1e \longrightarrow Fe^{2+} \qquad [4.9]$$

In the flow cell the reduction of Fe^{3+} to Fe^{2+} is monitored as a function of time (reaction [4.9]). In this case the working electrode was a 3 mm diameter glassy carbon disk. This was employed as the reaction proved more reproducible on glassy carbon than platinum (as the MTLP for Fe^{3+} was –0.4 V, hence considering the pH, H^+ reduction on platinum occurs).

Figure 4.6 is illustrating cyclic voltammograms of a Fe^{3+} solution recorded under forced convection conditions. The experiment was performed under both aerobic and degassed conditions within the flow cell. The CV's overlap illustrating that there is no oxygen interference for the Fe^{3+} reduction on glassy carbon. Figure 4.6 was also used to calibrate the flow cell (see chapter 2 section 2.3 equation (2.2), $k' = 1$). MTL detection of Fe^{3+} was performed at -0.45 V versus. SCE.

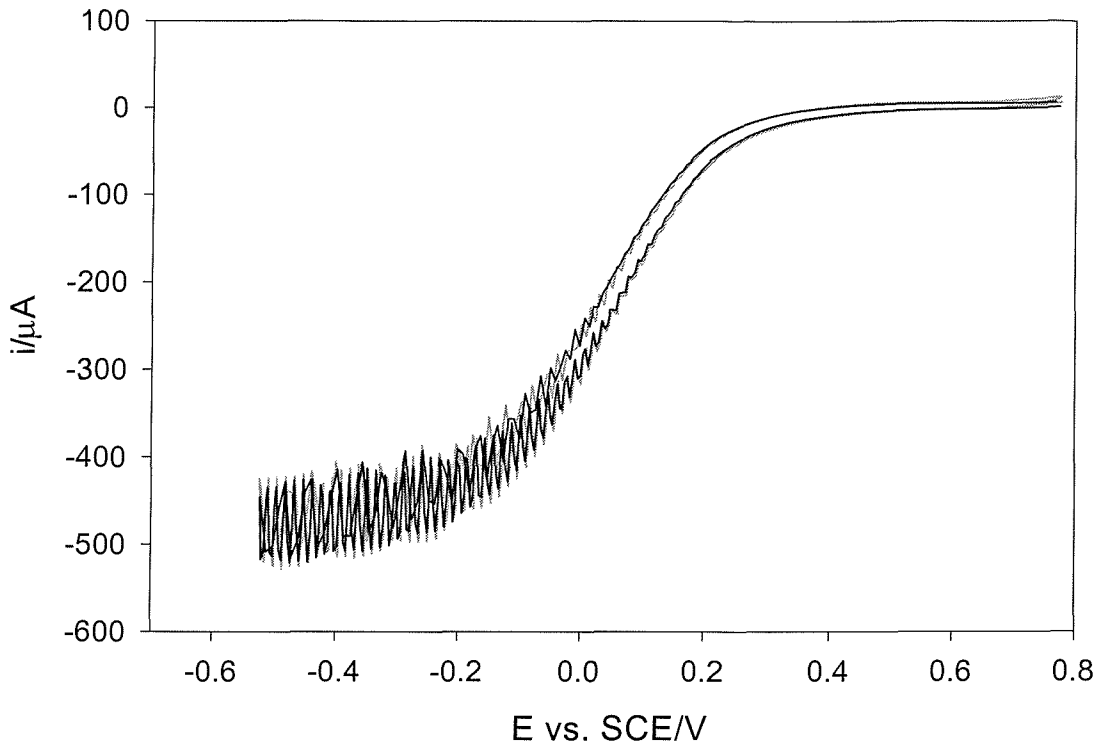

Figure 4.6 Cyclic Voltammograms of 10 mmol dm^{-3} $FeCl_3$ in 100 mmol dm^{-3} KCl at 20 mVs^{-1} in both anaerobic (---) and aerobic (—) conditions on a 3 mm diameter glassy carbon electrode recorded versus SCE. The solution was pumped from cell (A) to the electrochemical flow cell using the peristaltic pump operating at maximum speed. The solution was temperature controlled at 25 °C.

Figure 4.7 shows a typical current time transient for the ultrasonic Fricke reaction with electrochemical detection. The irradiation of the solution commenced at time t = 0. The solution was pumped continuously to and from the ultrasonic reactor and flow cell. There was an initial time delay (t = 20-30 s) before the cathodic current increased. This was the time required for the irradiated solution to reach the flow cell through the tubing. The increase in cathodic current was due to the reduction of ultrasonically generated Fe^{3+} (see reaction [4.9]). The ultrasound was turned off at t = 130 s. The current then reached a plateau (t = 150-180 s). The solution was irradiated again at 180 s and the process repeated. The linear cathodic increases in current are nearly parallel yielding similar values for their slopes and hence the rate of Fe^{3+} production.

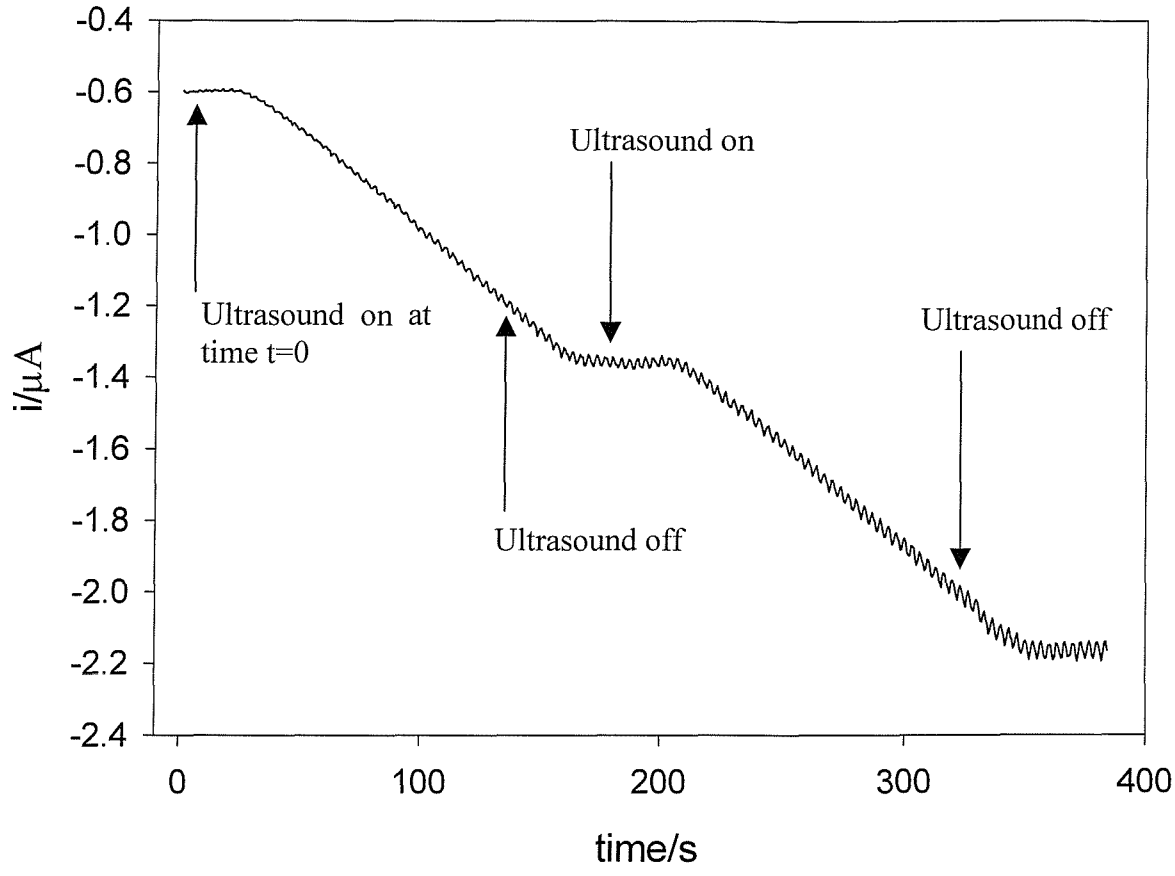

Figure 4.7 Example responses for the Fricke reaction performed using cell (A) and the peristaltic pump operating at maximum flow rate. The plot shows the variation of current as a function of time. The aerobic solution contains 1 mmol dm^{-3} $FeSO_47H_2O$, 99 mmol dm^{-3} K_2SO_4 and 1 mmol dm^{-3} NaCl in 0.4 mol dm^{-3} H_2SO_4. The potential was held at - 0.45 V vs. SCE. The frequency was 125 kHz and the maximum acoustic pressure amplitude was 220 kPa. The temperature was maintained at 25°C.

Figure 4.8 shows how the rate of production of Fe^{3+} varies as a function of Fe^{2+} concentration. The rate increases linearly up to 1 mmol dm^{-3} before levelling out and become independent of Fe^{2+} concentration. This result agrees with the results observed by other authors using different analytical techniques for the detection of Fe^{3+} formed during the Fricke reaction.[83, 87, 88]

It is interesting to note that if the maximum rates of product production are considered (see figure 4.8 and figure 4.2) then it is possible that the overall rate of $OH^{\bullet}$ production in the two systems are the same (considering the respective reaction stoichiometry see section 1.7.1 and 1.7.3). Finally it should also be noted that it is possible for $H^{\bullet}$ in the presence of H^{+} to react with Fe^{2+} to yield Fe^{3+} (see chapter 1, section 1.7.1). However $H^{\bullet}$ may also react with Fe^{3+} to regenerate Fe^{2+}.

In summary figures 4.6 - 4.8 illustrate that the electrochemical Fricke reaction works reproducibly in a cavitation environment. In addition, the results achieved agree with both sonochemistry and radiation experiments. The advantage of the Fricke reaction is that it can be used to estimate the equivalent dose of radiation exposed to the test solution. This is discussed in section 4.4.

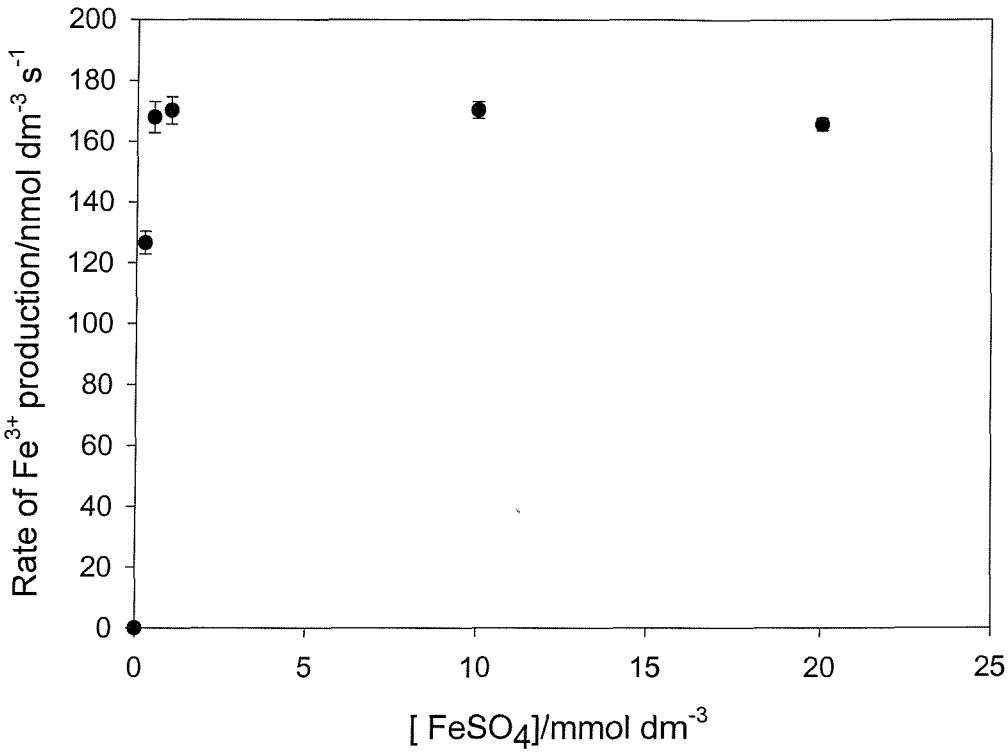

Figure 4.8 Plot showing the effect of concentration on the rate of the Fricke reaction. Experiments were performed in ultrasonic reactor cell (A) with the peristaltic pump operating at maximum flow rate. The irradiated solution contained 1 mmol dm^{-3} $FeSO_47H_2O$, and 1 mmol dm^{-3} NaCl in 0.4 mol dm^{-3} H_2SO_4 and x mol dm^{-3} K_2SO_4. The sum of the $FeSO_47H_2O$ and K_2SO_4 was 0.1 mol dm^{-3} in each case. The frequency was 125 kHz and the maximum acoustic pressure amplitude was 278 kPa. The solution was temperature controlled at 25 °C. Error bars represent one standard deviation calculated using three measurements.

4.4 Equivalent Dose Measurements

The primary use of the Fricke reaction is for the measurement of an equivalent dose of radiation exposed to the solution. This has been discussed in detail including details of how these values were calculated in (chapter 1, section 1.7.1 equation (1.13)).

Figure 4.9 illustrates the acoustic pressure amplitude dependence of the Fricke reaction as a function of the rate of Fe^{3+} production (left axis) and equivalent dose measurements (right axis). Figure 4.9 shows that the dependence of the rate of Fe^{3+} production on the acoustic pressure amplitude is similar to the acoustic pressure amplitude dependence of the

Weissler reaction (see figure 4.3). At low acoustic pressure amplitudes the amount of cavitation is low, and hence there is little variation in the rate or the equivalent dose. Below 80 kPa it appears to be impossible to detect sonochemical products. However, this is below the Blake threshold pressure (....). The calculated threshold pressure for the onset of inertial cavitation (see chapter 1, section 1.3) is indicated in figure 4.9 by the dashed line (---). Like figure 4.3, (the acoustic pressure amplitude dependence of the Weissler reaction) the Fricke reaction has a measurable rate below the transient cavitation threshold (see figure 4.9). As discussed for the Weissler reaction care is required in interpreting this result and further experiments are required. As the acoustic pressure amplitude is increased above the inertial cavitation threshold, the amount of cavitation increases which leads to higher rates and therefore higher equivalent doses. The rate of Fe^{3+} generation plateaus off at high acoustic pressure, which is again similar to the findings shown in figure 4.3 for the Weissler reaction.

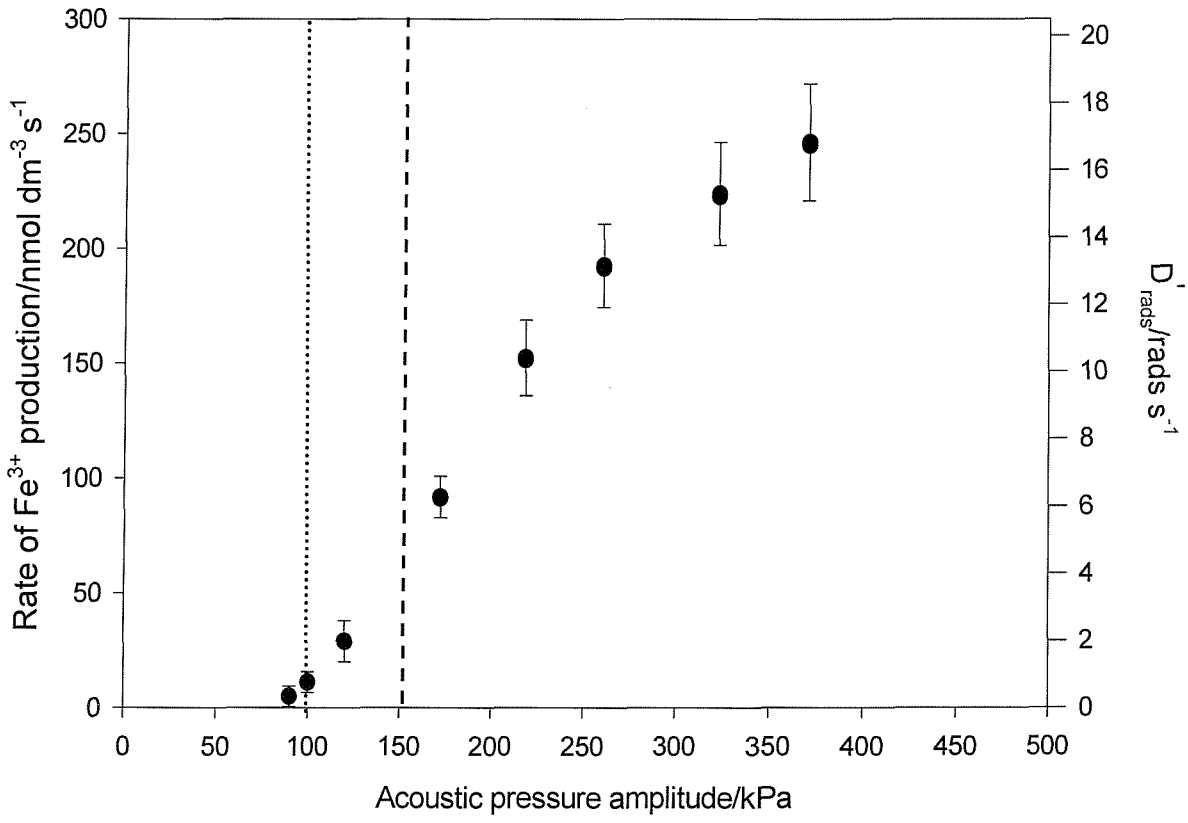

Figure 4.9 Plot showing the acoustic pressure dependence of the Fricke reaction as a function of the rate and the equivalent dose. Experiments were performed in ultrasonic reactor cell (A) using the peristaltic pump operating at maximum flow rate. The irradiated solution contained 1 mmol dm^{-3} $FeSO_47H_2O$, and 1 mmol dm^{-3} NaCl in 0.4 mol dm^{-3} H_2SO_4. The ultrasonic frequency was 125 kHz and the solution was temperature controlled at 25 °C. The acoustic pressure amplitude measurements in this case were performed using a solution containing 0.4 mol dm^{-3} Na_2SO_4, 1 mmol dm^{-3} $FeSO_47H_2O$, and 1 mmol dm^{-3} NaCl. The reason for this is explained in the text. The dotted line represents the Blake pressure. The dashed line represents the predicted acoustic pressure for the onset of inertial cavitation (see chapter 1, section 1.3).

In addition, it must be noted that the acoustic pressure amplitude measurements recorded for the Fricke reaction were performed in 0.4 mol dm^{-3} Na_2SO_4 instead of 0.4 mol dm^{-3} H_2SO_4. The reason for this is that the strong acidic conditions were believed to be detrimental to the hydrophone. However, the density of the solution employed was identical ($1.1 \times 10^3 \pm 0.02 \times 10^3$ kg m^{-3}) as the density of the H_2SO_4 solution.

It is important to note the sensitivity of the electrochemical detection technique presented here. It can measure doses as low as low as 1 rad s^{-1} which is orders of magnitude lower than any other technique that appears in the literature.[87, 92] This is because irradiation levels of this magnitude are usually difficult to measure using chemical dosimeters analysed using spectrophotometric techniques.[80, 86] The change in absorbance at this level of absorbed dose is relatively small. As an example, for the Fricke reaction it is expected that 0.28 rads of radiation should produce a concentration of Fe^{3+} of the order of 4.98×10^{-9} mol dm^{-3} (see chapter 1, section 1.7.1 equation (1.13)). This corresponds to a absorbance change of 1.09×10^{-5} (assuming a 1 cm pathlength and $\varepsilon_{304nm} = 2196$ M^{-1} cm^{-1}).[83] This level of sensitivity is difficult to achieve. However, the electrochemical system presented here is able to detect this level of absorbed dose, and perhaps could be extended to lower levels using more sensitive electrochemical technology (for example hydrodynamic voltammetry).[145, 146]

As a final test to ensure that the reaction rates determined in figure 4.9 for the Fricke reaction were indeed accurate a further control experiment was performed. The Fricke reaction was performed as described previously. Cell (A) was filled with 100 cm^3 of 1 mmol dm^{-3} $FeSO_47H_2O$ and 1 mmol dm^{-3} NaCl in 0.4 M H_2SO_4. The ultrasound was turned on at time $t = 0$ s and was switched off at time $t = 100$ s (see figure 4.10). The rate of production of Fe^{3+} was then calculated as 217 nmol dm^{-3} s^{-1} using the slope of the linear segment of the current against time trace. Since the solution was irradiated with ultrasound for 120 s in total the final concentration of Fe^{3+} was 26 μmol dm^{-3}. A solution containing Fe^{3+} corresponding to this concentration was prepared in 1 mmol dm^{-3} NaCl in 0.4 mmol dm^{-3} s^{-1} H_2SO_4 and placed in the reaction cell (A). The flow cell and tubing were filled with a solution containing only 1 mmol dm^{-3} NaCl in 0.4 mmol dm^{-3} s^{-1} H_2SO_4. The pump was turned on at time $t = 0$ s and the current time trace was recorded. This is shown as an insert in figure 4.10. It can be seen from figure 4.10 that within the constraints of experimental error there is excellent agreement between Δi_1 and Δi_2. $\Delta i_1 = 0.99 \times 10^{-6}$ A and $\Delta i_2 = 0.96 \times 10^{-6}$ A. The

percentage error in the measurement was 3%, which is good considering that the Fe^{3+} employed was 99% pure.[§]

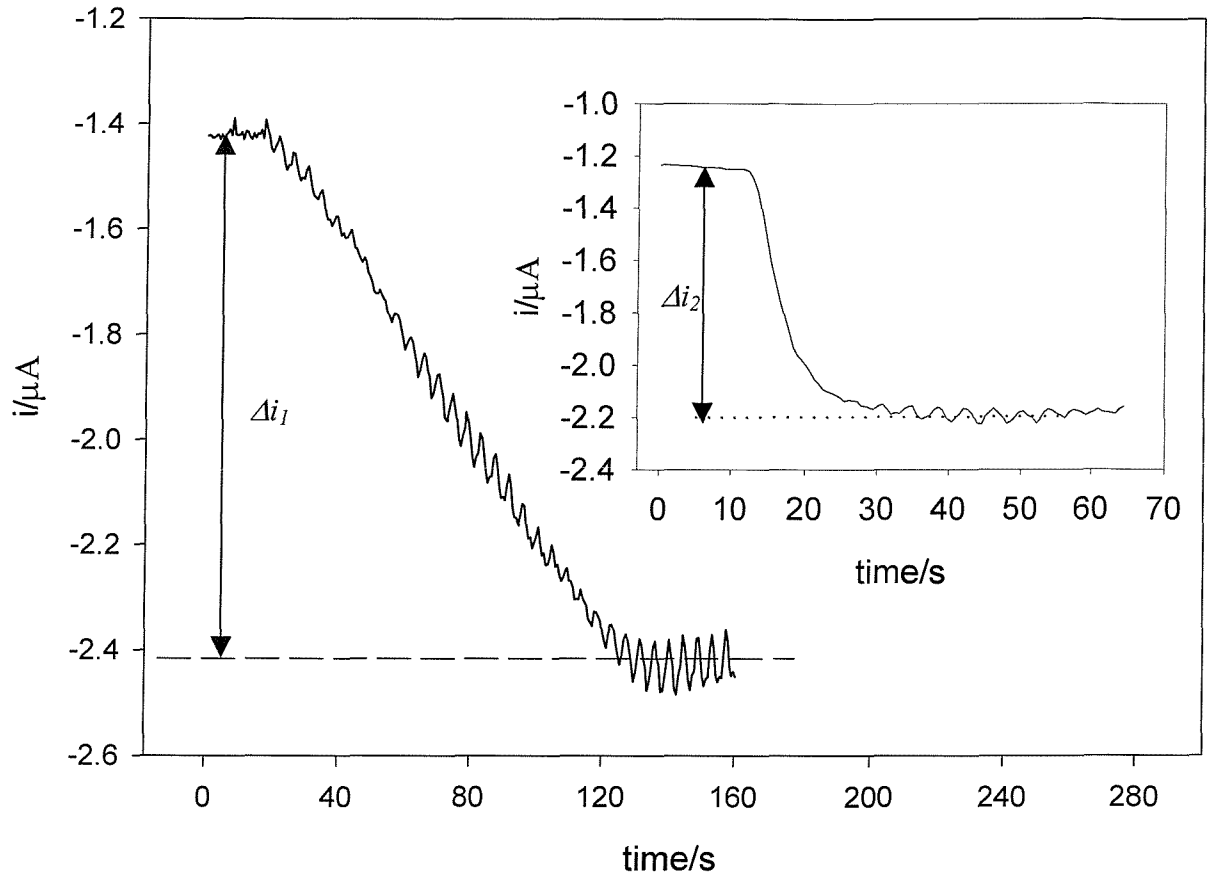

Figure 4.10 Plot showing the Fricke reaction under conditions where the solution has been irradiated for a known period of time. This allows the final concentration of Fe^{3+} to the determined accurately form the rate of the process. The Fricke reaction was performed using the peristaltic pump operating at maximum flow rate and ultrasonic reactor cell (A). The aerobic solution contained 1 mmol dm^{-3} $FeSO_47H_2O$, 1 mmol dm^{-3} NaCl in 0.4 mol dm^{-3} H_2SO_4. The potential was held at - 0.45 V vs. SCE. The frequency was 125 kHz and the spatial maximum acoustic pressure amplitude was 220 kPa. The temperature was maintained at 25 °C. The insert in the figure 4.9 illustrates the current against time trace achieved for a solution containing 26 μmol dm^{-3} of $NH_4Fe(SO_4)_2$ and 1 mmol dm^{-3} NaCl in 0.4 mol dm^{-3} H_2SO_4. The experiment was performed under the exact same conditions as the Fricke reaction except for the absence of sound irradiated and the pump and flow cell were pre-filled with 1 mmol dm^{-3} NaCl in 0.4 mol dm^{-3} H_2SO_4 prior to the experiment.

[§] Information supplied by BDH

4.5 Electrochemical Detection of H_2O_2

H_2O_2 is an indirect method of detecting hydroxyl radicals as it is formed in a solution irradiated with ultrasound as a geminate recombination product (reaction [4.10]). The presence of H_2O_2 (like Fe^{3+}or I_3^-) leaves a 'chemical memory' in the solution of the existence of hydroxyl radicals.[73] Several authors have realised the integral role played by H_2O_2 in the complex mechanisms of many of the established radical dosimeters.[14, 80, 87] This includes both the Fricke and the Weissler reactions. This is the principle reason why sonochemists have worked on the detection of H_2O_2.[76] Electrochemical detection of ultrasonically generated H_2O_2 was achieved using the flow cell technique described earlier.

$$OH^{\bullet} + OH^{\bullet} \longrightarrow H_2O_2 \qquad [4.10]$$

$$H_2O_2 \longrightarrow 2H^{+} + O_2 + 2e \qquad [4.11]$$

Experiments were performed in pH 5.5 buffer (citrate/phosphate)[147] using a 0.5 mm diameter Pt disk-working electrode. The potential was held at +0.8 V vs. SCE (MTLP for reaction [4.11]). Injecting known concentrations of H_2O_2 into the ultrasonic reactor (which contained 100 cm^3 of the buffer solution) and monitoring the increase in current as a function of the concentration of H_2O_2 enabled calibration of the flow system to be achieved. Figure 4.11 shows the initial current time plot recorded. Each increase in anodic current corresponds to the injection of a known concentration of H_2O_2 into the system.

The insert in figure 4.11 shows the calibration plot derived from the plateau currents produced by the addition of hydrogen peroxide. An approximately linear relationship between hydrogen peroxide concentration and current can be observed. It is known that the oxidation of hydrogen peroxide on platinum relies on a surface process that can be saturated at high hydrogen peroxide concentrations.[148] However, the low level of hydrogen peroxide employed ensures that this effect is not significant but may be responsible for the slight deviation from linearity observed in the calibration plot shown as an insert in figure 4.11. The calibration plot has a slope (CR) of 1.4×10^{-3} A mol^{-1} dm^3 (see equation (4.2)). This value can be use to calculate the rate of hydrogen peroxide generation in later experiments.

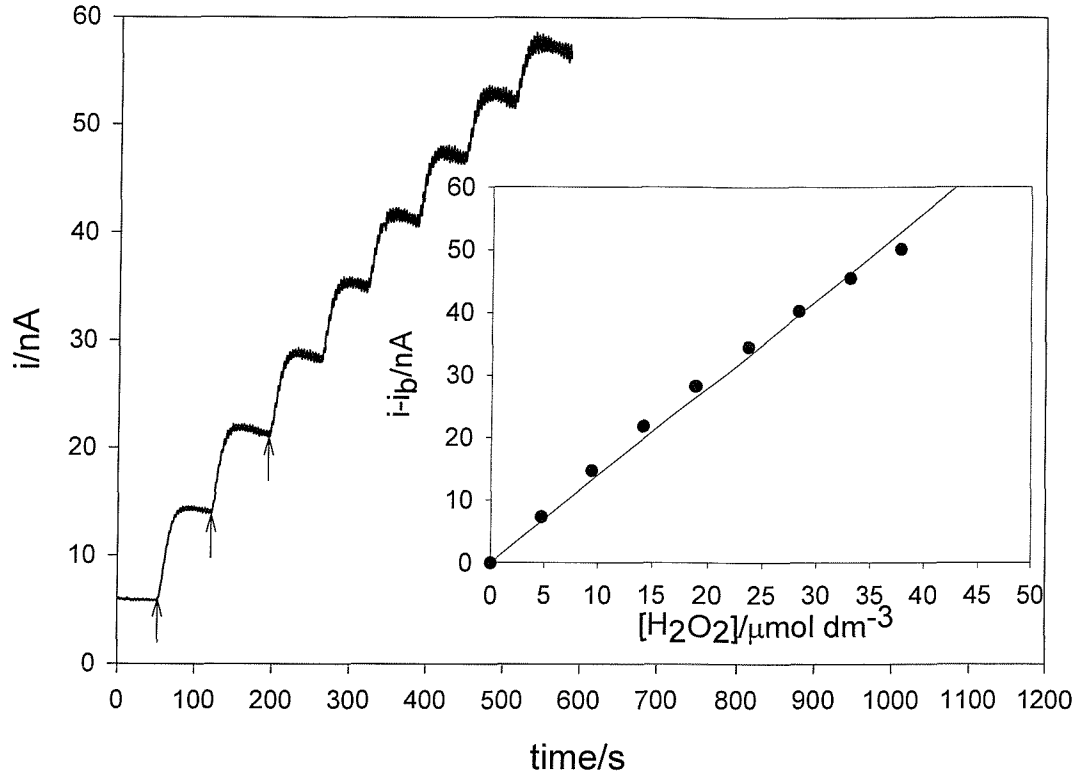

Figure 4.11 Plot showing the current recorded as a function of time as hydrogen peroxide was injected into the flow system (the arrows show the first three additions of hydrogen peroxide). The hydrogen peroxide was detected at +0.8V vs. SCE at a 0.5 mm diameter platinum electrode in pH 5.5 citrate/phosphate buffer.[147] Time was allowed for the current to reach a pronounced plateau before additional H_2O_2 was added to the flow system. The insert in figure 4.9 illustrates the mean linear increase in current as a function of H_2O_2 concentration.

Figure 4.12 shows the electrochemical detection of ultrasonically generated H_2O_2. The ultrasound was turned on at time $t = 0$ s and the current was monitored as a function of time. At time ca. $t = 25$ s (the time required for the solution to be pumped from the ultrasonic reactor to the flow cell) the current proceeds anodically corresponding to the oxidation of H_2O_2. At time $t = 125$ s the ultrasound was switched off and after a period of ca. 25 s the current reaches a plateau. The latter procedure was repeated at time ca. $t = 165$ s. The gradient of the current time transient recorded (SCR) can be measured and used with equation (4.2) to determine the actual hydrogen peroxide generation rate within the sonochemical reactor. The rate of production of H_2O_2 in figure 4.12 is 71 nmol dm^{-3} s^{-1}.

$$\text{Rate of hydrogen peroxide production} = \text{SCR/CR} \qquad (4.2)$$

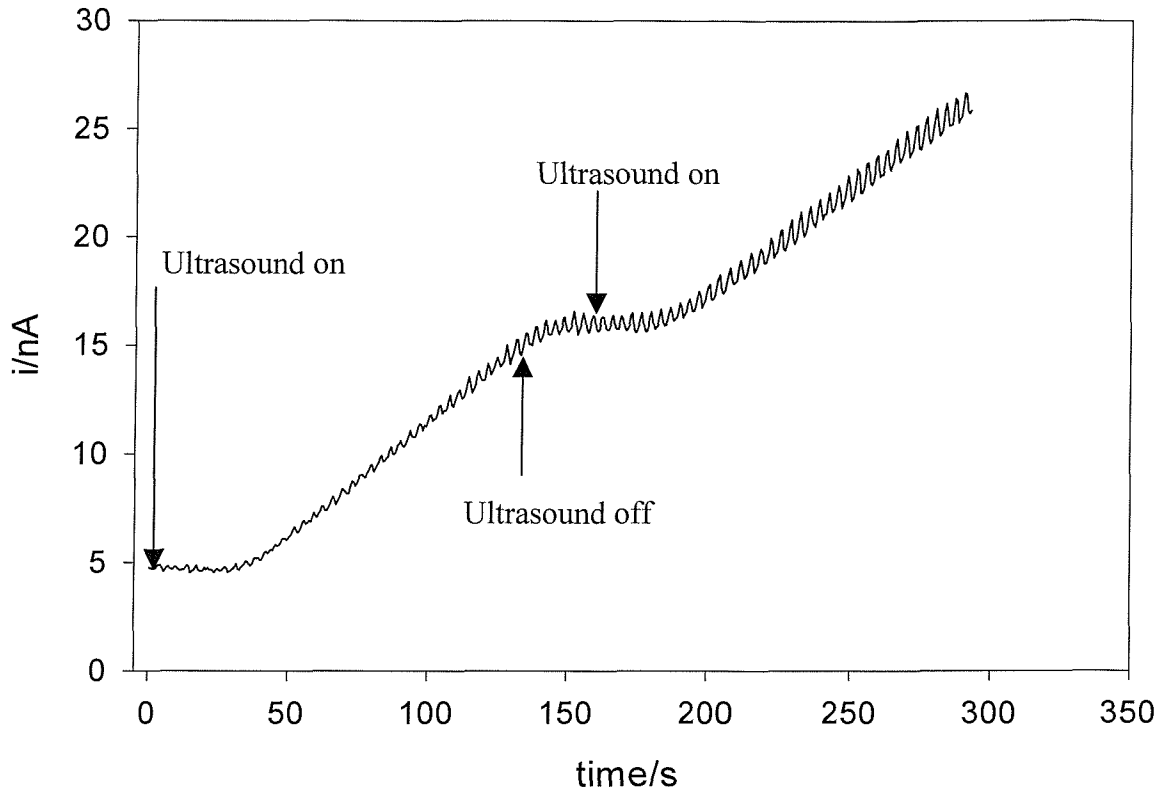

Figure 4.12 Plot showing a typical current time transient for the detection of ultrasonically generated H_2O_2 in 100 cm^3 of pH 5.5 buffer (citric acid and Na_2HPO_4).[147] The ultrasound was turned on at time t = 0 s. The potential was held at +0.8 V vs. SCE. The solution was pumped from the ultrasonic reactor cell (A) using the peristaltic pump operating at maximum flow rate to the flow cell and visa-versa. The frequency was 124 kHz and the spatial maximum acoustic pressure amplitude was kept constant at 182 kPa. At time t = 30 s the anodic increase in current represents the oxidation of H_2O_2 according to reaction [4.11]. The process was repeated to show that repeat measurements were possible with the same solution.

Figure 4.13 shows the rate of H_2O_2 production as a function of the acoustic pressure amplitude employed. Below 60 kPa no H_2O_2 production is detected. This is well below the Blake pressure indicated by (...) in the plot. Clearly at very low acoustic pressures, the cavitation process itself is unable to generate sufficient energy to drive the pyrolysis of the water vapour within the cavitation bubble. As a result there are no $OH^{\bullet}$ radicals generated, and in turn no geminate formation of hydrogen peroxide can be detected. As the acoustic pressure amplitude is increased 61– 152 kPa low but nevertheless measurable rate of H_2O_2 production can be determined. This is below the theoretical threshold for ultrasonic cavitation measured with a hydrophone. This result is similar to the result achieved for the Weissler and the Fricke reaction (see figures 4.3 and 4.9). As discussed in figure 4.3 care must be taken in interpreting this result. As the acoustic pressure amplitude was increased the cavitation 'activity' increases in tandem leading to higher production rates (152 – 354

kPa). Above this acoustic pressure amplitude the rate plateaus with respect to the error (see discussion on figure 4.3 section 4.1). The shape of the plot agrees with that achieved using other hydroxyl radical dosimeters (see figures 4.3 and 4.9).

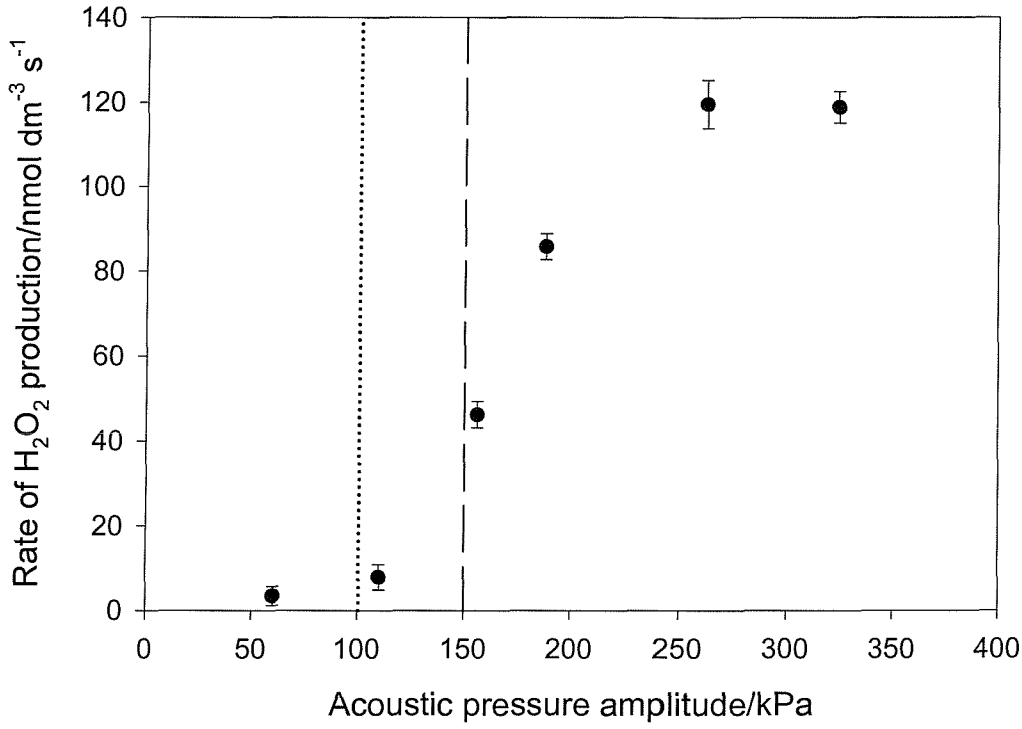

Figure 4.13 Plot showing the effect of the acoustic pressure amplitude on the rate of production of H_2O_2. For each experiment, cell (A) contained 100 cm^3 of pH 5.5 buffer (citric acid and Na_2HPO_4).[147] The potential was held at +0.8 V vs. SCE. The frequency was 124 kHz. The temperature was maintained at 25 °C. Error bars represent one standard deviation calculated using repeat measurements. The dotted line represents the Blake pressure. The dashed line represents the predicted acoustic pressure for the onset of inertial cavitation (see chapter 1, section 1.3). Experiments were performed using the peristaltic pump operating at maximum flow rate.

As a final test to ensure that the system was successfully detecting H_2O_2 oxidation a control experiment was performed using catalase. Catalase (EC 1.11.1.6), from bovine liver, activates the decomposition of hydrogen peroxide into water and oxygen (see reaction [4.12]).

$$H_2O_2 + \text{catalase} \longrightarrow 1/2O_2 + H_2O \qquad [4.12]$$

This enzyme was added to the ultrasonic reactor at the end of an experimental run. The ultrasound was turned off, but the solution was pumped from the ultrasonic reactor to the flow cell and back to the ultrasonic reactor. During this process the current was continually

monitored. Figure 4.14 illustrates the effect of adding this enzyme to the ultrasonic reactor. As expected, after the usual time delay the current starts to proceed anodically. At t = 140 s an excess of catalase was added to the ultrasonic reactor. When the treated solution reached the flow cell the current immediate dropped to the initial background level. This is understandable as there was no longer any H_2O_2 in the system. This confirms that H_2O_2 is being detected under the conditions employed.

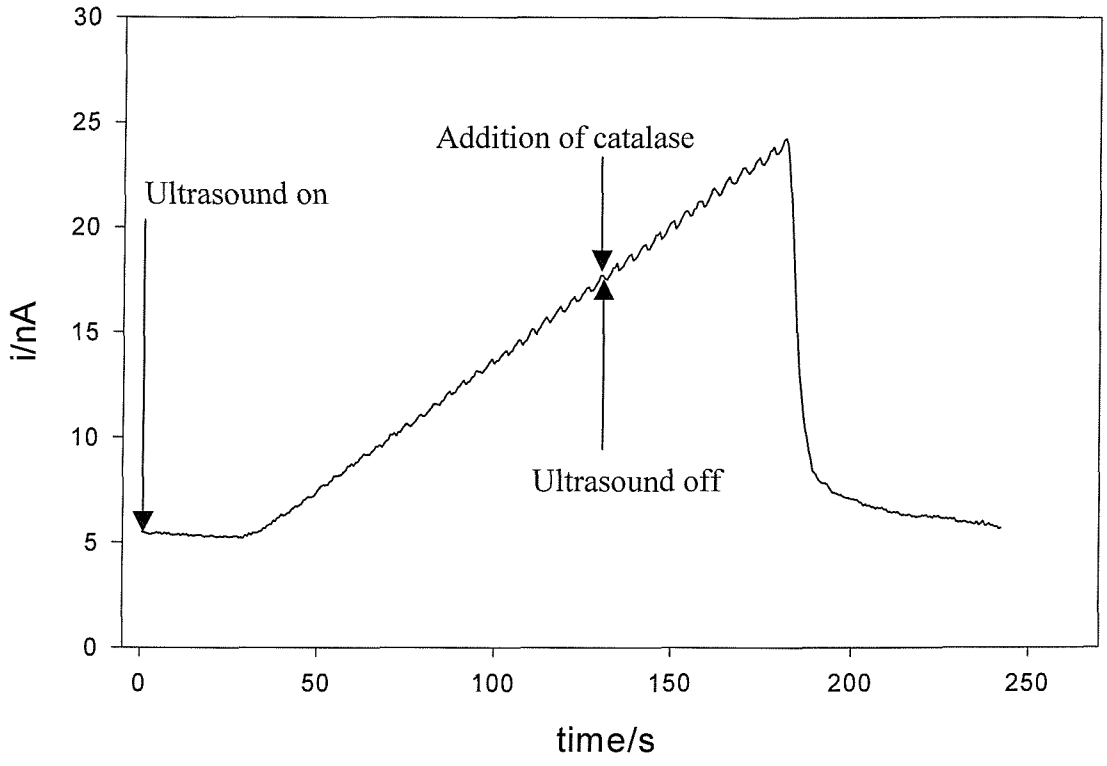

Figure 4.14 Plot showing the effect of adding an excess of catalase to the ultrasonic reactor. The cell contained 100 cm^3 of pH 5.5 buffer. The ultrasound was turned on at time t = 0 s. The plot shows the variation of current as a function of time. The potential was held at +0.8 V vs. SCE. The frequency was 124 kHz and the voltage amplitude was 110 V corresponding to a spatial maximum acoustic pressure amplitude of 247 kPa. The temperature was maintained at 25 °C. The experiment was performed using ultrasonic reactor cell (A) and the peristaltic pump operating at maximum flow rate.

Monitoring the build up of hydrogen peroxide is interesting from the fundamental standpoint of understanding the sonochemistry within a particular reactor. However, it also has important industrial applications. One such example is the destruction of organic molecules.[149-151] Ultrasound is known to destroy organics through the generation of the extremely oxidising hydroxyl radicals[94] ($OH^{\bullet}$, redox potential +2.8 V). However, the geminate coupling reaction forming hydrogen peroxide clearly removes two radicals for every hydrogen peroxide molecule produced. While this is a potential disadvantage, as the

oxidising power of hydrogen peroxide alone is relatively low, destruction of organics using hydrogen peroxide can be efficient if catalysed with a suitable ion. One such system is the employment of Fe^{2+} to produce Fenton's reagent.[152, 153] Birkin *et al.*[154] showed a significant increase on the rate of ultrasonic destruction of the dye, amaranth, on the addition of Fe^{2+}. The authors calculated the rate constant for the destruction of the dye in the presence and absence of Fe^{2+} as 1.97 x 10^{-2} min^{-1} and as 2.23 x 10^{-3} min^{-1} respectively. In addition Abdelsalam and Birkin[155] showed a significant increase in the rate of ultrasonic degradation of a model organic compound meldola blue in the presence of H_2O_2. This is good evidence that ultrasound will cleave the O-O bond in H_2O_2.

4.6 Electrochemical Evidence for ($H^{\bullet}$) Using Cu^{2+}

A number of authors have isolated $H^{\bullet}$ using spin trapping agents such as DMPO and identified the trapped species using ESR[74, 75] (see chapter 1, section 1.6). However, even though it is generated in equivalent quantities to $OH^{\bullet}$ in the primary solvent degradation step, little evidence appears in the literature for its detection. This is due to the different aqueous chemical reactivity of the species in question (see chapter 1, section 1.6). This section introduces a novel electrochemical system, which gives strong evidence for the production of $H^{\bullet}$ produced by ultrasound. A Cu^{2+}/Cu^{+} redox system is employed. The electrochemistry of this system will be discussed first prior to discussing the results.

Figure 4.15 is a plot showing a CV of 10 mmol dm^{-3} $CuSO_4$ in 1.5 mol dm^{-3} NaCl recorded on a 3 mm diameter glassy carbon disk. The reason for employing 1.5 mol dm^{-3} of NaCl is to stabilise the Cu^{+} species formed as Cu^{+} can be stabilised[139] using a strong halide solution forming the complex $CuCl_2^{-}$ (see reaction [4.13]). Figure 4.15 shows the two waves Cu^{2+} to $CuCl_2^{-}$ to Cu. The section from +0.5 V to +0.05 V is due to $Cu^{2+}/CuCl_2^{-}$ wave. The section from +0.05 V to –0.9 V is due to $CuCl_2^{-}$/Cu wave. The potential was swept from +0.5 V to –0.9 V at 20 mV s^{-1} versus SCE. The peak (A), at +0.2 V is due to the reduction of Cu^{2+} to $CuCl_2^{-}$ (see reaction [4.14]). The peak at –0.4 V, (B) is due the reduction of $CuCl_2^{-}$ to Cu (see reaction [4.15]). On the reverse sweep the peak (C) at –0.1 V is a copper stripping peak, the reverse of reaction [4.15]. The peak (D) at +0.3 V is due to the oxidation of $CuCl_2^{-}$ to Cu^{2+} the reverse of reaction [4.14].

$$Cu^{+} + 2Cl^{-} \longrightarrow CuCl_2^{-} \qquad [4.13]$$

$$Cu^{2+} + 1e \longleftrightarrow Cu^{+} \quad [4.14]$$

$$Cu^{+} + 1e \longleftrightarrow Cu \quad [4.15]$$

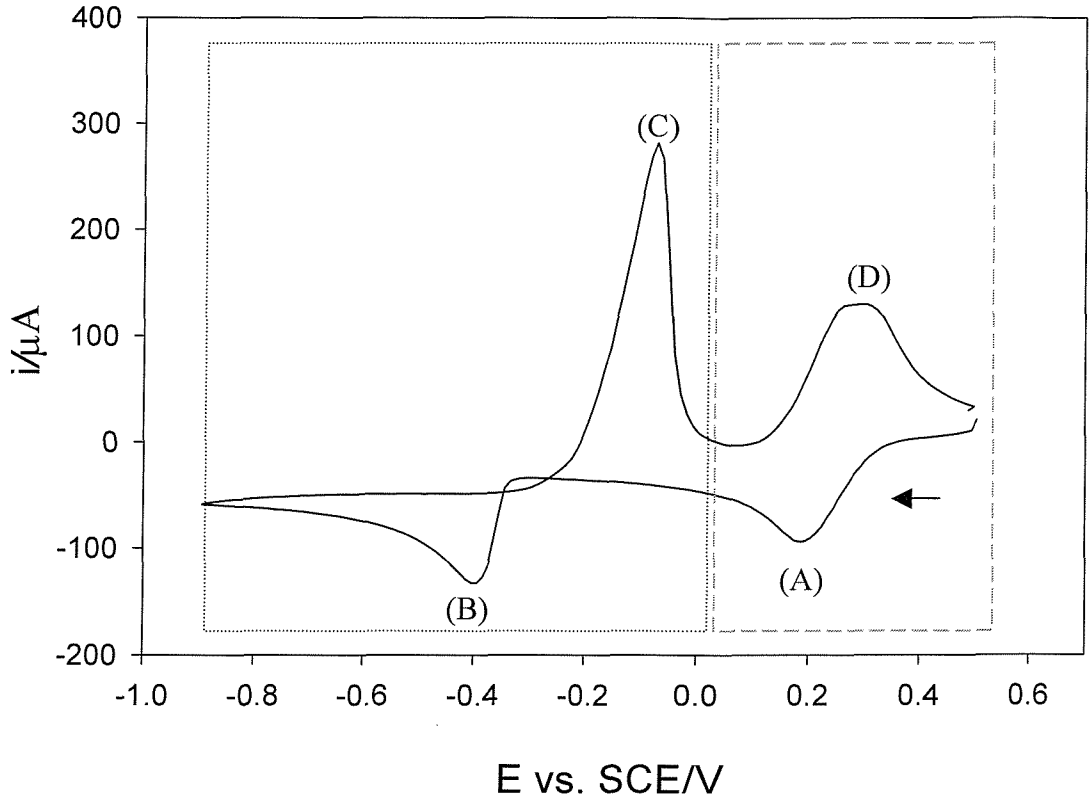

Figure 4.15 Plot showing a CV of 10 mmol dm^{-3} $CuSO_4$ in 1.5 mol dm^{-3} NaCl recorded on a 3 mm diameter glassy carbon disk working electrode at 20 mV s^{-1} versus SCE under aerobic conditions. The CV shows the two waves (Cu^{2+} to Cu^{+} (----) and Cu^{+} to Cu (·····).The solution was thermostated at 25 °C. The arrow in the figure indicates the direction in which the potential was swept. The reader is referred to the text for explanation of peaks (A-D).

On irradiation of a Cu^{2+} solution with ultrasound, reaction [4.16] is thought to be the main reaction occurring as the $H^{\bullet}$ diffuses into the liquid phase of the reaction mixture employed. The rate constant for reaction [4.16] is known[87] to be 9.1 x 10^{7} $dm^{3}mol^{-1}s^{-1}$. There are several possible competing reactions [4.17-4.22]. Reaction [4.18] can also produce Cu^{+}. The formation of $HO_2^{\bullet}$ can be attributed to both $H^{\bullet}$ and $OH^{\bullet}$ (reactions [4.17, 4.19]). However, in the absence of a scavenger $OH^{\bullet}$ forms predominantly the geminate recombination product H_2O_2 (reaction [4.20]).[87] In addition reaction [4.19] requires the presence of significant concentrations of H_2O_2. If this reaction were very important a non-linear response in figure 4.19 would be expected. This is because time is required to generate H_2O_2. Reaction [4.21] shows that $HO_2^{\bullet}$ can also be consumed. The reduction of Cu^{2+} by

H_2O_2 reaction [4.22] has been investigated by a number of authors.[156, 157] The rate of this reaction is known to be very pH dependent.[156] The pH of the solution was 4.5 under the conditions employed for these experiments.

$$Cu^{2+} + H^{\bullet} \longrightarrow Cu^{+} + H^{+} \quad [4.16]$$

$$H^{\bullet} + O_2 \longrightarrow HO_2^{\bullet} \quad [4.17]$$

$$Cu^{2+} + HO_2^{\bullet} \longrightarrow Cu^{+} + H^{+} + O_2 \quad [4.18]$$

$$OH^{\bullet} + H_2O_2 \longrightarrow HO_2^{\bullet} + H_2O \quad [4.19]$$

$$OH^{\bullet} + OH^{\bullet} \longrightarrow H_2O_2 \quad [4.20]$$

$$HO_2^{\bullet} + HO_2^{\bullet} \longrightarrow H_2O_2 + O_2 \quad [4.21]$$

$$Cu^{2+} + H_2O_2 \longrightarrow Cu^{+} + HO_2^{\bullet} + H^{+} \quad [4.22]$$

$$CuCl_2^{-} \longrightarrow Cu^{2+} + 2Cl^{-} + 1e \quad [4.23]$$

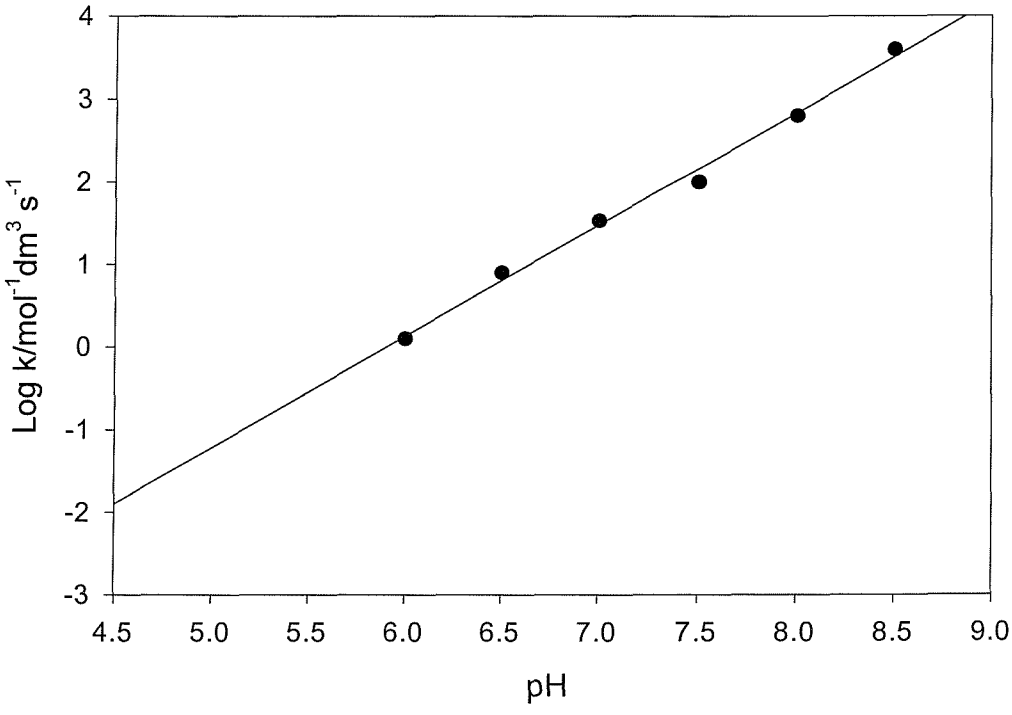

Figure 4.16 Plot showing the reduction of Cu^{2+} with H_2O_2 in sea water as a function of pH performed at 25 °C by Millero *et al.*[156] The graph has been extrapolated to calculate k_{rxn} at the pH employed for experiments.

Millero *et al.*[156] showed that below pH 5.9 (25 °C) the rate of this reaction was negligible. Figure 4.16 shows experimental data plotted form Millero *et al.*[156] The graph is extrapolated to estimate the value of the rate constant (k_{rxn}) at pH 4.5. Reaction [4.22] is a second order process so the rate may be calculated from equation (4.3):

$$\text{Rate} = k_{rxn} [CuSO_4] [H_2O_2] \qquad (4.3)$$

where k_{rxn} is the rate constant (calculated from Millero *et al.*[156]), $[CuSO_4]$ is 10 mmol dm^{-3} and the estimated maximum $[H_2O_2]$ is 20 μmol dm^{-3}.

From equation (4.3) the rate of this reaction at pH 4.5 can be calculated as 2 nmol dm^{-3} s^{-1}. This reaction is discussed in more detail later (see figure 4.22 and associated text). Hence, under the conditions employed the dominant reaction pathway leading to the formation of $CuCl_2^-$ will involve the generation of $H^\bullet$. Ultrasonically generated $CuCl_2^-$ can be detected electrochemically on glassy carbon by monitoring the anodic variation of current as a function of time.

Figure 4.17 shows a CV of 10 mmol dm^{-3} $CuSO_4$ in 1.5 mol dm^{-3} NaCl on glassy carbon, recorded in the flow cell. The mass transport limiting potential for the oxidation of the copper (I) complex to copper (II) occurs at potentials in excess of +0.45 V versus SCE. Hence this potential was initially employed to detect ultrasonically generated $CuCl_2^-$ (see figure 4.18). In addition, figure 4.17 was also used to calibrate the flow cell under the conditions employed. This of course assumes that the diffusion coefficient of Cu^{2+} is similar to the diffusion coefficient of $CuCl_2^-$.

Figure 4.18 shows the attempted detection of ultrasonically generated $CuCl_2^-$ at +0.45 V versus SCE. The ultrasound was turned on at time t = 0. After time t = ca. 25 s the current proceeds anodically (believed to be due to the production of $CuCl_2^-$). However, at time t = 40 s the current proceeds cathodically. This was assumed to be due to interference from other sonochemical products. At present the source of this interference is unclear but it could be HOCl or H_2O_2. It was found that a potential greater than +0.45 V was required (+1.0 V) to avoid the latter interference effects.

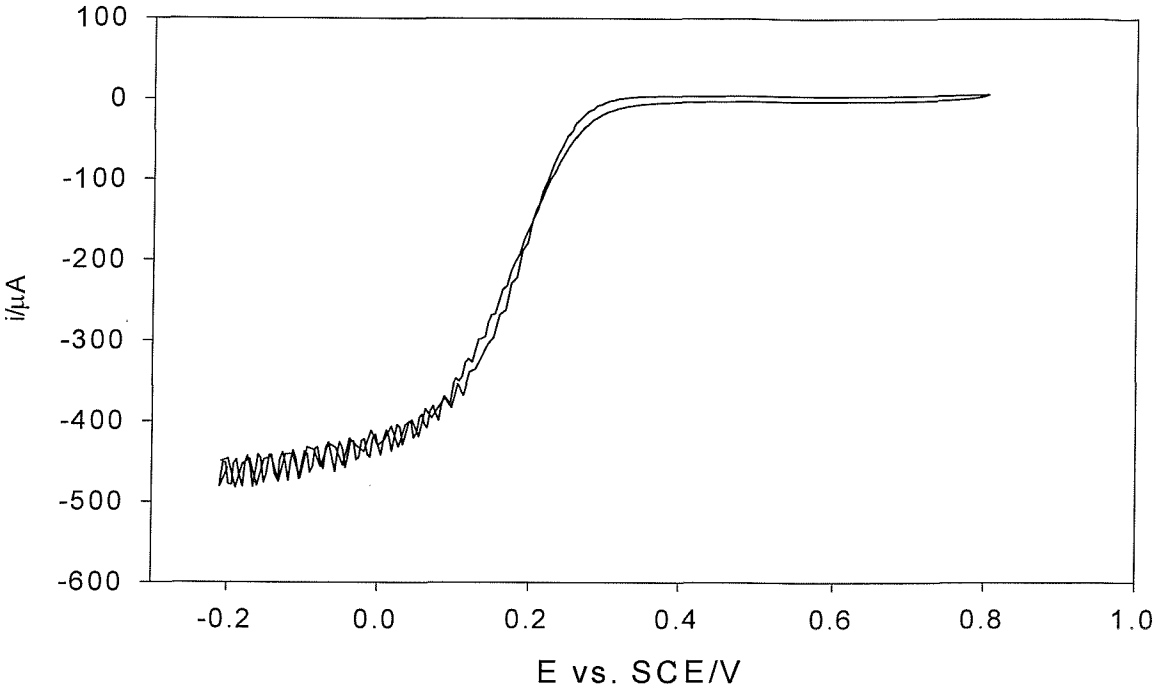

Figure 4.17 Plot showing a CV of 10 mmol dm^{-3} $CuSO_4$ in 1.5 mol dm^{-3} NaCl recorded under aerobic conditions on 3 mm diameter glassy carbon disk working electrode at 20 mVs^{-1} versus SCE with the peristaltic pump operating at maximum speed. The cell was temperature controlled at 25 °C.

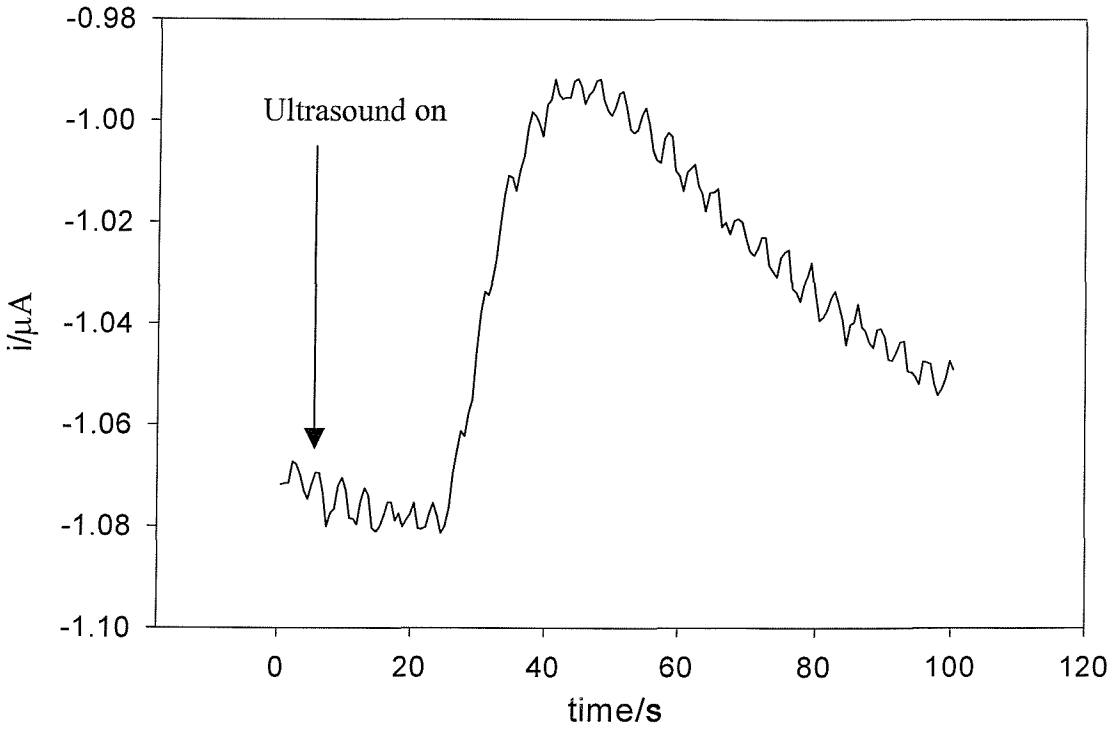

Figure 4.18 Sample current versus time response for the attempted detection of ultrasonically generated $CuCl_2^-$ with the potential held at +0.45 V versus SCE. The ultrasound was turned on at time t = 0 s and the solution was pumped from the ultrasonic reactor, cell (A) to the flow using the peristaltic pump operating at maximum flow rate. The irradiated solution contained 10 mmol dm^{-3} $CuSO_4$ in 1.5 mol dm^{-3} NaCl. The frequency was 125 kHz and the acoustic pressure amplitude was 256 kPa. The cell temperature was maintained 25 °C.

The electrochemical detection of $CuCl_2^-$ is illustrated in figure 4.19. The ultrasound was turned on at time t = 0 s and the current was monitored as a function of time. At time ca. t = 40 s (the time required for the solution to be pumped from the ultrasonic reactor to the flow cell) the current proceeds anodically corresponding to the oxidation of the $CuCl_2^-$ complex (see reaction [4.23]). At time t = 125 s the ultrasound was switched off and after a period of ca. 25 s the current reaches a plateau. The entire process was repeated to illustrate the reproducibility of the system. The measured rate of $CuCl_2^-$ is high in comparison to the measured yield of $OH^\bullet$ determined using the Weissler and Fricke reactions (see figures 4.3 and 4.9 and discussion of figure 4.21) but this could be a reflection of the efficiency of the radical trapping system.

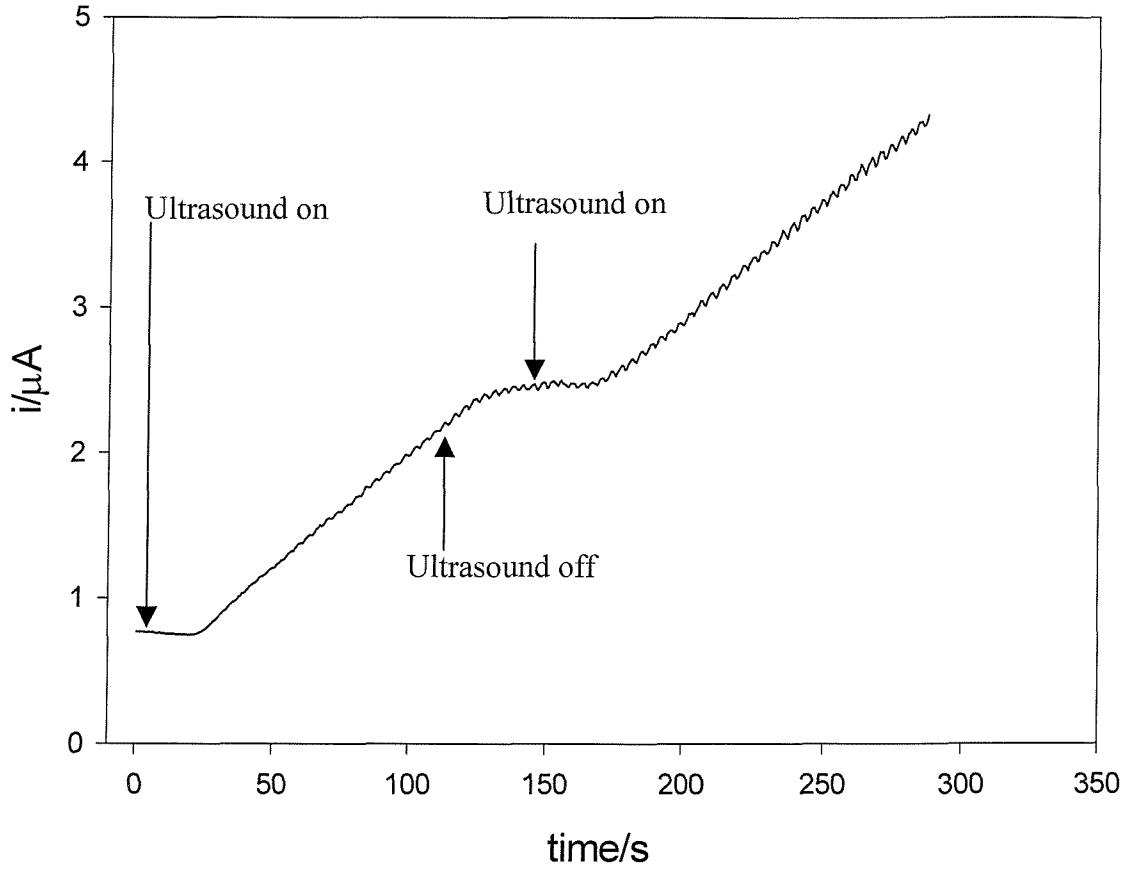

Figure 4.19 Sample current versus time response for the detection of ultrasonically generated $CuCl_2^-$. The potential was held at + 1.0 V versus SCE. The ultrasound was turned on at time t = 0 s and the solution was pumped from the ultrasonic reactor, cell (A) to the flow using the peristaltic pump operating at maximum flow rate. The irradiated solution contained 10 mmol dm^{-3} $CuSO_4$ in 1.5 mol dm^{-3} NaCl. The frequency was 125 kHz and the spatial maximum acoustic pressure amplitude was 256 kPa The cell temperature was maintained 25 °C.

Figure 4.20 shows the dependence of the rate of $CuCl_2^-$ production on the concentration of $CuSO_4$. In this experiment the ionic strength of the medium was maintained by the addition of Na_2SO_4. Figure 4.20 shows a rapid linear increase up to 10 mmol dm^{-3} $CuSO_4$ before the rate becomes independent of concentration. This is consistent with measurements performed on other electrochemical trapping systems (Weissler and Fricke dosimeters). The insert in figure 4.20 shows that no signal is achieved (i.e. the background is equal to zero) in the absence of $CuSO_4$. Two solutions were employed for this experiment. Solution (A) (—) contained 10 mmol dm^{-3} $CuSO_4$ in 1.5 mol dm^{-3} NaCl. Solution (B) (—) contained 1.5 mol dm^{-3} NaCl. In both cases the ultrasound was turned on at time t = 0. After time t = ca. 25 s the current proceeds anodically in the case of solution (A). However, no signal is observed in solution (B) in the absence of $CuSO_4$. Hence the zero point in figure 4.20 is real.

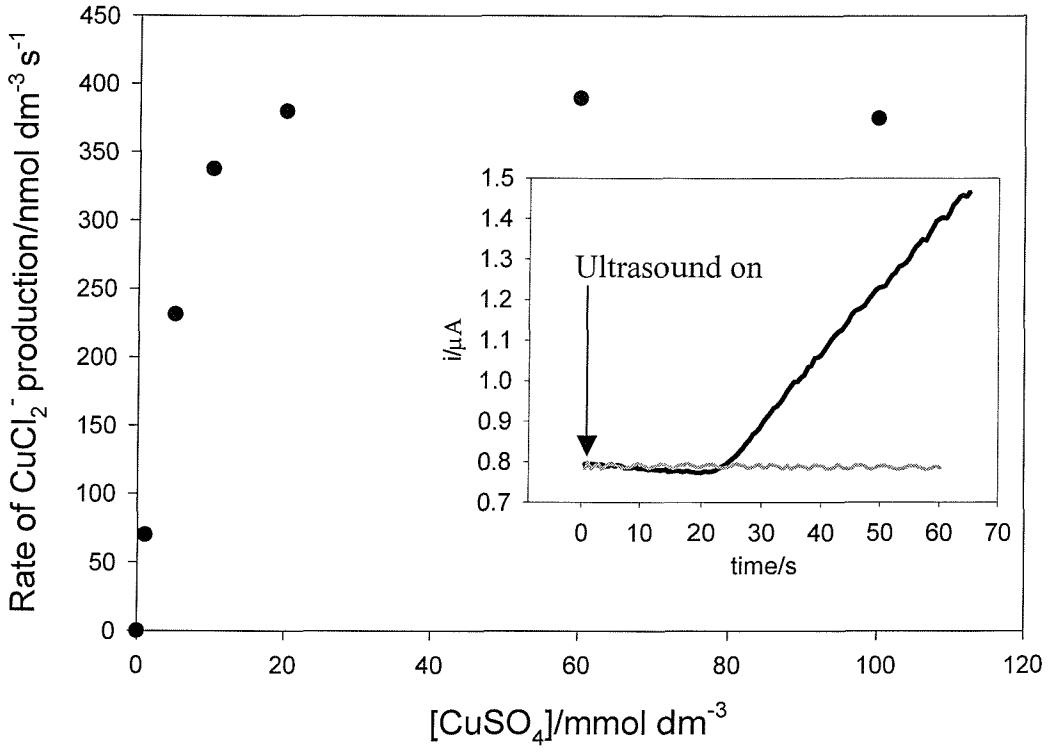

Figure 4.20 Plot showing the effect of the concentration of $CuSO_4$ on the sonochemical rate of $CuCl_2^-$ formation. The irradiated solution contained 10 mmol dm^{-3} $CuSO_4$ in 1.5 mol dm^{-3} NaCl. Ionic strength was maintained using Na_2SO_4. The frequency was 125 kHz and the spatial maximum acoustic amplitude was 252 kPa. The cell temperature was controlled at 25°C. The insert in the plot shows a sample current against time response for the detection of $CuCl_2^-$ under the same conditions as above (the black line solution (A)). In addition to the latter response the insert contains the signal achieve in the absence of $CuSO_4$ solution (B) (i.e. 1.5 mol dm^{-3} NaCl (the grey line)). In both cases the potential was held at + 1.0 V versus SCE. The ultrasound was turned on at time t = 0 s and the solution was pumped from the ultrasonic reactor, cell (A) to the flow cell using the peristaltic pump operating at maximum flow rate.

Figure 4.21 illustrates the effect of the acoustic pressure amplitude on the rate of production of $CuCl_2^-$. At low acoustic pressure there is little variation in the rate of reaction [4.23]. This is similar to the other systems studied i.e. the Fricke, and the Weissler reaction (see figures 4.3 and 4.9 respectively). Measurements below the theoretical pressure threshold for inertial cavitation were again recorded. This has been discussed in detail in figure 4.3 and in chapter 1, section 1.3. However, as the acoustic pressure amplitude was increased higher levels of cavitation 'activity' was expected and therefore, the rate of generation of $CuCl_2^-$ increases. This effect stabilises at higher acoustic pressure amplitudes.

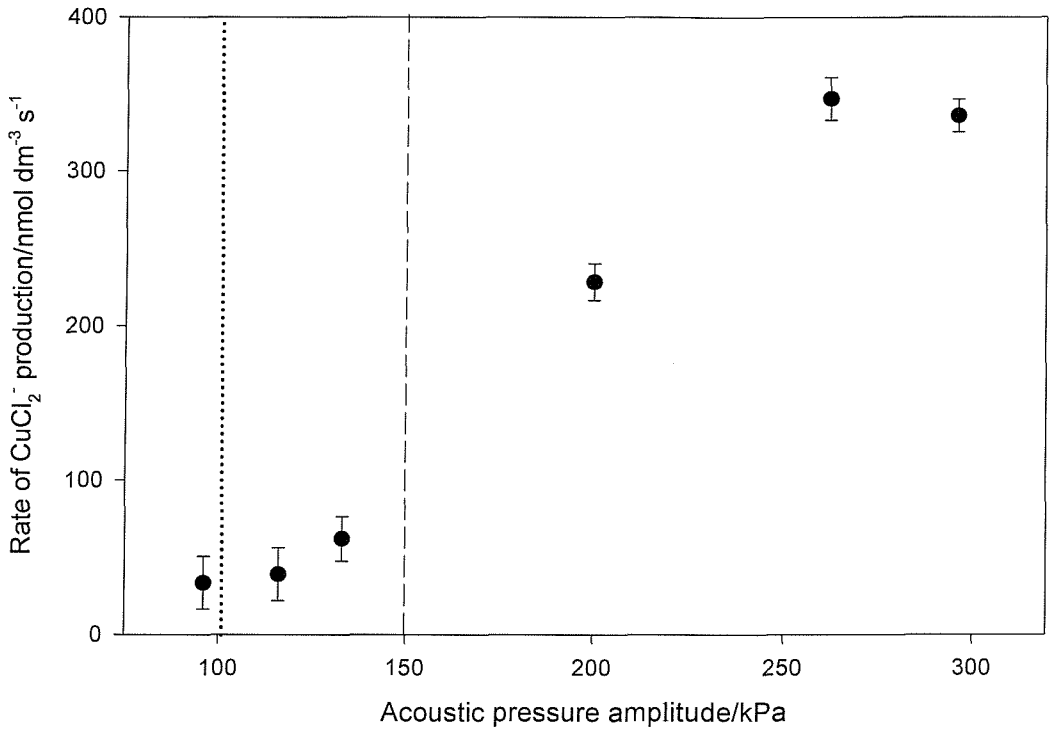

Figure 4.21 Plot showing the effect of the acoustic pressure amplitude on the rate of $CuCl_2^-$ formation. The irradiated solution contained 10 mmol dm^{-3} $CuSO_4$ in 1.5 mol dm^{-3} NaCl. The frequency was 125 kHz and the cell was temperature controlled at 25°C. Error bars represent one standard deviation calculated using three repeat measurements. The dotted line represents the Blake pressure. The dashed line represents the predicted acoustic pressured for the onset of inertial cavitation (see chapter 1, section 1.3). Experiments were performed in cell (A) using the peristaltic pump operating at maximum flow rate.

The rates of production of $CuCl_2^-$ are high compared to previous work (the Weissler and Fricke reaction, figures 4.3 and 4.9). However, it is interesting to note that, in figure 4.13 the rate of production of H_2O_2 in pH 5 buffer at 252 kPa was 100 nmol dm^{-3} s^{-1}. This equates to 200 nmol dm^{-3} s^{-1} $OH^\bullet$ (and therefore 200 nmol dm^{-3} s^{-1} $H^\bullet$). The rate of production of $CuCl_2^-$ at 252 kPa was 350 nmol dm^{-3} s^{-1}. However, the MBSL photon count for both of these systems is measured in chapter 5 (see section 5.5 and 5.6) under identical conditions to

those employed in these experiments. The mean MBSL photon count in the case of the H_2O_2 (see section 5.5) and $H^\bullet$ (see section 5.6) system was 280 and 560 photons per 50 ms respectively (at 125 kHz). In chapter 5 the MBSL photon count is shown to be an excellent indicator of chemical activity. Combining data from chapter 4 and chapter 5 and employing the following equations:

$$\text{Predicted rate of } H^\bullet = 200 \times [^{560}/_{280}] \text{ nmol dm}^{-3} \text{ s}^{-1}$$

$$\text{Predicted rate of } H^\bullet = 400 \text{ nmol dm}^{-3} \text{ s}^{-1}$$

Hence, it appears that almost quantitative $H^\bullet$ capture occurs in figure 4.21.

A number of control experiments were performed to ensure that the sensor was indeed detecting $CuCl_2^-$ formation and that the calculated rates were correct. These included the following:

- To investigate the effect of H_2O_2 on the reduction of Cu^{2+} (reaction [4.22]) the sweep rate dependence of this reaction was investigated by recording CV's in the presence and the absence of H_2O_2. Figure 4.22 (a) illustrates the effect of adding 1 mmol dm^{-3} H_2O_2 to the Cu^{2+} solution at 100 mV s^{-1}. It can be seen that there is little difference in the CV's at high sweep rate. The ratio of the peak currents is 1.03 and 1.10 in the presence and absence of H_2O_2 respectively. A lower sweep rate 10 mV s^{-1} was employed in figure 4.22 (b). The ratio of the peak currents is 1.12 and 1.06 in the presence and absence of H_2O_2 respectively. The consequence of adding H_2O_2 is difficult to quantify. It is not a simple EC' mechanism.[78] However, even at low sweep rates there is little effect on the addition of H_2O_2. Even though the experiments were performed under degassed conditions the difference observed between the CV's may be caused by oxygen produced from the decomposition of H_2O_2. The results achieved agree with the work carried out by Millero *et al.*[156] where the rate of this process was difficult to quantify under the conditions employed. Additionally Millero[157] has shown that the product of reaction [4.16], $CuCl_2^-$ is resistant to oxidation by $HO_2^\bullet$, H_2O_2 and O_2. The proposed reaction scheme is summarised in figure 4.23.
- To confirm that H_2O_2 had little effect on the measured rate of formation of $CuCl_2^-$, catalase (an enzyme which destroys H_2O_2) was added to the ultrasonic reactor prior to an experimental run. This eliminated H_2O_2 from the system (see figure 4.14). This had no notable effect on the rate of production of $CuCl_2^-$.
- An experimental run was also performed in the absence of $CuSO_4$ (1.5 mol dm^{-3} NaCl). No oxidation signal was observed (see insert figure 4.20).

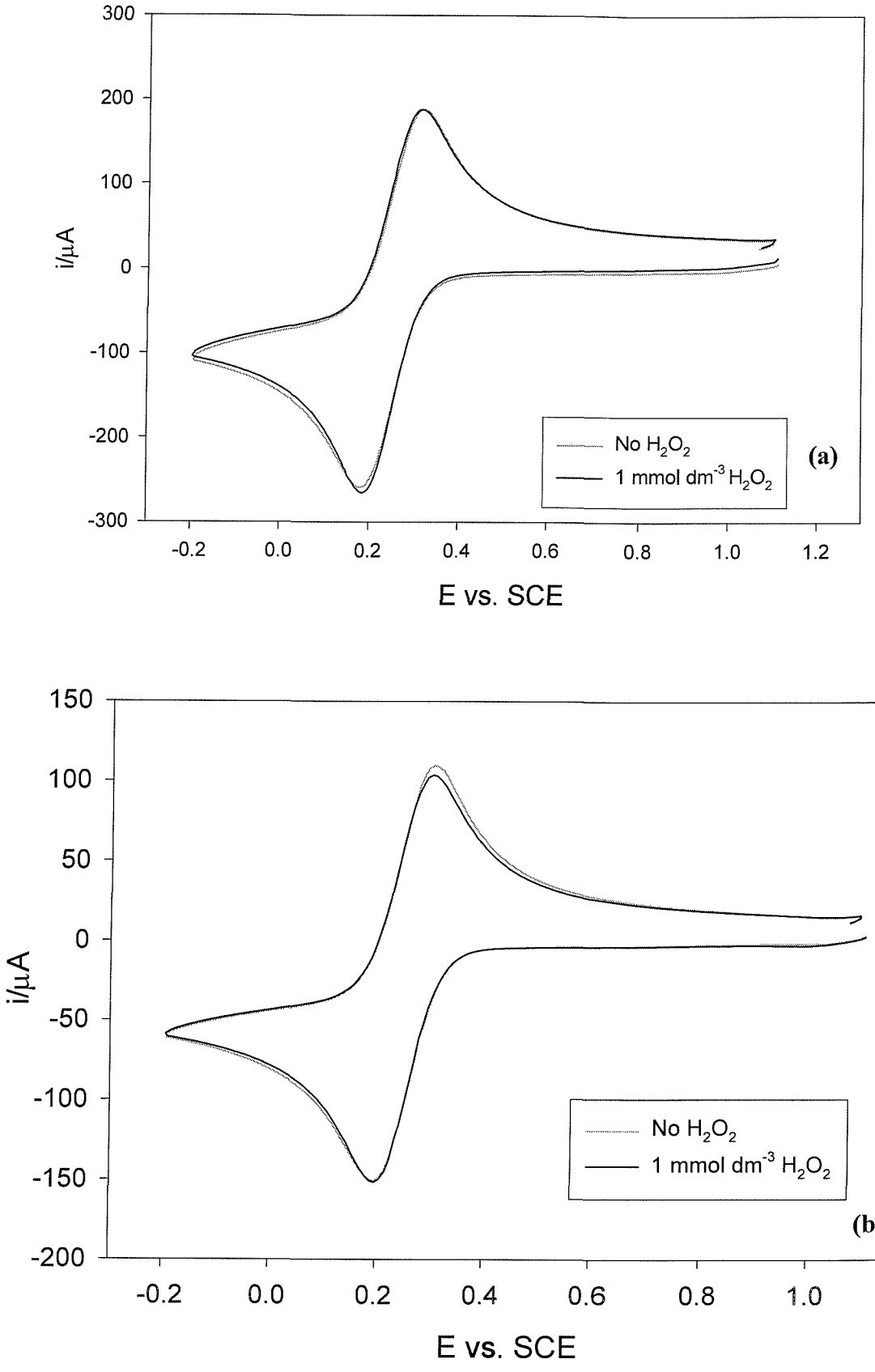

Figure 4.22 Cyclic Voltammograms recorded of a degassed solution containing 10 mmol dm^{-3} $CuSO_4$ in 1.5 mol dm^{-3} NaCl (—) with 1 mmol dm^{-3} H_2O_2 (—) recorded on a 3 mm diameter glassy carbon disk at (a) 100 mV s^{-1} and (b) 10 mV s^{-1} versus SCE at 25 °C.

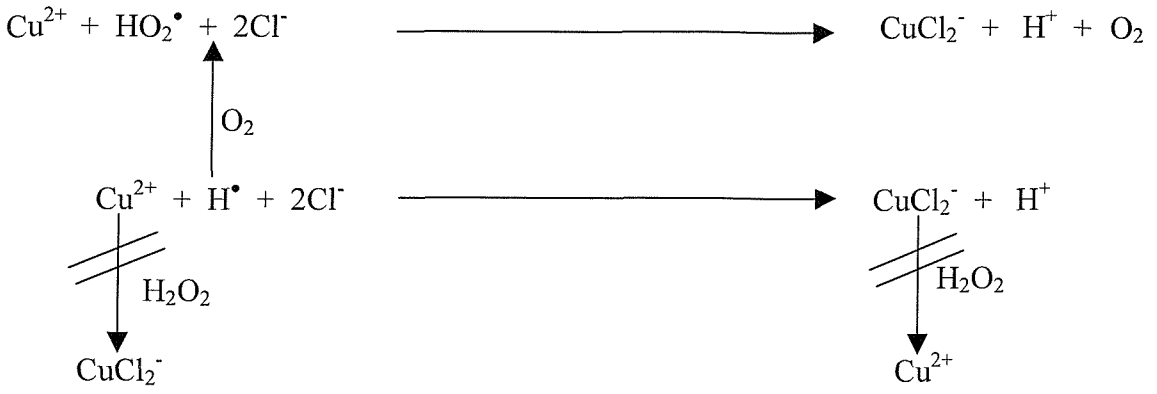

Figure 4.23 Proposed reaction scheme for the capture of $H^{\bullet}$ by Cu^{2+}.

4.7 Effect of Heating During Irradiation Experiments

Heating of the solution during the experiments was found to be relatively small. Typically the temperature within the cell rose by ca. 0.5 °C during initial ultrasonic irradiation of the liquid. However, for prolonged exposure (e.g. 100 s for the electrochemical radical experiment) a measured temperature rise of < 1 °C was determined using a temperature probe placed within the cell containing 100 cm^3 of pure water exposed to 125 kHz ultrasound at 100 V drive amplitude. Hence, heating effects are likely to be negligible in the experimental set-up employed. If heating effects were a problem the mode excited in the ultrasonic reactor would change with time as temperature affects the speed of sound in the liquid (see chapter 3, section 3.3 discussion of figure 3.10). This does not occur as the acoustics modes were observed to be stable with time (see figure 3.10).

4.8 Conclusions

It has been shown that electrochemical detection of sonochemical products can be applied as a sensitive real time technique. A novel flow cell technique capable of *ex-situ* detection of sonochemically generated products on a semi real time basis has been reported. The novel technique applied has been shown to be extremely sensitive (nmol dm^{-3} s^{-1}) with a number of direct advantages over conventional spectrophotometric and *in-situ* electrochemical assaying of the solution. The Weissler reaction, the Fricke reaction, the detection of hydrogen peroxide and the detection of ultrasonically generated $H^{\bullet}$ were studied successfully using this electrochemical technique. An equivalent dose of up to 16.8 rad s^{-1} has been calculated for the sonochemical reactor.

Chapters three and four follow Apfel's[20] advice in characterising the sound field/ultrasonic reactor and the electrochemical sensors. Chapter 5 presents a comprehensive investigation of ultrasonic frequency and its role in sonochemical activity and sonoluminescence.

CHAPTER 5

IMPACT OF ULTRASONIC FREQUENCY ON SONOCHEMISTRY AND SONOLUMINESCENCE

Ultrasound is known to enhance the rate of many chemical reactions both homogeneous[13-15] and heterogeneous[16, 17] through a variety of mechanisms involving cavitation.[1, 12, 13] One chemical consequence of cavitation is the generation of radicals which are produced by the breakdown of the solvent matrix caused by the high pressures and temperatures generated. Evidence for the formation of these radical species was reported in chapter 1, section 1.6. Sonoluminescence, like radical production, is a process, which is inexorably linked to cavitation. This process can be classed as multiple bubble sonoluminescence (MBSL) or single bubble sonoluminescence (SBSL) (see chapter 1 section 1.10). The exact mechanism by which sonoluminescence occurs is still a matter of debate[103-106, 112] (see chapter 1, section 1.11).

MBSL and radical formation occur as a direct result of cavitation. Therefore, one would expect that there might be a correlation between the MBSL light output and the rate of radical production. Hence the best conditions for an efficient chemical reaction and maximum light output may be expected to be the same. This study indicates that this is indeed the case.

Vinçotte[158] performed the first combined study of the correlation between the frequency dependence of MBSL and chemical reactivity. The sonochemical degradation of a model organic molecule, medola blue[155], was investigated between 20-160 kHz. The degradation of the ring system resulted in the loss of the chromphore responsible for the intense visible absorbency, and this was monitored with UV-Vis spectroscopy. Vinçotte[158]reported that the frequency dependence of the rate of degradation and the sonoluminescent output from the cell showed a remarkable correlation. The study showed that the rate of degradation varied markedly with frequency, thus illustrating the need for fine frequency resolution when investigating the effects of ultrasonic frequency.

There are many studies on the influence of ultrasound on the rate of a chemical reaction. However, in general the frequency of sound employed is usually kept to a few fixed values. Comparison is then made between the different behaviour observed at high (e.g. 500 kHz) and low (e.g. 20 kHz) frequencies [99, 150, 151] or a set of predetermined[23, 159, 160] values. Figure

5.1 is a plot, which summarises five recent studies on the frequency dependence of ultrasonic reactions, which appeared in the recent literature.[23, 87, 159-161]

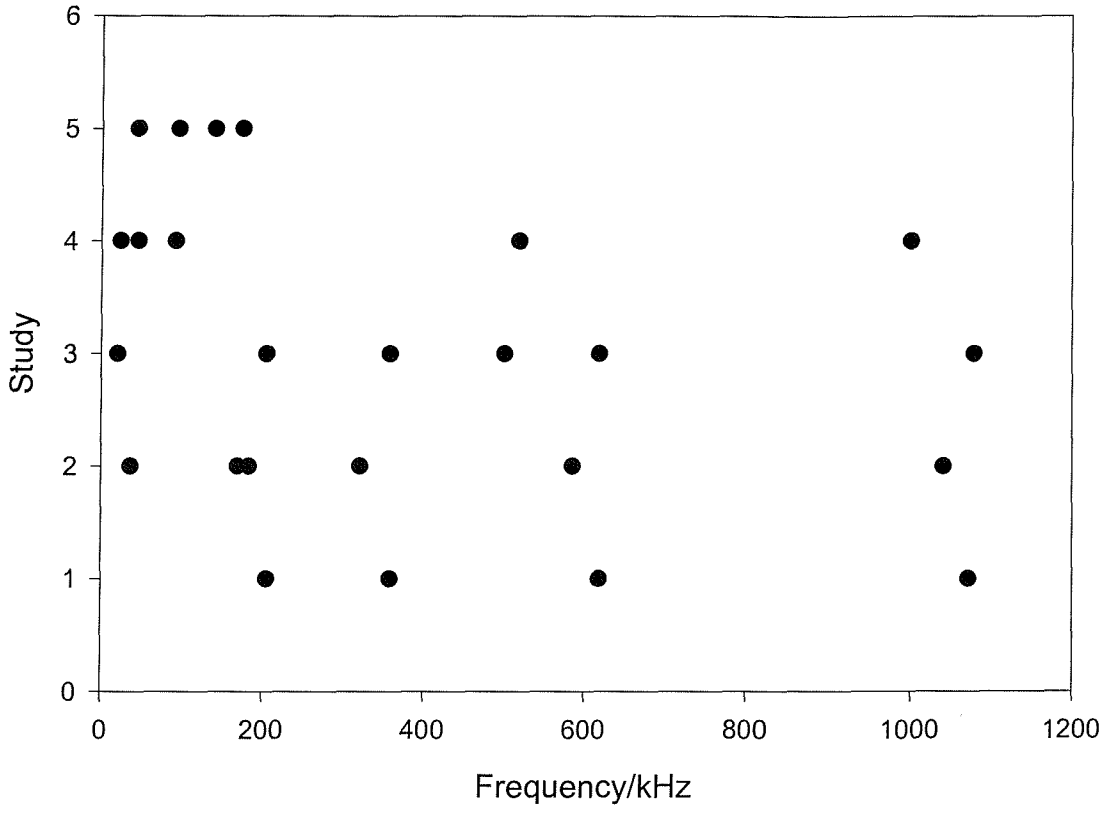

Figure 5.1 Plot, which summarises five studies on the frequency dependence of ultrasonic reactions, which were taken from recent literature. Study 1 was performed by Beckett and Hua[23] study 2 was performed by Mark *et al.*[87], study 3 was performed by Hung and Hoffmann[159], study 4 was performed by Kojima *et al.*[160], and study 5 was performed by Sato *et al.*[161]

Figure 5.1 show that the authors of these studies are examining sonochemical trends at dramatically different frequencies. For example in study 1 performed by Beckett and Hua[23] investigate the role of sonoluminescence and chemical activity (1-4 dioxane decomposition and H_2O_2 formation) at four different frequencies (205, 358, 618 and 1071 kHz respectively). The authors fail to measure the sound field in their reactor, thus neglecting the dominant cause of frequency dependence, that of the amplitude of the driving field as a result of the frequency characteristics of the driving transducer and the sound field. They then construct a speculative model to interpret their data based on non-linear bubble implosions at lower frequencies and species flux rates at higher frequencies. In studies 2 and 3 the authors[87, 159] have even compared results obtained at discrete frequencies employing different ultrasonic reactors for separate measurements. Clearly this neglects the frequency characteristics of the transducers and the cells employed. In addition the use of calorimetric

analysis rather than mapping the sound field appears common practice.[131, 159, 161] This makes comparison of published data extremely difficult. The studies performed by other authors are discussed in more detail in section 5.10.

In this chapter the variation of light emission, acoustic pressure, broadband airborne audible noise ($20 < f < 20$ kHz) and reaction rates are compared as a function of the driving frequency employed within a simple sonochemical reactor. The results presented demonstrate the importance of accurate control of experimental conditions and equipment design as well as demonstrating how light output from a cell or ultrasonic reactor will indicate frequencies of high sonochemical reactivity. It will be shown that, in order for correct and precise conclusions to be drawn on the influence and efficiency of sonochemical reactions, it is necessary to study the system over a wide range of frequencies, with a high frequency resolution (at least 1 kHz see chapter 3, section 3.3 figure 3.10). In such circumstances, it is suggested that undertaking comparative frequency trials at a small number of spot frequencies, is invalid.

5.1 Sonoluminescent and Sonochemiluminescent Light Emission

Figure 5.2a shows a plot of the MBSL photon count recorded for a 50 mmol dm^{-3} Na_2CO_3 solution as a function of frequency recorded by the author and colleagues.[162] The insert in the plot shows an actual set of data recorded in the range 120-124 kHz in 1 kHz increments. Four major peaks are clearly observed in figure 5.2a. This includes one large emission peak beginning at 117 kHz. Figure 5.2b shows the measured light emission for MBSCL as a function of ultrasonic frequency for a luminol solution. A comparison of the results shown in figure 5.2a and figure 5.2b shows that there are slight differences in the light emission spectra. However, in general the light emission occurs at the same frequencies within the range studied. The photon detection rate from the MBSCL system is approximately 30 times greater than MBSL and thus easier to detect. It is important to note that in all MBS(C)L measurements the photon counter is positioned above the ultrasonic reactor cell (A) and that the sensor footprint has been accurately determined (see chapter 2, section 2.4).

In the following sections the rates of a number of reactions, known to be sensitive to radical production, are reported as a function of frequency within a sonochemical reactor (see chapter 4 for detailed discussion on how these systems operate). These systems are then compared to MBS(C)L under identical conditions.

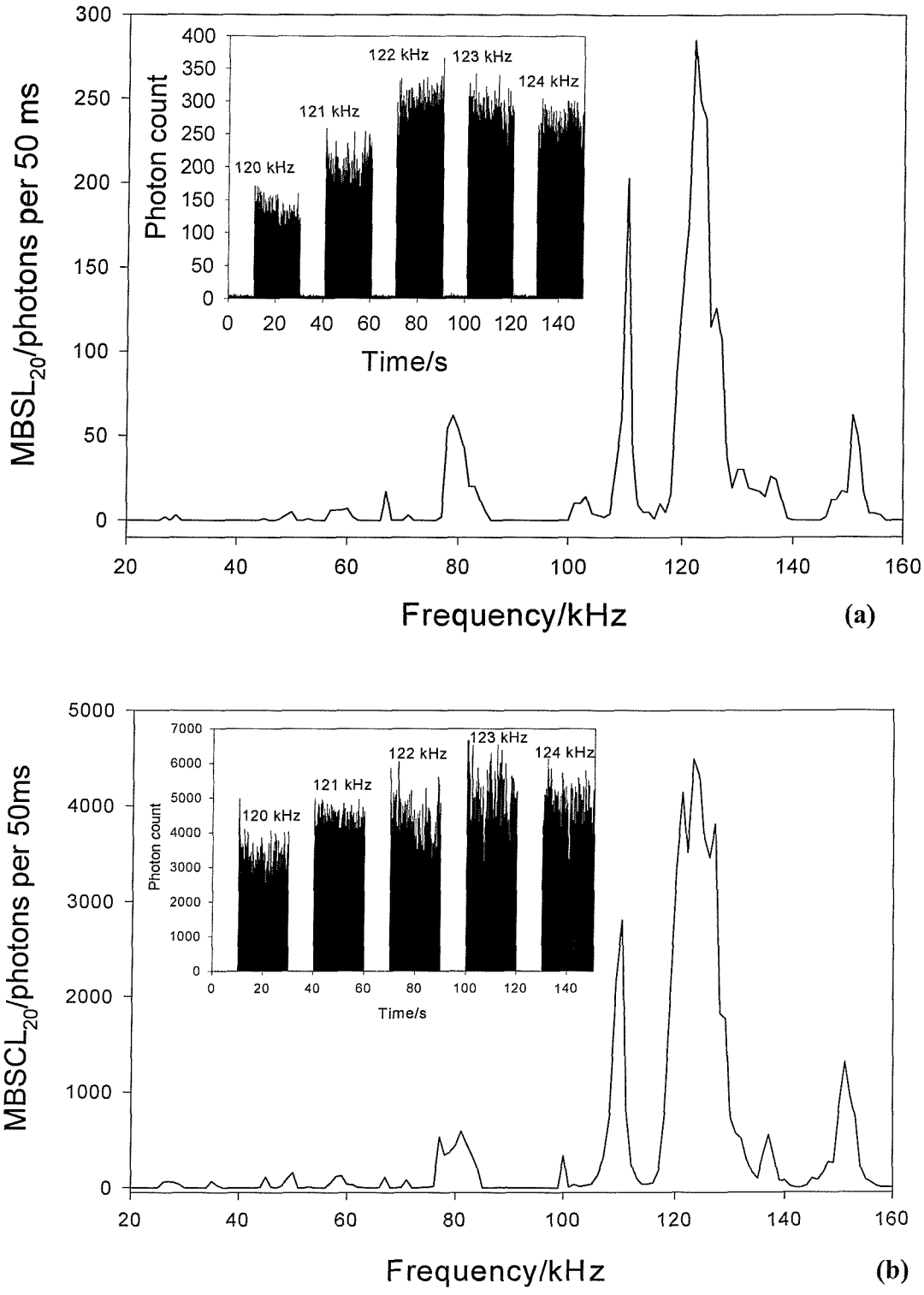

Figure 5.2 Plot (a) shows the variation in the sonoluminescence output of the ultrasonic reactor cell (A) as a function of frequency in 1 kHz increments. The cell contained 100 cm^3 of 50 mmol dm^{-3} Na_2CO_3(aq). The insert in the plot shows a section of the actual photon count at the labelled frequency range. Plot (b) shows the variation in the sonochemiluminescence output of ultrasonic reactor cell (A) as a function of frequency in 1 kHz increments. The cell contained 100 cm^3 of 1 mmol dm^{-3} luminol in 50 mmol dm^{-3} Na_2CO_3(aq). The insert in the plot shows a section of the actual photon count at the labelled frequency range. The solution temperature was maintained at 25 °C under aerobic conditions throughout both experiments. The cylindrical glass reactor had an internal diameter of 5.8 cm. The driving voltage amplitude was kept constant at 100 V throughout both experiments.

5.2 The Weissler Reaction

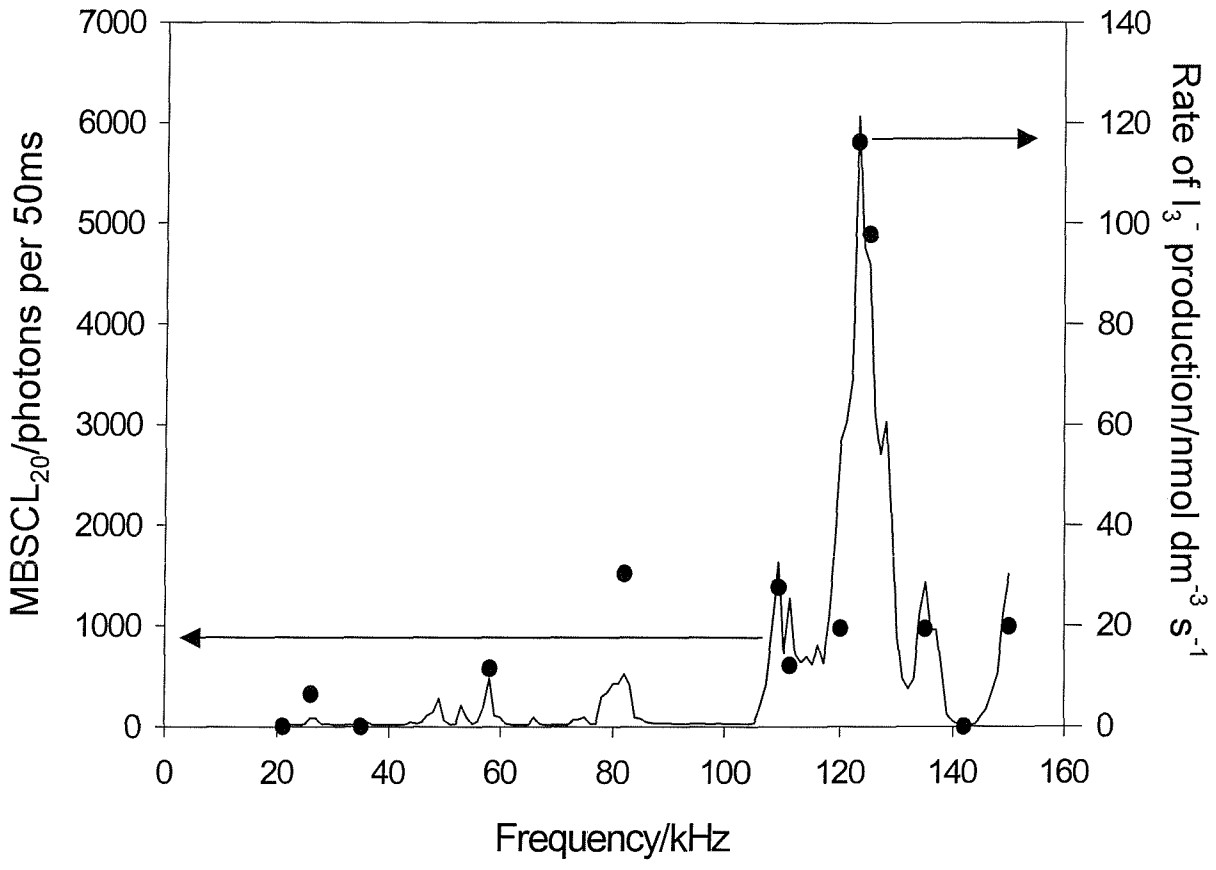

Figure 5.3 Plot showing the frequency dependence of both sonochemiluminecent output of ultrasonic reactor cell (A) (—) and the rate of Weissler reaction (•). For each Weissler measurement the cell contained 100 cm^3 of 100 mmol dm^{-3} of KI. The points on this graph (•) represent the average of three repeat measurements. Error bars were calculated but removed for clarity. The maximum error on these measurements is ca. ± 3 nmol dm^{-3} s^{-1}. For each sonochemiluminescent experiment the cell contained 100 cm^3 of luminol solution (1 μmol dm^{-3} luminol, 100 mmol dm^{-3} Na_2CO_3, 0.1 mmol dm^{-3} EDTA and 0.1 mol dm^{-3} H_2O_2). The cell was temperature controlled at 25 °C. The drive voltage amplitude was kept constant at 100 V throughout each experiment. This corresponded to acoustic pressure amplitude of 258 kPa at the peak in figure 5.3 (125 kHz).

In the first example the Weissler reaction was monitored as a function of acoustic frequency. In this reaction iodide ions are oxidised by radicals (e.g. $OH^{\bullet}$) produced by cavitation action (see chapter 1 section 1.7.3). The rate of I_3^- production was determined electrochemically. Figure 5.3 shows the variation in I_3^- production as a function of frequency. This is compared to MBSCL recorded over the same frequency range under the same experimental conditions. It can be seen that the variation in I_3^- production, over this frequency range, follows light emission from the solution. This infers that radical production is coupled with high levels of MBSCL activity. This is perhaps not surprising as OH^* emission has been observed in the emission spectra of MBSL[110] and in turn both MBSCL

and I_3^- production would be expected to be high at high concentrations of $OH^\bullet$. Clearly there is a strong correlation between I_3^- production rates and high MBS(C)L output under the conditions stated.

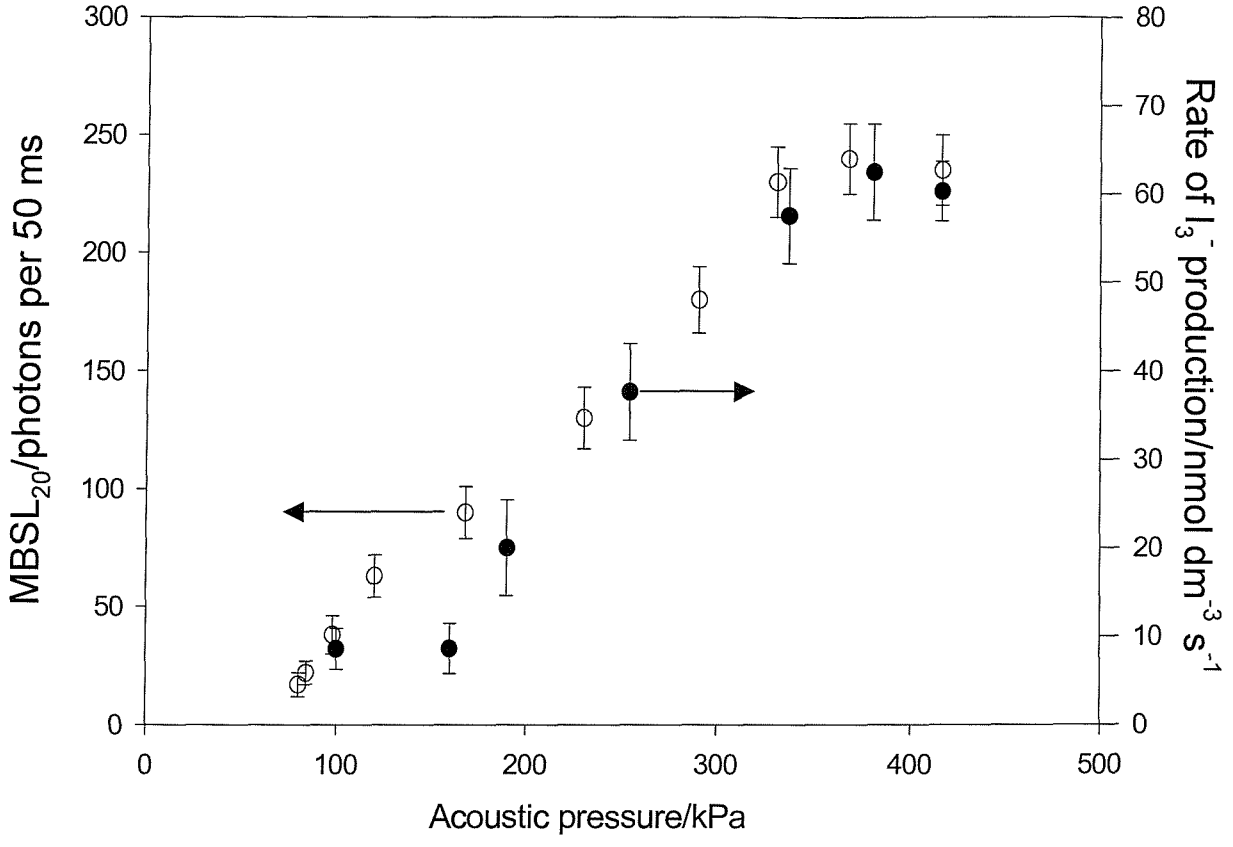

Figure 5.4 Plot showing the spatial maximum acoustic pressure amplitude dependencies of MBSL (o) and the rate of Weissler reaction (•) for ultrasonic reactor cell (A). For each measurement the cell contained 100 cm^3 of 10 mmol dm^{-3} of KI in 90 mmol dm^{-3} KCl. The solution was irradiated with 125 kHz ultrasound and the cell was temperature controlled at 25 °C. Error bars represent one standard deviation calculated using 3 repeat measurements.

Figure 5.4 illustrates the effect of varying the acoustic pressure amplitude on the rate of I_3^- production. This is compared to MBSL of the same solution recorded under identical conditions. Both the rate of I_3^- production and the sonoluminescent output correlate at high acoustic pressure (above 140 kPa, which corresponds to driving voltage amplitude of 60 V). As the acoustic pressure amplitude increases cavitation 'activity' increases. Therefore, more radicals are generated resulting in increased reaction rates. Similarly an increase in cavitation is coupled to a rise in the sonoluminescent output from the reactor.

Below 140 kPa the rate of production of I_3^- remains constant even though the light output is seen to decrease marginally. This indicates that MBS(C)L appears to be more

responsive to changes in acoustic pressure amplitudes. However, in this range it could be a detection limit problem. It must be remembered that the dose level is very small (less than 5 rad s^{-1}). The acoustic pressure recorded in figure 5.4 represents the maximum pressure recorded by the hydrophone under the conditions employed. For further experimental details see chapter 2, section 2.9.

5.3 Experimental Protocol

In the following sets of results the rate of reaction and the MBSL output of the cell have been determined over a narrower ultrasonic frequency band (120-130 kHz). This is because in all the previous results presented here, (see figures 5.2 and 5.3) the maximum rates and light output was observed in this frequency range (120-130 kHz). This allowed reduced frequency increments (1 kHz) thus avoiding aliasing and allowing a more accurate correlation between the MBSL light emission and chemical activity to be presented.

5.4 The Fricke Reaction

Figure 5.5 illustrates the rate of the Fricke reaction, (the rate of production of Fe^{3+}; see chapter 4 section 4.3) and the MBSL output of the same solution as a function of frequency. Again it is remarkable how close the luminescence pattern follows the radical trapping reaction in the reactor. This reaction is particularly useful as it is well characterised as a result of its use as a chemical dosimeter for monitoring radical generation through radiation exposure of a sample.[83] The figures in the brackets represent equivalent dose measurements. In the results shown an equivalent dose of up to 10.88 rads s^{-1} can be achieved through ultrasonic irradiation of the liquid under the conditions employed (see section 4.4).

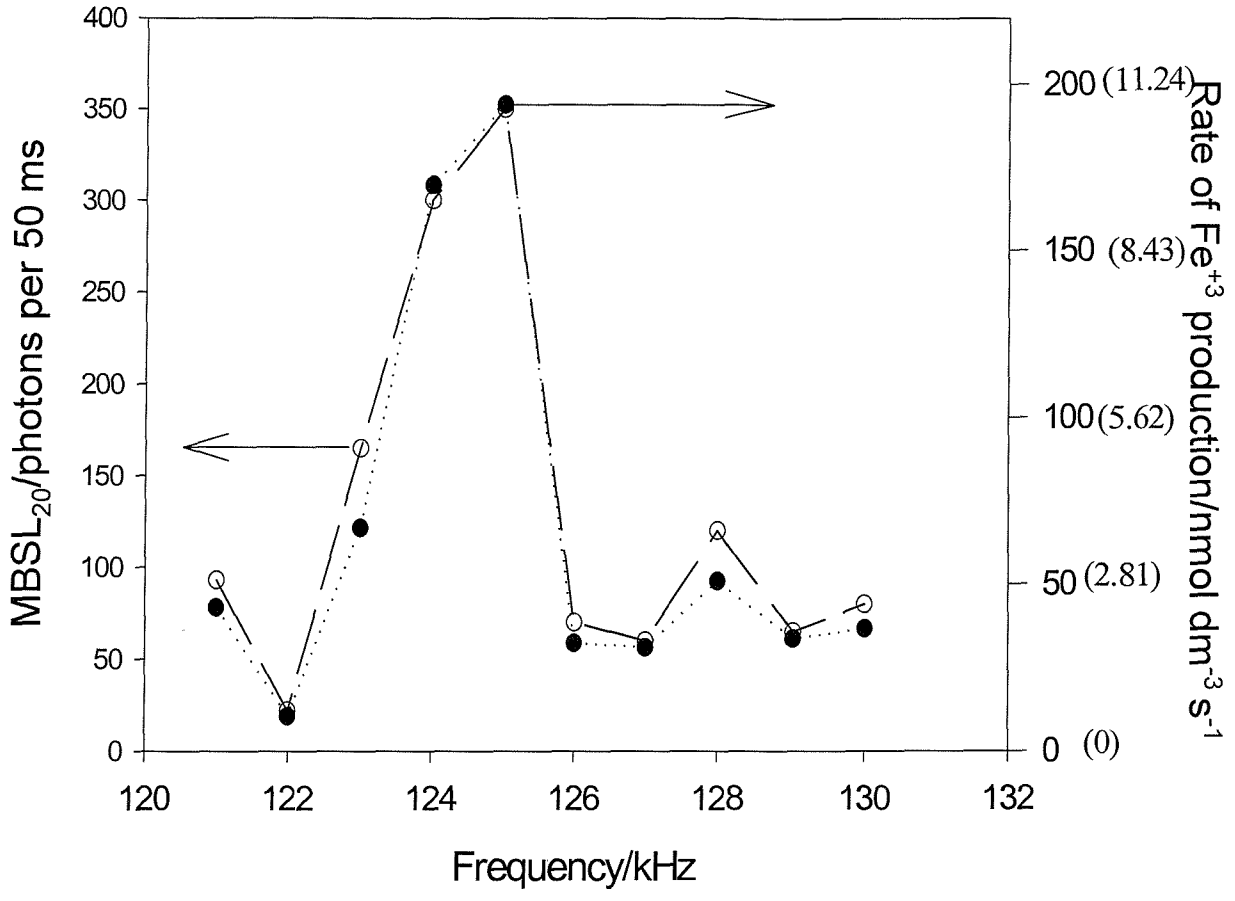

Figure 5.5 Plot showing the frequency dependence of both MBSL output of the ultrasonic reactor cell (A), (o) and the rate of the Fricke reaction (•).The points on this graph (•) represent the average of three repeat measurements. Error bars were calculated but removed for clarity. The maximum error on these measurements is ca. ± 7 nmol dm^{-3} s^{-1}. The numbers in brackets are the equivalent dose for the particular rate of Fe^{3+} production. In both cases the cell contained 100 cm^3 of an aerobic solution containing 1 mmol dm^{-3} of $FeSO_4$, 1 mmol dm^{-3} NaCl and 0.4 mol dm^{-3} H_2SO_4 thermostated at 25 °C. The drive voltage amplitude was kept constant at 100 V throughout each experiment. This corresponded to an acoustic pressure amplitude of 219 kPa at the peak in figure 5.5 (125 kHz). The cell was temperature controlled at 25 °C.

5.5 Frequency Dependence of Ultrasonically Generated H_2O_2

Both the Weissler and Fricke reactions are associated with the production of $OH^{\bullet}$.[137] Hence, it is likely that hydrogen peroxide will be produced through geminate recombination. Figure 5.6 shows the rate of production of ultrasonically generated H_2O_2 and MBSL of the same solution as a function of frequency. The frequency dependence of the rate of production of H_2O_2 agrees well with MBSL. This is not surprising given the results achieved using the Weissler and the Fricke reaction.

Sections 5.2, 5.4 and 5.5 contain conclusive evidence for the correlation between hydroxyl radical formation (chemical activity) and MB(C)SL. Section 5.6 investigates whether the rate of production of $H^{\bullet}$ also follows this trend with MBS(C)L.

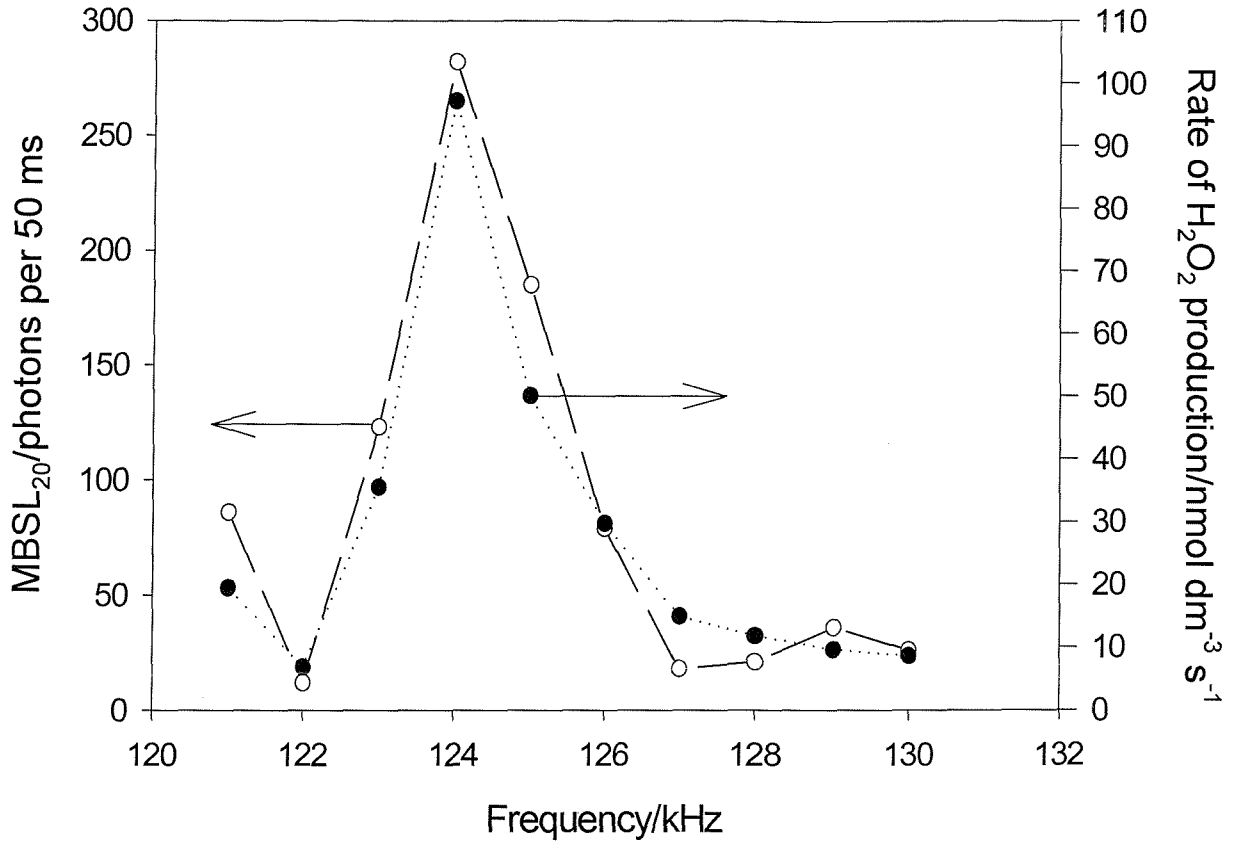

Figure 5.6 Plot showing the frequency dependence of both MBSL output of ultrasonic reactor cell (A), (o) and the rate of H_2O_2 production (•). The points on this graph (•) represent the average of three repeat measurements. Error bars were calculated but removed for clarity. The maximum error on these measurements is ca. ± 6 nmol dm^{-3} s^{-1}. In both cases the cell contained 100 cm^3 of aerobic pH 5.5 buffer (citric acid/phosphate. The drive voltage amplitude was kept constant at 100 V throughout each experiment. This corresponded to acoustic pressure amplitude of 232 kPa at the peak in figure 5.6 (125 kHz). The cell was temperature controlled at 25 °C.

5.6 Frequency Dependence of Ultrasonically Generated H•

It is known that hydrogen atoms (H•) are also generated ultrasonically by the breakdown of the solvent matrix in cavitation. However, there is less evidence for the detection of H• than OH• due to the complex aqueous chemistry of this species (see chapter 1, section 1.6). As outlined in chapter 4 (section 4.6) it is possible to trap H• using a Cu^{2+} system.

Figure 5.7 shows the rate of $CuCl_2^-$ production (the product of H• or HO_2• reactions with Cu^{2+} (see section 4.6) in a chloride medium) measured electrochemically plotted as a function of the ultrasonic frequency employed. The MBSL output of the cell is also shown in figure 5.7. It is evident that the production of $CuCl_2^-$ (and hence the production of H•) can be predicted by the MBSL output of the ultrasonic reactor. The MBSL output of the cell

also shows a broader response compared to those shown previously (see figure 5.5 and 5.6). This may be due to a number of factors. In this experiment a high NaCl concentration was employed. This will change the acoustic properties of the cell, and hence the modal structure (see chapter 3, section 3.3). In addition sonoluminescence has been shown to be dependent on the ions present within the solution.[110] However, it is clear that the sonochemical rate and the light emission still give remarkable agreement.

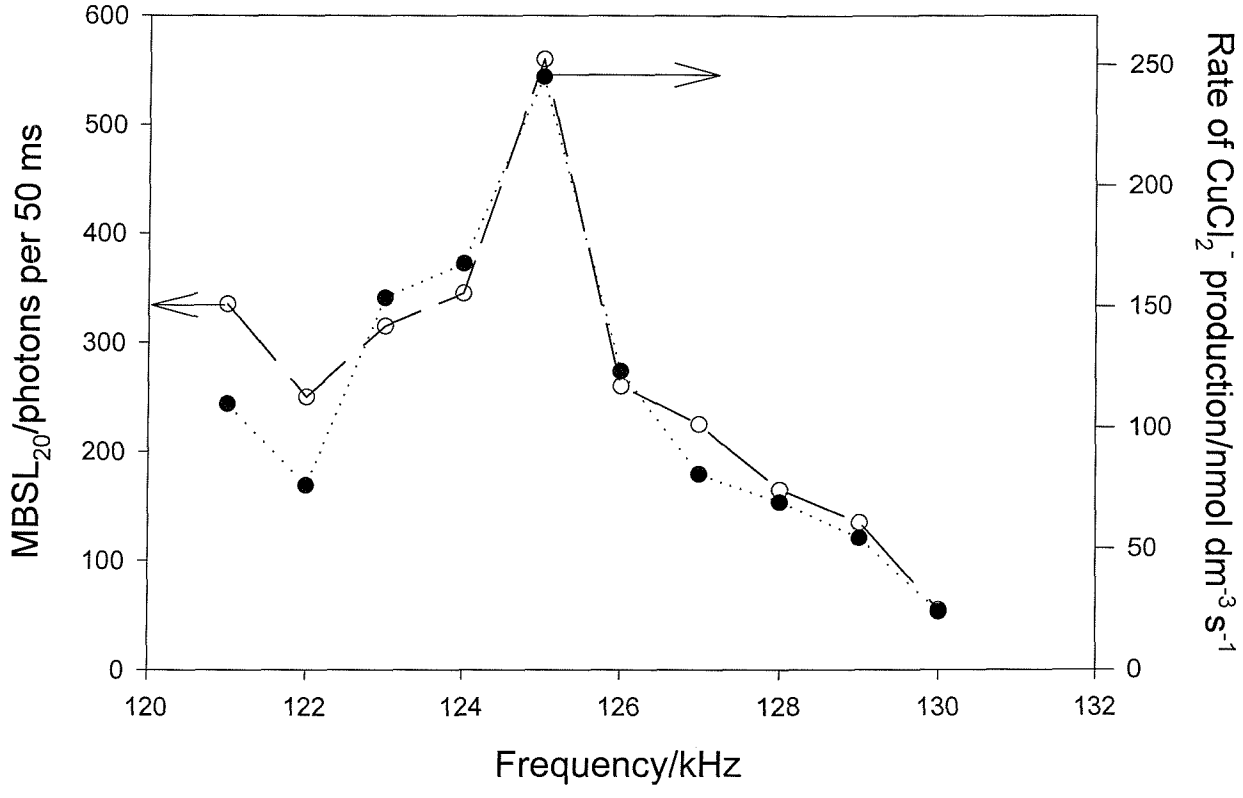

Figure 5.7 Plot showing the frequency dependence of both MBSL output of the ultrasonic reactor cell (A), (o) and the rate of formation of $CuCl_2^-$ due to $H^\bullet$ generation (•). The points (•) on this graph represent the average of three repeat measurements. Error bars were calculated but removed for clarity. The maximum error on these measurements is ca. ± 8 nmol dm^{-3} s^{-1}. In both cases the cell contained 10 mmol dm^{-3} of $CuSO_4$ in 1.5 mol dm^{-3} NaCl. The drive voltage amplitude was kept constant at 100 V throughout each experiment. This corresponded to acoustic pressure amplitude of 262 kPa at the peak in figure 5.7. This was kept constant throughout experiments. The cell was temperature controlled at 25 °C.

5.7 Pressure Measurements

Pressure measurements within the liquid phase of a reactor are vital to the understanding of cavitation inception and bubble dynamics. A hydrophone, placed within the liquid, will monitor the time-varying component of the pressure field. This consists of two components

(see chapter 2, section 2.9). It has been shown that for vessels of this size and within this frequency range, the driving field is strongly modal[131] (see chapter 3, section 3.3). As a result the driving acoustic pressure amplitude exhibits spatial maximums and minimums where, for example, the MBSCL images appear bright and dark, respectively (see chapter 3 section 3.3). These images contain patterns of concentric rings typical of a cylindrical Bessel function, as viewed from above the ultrasonic reactor. These patterns are frequency-dependent, so that as one moves to higher frequencies one tends to obtain more rings, of increasingly narrow thickness and spacing[131] (see chapter 3, figure 3.11). This results in pressure fluctuations within the cell depending on the position of the hydrophone.

Figure 5.8 is a plot showing the variation in pressure amplitude recorded in three positions in ultrasonic reactor cell as a function of frequency for a constant 100 V driving voltage amplitude applied to the transducer. These data show that the pressure measured within the cell not only follows the transducer resonance (in this case *ca.* 27 kHz) but also has the pressure components contributed by a combination of the transducer/cell geometry. This can be seen as a series of pressure peaks within figure 5.8 which vary depending on the position of the measurement. Indeed there is a pressure maximum in the region of 120 - 125 kHz which is the same frequency region as the luminescence maximum and reaction rate maximum recorded for the same cell and shown previously (see figure 5.5 and 5.6). However, the pressure maximums shown in figure 5.8 at lower pressures do not coincide with high reaction rates. Only luminescence appears to predict where reaction rates will be highest.

It can be deduced that pressure measurements, at points within the cell, cannot be relied on to predict where all high sonochemical reaction rates will be observed. It is also important to consider in this case the effect the modal structure of the sound field within the cell will have on the MBS(C)L light measurements recorded with the photon counter.

MBS(C)L in a given volume depends on exceeding the stable cavitation threshold. As the acoustic pressure is increased the volume of the liquid super-threshold increases (once the threshold is exceed). But as acoustic pressure increases activity in areas, which are super-threshold also increases. However, since the detector exhibits a finite 'footprint' (see chapter 2 section 2.4) it will in general follow the amplitude of the driving field as it measures at a few points along the axis of the cylinder.

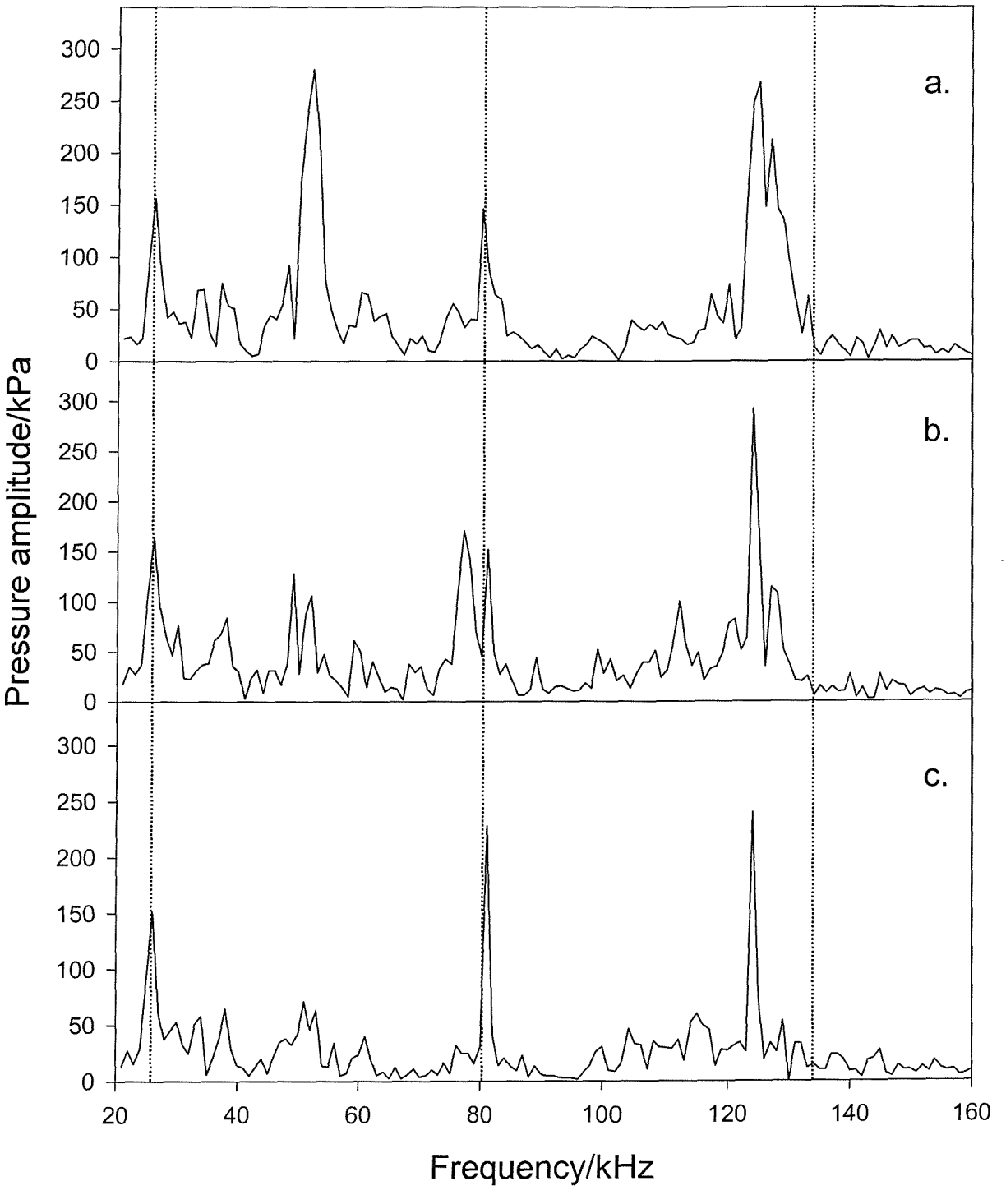

Figure 5.8 Plot showing the variation in pressure amplitude recorded in three positions in ultrasonic reactor cell (A) as a function of frequency. The cell contained 100 cm^3 of solution containing 10 mmol dm^{-3} KI and 90 mmol dm^{-3} KCl. The volume in the cell matched that employed in all the other experiments. The hydrophone was positioned *ca.* 1.5 cm from the base of the cell. 'a', 'b' and 'c' represent the hydrophone in the centre, 1 cm off centre and next to the wall respectively. The dashed lines represent multiples of the resonance frequency of the transducer. The cell was temperature controlled at 25 °C.

5.8 Audible Output of the Cell

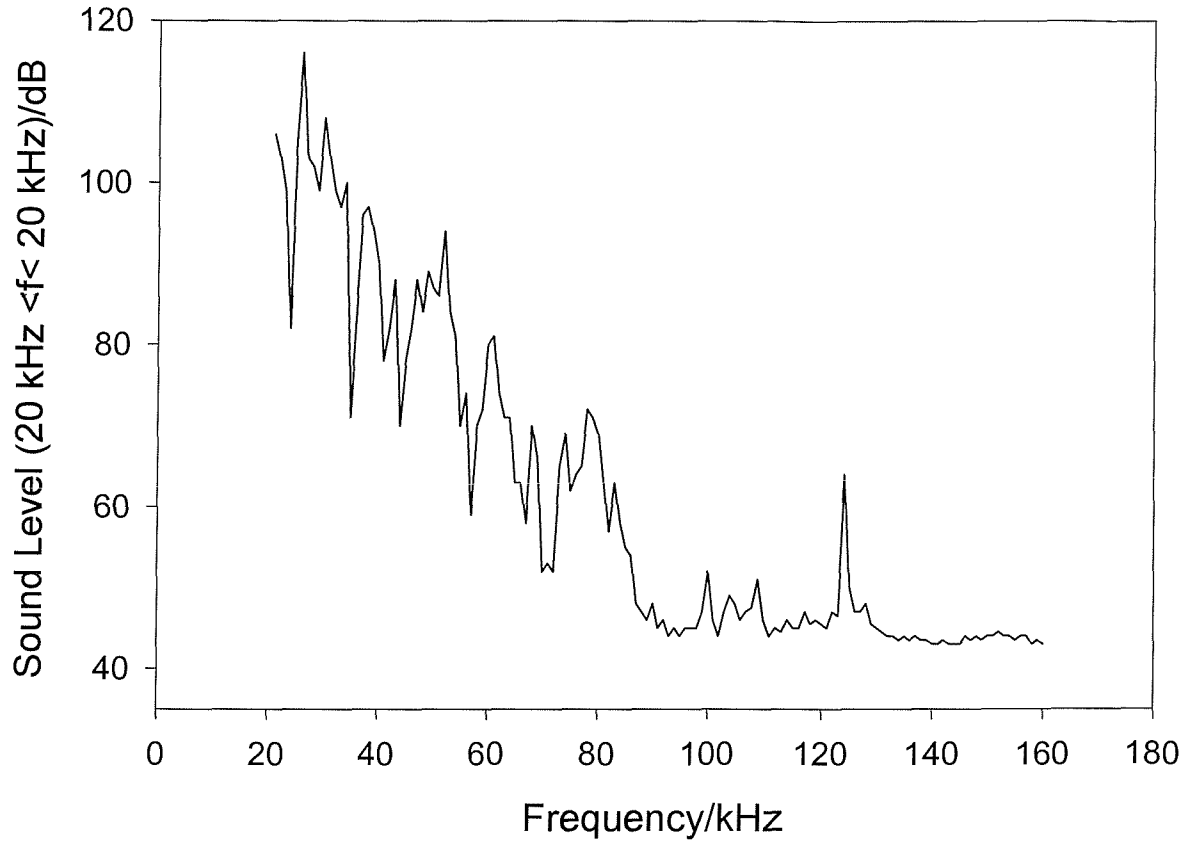

Figure 5.9 Plot showing the variation in the broadband airborne audible output of the ultrasonic reactor cell (A) employed as a function of frequency. The cell contained 100 cm^3 of an aqueous 10 mmol dm^{-3} KI and 90 mmol dm^{-3} KCl solution. The drive voltage amplitude was kept constant at 100 V throughout the experiment. This corresponded to an acoustic pressure of 258 kPa amplitude at the peak at 125 kHz. All other physical parameters are the same as shown in figure 5.3.

Figure 5.9 shows how the audible noise output of the cell varies as a function of acoustic driving frequency measured using a calibrated microphone 'A' rated for normal human hearing[128] ($20 < f < 20$ kHz; see chapter 2 section 2.8 for experimental procedure). In this case the highest acoustic output is at ca. 27 kHz, which coincides with the fundamental of the transducer. If the acoustic emission is compared to both MBSL and the rate of the radical trapping reactions, it is clear that the high acoustic emission does not predict where the highest rates of reaction are. This is surprising as the high acoustic emission indicates that there are large amounts of inertial cavitation within the cell. Hence one would expect the radical population to be high also at these frequencies. There appears to be little correlation between audible output and chemical activity (radical formation) despite the fact

that one would expect both processes to be inexorably linked. MBS(C)L alone appears to predict where reaction rates will be highest for a particular reactor under a given set of physical conditions.

5.9 Comparison of Detectors

When comparing results from different techniques a number of points most be considered. Of paramount importance is whether the detector employed is a point or a global sensor. In the case of pressure measurements the hydrophone measures the pressure at the point in the liquid at which it is placed. However, there can be a strong spatial variation in pressure below the Schreoder frequency.[134] Pressure measurements therefore are inadequate when assessing the activity over the complete volume of the cell. This may also be the case with light measurements depending on the sensing volume of the light detector. Care must be taken that the detector senses the entire volume of the cell. This will depend on the solid angle of the detector and the position of the detector in the experimental set-up. Clearly, above the cell at a suitable height to detect the entire volume of the cell is most appropriate. In a recent paper by Beckett and Hua[23] the light detector was placed at the side of the cell. There is a danger with this configuration in that the detector could be sensing maximums or minimums in the band pattern (see chapter 3 figure 3.11) and hence an inaccurate response may be obtained.

Chemical sensors are truly global with the results reflecting the overall activity within the cell (providing the solution within the cell mixes reasonably well). It is also possible with chemical tests like the Fricke reaction to compare results directly to standardised systems (dosimeters for radiation) and in turn a calibrated reactor can be produced. It was also illustrated in chapter 4 that the chemical sensor gave a small but measurable response below the theoretical pressure amplitude for stable cavitation. However, this is probably spatial averaging of the hydrophone in addition to the difficulty of positioning the hydrophone at the pressure maximum.

5.10 Frequency Dependence of Chemical Rates

A number of investigations have reported the effect of ultrasonic frequency on a variety of sonochemical reactions. In many cases the sonochemical rates have been determined and compared at spot frequencies (e.g. a range of spot frequencies from 20 kHz to 1.7 MHz).[99,

[150, 151] However, the results reported here suggest that the study of discrete frequencies over a wide frequency band may produce misleading results. It has been shown here that a change in frequency of the order of 3 kHz can produce up to 3 orders of magnitude change in the rate of the reactions studied. Clearly discrete frequencies may miss the most efficient reactor frequency. The influence of frequency on acoustic cavitation and sonochemistry is poorly understood.[131] Neglect of the dominant cause of frequency-dependence, that of the amplitude of the driving field as a result of the frequency characteristics of the driving transducer and the sound field, is common place.[23, 159]

The frequency dependence of the normal components of a sonochemical reactor was shown in chapter 2 (see section 2.6). All the components have frequency dependence to a greater or lesser extent. It should be noted that if the acoustic pressure field within the vessel is mapped, none of these dependencies need be known bar that of the detector. Mapping the field is not a difficult task when there is no cavitation, but it is time consuming, and often a measurement of the spatial peak pressure is adequate (e.g. for threshold measurements). However, in many studies no acoustic pressure measurements are taken, and in such circumstances the frequencies dependencies of the various components needs to be considered. The great majority of sonochemical studies, however, simply note that the driving transducer is resonant, and drive it at the resonance quoted by the manufacturer. Some commercial systems rely on electrical matching of the transducer to the amplifier. Although this leads to a high-energy transfer to the transducer, it does not necessarily correspond to a high resonance of the cell. However, in studies where the frequency dependence of a reaction is to be investigated, keeping to a resonance is not an option. Even if the driver has multiple resonances and measurements are restricted to these, the acoustic pressure field needs to be measured not only because the quality factors and efficiencies of the different transducer resonances will likely differ, but also because the spatial in homogeneity of the modal sound field must be reconciled with the spatial averaging inherent in the detector system. Whilst ignoring the frequency dependence of the signal generator and power amplifier does not often lead to great error, neglect of the frequency dependence of the vessel is to ignore the most important frequency dependency in the system.

However, studying the MBSL or MBSCL output over a wide and continuous frequency range of a particular system will enable the optimum of the particular cell, transducer, reactor geometry, solution and wall properties to be found. It is suggested that statements claiming 'the optimal frequency' for sonochemistry in general are to be avoided. These

conclusions are highly dependent on the experimental set-up, and are a direct result of the combination of transducer efficiency, vessel acoustics and chemistry of the experimental arrangement employed, and hence are ultimately misleading.

It is also usual for authors to assume that at all frequencies an identical acoustic power is delivered to the liquid sample (which neglects the frequency characteristics of the transducer).[23, 159] Furthermore, a common practice is to maintain the same 'power/volume ratio' in the test sample over a wide frequency range. Considering that cavitation is a non-linear threshold phenomenon, it is the spatial peak (and not spatially averaged) acoustic pressure, which will be important for cavitation inception; and, if the sound field in the vessel is inhomogeneous (see chapter 3, section 3.3 and figure 5.8), these two measures of the pressure can be drastically different. Indeed as the modal character of the sound field changes so-too does the volume of the reagent, which is ultrasonically treated (i.e. exposed to a sufficiently high amplitude driving field to generate cavitation). It is suggested here that authors should refer to the threshold for cavitation, which exists in pressure/radius/frequency space, and also the consequences of differing bubble populations within the liquid.[131]

It is also important to remember that the comparison of chemical rates and cavitation activity produced by a variable frequency ultrasonic field requires consideration of the time dependence involved. As an example chemical rates are always quoted as a 'per second' measurement. Clearly as the frequency of the ultrasonic field is raised, the number of cycles per second also increases. There will clearly be more opportunities to generate cavitation events at higher frequencies compared to lower frequencies in the 'per second' sense. However, it also must be remembered that at the same time as the frequency is increased the cavitation threshold will rise.[2] In turn one would expect that for a given bubble population there would be less inertial cavitation at higher frequencies. This is of course if it is assumed that inertial cavitation is solely responsible for sonochemistry. These opposing effects will complicate the interpretation of comparative rate measurements over a wide frequency range.

It is also interesting to note that in the majority of cases studied both here and in the literature, the rates of reactions seem to have been solely focussed on the rich radical chemistry that can be generated. While this gives a good indication of some aspects of sonochemistry, it clearly does not address the fundamental question of reactions that are driven by temperature within the gas phase of the bubble. The relationship between these gas phase rates and MBS(C)L has still to be ascertained. This remains a key question to be addressed.

5. 11 Conclusions

The study presented in this chapter shows that it is possible to measure both accurately and quantitatively the rate of radical production over a frequency ranges 20-160 kHz under controlled physical and acoustic conditions. It was shown that reaction rates of nmol dm^{-3} s^{-1} could be determined. It was also illustrated that MBS(C)L followed the rate measurements precisely with the added complication of decreasing transducer efficiency for frequencies in excess of the resonance frequency. Luminescence appears to be an extremely good sensor for predicting optimum performance from an ultrasonic reactor. The most important finding from this frequency study is the need for fine frequency resolution of the sound field in an ultrasonic reactor around the test frequency.

Having in chapter 3 characterised my sound field and vessel and in chapters 4 and 5 characterised a range of sonochemical sensors, I was invited by Prof. Leighton to test these sensors in a proposed standard vessel and liquid being put forward by NPL (National Physics Laboratory). Cavitation in this proposed "standard cavitation system" was to be set up and monitored by NPL's proposed "standard cavitation detector". To compare detectors a range of researchers were invited to NPL to test their sensors. Not only was I invited, I assisted in the deployment and testing of a range of sensors from other partners.

CHAPTER 6

COMORAC: CHARACTERISATION OF MEASURES OF REFERENCE ACOUSTIC CAVITATION

NPL acknowledged the need to follow Apfels "know thy" advice. Prior to this test they developed a sound field/vessel, which they hoped would be standard. They already had proposed a standard liquid and a standard detector. Prof. Leighton suggested that they test their detector against other sensors; and also see if those other sensors could tell us about how well their liquid and vessel meet the requirements of a standard. A number of other partners were involved in the COMORAC experiment. A series of experiments were performed in an ultrasonic cleaning bath, which was located in NPL (see chapter 2, section 2.11). Both acoustic and chemical sensors, designed by the partners, were tested in the bath. Experiments were performed with solutions prepared with filtered de-ionised water (20 litres) degassed to 1.5-2 ppm, in the temperature range 21-26.5 ^{o}C. In contrast to the experimental conditions employed in chapter 4 (where experiments were performed under aerobic conditions) an attempt was made to control the number of random nucleation sites for the onset of cavitation. Prior to undertaking experiments NPL believed the sound field in the bath to be diffuse (though the MBSCL images in this thesis proved otherwise (see figure 6.1)). In addition the frequency was fixed at 40 kHz for all experiments. The results obtained from these test sensors employed were critically analysed with view to the development of a standard reference system comprising of a vessel, sound field and sensor.

This chapter summarises the results obtained in the COMORAC experiment. Three sensors were successfully tested by the present author including: MBSL, MBSCL and the electrochemical Weissler reaction. The results obtained from these sensors are compared to the other chemical tests performed by the other partners (e.g. the Fricke and terephthalic acid dosimeters were performed spectrophotometrically by Dr. Gareth Price, University of Bath). Finally section 6.8 discusses the results obtained by the other partners using acoustic sensors. The difficulties in performing such experiments under the conditions imposed will also be emphasised. This included the fact that due to time restrains, much of the chemical tests (the Weissler and Fricke reactions) could only be performed once.

TEST RESULTS

6.1 Multi Bubble Sonochemiluminescence (MBSCL)

Figure 6.1 illustrates sonochemiluminescence pictures recorded of the bath using a luminol solution at each of the power settings (see chapter 1, section 1.8, for mechanism of light formation and chapter 2 section 2.11, table 2.1 for the relationship between the %power and the drive voltage). The images were recorded using an image intensified CCD camera. The experimental rig and an account of the experimental procedures employed were discussed in chapter 2, section 2.11 and 2.12.

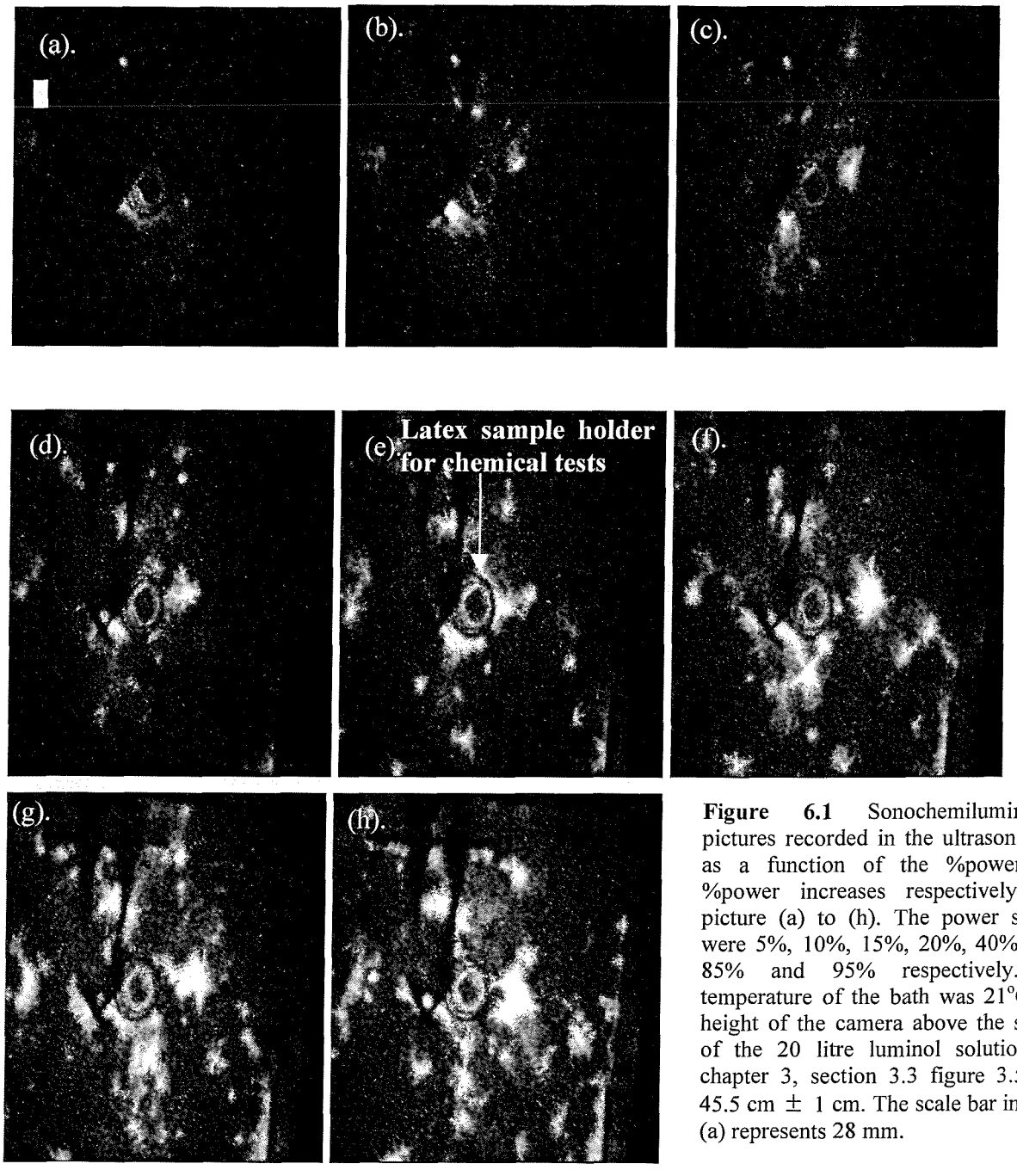

Figure 6.1 Sonochemiluminescent pictures recorded in the ultrasonic bath as a function of the %power. The %power increases respectively from picture (a) to (h). The power settings were 5%, 10%, 15%, 20%, 40%, 65%, 85% and 95% respectively. The temperature of the bath was 21°C. The height of the camera above the surface of the 20 litre luminol solution (see chapter 3, section 3.3 figure 3.5) was 45.5 cm ± 1 cm. The scale bar in frame (a) represents 28 mm.

The results obtained from these pictures proved to be the most valuable of the entire experiment. Prior to obtaining the MBSCL pictures the sound field in the bath was believed by NPL to be diffuse. However, the MBSCL pictures show that this is clearly not the case. The sound field in the bath is spatially non-uniform. The spatially non-uniform nature of the sound field is exemplified by the existence of hot and cold spots within the bath (see figure 6.2). However, in contrast to ultrasonic reactor cell (A) (see chapter 3, section 3.3) the modal nature of the sound field is difficult to understand. At a glance the MBSCL pictures enabled the identification of the chemically 'active' and chemically 'inactive' zones within the ultrasonic bath (hot and cold spots respectively). In addition it is important to note that the presentation of results in terms of the %power was enforced by NPL.

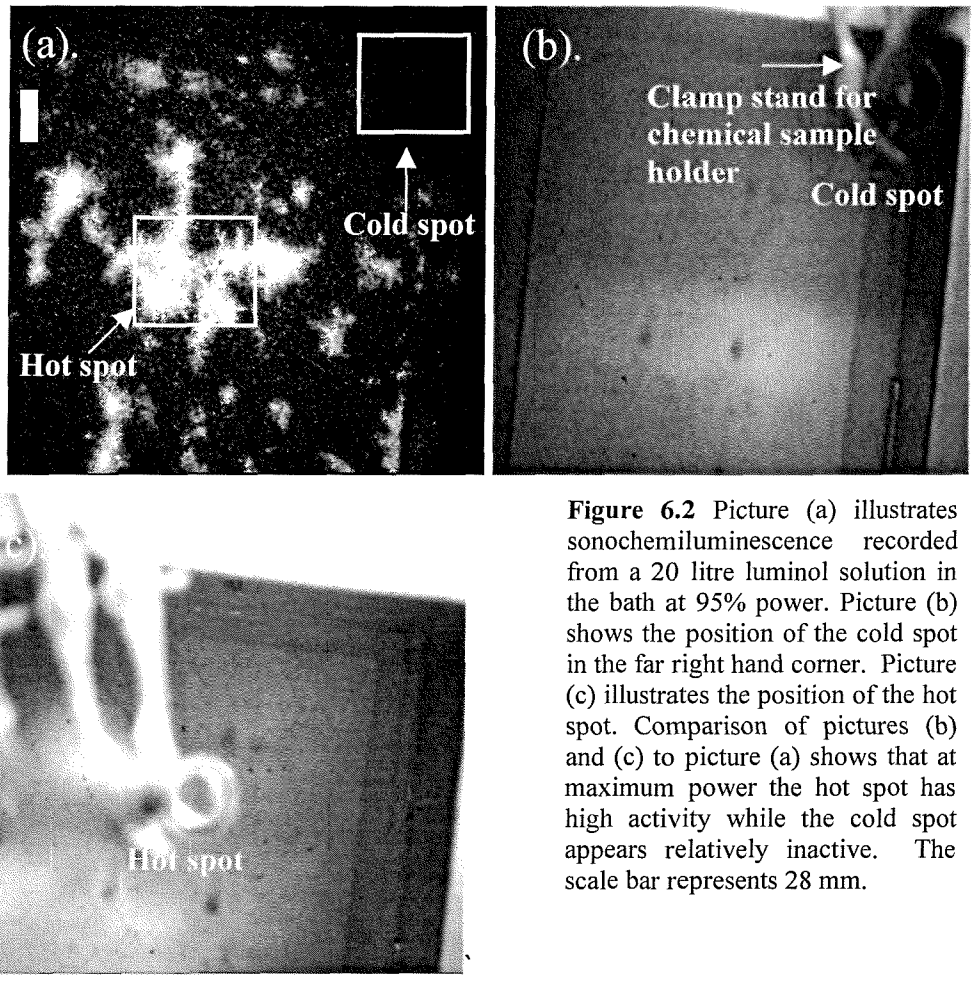

Figure 6.2 Picture (a) illustrates sonochemiluminescence recorded from a 20 litre luminol solution in the bath at 95% power. Picture (b) shows the position of the cold spot in the far right hand corner. Picture (c) illustrates the position of the hot spot. Comparison of pictures (b) and (c) to picture (a) shows that at maximum power the hot spot has high activity while the cold spot appears relatively inactive. The scale bar represents 28 mm.

As a result of the results presented in figure 6.1 the experimental protocol suggested by NPL for the COMORAC experiment had to be revised. Initially it was suggested that the cavitation 'activity' sensors be positioned in the centre of the ultrasonic bath. However, due to the spatially non-uniform nature of the sound field, the position in which the cavitation sensors (the sample holder in the case of the chemical sensors) were placed in the bath proved

crucial. To overcome this problem it was decided that measurements would be performed in two positions with each sensor notably the hot and the cold spot. The position of the "hot" and "cold" spots in the bath employed for tests during the COMORAC experiment are illustrated in figure 6.2. The difference in the chemical activity of these two positions is emphasised in section 6.3 where the Weissler reaction was the only chemical test sensitive enough to yield data in the cold spot.

The photon count was recorded in both the "hot" and the "cold" spot (see figure 6.2) and in the centre of the tank over the range of power settings in the bath. The results obtained are illustrated in figure 6.3 and 6.4.

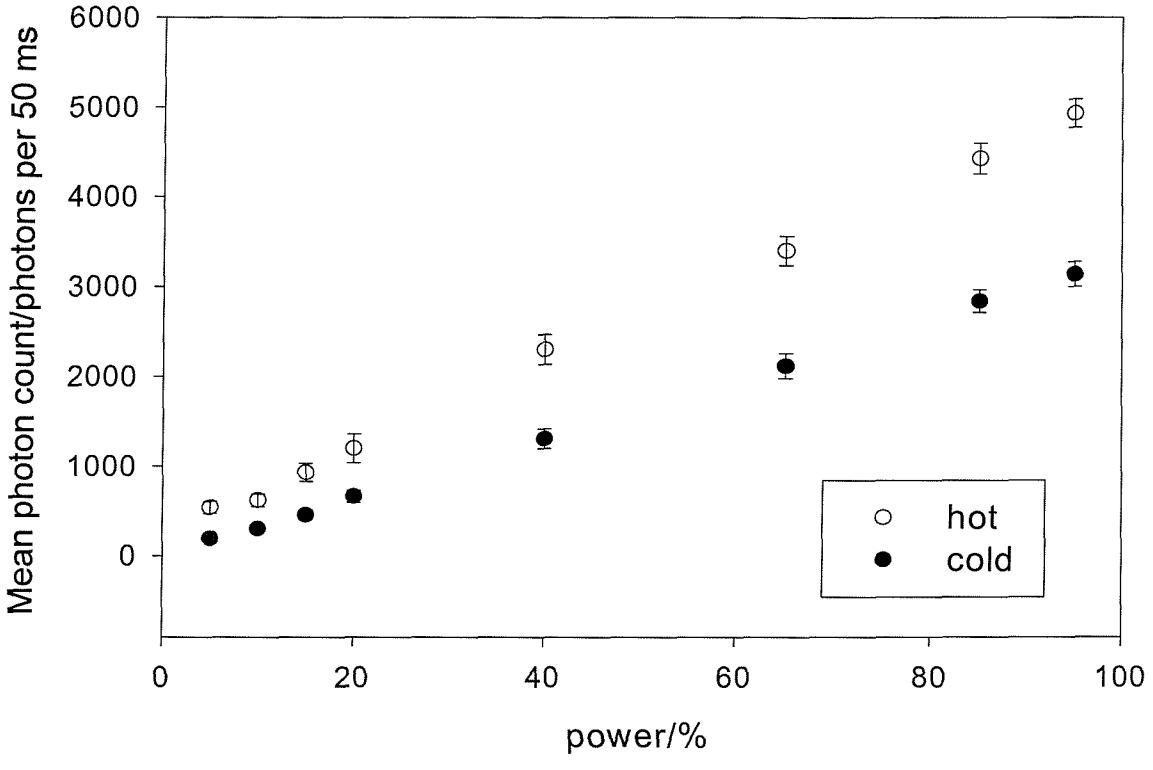

Figure 6.3 Plot showing the mean photon count recorded from a 20 litre luminol solution (see chapter 3, section 3.3 figure 3.5) with the photon counter positioned directly above the hot (o) and cold spot (•) recorded as a function of time. In the case of the hot spot the temperature was 22.8 °C. The height of the photon counter above the surface of the water was 18 ± 0.5 cm. The temperature in the cold spot was 23.4 °C. The error bars represent ± one standard deviation from the mean photon count. There are no dissolved oxygen measurements (DO_2), as the sensor could not be deployed in the alkaline pH of the bath.

The MBSCL photon count increases linearly with power above 20%. At lower power levels there is little variation in the photon count. This effect is not surprising if the MBSCL pictures are examined (see figure 6.1). Above 20% there is an observable increase in the light

output and hence cavitation activity. It can also be seen that there is a much larger photon count achieved when the photon counter is position over the hot spot (figure 6.3, 5000 photons per 50 ms) compared to the photon count achieved when the sensor is position above the centre of the bath (1700 photons per 50 ms). This is as expected and agrees with the MBSCL pictures recorded in figure 6.1. It should also be noted that the sensor footprint of the photon counter is relatively large. Also the metallic nature of the ultrasonic bath (see chapter 2, section 2.11) would scatter light resulting in a signal when the sensor was placed over the cold spot. This effect was observed in figure 6.3 where the photon count in the cold spot was higher than expected considering the MBSCL images recorded in the same position (see figure 6.2). Figure 6.4 shows that there is marginal hysteresis between the forward and the reverse scan (not unexpected with cavitation[22]).

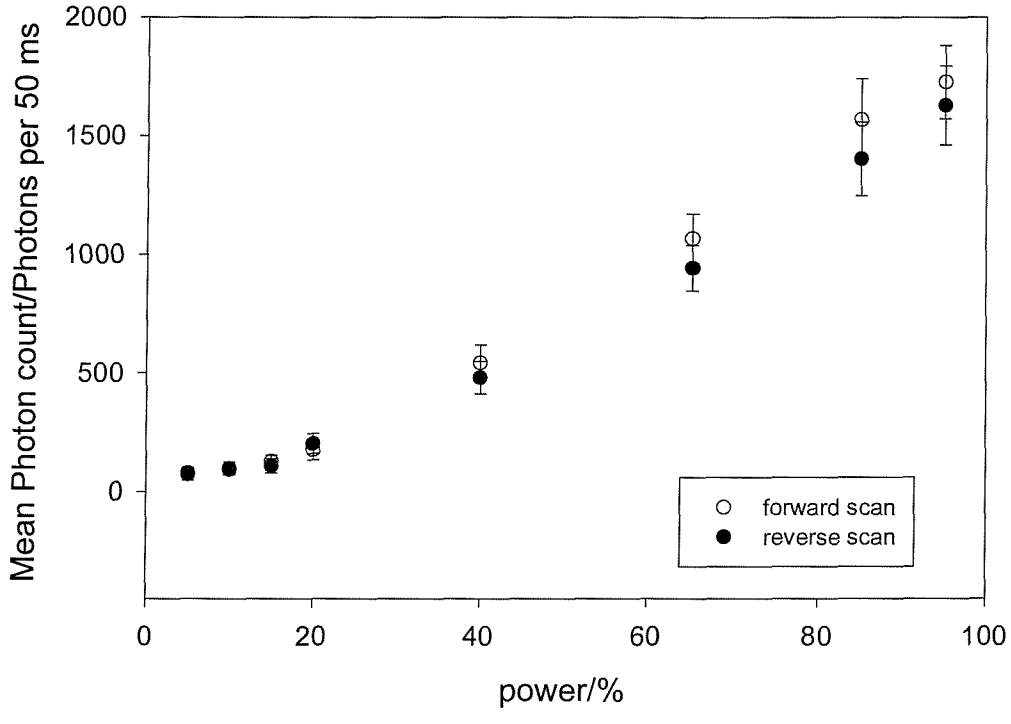

Figure 6.4 The sonochemiluminescence of a 20 litre luminol solution (see chapter 3, section 3.3 figure 3.5) recorded in the centre of the bath. Measurements were performed in both the forward (o) and the reverse direction (•) at the different powers respectively. The temperature was 21.7 ^{0}C. The height of the photon counter window above the surface of the water was 20 ± 1 cm. The error bars represent ± one standard deviation from the mean photon count. There are no DO_2, as the sensor could not be deployed in the alkaline pH of the bath.

MBSCL has a number of advantages including the following:

• A high photon count is achieved when a luminol solution is employed. This makes it easy to detect the light emission in comparison to sonoluminescence (5000 photons at 95% power compared to 8 photons in the case of MBSL see figure 6.5).

• The detectors are non-invasive. They are positioned above the ultrasonic bath so they do not affect the sound field within it.

• MBSCL allows visual imaging of the cavitation activity within the tank. This allows easy identification of the hot and cold spots within the bath. It is possible to distinguish a hot spot from a cold spot using the photon counter (see figure 6.3). This assumes that the hot and cold spots are sufficiently separated to be resolved and is dependent on the footprint of the detector (see chapter 2, section 2.4). The photon counter used in these experiments was not a local sensor. However, with the use of a lens to focus the light from a point within the test environment this sensor can be converted to the latter.

The main disadvantages of MBSCL are as follows:

• The technique requires the use of pure specialised chemicals. Highly basic conditions are required (pH 12). This prevents some other techniques being employed at the same time (acoustic sensors). However, it can be performed simultaneously with any of the chemical techniques used, provided an immersed cell with an "acoustically transparent" window is employed.

• Expensive equipment and blackout conditions are required to measure low-level light emission.

6.2 Multi Bubble Sonoluminescence (MBSL)

Sonoluminescence from a treated (filtered and degassed) water sample was recorded with the photon counter positioned in the region of the hot spot (see figure 6.2). The photon count as a function of power is illustrated in figure 6.5.

The error bars in the figure 6.5 appear large but the low photon count must be noted. MBSL is linear with time above 20% power. Below this level a plateau was observed. This was due to the low photon count for MBSL at the lower power levels (1 photon). This makes it difficult to detect and to distinguish it from the background reading. The results obtained compare well with the MBSCL photon count (40-80 %). However, with MBSL a plateau was observed at higher power levels in comparison to MBSCL experiments, which was linear with the %power. This may be due to the difficulty in detecting such low light levels from the background photon count.

The advantages of this technique are as follows:

• Experiments were performed under aqueous conditions (e.g. no chemicals were required).

• MBSL can be used in tandem with other sensors as it is performed under such mild conditions. This is in contrast to MBSCL (see section 6.1).

The main disadvantages of this technique are as follows:

• The MBSL photon count is so low it makes it difficult to detect. In contrast to MBSCL the technique does not allow the identification of hot and cold spots within the tank.

• Blackout conditions are required to detect the low level light emission.

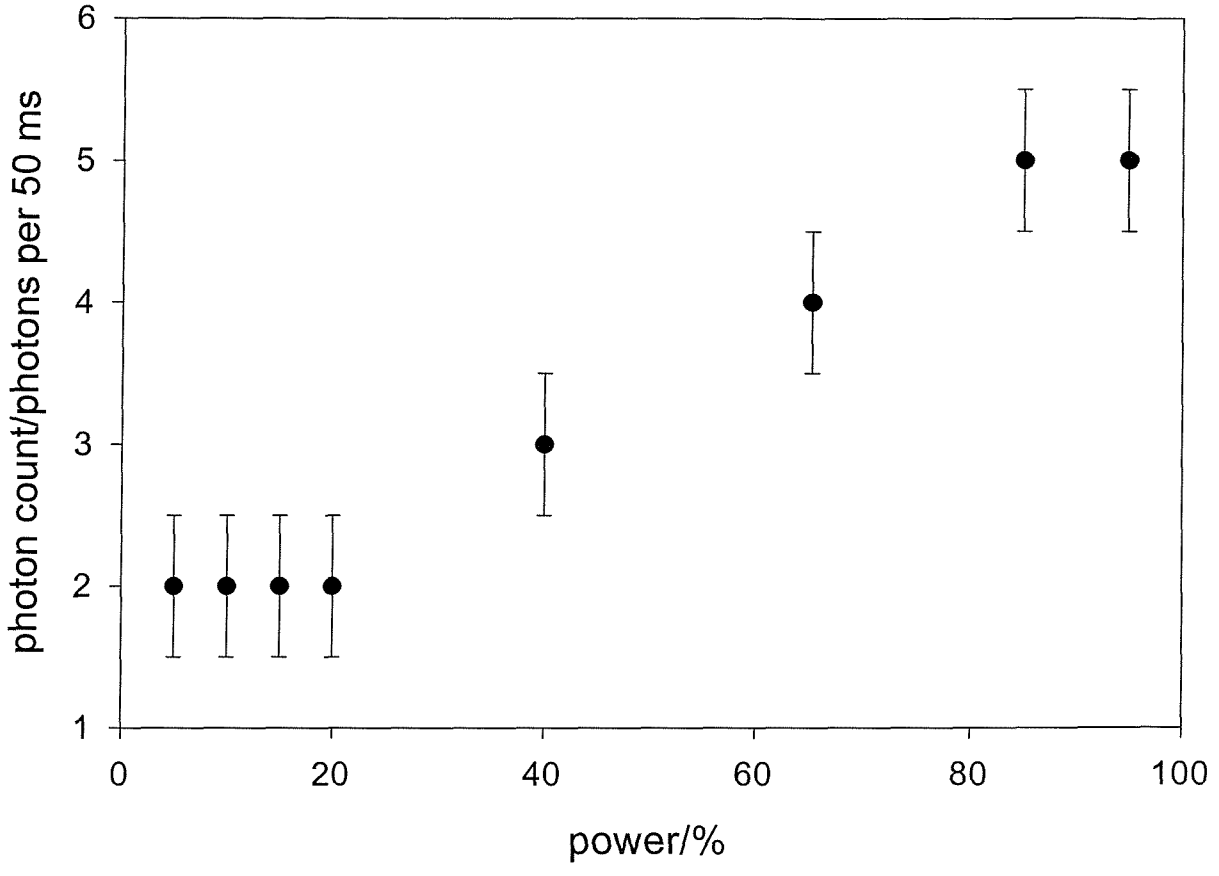

Figure 6.5 Plot showing the mean photon count recorded from a 20 litre solution of water with the photon counter positioned in the region of the hot spot. The initial DO_2 was 3.91 ppm and the temperature was 25.5 °C. The height of the photon counter above the surface of the water was 22.5 ± 0.5 cm. The final DO_2 was 4.44 ppm and the temperature was 26.5 °C. The error bars represent ± one standard deviation from the mean photon count.

6.3 The Weissler Reaction

The Weissler reaction was the only chemical test, which was conducted electrochemically during the COMORAC exercise. The Weissler reaction was performed by positioning an "acoustically transparent" cell in the ultrasonic bath. The employment of this cell was found to be necessary to overcome the noise associated with the grounded bath. The

cell was prepared using the finger of a latex glove (see chapter 2, section 2.11, for cell design). The solution was pumped from the acoustically transparent cell to the flow cell (see chapter 2, section 2.2) and back to the acoustically transparent cell in a closed loop system during the irradiation process. The experimental set-up (the flow cell and peristaltic pump) was the same as in section 4.1. The reaction was carried out in the hot spot and a MBSL photon count was recorded simultaneously. An example of the experimental results achieved is illustrated in figure 6.6.

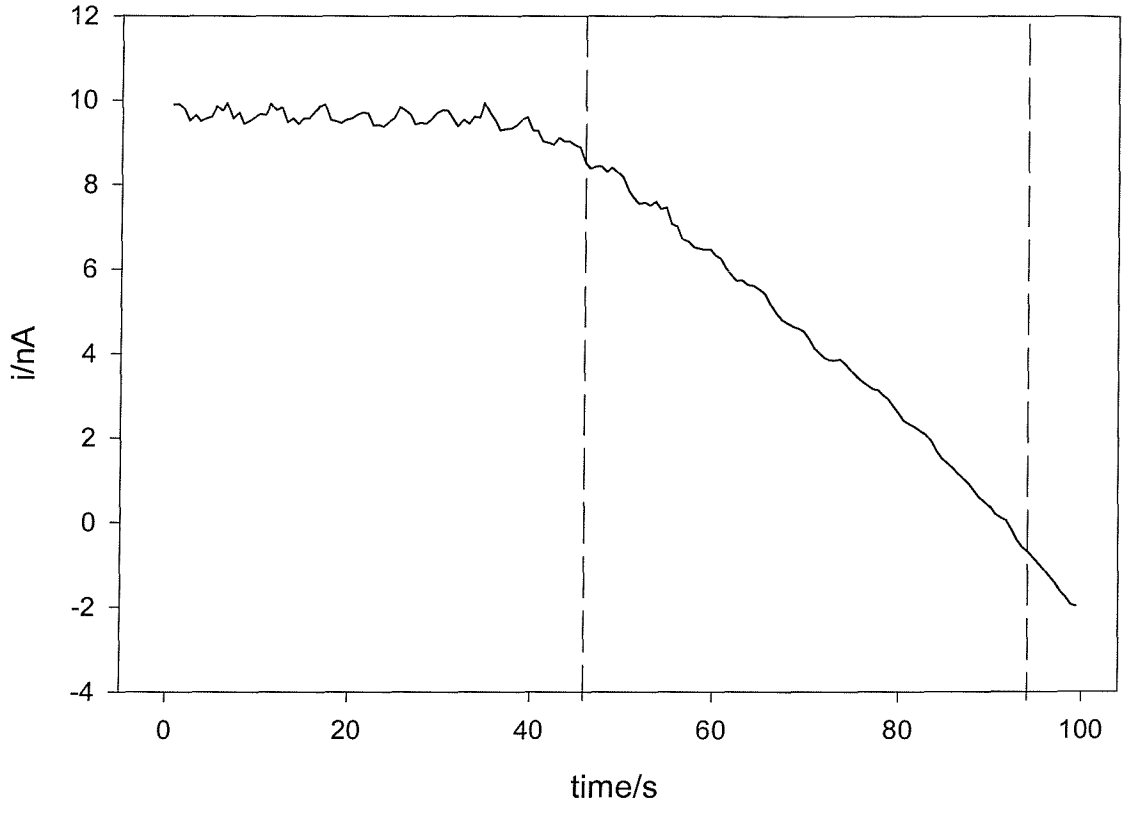

Figure 6.6 Plot showing an example of the experimental results achieved from the electrochemical Weissler reaction performed at COMORAC. The "acoustically transparent" cell positioned at the hot spot contained 20 cm^3 of 100 mmol dm^{-3} KI. The 0.5 mm diameter platinum electrode was held at +0.2 V vs SCE. The ultrasound (85% power) and the peristaltic pump (A) was turned on at time t = 0. The dissolved oxygen was 17.16 ppm and the temperature was 22.8 °C. The linear section between the two dashed lines (---) was used to calculate the slope, which was required to calculate the rate of the reaction (see chapter 2, section 2.3 equation (2.2)).

The rate of the Weissler reaction (•) recorded as a function of the % power is illustrated in figure 6.7. The rate of the Weissler reaction increases linearly with power up to 40% but then it can be seen to plateau with respect to the % power. The MBSCL photon count recorded simultaneously as the Weissler reaction at each power setting is also plotted in figure 6.7. In contrast to the Weissler reaction, the MBSCL photon count increases linearly with power

above 20%. It is important to note that due to the time constraints during the project only one set of data was recorded for the Weissler reaction.

- The difference between the Weissler reaction and MBSCL is summarised in figure 6.8. The Weissler reaction is a local sensor (20 cm^3 of 100 mmol dm^{-3} KI solution placed at the hot spot site (A) in figure 6.8) while the photon counter spatially averages. Examination of the sonochemiluminescent pictures in figure 6.1 shows that there is a considerable increase in light output when the power is increased above 40 % at the hot spot. When the power is increased further the light output increases but the magnitude of this effect is not as large. In addition, the photon counter samples a large volume of the tank. Hence the increase in photon count with power may be the result of the following:
- Reflections from the tank.
- More active sites contributing to the recorded signal (B-E) in figure 6.8.

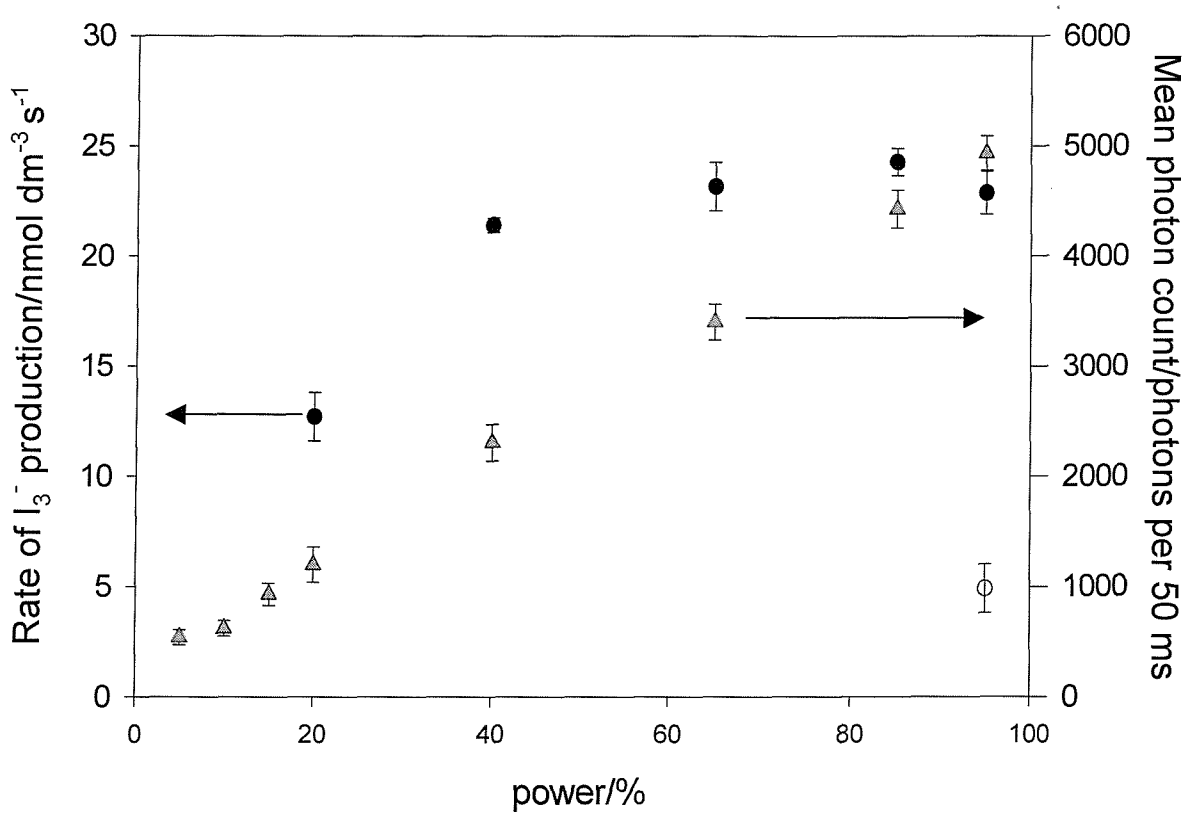

Figure 6.7 Plot showing the rate of the Weissler reaction in comparison to the sonochemiluminescence of luminol as a function of the % power. Initially the DO_2 was 11.16 ppm and the temperature was 22.8 °C. The height of the photon counter above the surface of the luminol solution (see chapter 3, section 3.3 figure 3.5) was 18 ± 0.5 cm. The photon count is represented by the grey triangle, the rate of the Weissler reaction at the hot spot is represented by (•) and the rate of the Weissler reaction recorded at the cold spot is represented by (o). In each case 20 cm^3 of 100 mmol dm^{-3} KI was placed in the sample holder and this was positioned in the hot spot. There was 10 minutes between each insonification. The DO_2 = 13.22 ppm and the final temperature was 22 °C. A measurement of the Weissler reaction was also performed in the cold spot at maximum power (95%) under the exact same conditions.

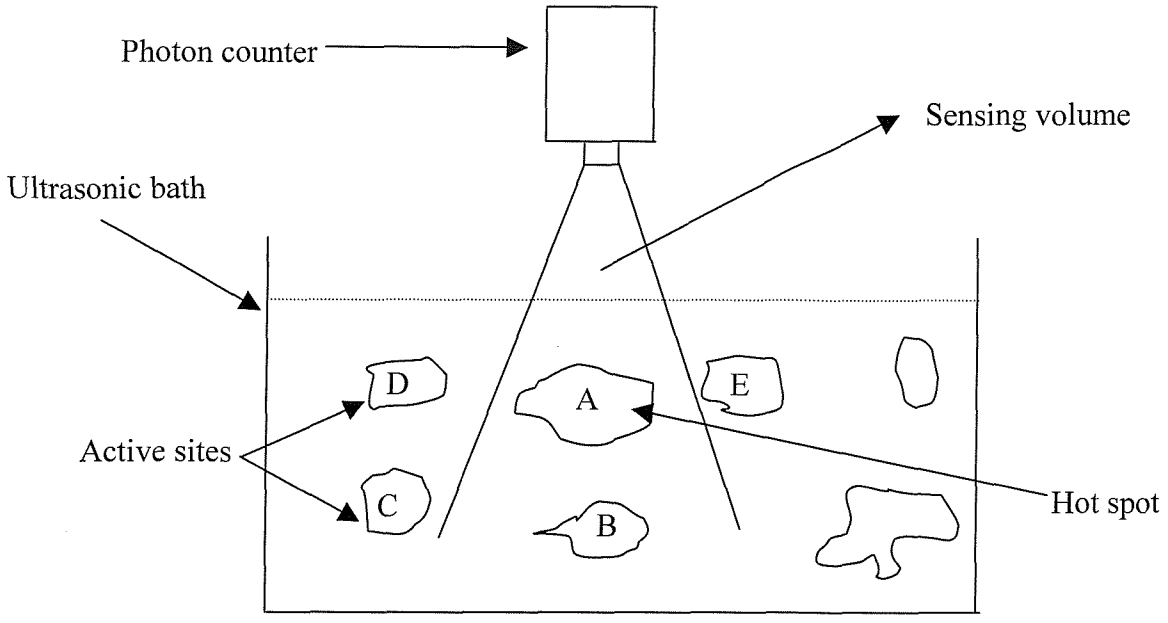

Figure 6.8 This figure illustrates the sensing volume of the photon counter during experiments performed at COMORAC. Sites (A-E) represent active sites in the bath. Site (A) also represents the hot spot. At low power site (A) was the only active site in the bath. However as the power was increased sites (B-E) also became active. In the case of the Weissler reaction the acoustically transparent cell was placed at site (A). The figure supposes that the in homogeneity seen in 2 dimensions in figure 6.1 can be extrapolated into the 3rd dimension (depth).

However, the Weissler only samples at (A). Shielding within the active zone may be responsible for the observed plateau in the Weissler reaction rate. The other possibility is that the Weissler reaction has an inherent upper limit. However, it is important to note that rates of up to three times greater than those recorded in the COMORAC experiment have been measured for the Weissler reaction (see chapter 4, section 4.1). It is suggested therefore, that the plateau in the rate was due to the conditions employed in the experiment/experimental set-up.

There are two points at 95% power for the Weissler reaction (see figure 6.7). The lower one (o) represents data recorded in the "cold spot" (see figure 6.2). The rate recorded in this position is four orders of magnitude reduced compared to the rate at the equivalent power in the "hot spot". In the sonochemiluminescent pictures recorded, the cold spot appeared black at the maximum power (see figure 6.1 picture (h and figure 6.2)). However, the Weissler reaction had a measurable rate in this position. Therefore, while the activity of the bath in this position was low, there was still some chemical activity. The Fricke reaction gave no absorbance measurement in the "cold spot". This highlights the sensitivity of the electrochemical measurement technique as illustrated in chapter 4.

As only one set of data was recorded for the Weissler reaction the reproducibility of the technique in the environment is unknown. In addition in chapter 5 (see section 5.2), the

Weissler reaction performed in the glass water jacketed cell (A) was observed consistently to follow sonochemiluminescence output over a wide acoustic pressure range.

The advantages of the electrochemical Weissler are as follows:

- It is a well-known reaction from the literature.[14, 85] The mechanism has been well established and the reaction has been used as a chemical dosimeter (see chapter one, section 1.7.3).
- The electrochemical detection method employed allows continuous measurement of the reaction throughout the insonification process. This is in contrast to the absorption method used in the case of the Fricke reaction (see section 6.4). Here, the solution was insonicated for a known duration of time and then a sample was removed and its absorbance was recorded relative to a time zero sample. However, other reactions may have occurred in the sample by the time its absorption was measured. The latter can lead to errors in the analysis of these reactions. Therefore, continuous analysis will be a more accurate method of detection for these processes.

The disadvantages of the Electrochemical Weissler reaction are as follows:

- The Weissler reaction is sensitive to any oxidising species present in the solution (see chapter 1, section 1.7.3). However, this is also the case with the Fricke reaction[83] (see chapter 1, section 1.7.1).
- As with any technique specialised equipment is required.

6.4 The 'Fricke' Reaction

Dr. Gareth Price, ('University of Bath'), performed this technique using absorbance spectroscopy. Figure 6.9 illustrates a plot of the experimental results achieved. The results at each power setting were analysed (by the current author) and the rate of production of Fe^{3+} at the hot spot as a function of the % power was plotted in figure 6.10. It can be seen that the rate increases linearly with power. This is in contrast to the Weissler reaction as this plateaus out above 60 % power. It is important to note that the zero point was measured and not assumed. Repeat measurements for the Weissler reaction and the Fricke reaction are required.

The rate of the 'Fricke' reaction in the cold spot was zero. This result is in contrast to the results achieved for the Weissler reaction. This was surprising as the rates recorded in the hot spot were particularly high. In addition to the rate of generation of Fe^{3+} as a function of power

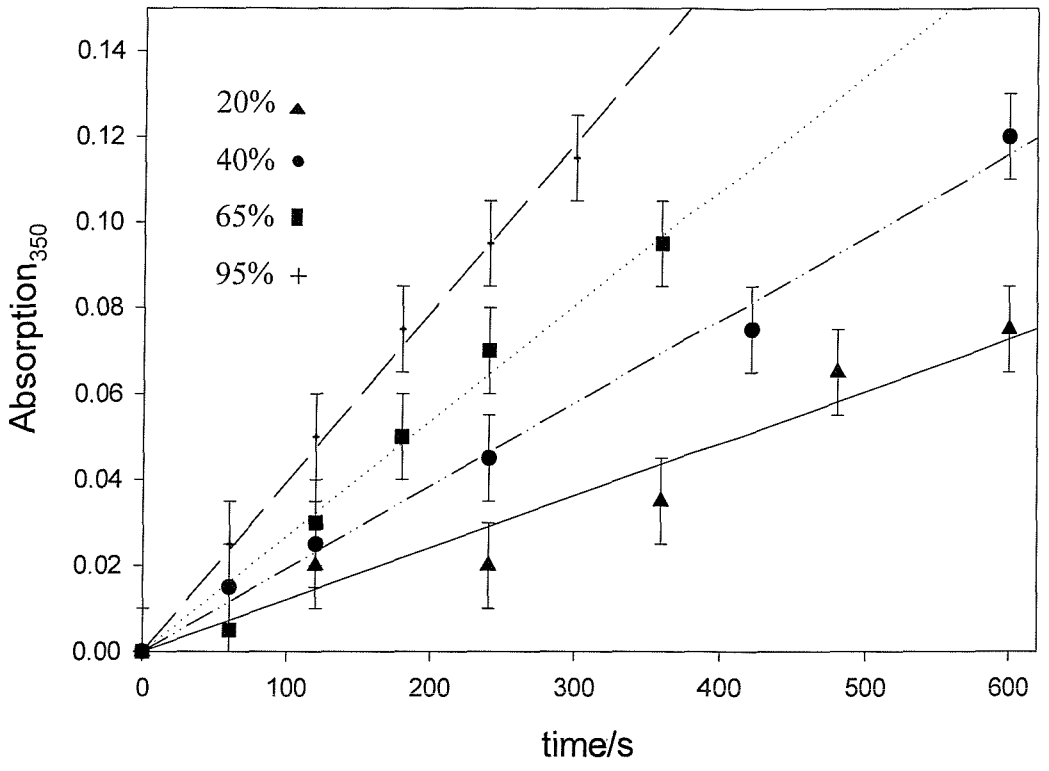

Figure 6.9 Plot showing Fricke dosimeter results - absorbance as a function of time for four different power settings in the bath. 20 cm^3 of 5 mmol dm^{-3} $FeSO_4$ solution was placed in the latex sample holder. This was positioned in the hot spot (see figure 6.2). The absorbance was then measured as a function of time. The temperature of the bath rose from an initial value of 22 °C to 30°C. Note there are no DO_2 measurements as chemiluminescence measurements were performed in tandem with the Fricke reaction. The error bars were calculated using the sensitivity of the spectrometer employed.

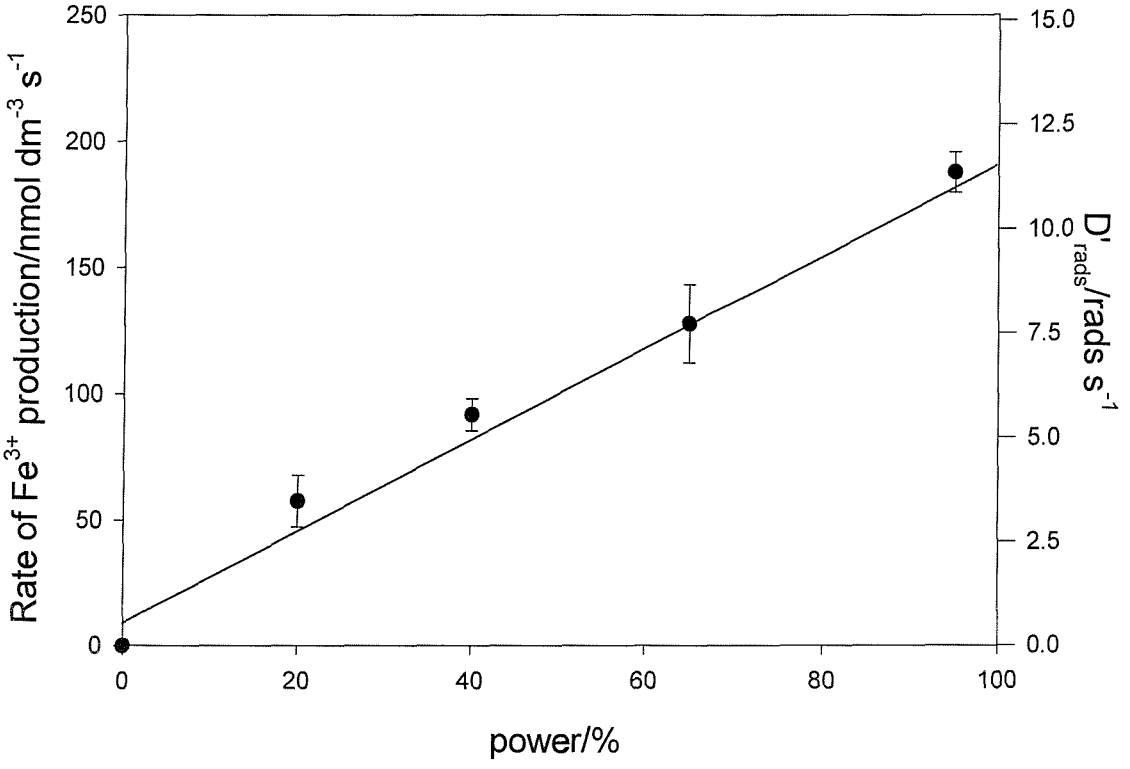

Figure 6.10 Plot showing the rate of Fe^{3+} production as a function of power. The plot shows the equivalent dose calculated from the data in figure 6.9 (calculations performed by the current author). In these calculations ε_{350} = 2100 mol^{-1} dm^{+3} cm^{-1}. The error bars represent 95% confidence interval determined using the data from the linear regression for each power setting in figure 6.9.

figure 6.10 also illustrates the equivalent dose of radiation exposed to the solution (calculated based on ionising radiation studies see chapter 1, section 1.7.1).

The Fricke reaction has a number of advantages including the following:

- It is based on a well-established radiochemical dosimeter, which monitors the oxidising reactions caused by ionising radiation.
- The linear increase in absorbance and the dependence of the rate on the % power mean that it could be applied over a range of conditions.

The main disadvantages of the Fricke reaction under the conditions employed are as follows:

- The sensitivity of the absorption method at low levels of cavitation is in question since no reading was obtained in the cold spot.
- This technique relies on accurate knowledge of the positions of the hot spots within the bath. This means that chemiluminescence pictures are essential for reproducible results using this sensor. However, this is also the case for the Weissler reaction.

6.5 Terephthalate Dosimetry

Dr. Gareth Price, ('University of Bath'), performed this technique. Hydroxyl radicals produced on cavitational collapse react with terephthalate to form hydroxy terephthalate, HTA, which is fluorescent (see chapter 1, section 1.7.2). Measurement of the fluorescence emission at 425 nm with an excitation wavelength of 310 nm gives a value proportional to the concentration of HTA formed. Figure 6.11 illustrates a plot of the experimental results achieved. The results at each power setting were analysed (by the current author) and the rate of production of hydroxy terephthalate at the hot spot as a function of the % power was plotted in figure 6.12.

The fluorescence is linear with time at each power setting. This is similar to the Fricke reaction. The rate of HTA formation is not linear with power but peaks at 65% before dipping dramatically (below 40% power level) at maximum power. This is in contrast to the Weissler reaction, which reaches a plateau at above 60 % power (see figure 6.7). Like the Fricke reaction, this technique failed to yield any data after insonification at the cold spot for ten minutes at maximum power. Repeat measurements are required to ensure that the point at 95% power is accurate. Note that the fluorescence emission is shown in arbitrary units; these are proportional to the HTA concentration. It is possible to convert the fluorescence data to

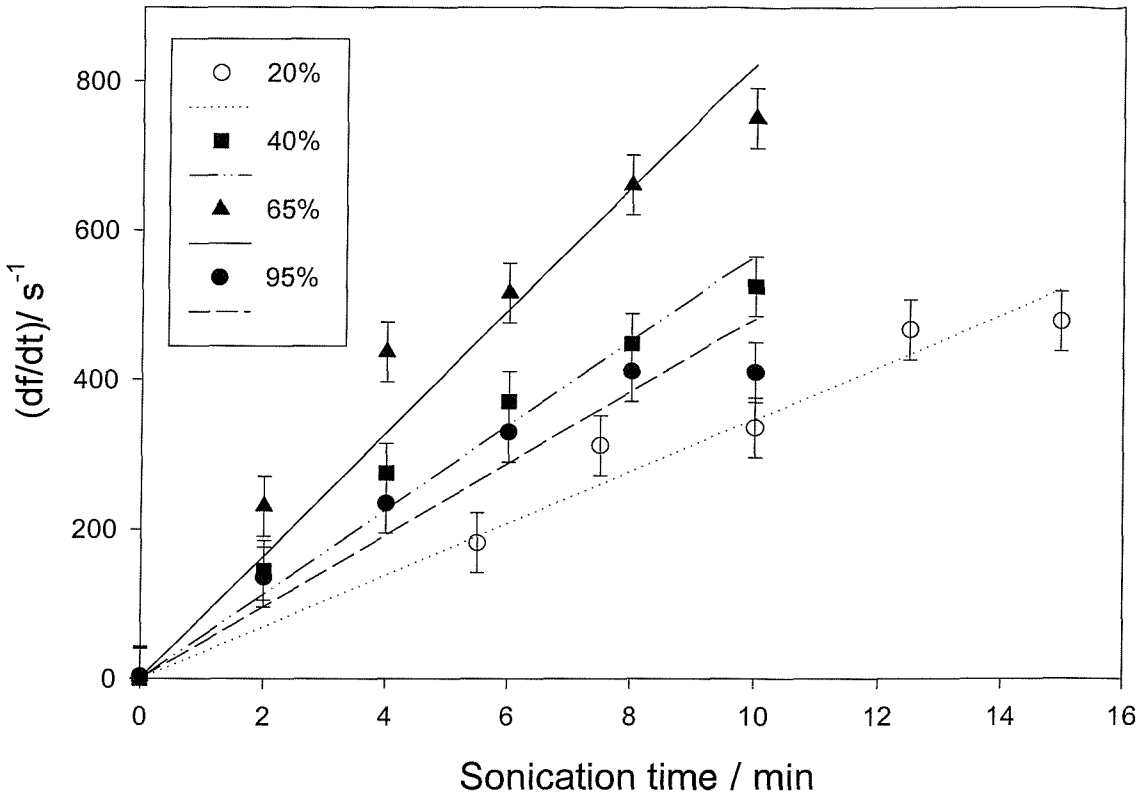

Figure 6.11 Fluorescence emission from HTA formed on sonication at various powers. In each case 20 cm^3 of 2 mmol dm^{-3} sodium terephthalate in 5 mmol dm^{-3} NaOH was placed in the sample holder and this was positioned in the hot spot. The initial and final DO_2 was 2.84, 3.62 ppm respectively. The initial and final temperature was 23 and 24.6 °C respectively.

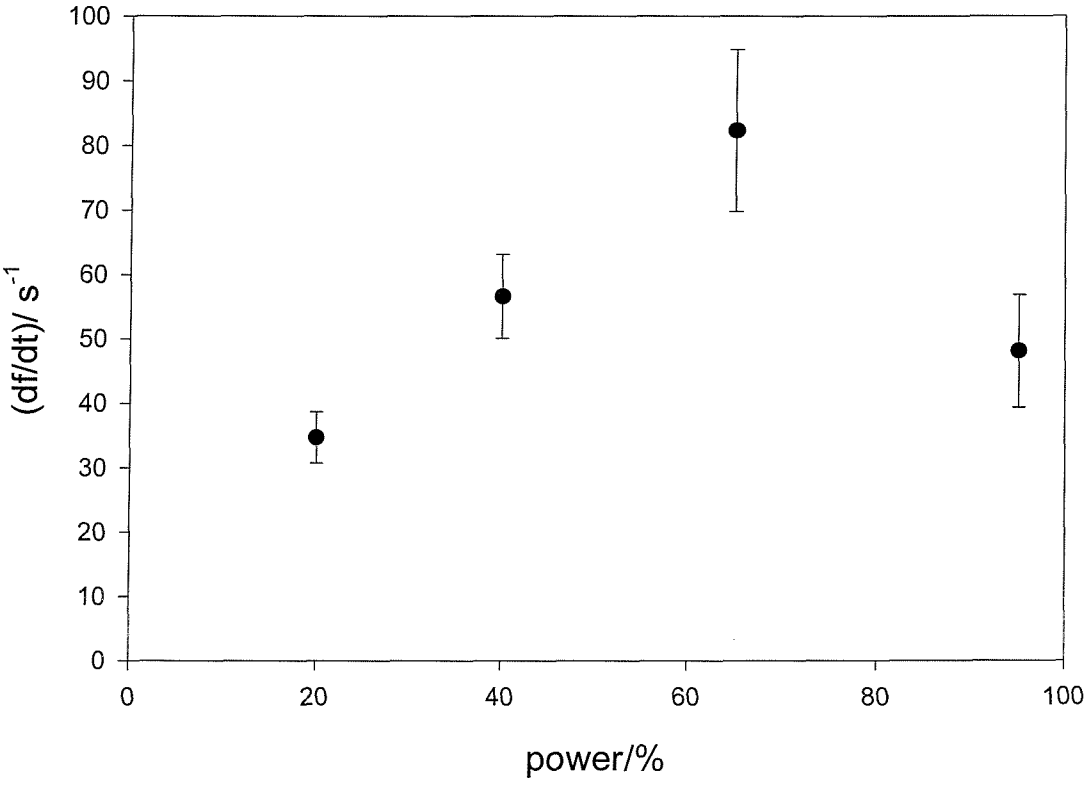

Figure 6.12 Dependence of the rate of HTA production as a function of the applied power. The error bars represent 95% confidence interval determined using the data from the linear regression for each power setting in figure 6.11.

concentrations by calibrating the fluorescence spectrometer. Dr Price did not provide this data. However, this does not affect the conclusions of the work.

The main advantage and disadvantages of the terephthalate dosimetry are as follows:

- It is specific for the hydroxyl radical and is not sensitive to other oxidants in solution.
- Low sensitivity at the lower power levels - no results obtained in the cold spot.
- The solutions need to be prepared a short time before use as they "go off" over a period of a week or so unless kept cold and dark and the preparation is a little involved and tedious.

6.6 Discussion of the Sonochemical Results Achieved at COMORAC

There is clear disagreement between the COMORAC results achieved using the Weissler reaction, the Fricke reaction and the terephthalate dosimeter. It is difficult to compare the terephthalate dosimeter without actual concentration measurements. In addition this reaction was not performed in chapter 4. Table 6.1 compares the chemical results achieved in COMORAC to the chemical results obtained in chapter 4 for ultrasonic cell (A). The Weissler and the Fricke experiments were performed under identical solution conditions. There is no apparent reason for the ca. 2.5-fold difference in the rates (except for the difference in measurement method). However, the method employed (spectrophotometry) is standard and not expected to cause such an error.

	COMORAC	**Results From Chapter 4**	**Method of Analysis**
Weissler (Maximum Rate)	24 ± 1 nmol dm^{-3} s^{-1}	75 ± 7 nmol dm^{-3} s^{-1}	Electrochemical
Fricke (Maximum Rate)	190 ± 20 nmol dm^{-3} s^{-1}	240 ± 20 nmol dm^{-3} s^{-1}	Electrochemical in chapter 4. *Spectrophotometric in COMORAC

Table 6.1 Comparison of results achieved for the Fricke and Weissler reaction in COMORAC and chapter 4.

The MBSCL photon count obtained during COMORAC was 5000 photons at maximum power (see figure 6.3). Similar values for the MBSCL photon count was achieved in chapter 5 section 5.2 using the cylindrical glass jacketed cell (A). The rates achieved from the Fricke reaction in COMORAC and those achieved in chapter 4 are also similar (see table 6.1). However, it is difficult to assess (without further testing) whether the rate of the Weissler reaction is low or the rate of the Fricke reaction is high. Reflections from the walls of the ultrasonic bath employed for the COMORAC experiment may cause the photon count to be artificially high.

6.7 Calorimetry

Prof. T. Mason ('School of Natural and Environmental Sciences, University of Coventry, Coventry') performed this technique. A K-type thermocouple was employed to measure the rate of heating produced when the system is irradiated by power ultrasound. The temperature rise in a reactor is equated to the amount of ultrasonic power entering a sonochemical reactor. For the system under study the temperature is recorded against time t, at intervals of a few seconds using a thermocouple placed in the bath. From the temperature versus time data, the temperature rise at zero time, (dT/dt), is then estimated. This is achieved either by constructing a tangent to the curve at time zero, or by curve-fitting the data to a polynomial. That component of the ultrasonic power (W) which is converted at a given rate into heat (W_T) can then be obtained from the product $W_T=(\mathrm{d}T/\mathrm{dt})c_pM$, where c_p is the heat capacity of the solvent (J $kg^{-1}K^{-1}$) and M is the mass of solvent used.

Figure 6.13 illustrates the temperature against time plots obtained at three power settings in the bath. It can be seen that a very small rise in temperature was observed. Similar results were obtained when the K-type thermocouple was placed in the latex chemical sample holder used for the sonochemical experiments.

The data at each power setting was used to calculate the ultrasonic power, the power density and the ultrasonic intensity. This data is given in table 6.2. The temperature rises in the bath were very low. This is due to the large volume of the bath 20 litres and the length of time over which measurements were recorded. Cooling currents in the bath would dissipate energy in the system over this time period.

In general calorimetry is a poor technique. It encompasses many approximations including the following:

- It assumes that all the acoustic energy entering the system is transformed into heat.

Cavitation is a non-linear threshold phenomenon. Therefore, it's the spatial peak and not the spatially averaged pressure, which is important for inertial cavitation. In a spatially non-uniform sound field employed for these experiments (see figure 6.1) these two measurements will be drastically different.

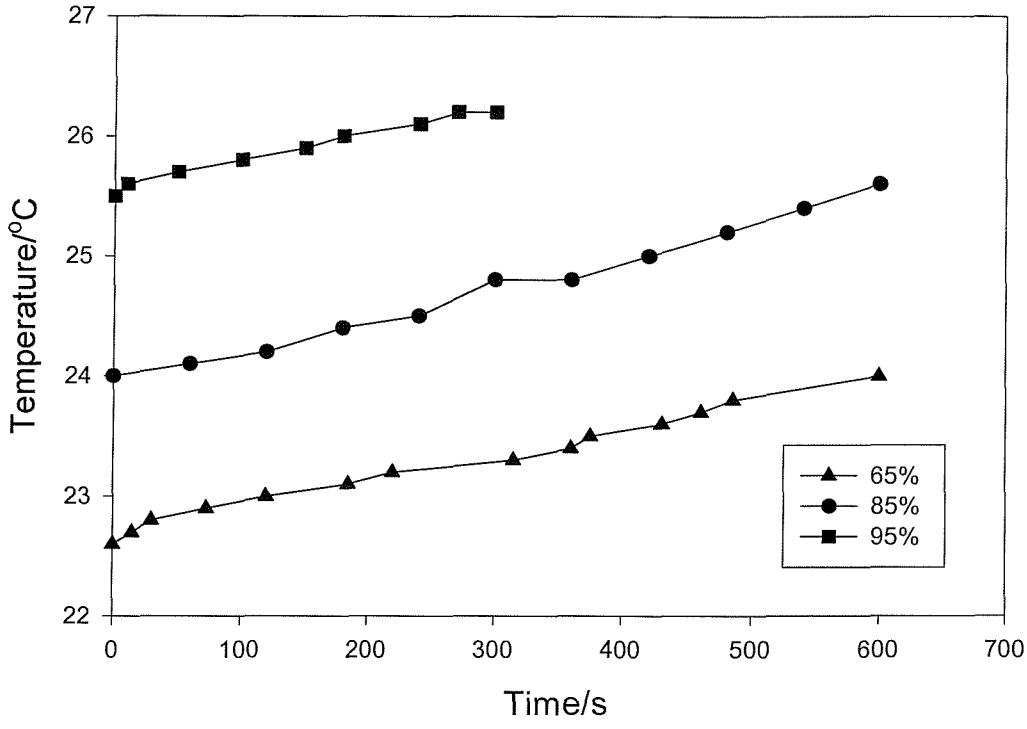

Figure 6.13 Temperature time curves for power settings 65%, 85% and 95% respectively measured using the K type thermocouple. The initial temperature at 65% was 22.6°C and the DO_2=2.90. At 85% the initial temperature was 23.5°C and DO_2=3.41. At 95% the initial temperature was 23.5°C and the DO_2=3.41.

		Area = 23 cm x 35.8 cm = 823cm^2	
Setting	*Ultrasonic Power* (W_T)	*Power density*	*Intensity*
65%	167 W	9.22 Wdm^{-3}	203 mWcm^{-2}
85%	205 W	11.32 Wdm^{-3}	249 mWcm^{-2}
95%	174 W	9.60 Wdm^{-3}	211 mWcm^{-2}

Table 6.2 This table shows the calculated power, the power density and the intensity of ultrasound entering the ultrasonic vessel employing the data shown in figure 6.13.

6.8 Acoustic Sensors

This section presents a sample of the acoustic results obtained by the other partners involved in the COMORAC experiment who gave permission to publish their results. The data is critically analysed and compared to the results obtained using the chemical sensors (see sections 6.1-6.5).

6.8.1 Focused-Bowl Hydrophone (Passive Acoustic Emission)

The results presented in section 6.8.1 were performed by Andy Coleman ('Guy's and St. Thomas' Health Trust, London'). A 1 MHz focal bowl hydrophone was employed as a passive device to detect acoustic emission from cavitation at this frequency. A sample response of the data obtained from this sensor is illustrated in figure 6.14. Figure 6.15 shows a comparison of the data obtained when this sensor was positioned in the hot and cold spot (see figure 6.2). It can be seen that there is little difference in the response achieved in the hot and cold spot.

The advantages of this sensor are as follows

- The response is linear with the %power and hence the drive voltage.
- This technique gives similar results to some of the chemical methods (chemiluminescence and Fricke dosimetry).

The disadvantages of this sensor are as follows:

- This sensor is not local and fails to distinguish the hot spot from the cold spot even though there is a dramatic difference in the activity of these two positions (see figure 6.2).

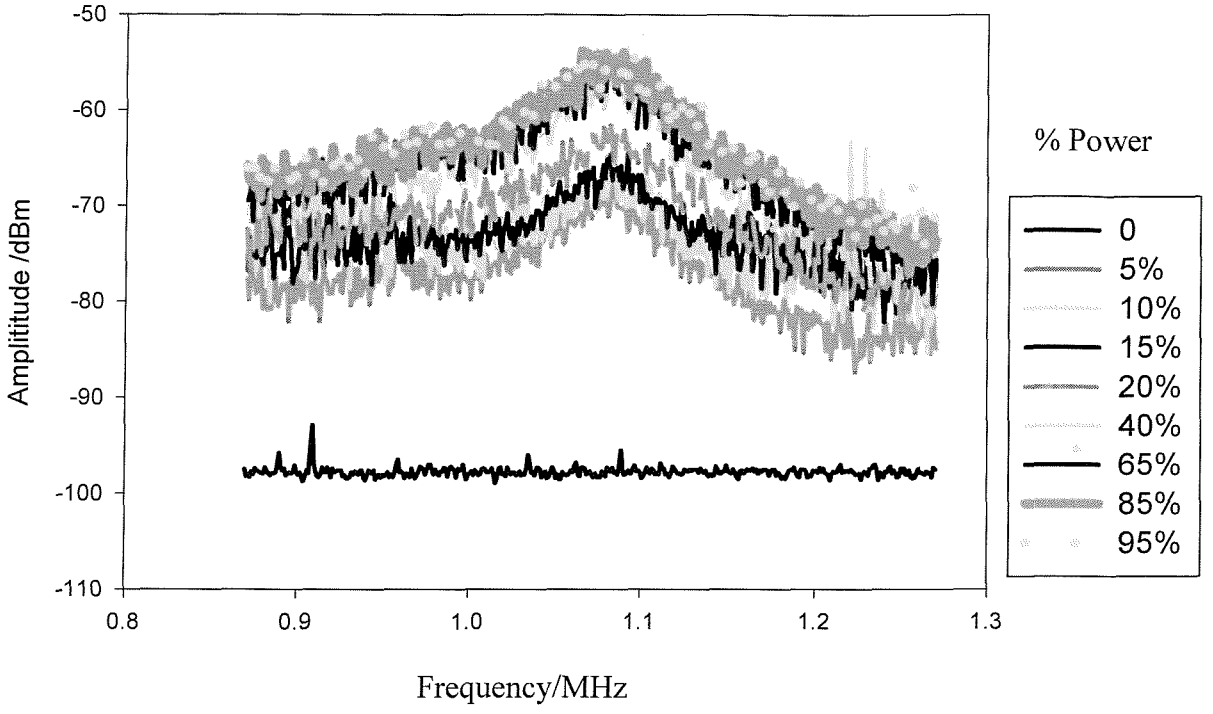

Figure 6.14 Focused bowl hydrophone raw data recorded from the hot spot. The results at the different power settings are illustrated in the figure. The initial and final temperatures were 22.8°C and 23.2°C respectively. Note in these results no DO_2 results are presented as simultaneous chemiluminescence measurements were recorded. The bath contained 20 litres of luminol solution (see chapter 3 section 3.3 figure 3.5).

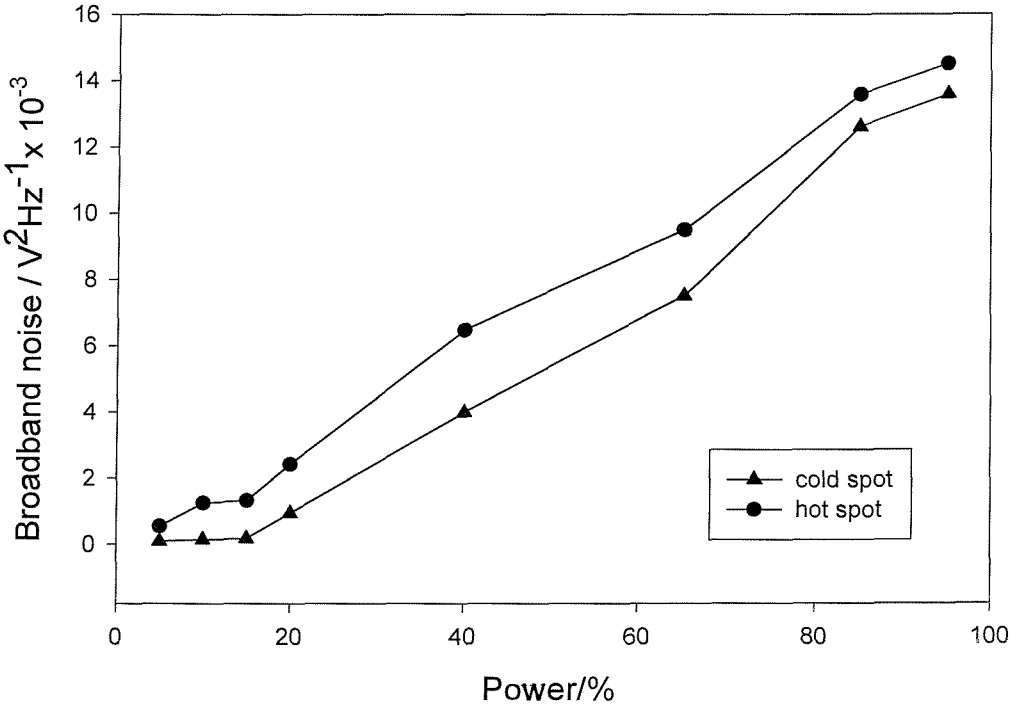

Figure 6.15 Data analysed over complete band for the hot spot and the cold spot. For the cold spot the initial and final temperature was 22.8 and 23.2 °C respectively. For the hot spot the initial and final temperature was 23.2 and 23.5 °C respectively. The bath contained 20 litres of luminol solution (see chapter 3 section 3.3 figure 3.5). Note in these results no DO_2 results are presented as simultaneous chemiluminescence measurements were recorded.

6.8.2 Cavitation Activity Indicator

Nikolai Dezhkunov, ('Laboratory of Ultrasound Technologies, Belarusian State University, Minsk, Belarus') performed the results presented in this section. The principle of operation of the sensor is based on cavitation noise spectra analysis for a frequency range of ultrasound driving fields between 5 kHz and 150 kHz using a wide band hydrophone protected against cavitation effects. In the experiments performed at COMORAC the apparatus measured the sub harmonic intensity.

An example of the results obtained using the IC-3 meter is presented in figure 6.16. These results are difficult to interpret due to the large variance of the signal observed as a function of time. This resulted in large errors bars in the graph.

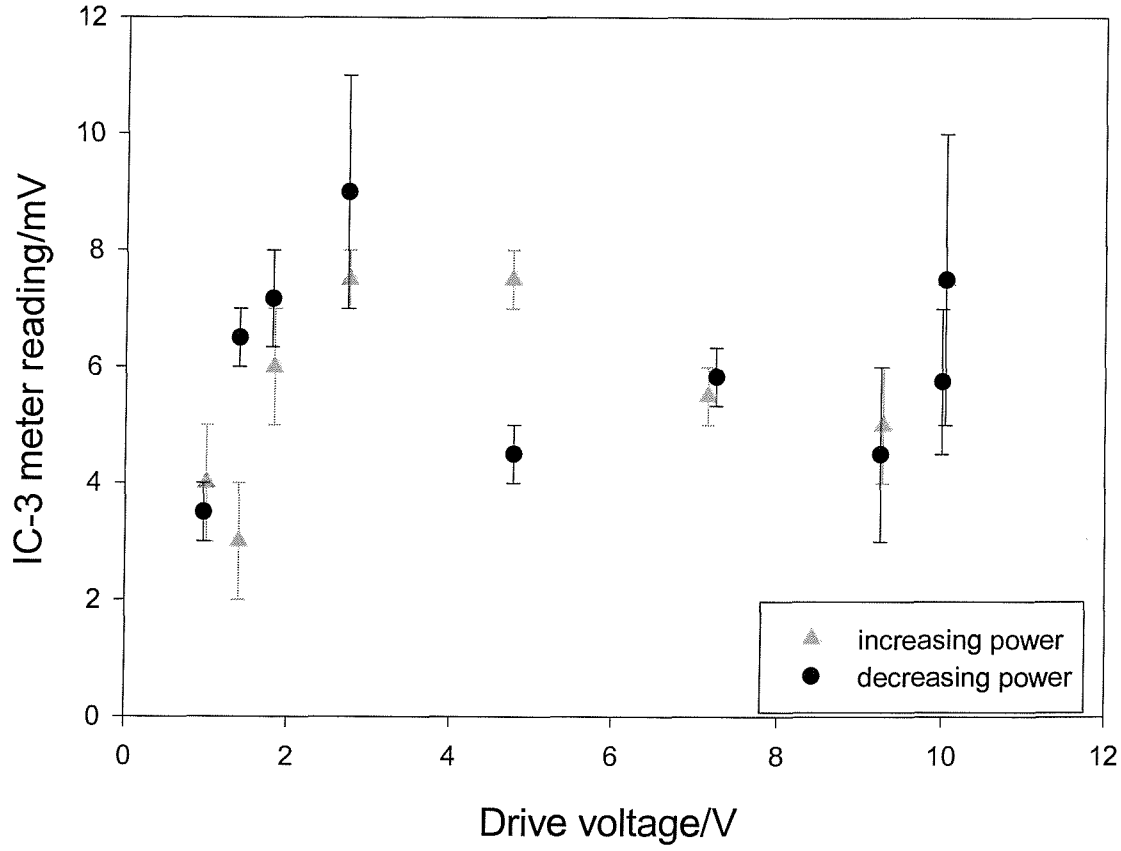

Figure 6.16 Plot show the results obtained from the IC-3 meter positioned in centre of the ultrasonic bath. The bath contained 20 litres of degassed filtered water. The figure shows the response of the sensor to increasing and decreasing power. Error bars represent one standard deviation of three repeat measurements. The initial temperature was 23.2°C and the initial DO_2 =1.84 ppm. The final temperature was 22.7 °C and the final DO_2=2.40 ppm.

6.9 Conclusions

The results in this chapter present an initial study with the ultimate aim of developing a reference sensor for cavitation. A "standard liquid" was employed using a "standard vessel" with fixed frequency. Of the preliminary results obtained, the MBSCL results proved the most valuable, as these were required to ascertain the location of the "hot and cold" spots. Chemical and acoustic sensors can then be positioned. They illustrate that an accurate knowledge of the acoustics within a reactor is essential to achieving reproducible results. However, even though the MBSCL images were valuable (see figure 6.1), there were still some problems to be overcome. These included the following:

- MBSCL – alkali media, not compatible with some materials.
- MBSCL – requires sensitive equipment.
- MBSCL – sensor has relatively large footprint.
- Imaging Cameras – shows light emission in a 2D sense. Hence 2 cameras are required to locate positional activity within the cell.

The suitability of the reference bath for an experiment of this kind is questionable. The spatially non-uniform sound field in the ultrasonic bath was very difficult to understand. The bath contained 20 litres of solution, which is not practical. An acoustically well-characterised cell similar to the one used in chapter 4 and 5 (ultrasonic reactor cell (A) see chapter 2, figure 2.1) would be more suitable. A cell of this nature has a standing wave sound field, which can be characterised in terms of acoustic modes, volume, temperature etc (see chapter 3, section 3.1).

Of the chemical tests performed the Fricke reaction seems the most promising technique. It would have been beneficial to perform this reaction electrochemically simultaneously with absorbance measurements. The reason this reaction was not performed electrochemically was that the electrochemical version was not fully developed until after the COMORAC experiment was completed. There is a need for repeat measurements to test for reproducibility of this system. However, reproducible results have been achieved for the Fricke reaction in the cylindrical ultrasonic reactor cell (A) (see chapter 4, section 4.3).

Of the acoustic sensors the focused bowl hydrophone seemed to provide the best results. The broadband noise was linear with the % power and the results compared well to the chemical results achieved (MBSCL and the Fricke reaction). The problem with this sensor, however, was that it was unable to distinguish the hot and the cold spot.

Removing the random nucleation sites from the liquid by degassing and filtering has a both advantages and disadvantages. Some experiments were performed over a relatively long period of time so the conditions (bubble populations, speed of sound, temperature) in the bath will change. The dissolved oxygen and temperature was measured where possible before and after each experiment. Both the dissolved oxygen and temperature were observed to vary (see figure 6.5). The exact effect of these parameters on the cavitation 'activity' and therefore the reproducibility of the bath are difficult to quantify. This is in contrast to the results achieved in chapter 4 where the ultrasonic reactor was temperature controlled and experiments were performed under aerobic conditions.

Finally, the conditions in which this project was performed were very difficult. These included the time constraints for experimental set-up, in addition to the location of the reference bath. This involved transport of equipment to and from NPL. The transport of such sensitive equipment is always problematic. It is recommended that if this project is to be undertaken again that the reference vessel be transported to the various partners for extended periods of time.

The previous chapters (3-6) have investigated MBSL in detail. In the next section single bubble sonoluminescence will be investigated electrochemically, photographically and spectrophotometrically with the ultimate objective of probing the differences and similarities between these two remarkable phenomena.

CHAPTER 7

AN ELECTROCHEMICAL, PHOTOGRAPHIC AND SPECTROSCOPIC STUDY OF SINGLE BUBBLE SONOLUMINESCENCE

The chapter presents the first electrochemical study of single bubble sonoluminescence (SBSL). The goal of the study was to investigate the production of chemical species in the high pressure and temperature environment of SBSL. Evidence for the existence of radicals and radical products, produced through the breakdown of the solvent matrix has been well established for MBSL. Although the experimental evidence suggests that the mechanism for light emission of MBSL and SBSL are likely to be different because of different spectroscopic properties and durations of light pulse (see chapter 1 section 1.9 and 1.10) researchers agree that the theoretical temperature calculated based on the light emission spectrum[112] is likely to be in excess of 5000 K. Water vapour will dissociate to form hydroxyl radicals and hydrogen atoms well below this temperature. It is therefore likely that radical species will also be produced in the case of SBSL.

The production of these radical species has been accounted for in some theories. Lohse *et al.*[163-164] suggest that the process of rectification occurs and that these species are removed from the bubble interior as they are formed in products such as H_2O_2 and HNO_2. They propose that the small argon content in air is responsible for SBSL. However, little work has been done on the detection of radical species as a result of SBSL.

Didenko and Suslick[165] recently reported evidence for the detection of radical species as a result of SBSL. The authors performed the terephthalate dosimeter and also detected evidence for the formation of NO_2^- by measuring the fluorescence of the product of its reaction with 2,3-diaminonaphthalene. The only other report of single bubble sonochemistry to the present knowledge of the author consists of the formation of solid particles (composition undetermined) during pulsation of a single bubble in an aqueous solution of carbon disulphide.[165]

In this chapter a novel detection technique employed to gather evidence for the production of radicals during SBSL is presented. The experimental set-up including an innovative set of needle microelectrodes have been discussed in the experimental section (see section 2.14). These needle-microelectrodes were designed so they could penetrate the standing wave sound field needed to generate SBSL while causing minimum disruption to

the sound field particularly around the bubble itself. This allowed the microelectrode to approach the single bubble to within a distance suitable for detection of chemical species. Radical trapping agents, in particular iodide ions (I^-), were employed to capture oxidative radicals as they were formed. This led to the production of the redox active triiodide product (I_3^-) (evidence for the existence of $OH^\bullet$ or other oxidising agents, see chapter 4, section 4.1) the reduction of which could be detected using the needle-microelectrode.

In addition to electrochemical analysis, a photographic and spectroscopic study of SBSL is also presented. Photographs were recorded using image-intensified cameras and spectra were recorded using an in-house designed spectrometer made from an image intensifier and diffraction grating (see chapter 2 section 2.16).

7.1 Electrochemical Investigation of Single Bubble Sonoluminescence – Experimental Method

One of the primary differences between SBSL and MBSL is their proposed chemical natures. It is known that during MBSL radicals are produced (e.g. see chapter 4, section 4.1, 4.3, and 4.6). However, little evidence for radical formation during SBSL has been reported. To investigate this fundamental difference between MBSL and SBSL a series of novel experiments were designed and performed. To obtain evidence for the existence of radicals for SBSL the Weissler reaction was performed. Prior to presenting the experimental results it is necessary first to explain how the experiments were undertaken. The cell contained a degassed solution of 3 mmol dm^{-3} KI in 97 mmol dm^{-3} Na_2SO_4. SBSL was achieved as explained in chapter 2, section 2.13. A needle microelectrode (50 μm diameter platinum active area) was positioned close to the surface of the single bubble using the *x*, *y*, *z*, micrometer and stage and a stepper motor and stage to perform controlled and automated approaches to the bubble (see chapter 2, section 2.15). The potential of the electrode was then set to +0.2 V vs. Ag. The steady state current for the reduction of I_3^- (see chapter 4, section 4.1) was monitored. As the microelectrode was slowly manoeuvred towards the bubble wall the steady state current was observed to proceed cathodically. Both the electrode and cell were moved on the micrometer scale relative to each other until the cathodic current reached a maximum steady state plateau (see figure 7.3). The microelectrode was positioned so as to achieve the highest current enhancement but not too close to remove the single bubble. This positioning distance was determined through trial and error. However, exact distance details are difficult to ascertain with the equipment

available. Once the electrode was in position the steady state current was monitored as a function of time. By adjusting the drive voltage (see chapter 2, section 2.6) of the ultrasonic signal, and thereby changing the acoustic pressure, it was possible to alter the bubble between a luminescing and non-luminescing state. Experiments were performed in both luminescing and non-luminescing conditions. This was applied as a control as radical production would not be expected in the non-luminescing case.

Altering the acoustic pressure will affect the mass transport of material to the electrode surface. To estimate the magnitude of this effect the potential applied to the electrode was switched to +0.9 V vs. Ag and the steady state oxidation of I^- was monitored as a function of time. This was performed for both the luminescing and non-luminescing case according to reaction [7.1]. It should be noted that the concentration of I^- employed in these experiments (3 mmol dm^{-3}) is considerably reduced compared to that used previously for multi bubble sonochemical reactions (typically 10 mmol dm^{-3}). This reduced concentration was employed to enable mass transfer limiting oxidation of I^- to be reproducibly attained at the microelectrode. At higher I^- concentrations, I_2 was found to "plate" out on the electrode. This was associated with a non-steady state response and a stripping peak when the electrode potential was returned to +0.2V vs. Ag.

$$I^- \longrightarrow 1/2I_2 + e \qquad [7.1]$$

Figure 7.1 illustrates a CV of the 50 μm diameter microelectrode in 3 mmol dm^{-3} KI and 97 mmol dm^{-3} Na_2SO_4. It can be seen that a certain amount of plating of I_2 still occurs under these conditions. However, the insert in the plot shows a potential step under the same conditions from + 0.2 V to + 0.9 V vs. Ag. This plot illustrates that a steady state current for the oxidation can be achieved under the conditions employed.

However, it is important to note that if the I^- concentration were lowered further, a reduced radical trap signal would be expected (see chapter 4, section 4.1 figure 4.2). Hence, a compromise between "perfect" electrochemistry and efficient radical capture conditions had to be reached. This compromise was for an I^- concentration of 3 mmol dm^{-3}.

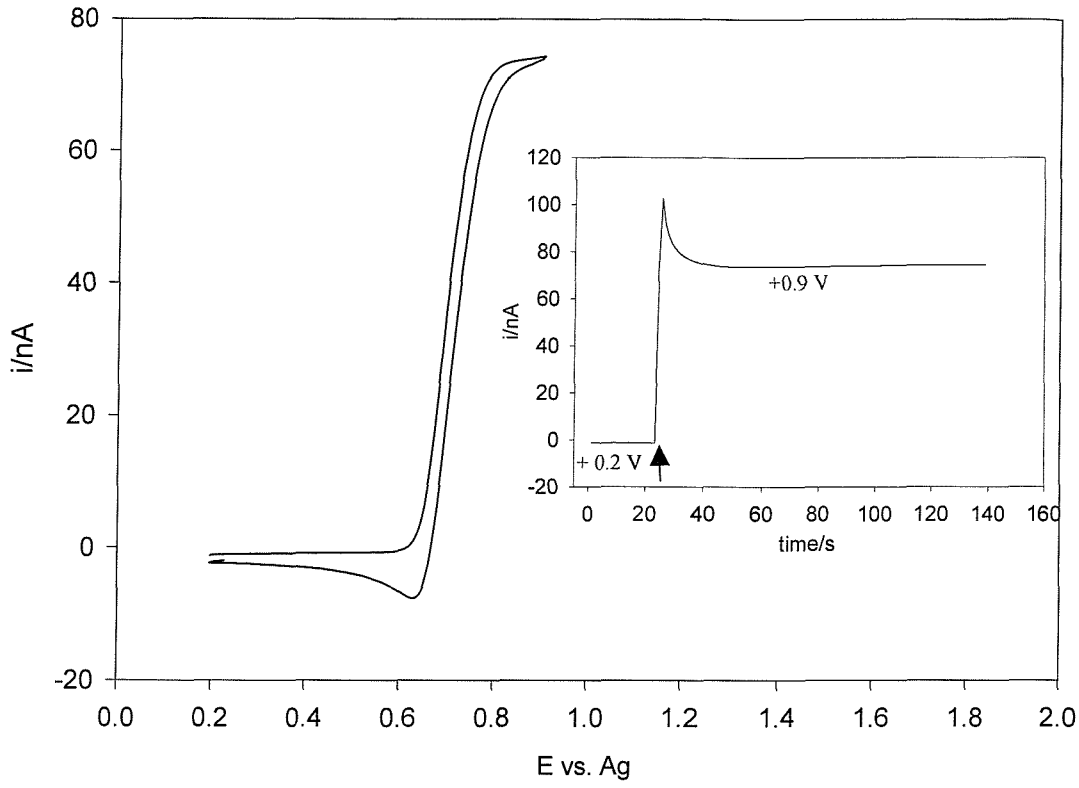

Figure 7.1 A cyclic voltammogram of the 50 μm needle microelectrode in a 3 mmol dm^{-3} solution of KI in 97 mmol dm^{-3} Na_2SO_4. The potential was swept at 5 mVs^{-1} vs. Ag and the cell was temperature controlled at 25 °C. The insert in the plot shows a potential step from + 0.2 V to + 0.9 V vs. Ag under the same conditions. The arrow in this plot indicates where the potential was stepped.

7.2 Single Bubble Sonoluminescence – The Weissler Reaction

Figure 7.2 illustrates a set of images obtained to show how the electrochemical Weissler reaction experiment was performed in the analysis of SBSL. Figure 7.2 will be discussed in conjunction with figure 7.3 since the images presented in this figure were recorded while the experimental results present in figure 7.3 were in progress. Figure 7.3 illustrates electrochemical evidence for the presence of oxidising species presumably radicals formed during SBSL using the Weissler reaction (performed as described in section 7.1). The bubble was located as described previously. The needle-microelectrode was held at + 0.2 V vs. Ag and the current was monitored as a function of time for the luminescing bubble from time t = 0 s. This is illustrated in the photographic evidence presented in figure 7.2 (see picture (b) and (d) figure 7.2).

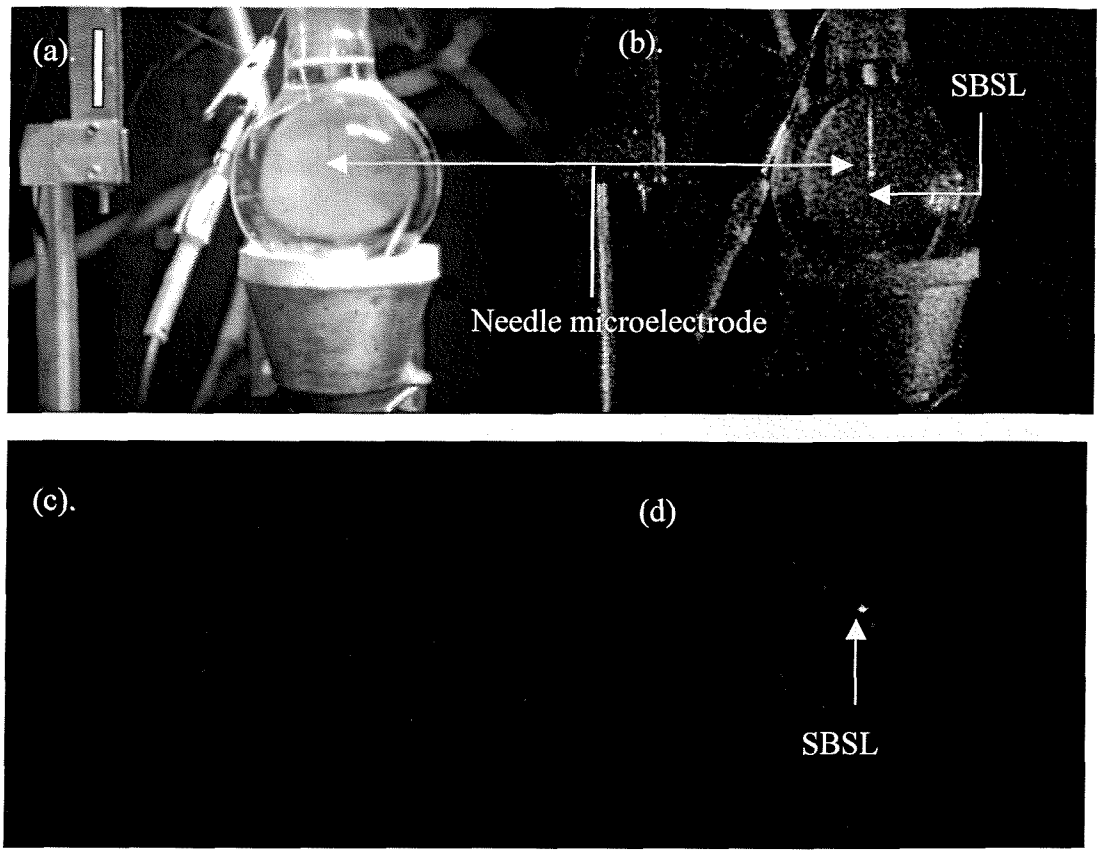

Figure 7.2 Photographs recorded of SBSL when the bubble was switched from a luminescing (d) to a non-luminescing state (c) using an image intensified CCD camera. Picture (a) illustrates the cell when the bubble is in the non-luminescing state. Picture (b) shows SBSL with the needle microelectrode position close to the luminescing bubble. The bubble is luminescing in the centre of the cell. The other light in this picture is scattered light. Pictures were recorded while experiment illustrate in figure 7.3 was in progress. The cell contained a solution of 3 mmol dm^{-3} KI in 97 mmol dm^{-3} Na_2SO_4. SBSL was generated employing 27.44 kHz ultrasound and 150 kPa acoustic pressure amplitude. The acoustic pressure amplitude was decreased by 2 kPa (148 kPa) when the bubble was altered between a luminescing and a non luminescing state. The scale bar in picture (a) represents 15 mm. The gain of the image intensified camera was 8 for frames (c) and (d).

At time t = 30 s the drive voltage and hence the acoustic pressure was adjusted so that the bubble was no longer luminescing (see picture (c) figure 7.2). The magnitude of the acoustic pressure amplitude change to alter the bubble form a luminescing to a non luminescing state was low ca. 2 kPa.* The current progresses anodically and reaches a steady state plateau. At time ca. t = 110 s the voltage was increased so that the bubble luminesced again. The current again proceeds cathodically and reaches a plateau at t = 150 s. The increase in cathodic current is believed to correspond to the reduction of I_3^- formed close to the luminescing bubble wall. The entire process is repeated a further two times in the figure to illustrate that the effect is reproducible. A possible reason for the sloped nature of

* Note that due to the finite size of the hydrophone active element the spatial maximum zero-to-peak pressure amplitudes cited are likely to be under estimates because of spatial averaging. This is particularly evident in the small changes in pressure observed in changing the bubble from a luminescing to a non luminescing state.

the current time response presented in figure 7.3 (and in the following sections) is that low pass filtering was employed to measure the pA current (see experimental section 2.15). It is important to note at this stage that filtering was essential to measure the low current signal.

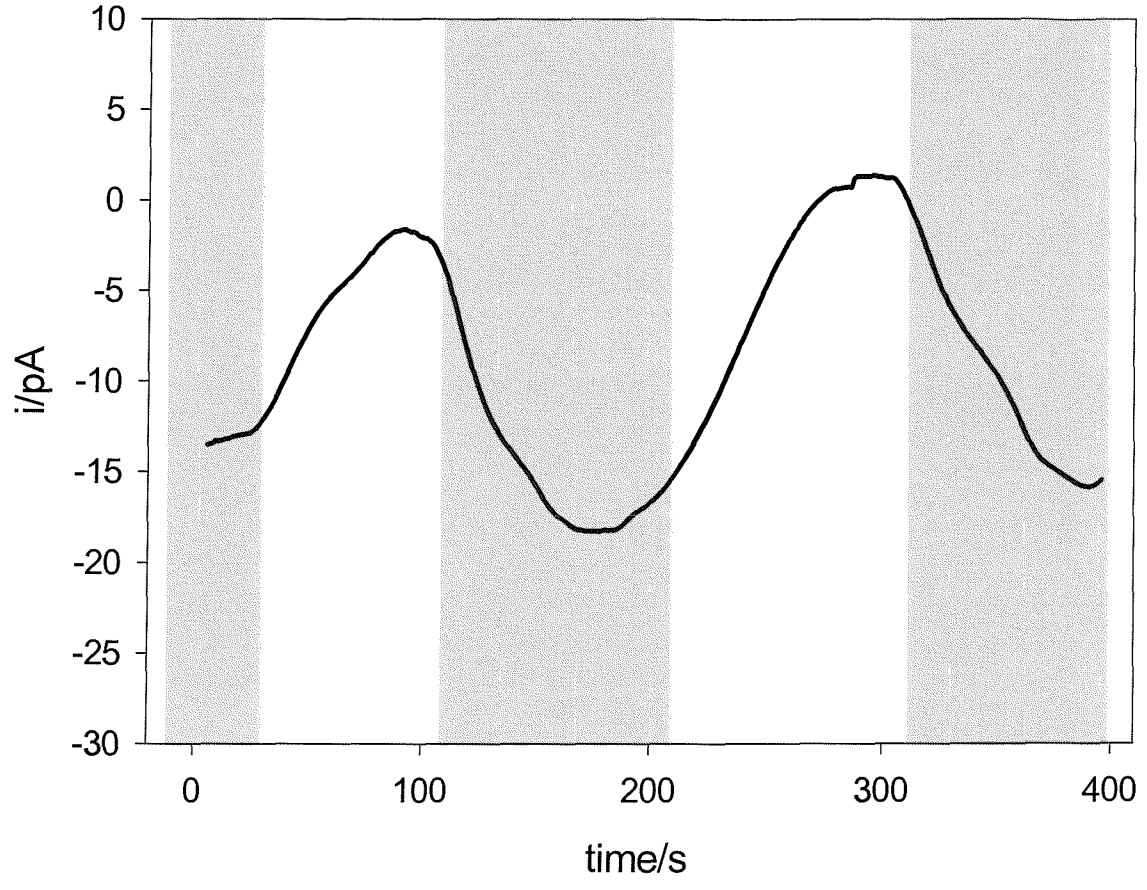

Figure 7.3 This figure illustrates the electrochemical Weissler reaction performed on SBSL generated employing 27.744 kHz ultrasound and 150 kPa acoustic pressure amplitude. The cell contained a degassed solution of 3 mmol dm^{-3} KI in 97 mmol dm^{-3} Na_2SO_4. The current was monitored as a function of time using a 50 μm needle microelectrode position close to the bubble wall. The electrode was held at +0.2 V versus Ag. The bubble was altered from a luminescing (grey shading) to a non-luminescing state (no shading) by adjusting the drive voltage. This resulted in the acoustic pressure amplitude decreasing by 2 kPa (148 kPa) when the bubble was altered between a luminescing and a non luminescing state.

The potential was then stepped to +0.9 V vs. Ag and the steady state current for the oxidation of I^- (see reaction [7.1] was monitored for the luminescing and non luminescing bubble. The results are illustrated in figure 7.4. At time $t = 0$ s the bubble is not luminescing (acoustic pressure amplitude 148 kPa) and the current is monitored as a function of time. At ca. $t = 10$ s the acoustic pressure amplitude is increased (up to 150 kPa) by adjusting the drive voltage so that the bubble luminesces. The anodic current can be seen to increase. This process was repeated a number of times to illustrate that the change in mass transfer

when the bubble was altered from a luminescing to a non-luminescing state was reproducible.

It can be seen (from figure 7.4) that there is a 2.5 % increase in the steady state current observed when the bubble is luminescing. Considering the low background signal achieved for the detection of I_3^- this cannot account for the magnitude of the cathodic reduction signal observed (see figure 7.3). If the change in current were due to mass transport alone a minimal effect (< 0.1 pA) would be observed in going from a luminescing to non-luminescing state (see figure 7.3).

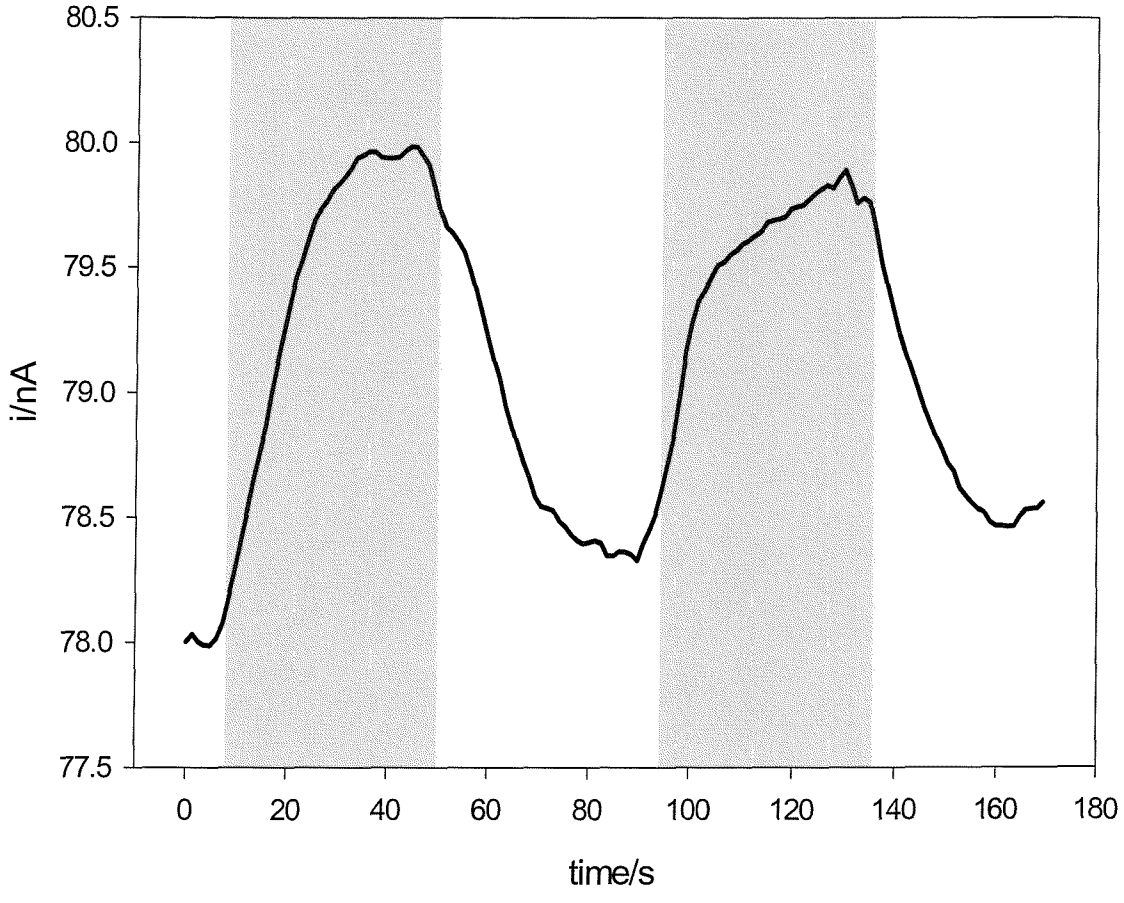

Figure 7.4 Plot showing the effect that altering the drive voltage (and thereby altering the acoustic pressure amplitude) has on mass transport. The cell contained a degassed solution of 3 mmol dm^{-3} KI in 97 mmol dm^{-3} Na_2SO_4. The acoustic pressure amplitude when the bubble was luminescing was 150 kPa. When the bubble was altered to a non-luminescent state the acoustic pressure amplitude was 148 kPa. The needle microelectrode was held at +0.9 V vs. Ag and the steady state current for the oxidation of I^- was monitored as a function of time. The bubble was altered from between luminescing (grey shading) and non-luminescing (white shading).

Assuming the diffusion coefficient[138] of I^- = 1.6 x 10^{-5} cm^2 s^{-1} and the diffusion coefficient of I_3^- is equal to 7.6 x 10^{-6} cm s^{-1} (calculate in chapter 4, section 4.1), the

concentration of I_3^- can be calculated using equation (7.1) where Δi is the change in cathodic current (reduction of I_3^-) in going from a non-luminescing to a luminescing state (ca. 20 pA) and $k' = 1.92$. All other terms have been explained in chapter 2, section 2.3. Using this equation the concentration of I_3^- can be calculated as 2×10^{-7} mol dm^{-3}.

$$\Delta i = nFAk_m k' c_{I_3^-} \qquad (7.1)$$

Recently Didenko and Suslick[165] published evidence for the production of radicals from SBSL. These authors performed the terephthalate dosimeter to detect evidence for the production of $OH^\bullet$ from SBSL. The authors generated SBSL in a cell containing 15 cm^3 of solution and performed fluorescence measurements using the bulk solution (15 cm^3). They measured the fluorescence of the indicator product (2 hydroxyterephthalate) for the terephthalate dosimeter. It is interesting to compare the results reported here with the available literature.

Didenko and Suslick[165] reported a maximum rate of 10^5 hydroxyl radicals per acoustic cycle. At 52 kHz this equates to 5.2×10^9 molecules of $OH^\bullet$ per second in the 15 cm^3 cell volume. Hence by employing Avogado's number[167] the concentration of $OH^\bullet$ can be calculated as 5.8×10^{-10} mol m^{-3}. The concentration of I_3^- (detected at distances from the bubble) calculated from the results presented in this chapter was 2×10^{-4} mol m^{-3}. It is known that 2 $OH^\bullet$ radicals are required to generate one I_3^-. This leads to an effective $OH^\bullet$ concentration of 4×10^{-4} mol m^{-3}. In addition, the experiments presented in this chapter were performed at 27 kHz. In order to get an equivalent concentration, to the bulk concentration obtained by Didenko and Suslick[165] (who performed their experiments at 52 kHz) equation (7.2) is employed. This yields a local $OH^\bullet$ concentration of 7.7×10^{-4} mol m^{-3}.

$$\left[\frac{52}{27}\right] \times \left(4x10^{-4}\right) = \text{Equivalent } OH^\bullet \text{ concentration} \qquad (7.2)$$

Finally, it is also important to remember that the efficiency of the Weissler reaction for the trapping of $OH^\bullet$ (or other oxidising species) is estimated to be of the order of 10 % (as a result of the low I^- concentration employed, see chapter 4 section 4.1 figure 4.2). Hence it is possible to estimate the concentration of $OH^\bullet$ responsible for the electrochemical signal recorded to be of the order of 7.7×10^{-3} mol m^{-3}.

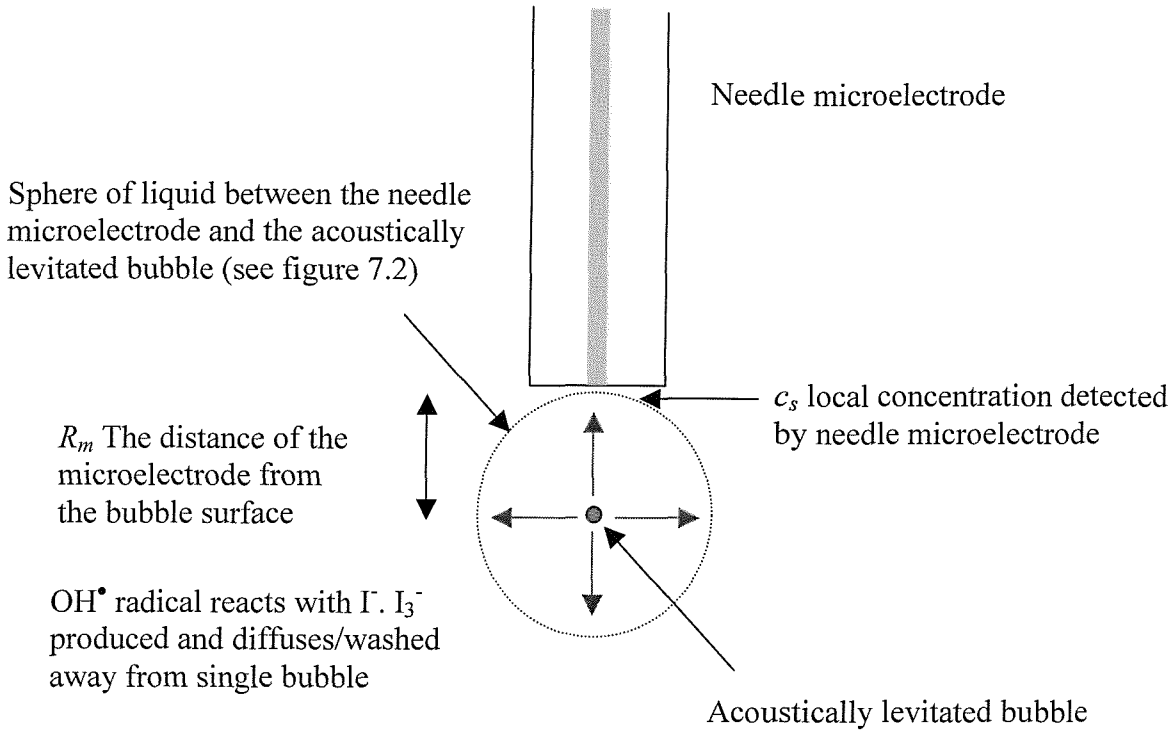

Figure 7.5 Diagram illustrating how Didenko and Suslick[165] bulk concentration is compared to the local concentration achieved employing the results achieved in this chapter.

To compare the local concentration (7.7 X 10^{-3} mol m^{-3}) to the bulk concentration results obtained by Didenko and Suslick[165] it is also necessary to consider the volume of dilution. The problem is illustrated in figure 7.5. As the local concentration interrogated by the needle microelectrode is much smaller than in the bulk, we would expect a higher local concentration. Assuming that the local concentration of I_3^- is evenly distributed in a spherical solution volume, it is possible to relate this local concentration to the bulk concentration obtained by Didenko and Suslick[165] (5.8 x 10^{-10} mol m^{-3}). If this assumption is correct this means that the volume change is 1.32 x 10^7, which is given by equation (7.3):

$$V_d = \frac{c_s}{c_b} \tag{7.3}$$

where V_d is the volume change close to the bubble surface compared to the bulk solution and c_s and c_b are the local and bulk concentrations respectively. This leads to an estimated volume of 1.12 x 10^{-12} m^3. This was calculated employing equation (7.4):

$$V_s = \frac{v_b}{V_d} \tag{7.4}$$

where V_s represents the local spherical volume and v_b represents the volume of the bulk solution (1.5 X 10^{-5} m^3, i.e. the volume employed by Didenko and Suslick[165]).

Employing equation (7.5) allows the value R_M, the distance of the microelectrode form the bubble surface to be calculated as 64 μm.

$$V_s = \frac{4}{3}\pi R_m^3 \tag{7.5}$$

Although the exact distance between the needle microelectrode and the acoustically levitated bubble is not known the value obtained on comparing the results obtained in this chapter with those obtained by Didenko and Suslick[165] seems unrealistic. Positioning the microelectrode 64 μm from the bubble wall would be very difficult. In addition, it should also be noted that the concentration of I_3^- produced at the bubble wall would probably fall off with distance as $1/R_m$ or $(1/R_m^2)$ law suggesting even higher concentrations at the bubble wall and a smaller volume of dilution.

Unfortunately it is difficult to compare the results achieved in this chapter for the local concentrations of I_3^- detected with the results reported by Didenko and Suslick.[165] This is in part due to the lack of experimental information reported by these authors.[165] Didenko and Suslick[165] calibrated their radical trap system by employing the results of Fang *et al.*[168] Fang *et al.*[168] performed the terephthalate dosimeter in the presence and absence of $IrCl_6^{2-}$ under a N_2O/O_2 atmosphere. However, Didenko and Suslick[165] used partially degassed solutions but did not report the employment of $IrCl_6^{2-}$ so it is difficult to see how these authors achieved an accurate calibration. In addition the authors did not report any calibration of the initial seeding effect of SBSL described by Brenner *et al.*[106] or whether they seeded the system with an argon bubble. The results reported here suggest that the amounts of $OH^{\bullet}$ produced by SBSL may be significantly higher than those reported by Didenko and Suslick.[165]

Finally in the case of MBSL, Henglein[76] estimates that the local concentration of radicals around a single cavitation event can reach the order of 4 mmol dm^{-3}. However, direct comparisons between MBSL and SBSL are difficult to make.

7.3 The Weissler Reaction in the Presence of Carbonate Dianion

Further complementary evidence that the signal achieved in figure 7.3 was indeed due to the reduction of I_3^- was obtained by performing the Weissler reaction in the presence of the carbonate dianion (1 mmol dm^{-3}). First however, to illustrate that the carbonate dianion could block the Weissler reaction a set of control experiments were performed using MBSL in ultrasonic reactor cell (A) and the electrochemical flow cell. (For further details about the procedures employed see chapter 4 section 4.1).

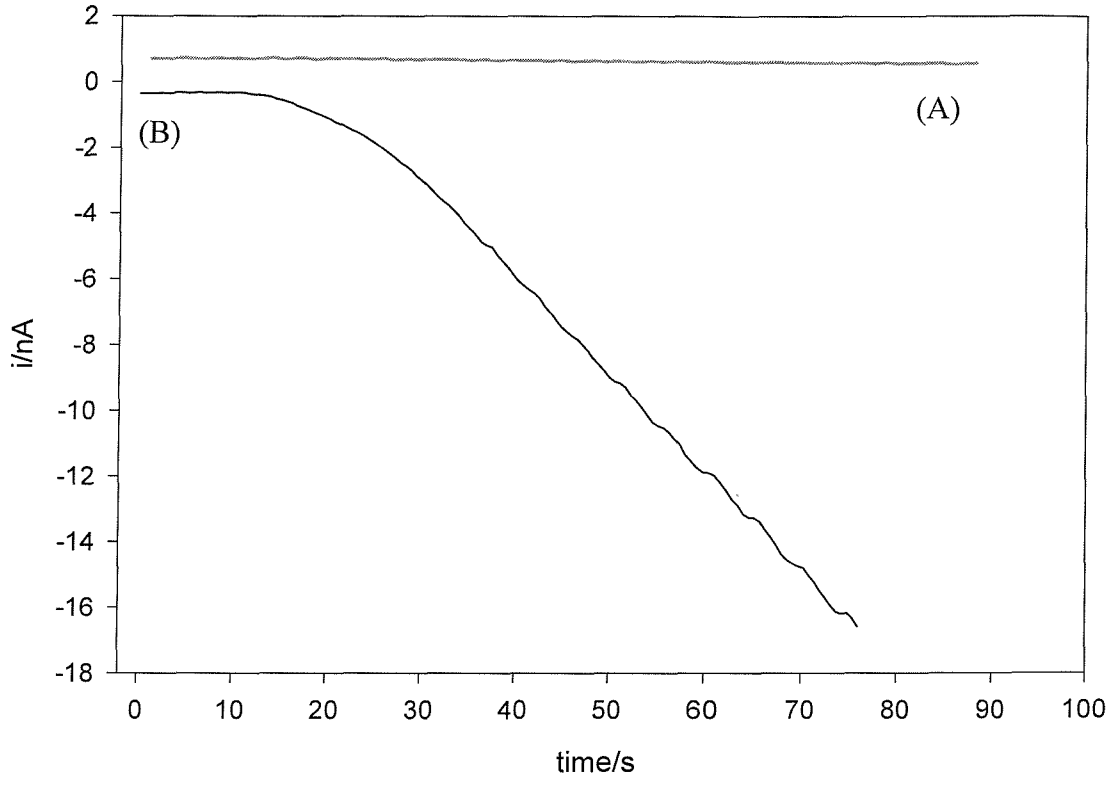

Figure 7.6 The Weissler reaction performed with solution (A), 1 mmol dm^{-3} of Na_2CO_3 and 3 mmol dm^{-3} KI in 96 mmol dm^{-3} Na_2SO_4 and solution (B), 3 mmol dm^{-3} KI in 97 mmol dm^{-3} Na_2SO_4. Ultrasonic reactor cell (A) was employed with the continuous flow pump. The solution was irradiated with 125 kHz ultrasound and the acoustic pressure amplitude was kept constant 317 kPa in both cases Solution was pumped from the ultrasonic reactor to the flow cell where electrochemical measurements were performed using a 0.5 mm diameter platinum working electrode. The working electrode was held at +0.2 V versus SCE. The ultrasonic reactor was temperature controlled at 25 °C.

A low concentration (1 mmol dm^{-3}) of Na_2CO_3 was added to 3 mmol dm^{-3} KI in 96 mmol dm^{-3} Na_2SO_4. The results are illustrated in figure 7.6. Solution (A) represents the Weissler reaction performed with 1 mmol dm^{-3} of Na_2CO_3 and 3 mmol dm^{-3} KI in 96 mmol dm^{-3} Na_2SO_4. Solution (B) represents the Weissler reaction performed with 3 mmol dm^{-3} KI

in 97 mmol dm^{-3} Na_2SO_4. Both reactions were performed under identical conditions. The ultrasound was turned on at time t = 0 s. For solution (A) no change was observed in the current time signal with time. For solution (B) the current proceeds cathodically after time t = 10 s (the time taken for the solution in the ultrasonic reactor to reach the flow cell) corresponding to the reduction of I_3^-. The linear section of the plot can be used to calculate the rate of production of this process (see chapter 2 section 2.3).

Two possible mechanisms exist to explain how the carbonate dianion blocks the Weissler reaction. These are as follows:

• In the presence of hydroxyl radicals carbonate is converted to a one-electron oxidant according to reaction [7.2].[169] The carbonate dianion competes with the I^- to react with the hydroxyl radical. However, I^- is a very efficient radical scavenger for $OH^\bullet$ so it is unlikely that this is the dominant mechanism. In addition the MBSCL experiments performed in chapter 3 employed a luminol solution containing 50 mmol dm^{-3} Na_2CO_3. It is known that $OH^\bullet$ is involved in the primary oxidation step (see chapter 1 section 1.8). Therefore, for the reasons stated above this is unlikely to be the prevailing mechanism.

$$CO_3^{2-} + OH^\bullet \longrightarrow CO_3^{-\bullet} + OH^- \qquad [7.2]$$

• However, I_2 is also known to react with OH^- (see reaction [7.3 - 7.5]).[139]

$$I_2 + 2OH^- \rightleftharpoons I^- + IO^- + H_2O \quad K = 30 \qquad [7.3]$$

However, the IO^- is extremely unstable,

$$3IO^- \rightleftharpoons 2I^- + IO_3^- \qquad K = 10^{20} \qquad [7.4]$$

Hence, overall no IO^- is found in solution. The overall reaction is,

$$3I_2 + 6OH^- \longrightarrow 5I^- + IO_3^- + 3H_2O \qquad [7.5]$$

Reaction [7.3] is slow owing to the low concentration of OH^-. However reactions [7.4] is fast and by Le Chatelier's principle[166] the process will go to completion (see reaction [7.5]).

Figure 7.7 illustrates a CV of the 50 μm diameter needle-microelectrode in 3 mmol dm^{-3} KI, 1mmol dm^{-3} Na_2CO_3 and 96 mmol dm^{-3} Na_2SO_4. The insert in figure 7.7 shows a

potential step under the same conditions from + 0.2 V to + 0.9 V vs. Ag. This plot illustrates that a steady state current for the oxidation of I^- can be achieved under the conditions employed (see figure 7.1 and reaction [7.1]).

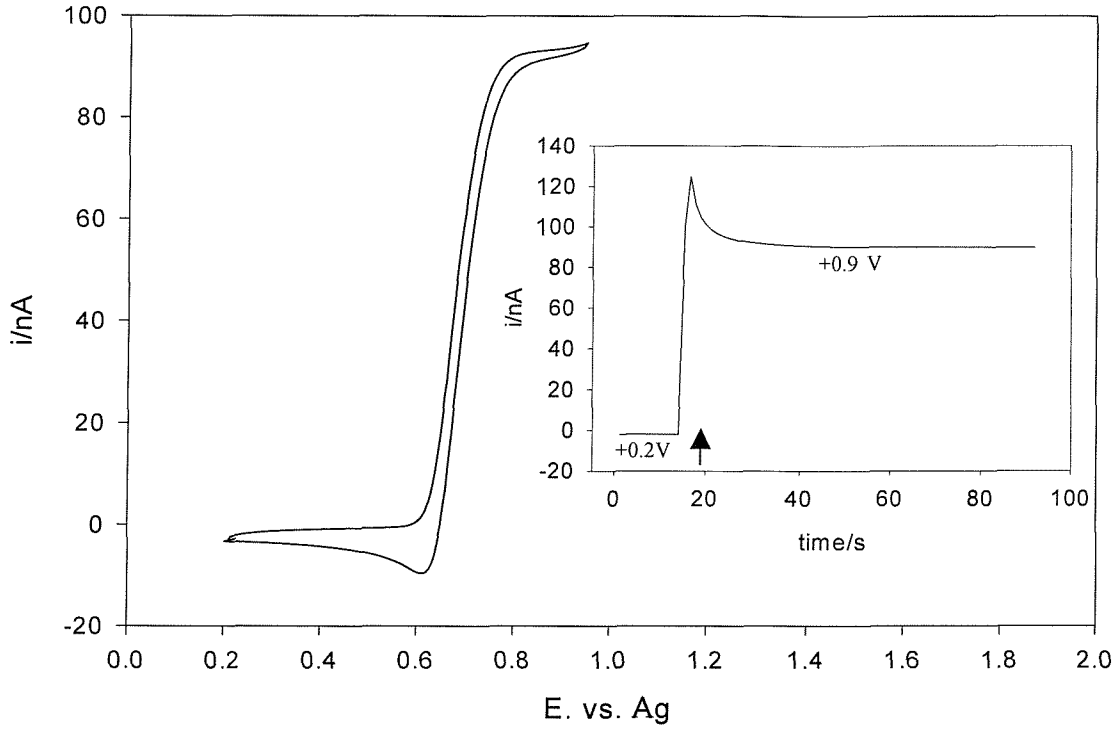

Figure 7.7 A Cyclic Voltammogram of the 50 μm needle microelectrode in a 3 mmol dm^{-3} solution of KI in 1 mmol dm^{-3} Na_2CO_3 and 96 mmol dm^{-3} Na_2SO_4. The potential was swept at 5 mVs^{-1} versus silver wire and the cell was thermostated at 25 °C. The insert in the plot shows a potential step from + 0.2 V to + 0.9 V under the exact same conditions. The arrow in the insert plot indicates where the potential was stepped to + 0.9 V. vs. Ag.

7.4 Electrochemical Investigation of SBSL – The Weissler Reaction Performed in the Presence of the Carbonate Dianion

Figure 7.8 shows images recorded during the electrochemical Weissler reaction in the presence of carbonate dianion (in addition see figures 7.9 and 7.10). Figure 7.8 (a) illustrates the illuminated cell. Figure 7.8 (b) shows SBSL with the needle microelectrode positioned close to the surface of the luminescing bubble. Figure 7.8 (c) shows the bubble in a non-luminescing state as the acoustic pressure was varied. Figure 7.8 (d) illustrates that SBSL may be generated again by increasing the acoustic pressure. The experiment was performed in the same manner as section 7.2.

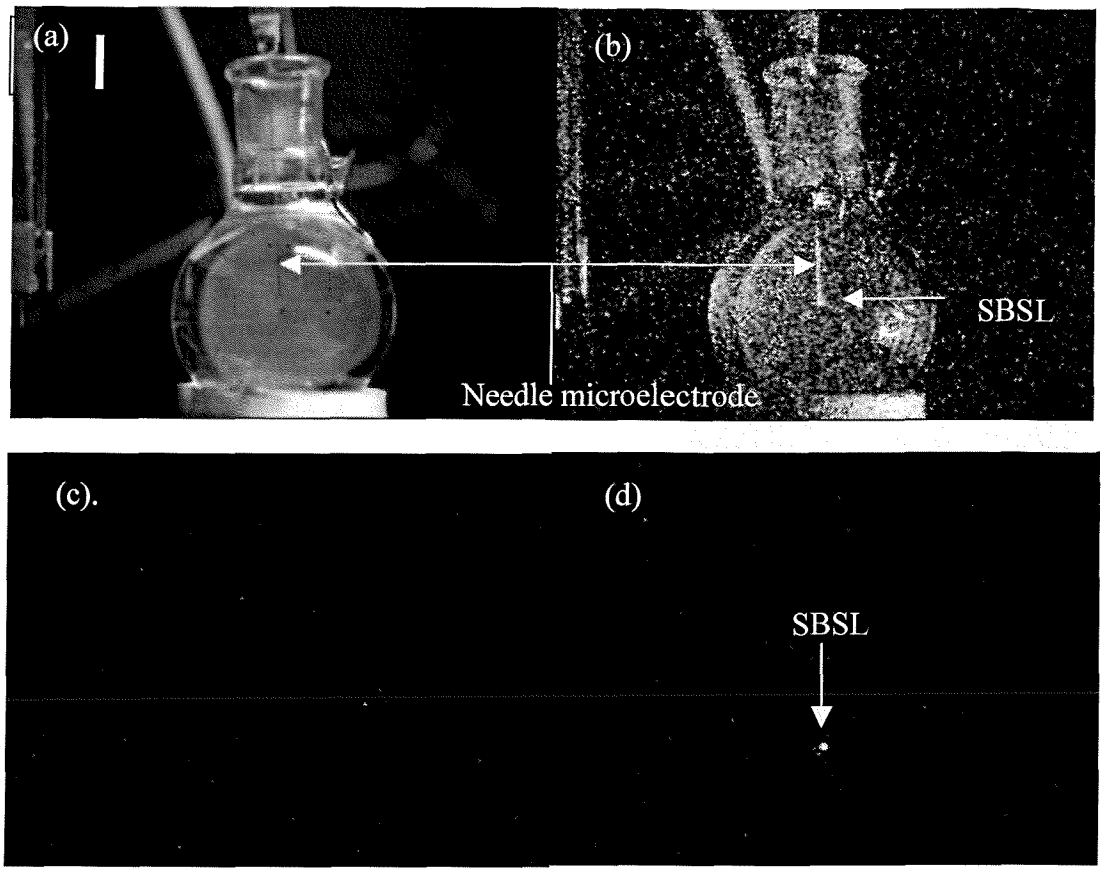

Figure 7.8 Photographs recorded of SBSL when the bubble was switched from a luminescing (d) to a non-luminescing state (c) using an image intensified CCD camera. Picture (a) illustrates the cell when the bubble is in the non-luminescing state. Picture (b) illustrates SBSL with the needle microelectrode positioned close to the luminescing bubble. The bubble is luminescing in the centre of the cell. The other light in this picture is scattered light. Pictures were recorded while the experiment illustrate in figure 7.9 and 7.10 was in progress. SBSL was generated at 27.744 kHz and 132 kPa acoustic pressure amplitude. The cell contained a degassed solution of 3 mmol dm^{-3} KI in 1 mmol dm^{-3} Na_2CO_3 and 96 mmol dm^{-3} Na_2SO_4. The scale bar in picture (a) represents 15 mm. Adjusting the drive voltage and thereby reducing the acoustic presuure amplitude to 130 kPa altered the bubble from a luminescing to a non-luminescent state.

Figure 7.9 illustrates the experimental results achieved. The 50 μm needle microelectrode was positioned as close as possible to the bubble wall (see picture (b) figure 7.8). The cell contained 1 mmol dm^{-3} of Na_2CO_3 and 3 mmol dm^{-3} KI in 96 mmol dm^{-3} Na_2SO_4. The working electrode was held at +0.2 V versus silver wire. The current was monitored as a function of time. At time t = 30 s the voltage was decreased so that the bubble no longer luminesced (white shading). The entire process was repeated to illustrate that the signal was reproducible. The signal does vary systematically with drive voltage (acoustic pressure) but the variation is small and cannot easily be discriminated against the noise.

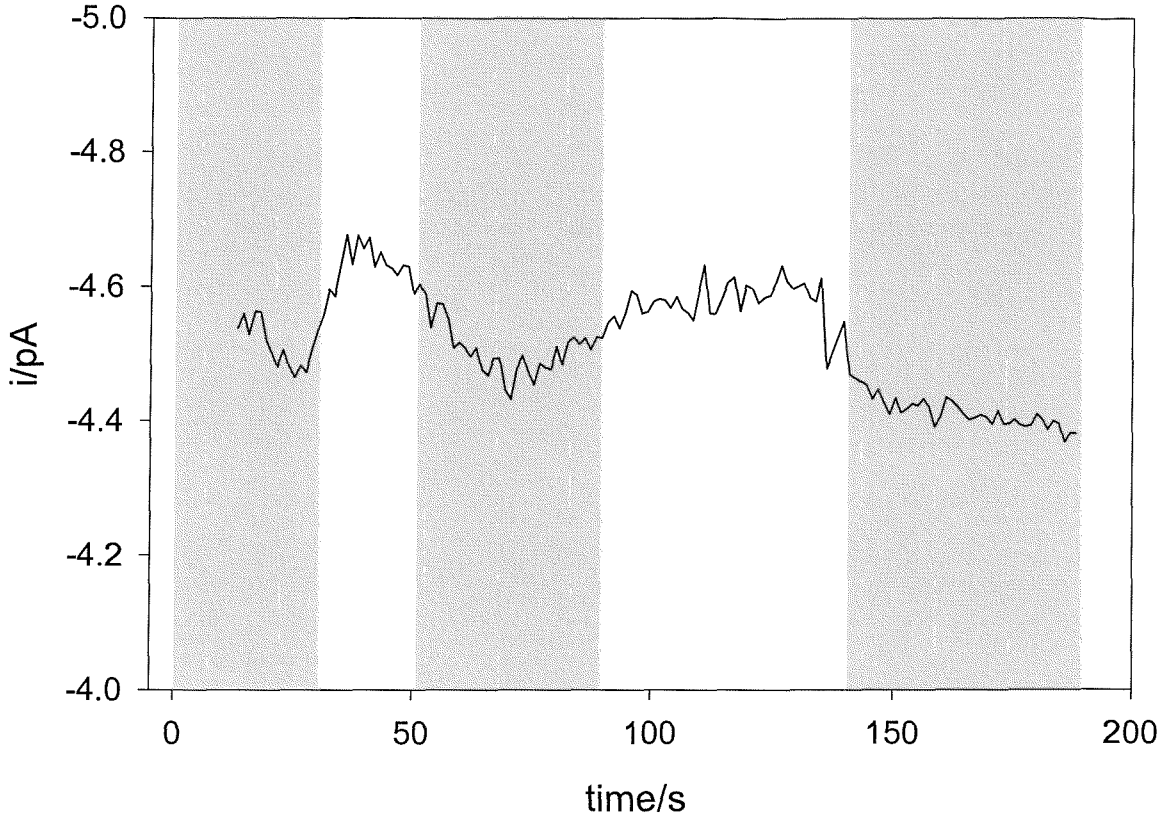

Figure 7.9 This figure illustrates the electrochemical Weissler reaction in the presence of the carbonate dianion performed on SBSL generated at 27.744 kHz and 132 kPa acoustic pressure. The cell contained a degassed solution of 3 mmol dm^{-3} KI in 1 mmol dm^{-3} Na_2CO_3 and 96 mmol dm^{-3} Na_2SO_4. The current was monitored as a function of time using a 50 μm needle microelectrode positioned close to the bubble wall. The electrode was held at +0.2 V versus silver wire. The bubble was altered from a luminescing (grey shading) to a non-luminescing state (white shading) by adjusting the drive voltage (and thereby altering the acoustic pressure amplitude to ca. 130 kPa).

The potential was then stepped to +0.9 V vs. Ag and the steady state current for the oxidation of I^- (see reaction [7.1]) was monitored for the luminescing and non-luminescing bubble. This is illustrated in figure 7.10. At time t = 0 s the bubble is luminescing and the current is monitored as a function of time. At ca. t = 25 s the drive voltage is adjusted so that the bubble no longer luminesces. The anodic current can be seen to decrease. This process was repeated a number of times to illustrate that the change in mass transfer when the bubble was altered from a luminescing to a non-luminescing state was reproducible. In this case a 3 % change in current was observed due to mass transfer as a result of the extra forced convection resulting from the increased acoustic pressure in the luminescent state. However, in contrast to figure 7.3 no quantifiable change in current from the background signal was observed in the presence of the carbonate dianion when the electrode potential was switched to +0.2V vs. Ag (a potential sufficient to reduce any I_3^- produced from radical capture). This is strong evidence that the signal observed at +0.2 V for the luminescing

bubble is indeed due to the reduction of I_3^- produced as a result of hydroxyl radicals (and associated reactions) generated from SBSL.

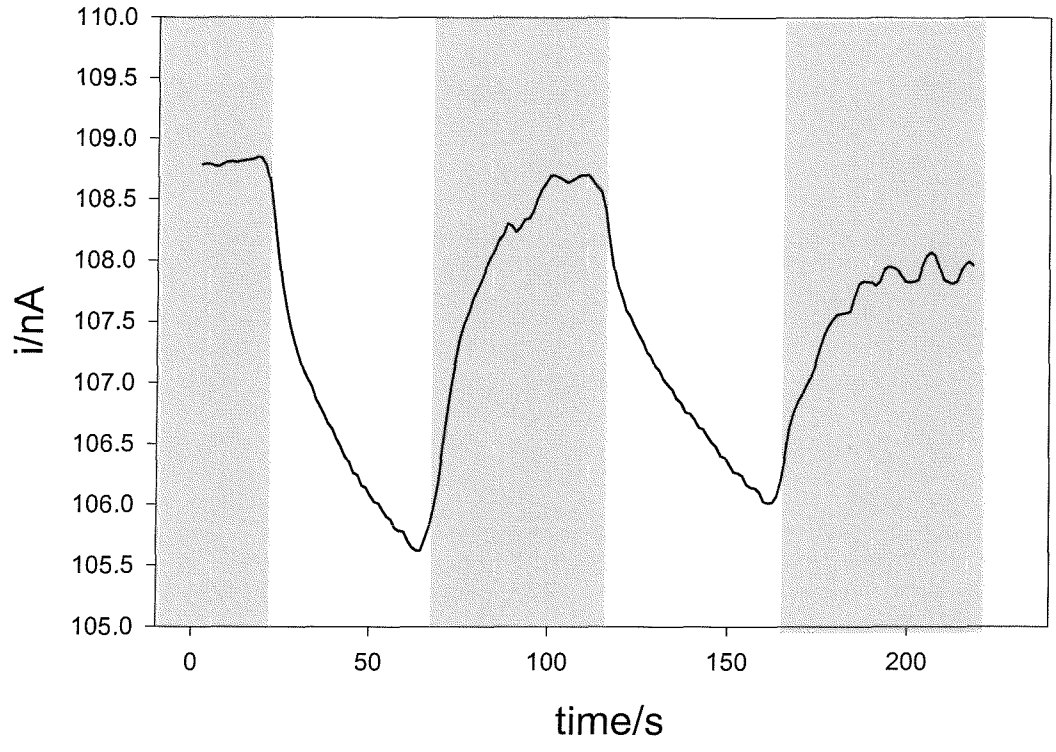

Figure 7.10 Plot illustrates the effect that altering the voltage (and thereby altering the acoustic pressure amplitude) has on mass transport. The cell contained a degassed solution of 3 mmol dm^{-3} KI in 1 mmol dm^{-3} Na_2CO_3 and 96 mmol dm^{-3} Na_2SO_4. The potential is switched to +0.9 V versus silver wire and the steady state current for the oxidation of I^- is monitored as a function of time. The bubble is altered between a luminescing (grey shading) and non-luminescing state (white shading). The acoustic pressure amplitude when the bubble was luminescing was 132 kPa and when the bubble was non luminescing was 130 kPa. The conditions employed in this experiment are the same as figure 7.8.

7.5 Spectrophotometric Study of SBSL

The light emission spectrum of SBSL was recorded using an in house designed spectrometer (see experimental section 2.16 for details of design and calibration). The spectrum of SBSL is illustrated in figure 7.11. The spectrum shows the characteristic continuum light emission spectrum of SBSL. The spectrum compares well with the work of other authors[110] (see chapter 1 section 1.10 and 1.11).

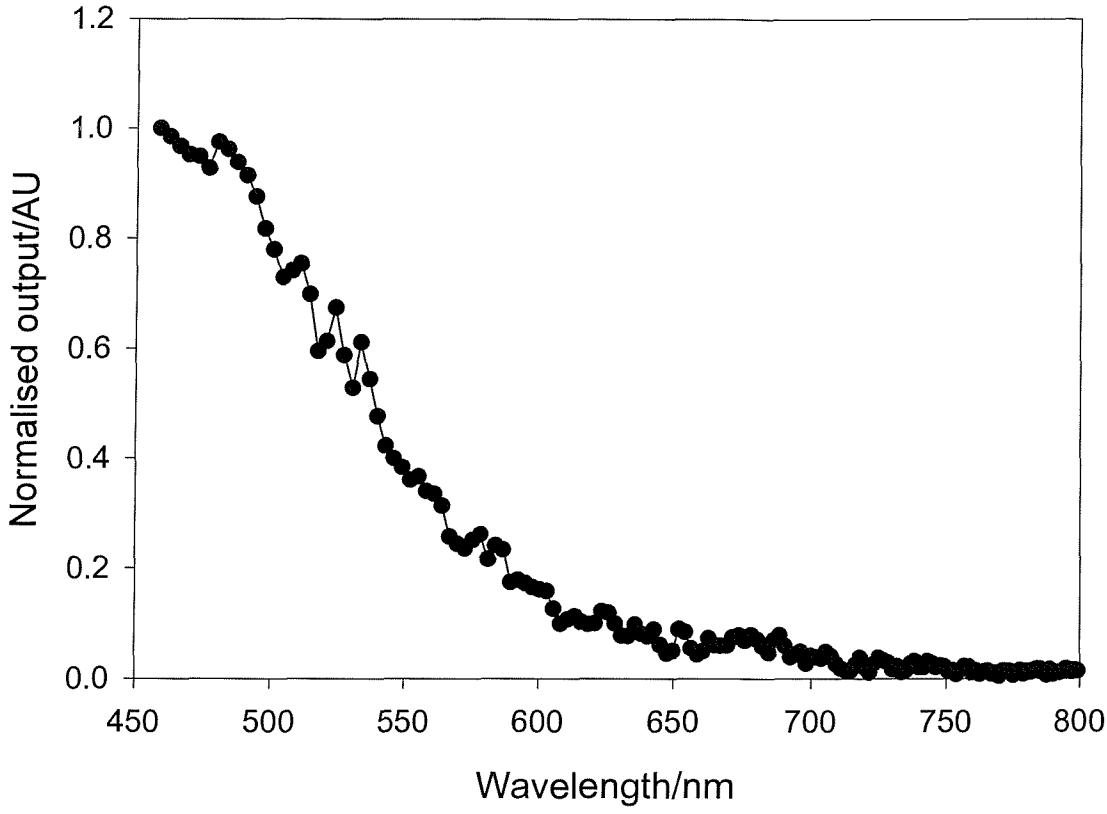

Figure 7.11 shows the light emission spectrum of SBSL recorded using an in-house built spectrometer (see experimental section 2.14). The cell contained a degassed solution of 1.5 mol NaCl. SBSL was generated at 27.744 kHz and 132 kPa acoustic pressure amplitude.

7.6 Conclusions

A novel electrochemical technique has been presented which provides the first quantifiable electrochemical evidence for the production of radicals oxidising species from SBSL. It was shown that it is possible to alter the bubble form a luminescent to a non-luminescent state by altering the drive voltage amplitude and associated acoustic pressure. A novel needle microelectrode was used to approach the bubble surface. A concentration of 2 x 10^{-7} mol dm^{-3} of I_3^- was calculated at the microelectrode surface when the bubble luminesced. This was compared to the recent results of Didenko and Suslick[165] who measured the bulk concentration of $OH^{\bullet}$ formed by SBSL by performing the terephthalate dosimeter.

The next chapter outlines the overall conclusions form the results presented in chapters 3-7 inclusive and recommendations are also made for future work in this area.

Chapter 8

CONCLUSIONS AND FUTURE WORK

8.1 Concluding Remarks

This thesis reports a combined electrochemical, acoustic and photographic and luminescent study of MBSL and SBSL. The purpose of the work was to measure the 'activity' of inertial cavitation. In contrast to much of the previous work on this notably difficult field emphasis was placed on the importance of understanding the acoustics of the ultrasonic reactor and how this knowledge is essential to interpret the chemical and physical effects of cavitation occurring within the reactor. Throughout the course of this thesis Apfel's advice was followed.[20] This chapter presents the general conclusions drawn from this investigation. Future work is also addressed in the present section.

Experiments were designed to characterise the sound fields in the ultrasonic reactors employed. The cylindrical cells employed for chemical analysis were characterised acoustically both experimentally and theoretically. For the first time a sonochemically active sound field was modelled with appropriate consideration of the boundary conditions at the vessel walls. An acoustic model was developed to predict the spatial distribution of acoustic pressure, which was compared with experimental measurements of the spatial characteristics of luminescent emission from a cylindrical cell. The model predicts the spatial distribution of acoustic pressure within the ultrasonic reactor. The theoretical analysis was combined with a photographic technique, which involved the use of a chemiluminescent reaction sensitive to hydroxyl radical formation. This was used to spatially resolve cavitation within the ultrasonic reactors. The main conclusions drawn from this analysis was as follows:

- The model predicted a series of concentric rings when viewed from above the cell and a series of bands when viewed from the side (see chapter 3 section 3.3). The theoretical model employed agreed with the photographical analysis. The acoustic modes excited in the cell were calculated. It was shown that the theoretical frequency predicted by the model was in excess of the applied frequency. However, the model assumed a speed of sound of 1500 m s^{-1}. The difference between the applied and predicted frequency was used to calculate the sound speed within the cavitation environment. This was in the range of 868 - 1062 m s^{-1}, which corresponded to a bubble void fraction range of 2.91 - 4.24 x 10^{-3} % (under certain assumptions see chapter 3 section 3.4).

• The acoustic mode excited in the cell under the conditions employed was shown to vary as a function of frequency with 1 kHz resolution. If the acoustic mode changes as a function of 1 kHz the chemistry occurring within the cell will also change. This is important as much of the sonochemical literature at present attempts to optimise the conditions for sonochemical processes by investigating reaction rates at dramatically different frequencies.[23, 159-161] Other factors investigated in this study include the effect of the solution height on the mode excited in the cell. It was shown that as the solution height was varied the mode changed and hence cavitation activity also changed. In general the study shows that to achieve optimum rate from a given ultrasonic reactor under a given set of physical conditions the cell must be characterised with kHz resolution.

After acoustically characterising the ultrasonic reactor the chemistry occurring within the reactor was investigated. Four novel electrochemical sensors for detecting evidence for the production of radicals as a result of inertial cavitation were developed. These included the Fricke reaction, the Weissler reaction, Cu ($H^{\bullet}$), and H_2O_2. The main conclusions drawn from this chapter were as follows:

• The radical detectors described in chapter 4 represent the first strong electrochemical evidence for free radicals. They have been shown to be working reproducibly within a cavitation environment. The electrochemical detection method employed has significant advantages over the conventional spectroscopic investigation of these systems. For the first time radical production as a result of ultrasonic cavitation has been measured on a semi real time basis. The sensitivity of the electrochemical sensors is unsurpassed at present in the literature. The detection limit for the detectors is as low as 4 nmol dm^{-3} s^{-1} corresponding to 1 rad s^{-1}.

• The Fricke reaction was used to compare the measured reaction rates to radiation chemistry and the equivalent dose of the ultrasonic reactor was calculated, 16 rad s^{-1} (see chapter 4 section 4.4).

• The Cu ($H^{\bullet}$) system represents a significant advance for the detection of evidence for the existence of $H^{\bullet}$. The majority of radical trap systems detect the presence of $OH^{\bullet}$, as this species is more easily detected than $H^{\bullet}$ owing to the different chemical activity of these two species. The Cu ($H^{\bullet}$) sensor represents the first electrochemical evidence for the existence of $H^{\bullet}$.

The effect of varying the ultrasonic frequency was examined in chapter 5. A frequency study of chemical activity (radical production) was performed in combination with MBSL in

a cylindrical water-jacketed ultrasonic reactor using the electrochemical radical detectors. This study yielded some valuable information including the following:

- A strong correlation was observed between the MBSL photon count and chemical activity. In each case the highest MBSL photon count corresponded with the highest reaction rate under the conditions employed. The study showed that kHz resolution of both MBSL and the rates were required. A frequency difference of 3 kHz could result in the rate changing by 3 orders of magnitude. This has obvious implications for the frequency dependence of ultrasonic reactions where spot frequency measurements are recorded and compared at dramatically different or predetermined frequencies (see chapter 5).
- The chemical results achieve in this section agreed with the frequency dependence of the modal pattern observed in chapter 3 (see figure 3.10). These results are in contrast to COMORAC (see chapter 6) where the modal pattern in the cell was difficult to understand.

In addition MBSL was proposed as a possible detector of chemical activity in ultrasonic reactors. MBSL was shown to be the only reliable indicator for chemical activity when compared to other techniques such as pressure measurements or airborne audible noise output from the cell.

In the next section an international collaboration experiment was under taken with NPL and other partners. NPL designed what they hoped would be a "standard ultrasonic bath" and a "standard detector system". The electrochemical sensors designed in chapter 4 were tested in the bath (in addition to sensors provided by the other partners) to investigate how well their system conformed to a "standard". Experiments were performed in a filtered degassed water solution tested using NPL's "standard" sensor. Prior to the test they informed the various partners that the sound field was diffuse. This fact was disproved in chapter 6 through the test results reported in this thesis. The main conclusions of the study were as follows:

- With a bath of this nature it is essential to employ MBSCL to visualise the sound field and to locate the hot and cold spots in the bath. It is important to note that MBSCL was employed in this experiment but with a powerful enough camera system incorporating image intensifiers and sufficient blackout conditions MBSL could be employed and this would remove the need for the extreme chemical conditions required for this technique allowing other sensors to be employed in tandem. Without this technique many of the chemical sensors may have yielded no results.
- Comparisons were made between the results obtained using local chemical sensors (acoustically transparent cell placed at the hot spot) and spatially averaging sensors (photon

counter placed above the hot spot). The electrochemical Weissler reaction was the only sensor to yield data in the cold spot. This is testament to the sensitivity of the electrochemical technique.

- The preliminary results achieved were promising. However, the project showed that the choice of reference vessel is critical to achieving reproducible results. A cell of the type used for the radical trapping experiments (see chapter 4) with a sound field that can be characterised may have yielded more reproducible results.

Chapter 7 describes the first electrochemical study of single bubble sonoluminescence. This chapter probes the differences and similarities between SBSL and MBSL. A number of important discoveries were made including the following:

- The first electrochemical evidence for the production of radicals as a result of SBSL is presented. The electrochemical Weissler reaction is performed by bring a novel microelectrode towards the surface of the luminescing bubble and detecting the local concentration of I_3^-. The bubble is altered from a luminescing to a non-luminescing mode and the signal can be seen to disappear. A detailed photographic study was also performed during the experiments to illustrate this effect. The results achieved are compared to the recent work of Didenko and Suslick.[165]
- A control experiment was also performed in the presence of the carbonate dianion, which blocks the Weissler reaction. In this case only mass transfer due to changes in acoustic pressure could be measured. The production of radicals may agree with the theory of rectification where radical species are removed from the bubble and the observed luminescence is due to the rare gas content.
- Finally the Spectrum of SBSL was measured using a novel in-house built spectrometer. The spectrum agrees with the work presented in the literature.[111]

8.2 Future Work

The potential exists for a vast amount of further research in this area. The work presented in this thesis was performed using aqueous solutions. Grieser *et al.*[170-173] investigate the effect of addition of additives such as surfactants on MBSL and SBSL and have devised a model for the effect of surfactant based on electrostatic effects of the additives. It would be interesting to test this model in our system by performing MBS(C)L and analysing the effect that the addition of surfactant has on the acoustic mode within the ultrasonic reactor.

In the case of SBSL it would be interesting to perform other radical trapping experiments possibly the detection of H_2O_2 and the Cu ($H^{\bullet}$) system. These are extremely difficult experiments to perform, as a very low background signal is required ("black background"). Otherwise the signal will be lost in the noise. Hence, this was the reason for choosing the Weissler reaction in the study performed in chapter 7. It may be possible to detect hydrogen peroxide on a mesoporous platinum electrode under similar conditions to those employed for the Weissler reaction. In addition it would be interesting to probe the spectroscopic differences between SBSL and MBSL. In particular it may be interesting to test the spectroscopic effect of adding H_2O_2 to the luminescing bubble since the concentration of H_2O_2 is far greater in the case of MBSL. This may be the reason for the observed OH^* peak in the MBSL spectrum.

Another COMORAC experiment would be interesting to perform with a longer time scale allowing numerous experimental tests to be carried out. Comparison could then be made of all the available sensors and a more detailed critical evaluation could be preformed based on accurate experimental data. It would be interesting to perform the complete range of electrochemical sensors designed in chapter 4. In addition some of the industrially favoured techniques such as lead block erosion could be compared to the more scientific techniques.

REFERENCES

1. Mason T. J. (Ed.), Sonochemistry: *The uses of Ultrasound in Chemistry* Coventry Royal Society of Chemistry, Cambridge **1989**.
2. Leighton, T. G., *The Acoustic Bubble'*Academic Press Limited, London **1994**.
3. Bioprocess Technology, *Technical Insights Inc.,* August **1989** (ISNN 0885-5625).
4. Solisova, M.; Toma, S. Mason, T. J. *Ultrason. Sonochem* **1997**, 4, 131.
5. Vinatoru, M.; Toma M.; Radu, O.; Filip, P. I.; Lazurca D.; Mason T. J. *Ultrason. Sonochem.* **1997**, 4, 135.
6. Serpone, N.; Terzian, R.; Hidaka, H.; Pelizzetti, E. *J. Phys. Chem.* **1994,** 98, 2634.
7. Reisz, P.; Kondo, T.; Murali Krishna, C. *Ultrasonics* **1990**, 28, 295.
8. Inazu K.; Nagata Y.; Maeda, Y. *Chem. Lett.* **1993**, 57, 57.
9. Kruss, P.; Burk, R. C.; Entezari, M. H.; Otson, R. *Ultrason. Sonochem.* **1997**, 4, 229.
10. Mason, T. J.; Newman, A.; Lorimer, J. P.; Lindey, J.; Hutt, K. (1996) *Ultrason. Sonochem.* **1996** 3, 53.
11. Suslick, K. S. *Scientific American* **1989**, 260, 62.
12. Maison, T. J.; Lorimer, J. P. *Sonochemistry - Theory, Applications and Uses of Ultrasound in Chemistry*, Horwood E., Chichester, **1988**.
13. Suslick, K. S., *Ultrasound Its Chemical Physical and Biological Effects* Chapter 4, VCH Publishers, New York, **1990**.
14. Weissler, A.; Copper, H. W.; Snyder S. *J. Am. Chem. Soc.* **1950**, 72, 1769.
15. Price, G. J.; White, A. J.; Clifton, A. A. *Polymer* **1995**, 36, 4919.
16. Abramov, O. V. *Ultrasound in Liquid and Solid Metals*, CRC Press, London, **1994**.
17. Flint, B.; Suslick, K. S. *Science* **1991,** 253, 1397.
18. Suslick, K. S.; Hammerton, D. A.; Cline, R.E. *J. Am. Chem. Soc.* **1986,** 108. 5641.
19. Birkin, P. R.; Leighton, T. G.; Watson, Y. E.; Power, J. F. *Acoustics Bulletin*, **2001,** 26, 24.
20. Apfel, R. E., *Ultrason.* **1984**, 22, 167
21. Apfel, R. E., *Methods in Experimental Physics Vol. 19* (Ed. Edmonds, P. D.) Academic Press, New York **1981, 355-413**
22. Leighton, T.G. *Ultrason. Sonochem.* **1995,** 2, S123.
23. Becket, M. A.; Hua I., *J. Phys. Chem. A* **2001**, 105, 3796.
24. Maisonhaute, E.; White, P.C.; Compton, R.G. *J. Phys. Chem. B.* **2001**, 105, 12087.
25. Bertholet, M. *Ann Chim. Phys.* **1850,** 30, 232.

26. Leighton, T. G. *J. Acoust. Soc. Am.* **2000**, 108, Part 2, 2516.
27. Neppiras, E. A. *Phys. Rep.* **1980**, 61, 159.
28. Walton, A. J.; Reynolds, G. T. *Adv. Phys.* **1984**, 33, 595.
29. Leighton, T. G. *The principles of cavitation*, Chapter 9, *In: ed. M J W Povey and T J Mason, Ultrasound in Food Processing*, Blackie Academic and Professional (an imprint of Chapman and Hall), **1997** 151.
30. Apfel, R. E.; Hollland, C. K. *Ultrasound Med Biol.* **1991**, 17, 179.
31. Holland, C.K.; Apfel, R.E. *IEEE Trans Ultrasonics Ferroelectrics Frequency Control* **1989**, 36, 204.
32. Birkin, P.; Martinez, S. S. *J. Chem. Soc., Chem. Commun*, **1995**, 1807.
33. Birkin, P.; Martinez, S. S. *J. Electroanal. Chem.* **1996**, 416, 127.
34. Lord Rayleigh *Phil. Mag.* **1917**, 34, 94.
35. Elder, S. A. *J. Acoust. Am.* **1958**, 31, 54.
36. Maksimov, A. O.; Leighton, T. G. *Acta Acustica,* **2001**, 26, 10.
37. Birkin P. R., Watson Y. E.; Leighton T.G. *Chem. Comm.*, **2001**, 2650.
38. Birkin P. R., Watson Y.E.; Leighton T. G.; Smith, K. L. *Langmuir*, **2002** 18, 2135.
39 Church, C. C. *J. Acoust. Soc. Am.* **1988**, 84, 1758
40. Eller, A. I. *J. Acoust. Soc. Am.* **1969**, 46, 1246.
41. Preece, C. M. (ed.) *Erosion, Vol. 16.* Academic Press, New York, **1979**.
42. Neppiras, E. A. *Phys. Rep.* **1980**, 61, 159.
43. Lauterborn, W.; Bolle, H. *J. Fluid. Mech.* **1975**, 2, 391.
44. Vogel, A.; Lauterborn, W. *J. Acoust. Soc. Am.* **1988**, 84, 719.
45. Plesset, M. S.: Chapman, R. B. *J. Fluid. Mech.* **1971**, 47, 283.
46. Prosperetti, A. *Ultrasonics* **1984,** 22, 115.
47. Blake, J. R.; Taib, B. B.; Doherty, G. *J. Fluid Mech.* **1986**, 170, 479.
48. Blake, J. R.; Gibson, D. C. *J. Fluid. Mech.* **1981**, 111, 123.
49. Blake, J. R.; Taib, B. B.; Doherty, G. *J. Fluid Mech.* **1987**, 181, 197.
50. Ball, G. J.; Howell, G.; Leighton, T. G.; Schofield, M. *Shock Wave* **2000**, 4, 265.
51. Birkin, P. R.; O'Connor, R.; Rapple, C.; Martinez, S. S. *J. Chem Soc. Faraday Trans.*, **1998**, 94, 3365.
52. Hickling, R.; Plesset, M. S. *Phys. Fluids* **1964**, 7, 7.
53. Plesset, M. S.; Prosperetti, A. *Ann. Rev. Fluid Mech.* **1977**, 9, 145.
54. Brunton, J. H. *Proc 2nd Int. Conf. Rain Eros.* (Fyall, A. A. and King, R. B. eds) Royal Aircraft Establishment, Farnborough, United Kingdom, **1967**, p291.

55. Wells PNT. *Biomedical Ultrasonics*. Academic Press, London, **1977**.
56. Klima, J.; Bernard, C.; Degrand, C. *J. Electroanal. Chem.* **1995**, 399, 147.
57. Bard, A. J. *Anal. Chem.* **1963**, 35, 1125.
58. Dewald, H. D.; Peterson, A. B. *Anal. Chem.* **1990**, 779.
59. Chyla, L. Lorimer, J. P.; Mason, T. J.; Walton, D. J. *J. Chem. Soc. Chem. Commun* **1989**, 603.
60. Zhang, H.; Coury, L. A. *Anal. Chem.* **1993**, 65, 1552.
61. Walton, D. J.; Phull, S. S.; Bates, D. M.; Lorimer, J. P.: Mason T. J. *Electrochim. Acta* **1993**, 38, 307.
62. Heinglein, A.; Hergurger, D.; Gutierrez, M. *J. Phys. Chem.* **1992**, 96, 1126.
63. Flint, E. B.; Suslick, K. S. *J. Am. Chem. Soc.* **1989**, 111, 6987.
64. Mason, T. J.; Lorimer, J. P.; Walton, D. J. *Ultrason.* **1990**, 28, 333.
65. Chyla, A.; Lorimer, J. P.; Mason, G. S.; Walton, D. J. *J. Chem Soc. Chem. Commun.* **1989**, 28, 603.
66. Hardcastle, J. L.; Ball, J. C.; Hong, Q.; Marken, F.; Compton, R.G.; Bull, S. D.; Davies, S. G. *Ultrason. Sonochem.* **2000**, 1, 7.
67. Maisonhaute, E.; Brookes, B. A.; Compton, R. G. *J. Phys. Chem. B* **2002**, 106, 3166.
68. Goldfarb, D. L.; Corti, H. R.; Marken, F.; Compton, R. G. *J. Phys. Chem. A.* **1998**, 102, 8888.
69. Reisse, J.; Francois, H.; Vandercammen, J.; Fabre, O.; Kirsh-de Mesmaeker, A.; Maerschalk, C.; Delplancke, J. – L. *Electrochimica Acta* **1994**, 39, 37.
70. Compton, R.G.; Eklund, J. C.; Marken, F.; Waller, D. N. *Electrochimica Acta* **1996**, 41, 315.
71. Birkin, P. R.; Delaplace, C. L.; Bowen, C. R. *J. Phys. Chem. B.* **1998**, 102, 10885.
72. Valdimir, M.; Riesz, P. *Ultrason. Sonochem.* **1996**, 3, S173.
73. Weissler, A. *J. Am. Chem. Soc.* **1959**, 81, 1077.
74. Makino, K; Mossoba, M. M.; Riesz, P. *J. Phys. Chem.* **1983**, 87, 1369.
75. Makino, K; Mossoba, M. M.; Riesz, P. *J. Am. Chem. Soc.* **1982**, 104, 3537.
76. Henglein, A. *Ultrason. Sonochem.* **1995**, 2, S115.
77. Gutierrez, M.; Henglein, A.; Ibanez, F. *J. Phys. Chem.* **1991**, 95, 6044.
78. Eklund, J. C.; Waller, D. N.; Rebbitt, T. O.; Marken, F.; Compton, R. G. *J. Chem. Soc. Perkin Trans.* **1995**, 2, 1981.
79. Gutierrez, M.; Henglein A.; Dohrmann, J. K. *J. Phys. Chem.* **1987**, 91, 6687.
80. Henglein, A. *Ultrasonics* **1987**, 25, 6.

81. Makino, K.; Mossoba M. M.; Riesz, P. *Radiat. Res.* **1983**, 96, 416.
82. Anabar, M.; Precht, I. *J. Phys. Chem* **1964**, 68, 1460.
83. Fricke, H.; Hart. E. J. *Radiation Dosimetry* chapter 12 Ed. 2 Vol. 2. Academic Press, London edited by F. H. Attix, and William C. Roesch **1966**.
84. Hart, E. J.; Henglein A. *J. Phys. Chem.* **1985**, 89, 4342.
85. von Sonntag, C.; Gertraud, M.;Tauber, A.; Schuchmann, H-P. **1999** *Adv. Sonochem.* **1999**, 5, 109.
86. Hart, E. J.; Henglein, A. *J. Phys. Chem.* **1987**, 91 3654.
87. Mark, G.; Tauber, A.; Laupert, R.; Schuchmann, H. P.; Schulz, D.; Mues, A.; von Sonntag, C. *Ultrason. Sonochem.* **1998**, 5, 41.
88. Price, G. J.; Lenz, E. J. *Ultrasonics* **1993**, 31 451.
89. Price, G. J.; Duck, F. A.; Digby, M.; Holland, W.; Berryman, T. *Ultrason. Sonochem.* **1997**, 4, 165.
90. Upadhyay, S. N.; Gupta, K.; Gupta, M. M. *J. Sci. Ind. Res.* **1985**, 44, 416.
91. Gutierrez, M.; Henglein, A.; Mockel, H. *Ultrason. Sonochem.* **1995**, 2, S111.
92. Matthews, R. W. Int. *J. Appl. Radiat. Isot.* **1982**, 33, 1159.
93. Merenyi, G.; Lind, J. S., *J. Am. Chem. Soc.* **1980**, 102, 5830.
94. McMurray, H. N.; Wilson, B. P. *J. Phys. Chem. A* **1999** 103, 3955.
95. Renaudin, V.; Gondrexon, N.; Boldo, P.; Bernis, A.; Gonthier, Y., *Ultrason. Sonochem.* 1994, 1, S81.
96. Singh, G. *MSC. Project.* Department of Chemistry University of Southampton **2000**.
97. Paul, D. B. *Talanta* **1978**, 25, 377.
98. Weissler, A.; *J. Am. Chem. Soc.* **1959**, 81, 1077.
99. Petrier, C.; Lamy, M.-F.; Francony, A.; Benahcene, A.; David, B.; Renaudin, V.; Gondrexon, N. *J. Phys. Chem.* **1994**, 98, 10514.
100. Frenzel, H.; Schultes, H., *Z. Phys. Chem.* **1934**, 27B 421.
101. Gaitan, D. F.; Crum, L. A.; Roy, R. A.; Church, C. C. *J. Acoust. Soc. Am.* **1992**, 91, 3166.
102. Saksena, T. K.; Nyborg, W. L. *J. Chem. Phys.* **1970**, 53, 1722.
103. Blake, J. R. *Phil. Trans. R. Soc. (London) Ser. A- Math. Phys. Eng. Sci.*, **1999**, 357.
104. Barber, B. P. *et al. Phys. Rep.*, **1997**, 281, 65.
105. Cheeke, J. D. N., *Can. J. Phys.*, **1997**, 75, 77.
106. Brenner, M. P.; Hilgenfeldt, S.; Lohse, D. *Rev. Mod. Phys.* **2002**, 74, 425.
107. Matula, T. J. *Phil. Trans. R. Soc.* (London) **1999**, 357, 225.

108 Gompf, R.; Gunter, G.: Nick, W.; Eisenmenger, W. *Phys. Rev. Lett.* **1997**, 79, 1405.

109. Barber, B. O.; Hiler, R. A.; Lofstedt, R.; Putterman, S. J.; Weninger, K. R. *Phys. Reports* **1997**, 281, 65.

110. Crum, L. A. *Phys. Today* **1994**, September 22.

111. Matula, T. J.; Roy, R. A.; Mourad, P. D.; McNamara, W. B.; Suslick, K. S. *Phys. Rev. Lett.* **1995**, 75, 2602.

112. Hammer, D.; Frommhold, L. *J. Mod. Optics*. **2001**, 48, 239.

113. Griffing, V., *J. Chem. Phys*. **1952**, 20, 939.

114. Suslick, K. S. Doktycz, S. J. Flint, E. B. *Ultrasonics*. **1990**, 28, 280.

115. Frenkel Y. *Acta, Phisiochemica* (USSR) **1940**, 12, 323.

116. Lepoint, T.; De Pauw, D.; Lepoint-Mullie, F.; Goldman, M.; Goldman A. *J. Acoust. Soc. Am.*, **1997**, 101, 2012.

117. Jarman, P. D. *J. Acoust. Soc. Am. 1960*, 32, 1459

118. Barber, B. P.; Putterman, S. *Phys. Rev. Lett.***1992**, 69, 3839.

119. Lofstedt, R.; Barber, B. P.; Putterman, S. *Phys. Fluids A* **1993**, 5, 2911.

120. Wu, C. C.; Roberts, P. H. *Proc. R. Soc. London, Ser. A* **1994**, 323.

121. Moss, W. C.; Clarke, D. B.; Young, D. A. *Phys. Fluids* **1994**, 6, 2979.

122. Frommhold, L.; Atchley, A. A. *Phys. Rev. Lett.* **1994**, 73, 2883.

123. Kamath, V.; Prosperetti, A.; Egolfopoulos, F. N. *J. Acoust. Soc. Am.* **1993**, 94, 248.

124. Moss, W. C.; Clarke, D. B., Young, D. A. *Science* **1997**, 276, 1398.

125. Eberlein, C. *Phys. Rev. A*. **1996**, 53, 2772.

126. Eberlein, C. *Phys. Rev, Lett.* **1996**, 76, 3842.

127. Chin, D-T.; Tsang, C-H. *J. Electrochem. Soc.* **1978**, 135, 1461.

128. Kinsler, L. E.; Frey, A. R.; Coppens, A. B.; Sanders, J. V. *Fundamentals of Acoustics, 3rd Edition*, John Wiley & Sons, New York, **1982**.

129. Leighton, T. G.; Ho, W. L.; Flaxman, R. *Ultrasonics* **1997**, 35, 399.

130. Reynolds, D. D. *Engineering Principles of Acoustics, Noise and Vibration Control.*; Allyn and Bacon Inc.: Boston, **1981**.

131. Birkin, P. R.; Leighton, T. G.; Power, J. F; Simpson, M. D.; Vinçotte, A. M. L.; Joseph P. F. *J. Phys. Chem. A.* In press **2002**.

132. Brekhovskikh, L. M. *Waves in Layered Media*, Academic Press, **1960**.

133. Cervenka, P.; Challande, P. *J. Acoust. Soc. Am.*, **1991**, *89*, 1579-1589.

134. Fahy, F. J. *Foundations in Engineering Acoustics* Academic Press, London, **2001**.

135. Fox, F. E.; Stanley R.; Larson, G. S. *J. Acoust. Soc. Am.* **1955**, 27, 534.

136. Mason, T. J.; Lorimer, J. P.; Bates, D. M. *Ultrasonics*, **1992**, *30*, 40.
137. Birkin, P. R.; Power, J. F.; Leighton, T. G.; Vincotte, A. M-L *Anal. Chem.* **2002**, 74, 2584.
138. Bertotti, M.; Pletcher, D. *Analytica Chimica Acta* **1997**, 337, 49.
139. Cotton, F. A.; Wilkinson, G.; *Advanced Inorganic Chemistry* Fifth edition John Wiley & Sons, New York, **1988**.
140. Robertson, P. M.; Gnehm, W.; Ponto, L. *J. Appl. Electrochem.* **1983**, 13, 307.
141. Czarnetzki, L.; Janssen, J. *Electrochimica Acta* **1998**, 33, 561.
142. Vogel, A. I., *Quantitative Inorganic Analysis, Theory and Practice, 2nd Edition* Longmans, Green and Co. London **1951**.
143. Thomas, J. K., *Trans. Faraday Soc.* **1965**, 61, 702.
144. Kraljic, I.; Trumbore, C. N. *J. Am. Chem. Soc.* **1965**, 87, 2547.
145. Macpherson, J. V., *Electroanalysis*, **2000**, 12, 1001.
146. Pratt, W. K.; Johnson, D. C., *Electrochim. Acta*, **1982**, 27, 115.
147. Dawson, R. M. C.; Elliott, D. C.; Elliott, W. H.; Jones, K. M. *Data for Biochemical Research, 3rd Ed.* Oxford Science Publications, **1986**.
148. Evans, S. A. G.; Elliott, J. M.; Andrews, L. M.; Bartlett, P. N.; Doyle, P. J.; Denuault, G. *Anal. Chem.* **2002**, 74, 1322.
149. Abdelsalam, M. E.; Birkin, P. R., *PCCP*, Submitted for publication **2002**.
150. Hoffmann, R. M.; Hua, I.; Hochemer, R. *Ultrason. Sonochem.* **1996**, 3, S163.
151. Francony, A.; Petrier, C. *Ultrason. Sonochem.* **1996**, 3, S77.
152. Pletcher, D.; Alverez-Gallegos, A. *Electrochim. Acta* **1998,** 44, 853.
153. Pletcher, D.; Alverez-Gallegos, A. *Electrochim. Acta* **1999,** 44, 2483.
154. Birkin, P. R.; Power, J. F.; Abdelsalam, M. E.; Leighton, T. G., *Ultrason. Sonochem.* Submitted for publication **2002**.
155. Abdelsalam, M. E.; Birkin, P. R. *Phys. Chem. Chem. Phys.*, **2002**, 4, 5340
156. Millero, F. J.; Sharma, V. K.; Karn, B. *Marine Chemistry*, **1991**, 36, 71.
157. Millero, F. J., Geochem, *Cosmochim. Acta*, **1985**, 49, 547.
158. Vincotte, A. M. L. *'A frequency study of Sonoluminescence and Sonochemical Activity'*, MPhil Thesis, University of Southampton, UK September **1999**.
159. Hung, Hui-Ming; Hoffmann, M. R. *J. Phys. Chem. A.* **1999**, 103, 2734.
160. Kojima, Y.; Koda, S.; Nomura, H. *Ultrason. Sonochem.* **2001**, 8, 75.
161. Sato, M.; Itoh, H.; Fujii, T. *Ultrason.* **2000**, 38, 312.

162. Birkin, P. R.; Power, J. F.; Leighton, T. G.; Vincotte, A. M-L. *Chemistry a European Journal* Submitted for publication **2002**.

163. Lohse, D. *Physics Rev. Lett.*, **1997**, 78, 1359.

164. Lohse, D.; Hilgenfeldt, S. **1997**, *J. Chem. Phys.*, **1997**, 107, 6986.

165. Didenko, Y. T.; Suslick, K. S. *Nature* **2002**, 418, 394.

166. Verraes, T.; Lepoint-Mullie, F.; Henglein, A. *J. Acoust. Soc. Am.* **2000**, 108, 117.

167. Harris D. C., *Quantitative Chemical Analysis* fifth edition W. H. Freeman and Co. New York.

168. Fang, X.; Mark, G.; von Sonntag, C. *Ultrason. Sonochem.* **1996**, 3, 57.

169. Lind, J.; Merenyi, G.; Eriksen, T. E. *J. Am. Chem. Soc.* **1983**, 105, 7655.

170. Vinodgopal, K; Ashokkumar, M.; Grieser, F. *J. Phys. Chem. B.*, **2001**, 105, 3338.

171. Ashokkumar, M; Vinodgopal, K; Grieser, F. *J. Phys. Chem. B.*, **2000**, 104, 6447.

172. Ashokkumar, M.; Crum, L. A.; Frensley, C. A.; Grieser, F.; Matula, T. J.; McNamara, W.B.; Suslick, K. S. *J. Phys. Chem. A.*, **2000**, 104, 8462.

173. Ashokkumar, M.; Hall, R.; Mulvaney, P.; Grieser, F. *J. Phys. Chem. B.*, **1997**, 101, 10845.

PUBLICATIONS

(1). Birkin, P. R.; Leighton, T. G.; Power, J. F; Simpson, M. D.; Vinçotte, A. M. L.; Joseph P. F., "Experimental and Theoretical Characterisation of Sonochemical cells, Part 1 Cylindrical Reactors and Their use to Calculate the Speed of Sound in Aqueous Solutions" *J. Phys. Chem. A.* **2003**, 107, 306-320

(2). Birkin, P. R.; Power, J. F.; Leighton, T. G.; Vinçotte, A. M-L, "Sonoluminescence: an indication of sonochemical activity?" *Phys. Chem. Chem. Phys.* Submitted for publication **2003**.

(3). Birkin, P. R.; Power, J. F.; Leighton, T. G.; Vinçotte, A. M-L, "Cathodic Electrochemical Detection of Sonochemical Radical Products" *Anal. Chem.* **2002**, 74, 2584-2590.

(4). Birkin, P. R.; Power, J. F.; Abdelsalam, M. E.; Leighton, T. G., "Electrochemical, Luminescent and Photographic Characterisation of Cavitation" *Submitted to the eight conference of European Sonochemistry*, Cagliari, Sardinia, Italy **2002**. Accepted for publication in *Ultrason. Sonochem.* December **2002**.

(5). Birkin, P. R.; Power, J. F.; Leighton, T. G. "Electrochemical evidence of $H^{\bullet}$ produced by ultrasound" *J. Chem. Soc. Chem. Commun.* **2001**, 2230-2231.

(6). Birkin, P. R.; Leighton, T. G.; Watson, Y. E.; Power, J. F., "Acoustoelectrochemistry" Acoustics *Bulletin*, **2001**, 26, 24-37.